NUMERICAL MODELLING OF COMPLEX THERMO-HYDRO-MECHANICAL INTERACTIONS IN THERMO-ACTIVE PILE FOUNDATIONS

A thesis submitted to the Imperial College London in partial fulfilment of the requirements for the degree of Doctor of Philosophy

by

RYAN YIN WAI LIU

Department of Civil and Environmental Engineering

Imperial College London

London SW7 2AZ

March 2022

DECLARATION

The work presented in this thesis was carried out in the Department of Civil and Environmental Engineering at Imperial College London. This thesis is the result of my own work and any quotation from, or description of the work of others is acknowledged herein by reference to the sources, whether published or unpublished. This thesis is not the same as any that I have submitted for any degree, diploma or other qualification at any other university. No part of this thesis has been or is being concurrently submitted for any such degree, diploma or other qualification.

The copyright of this thesis rests with the author. Unless otherwise indicated, its contents are licensed under a Creative Commons Attribution-Non Commercial 4.0 International Licence (CC BY-NC).

Under this licence, you may copy and redistribute the material in any medium or format. You may also create and distribute modified versions of the work. This is on the condition that: you credit the author and do not use it, or any derivative works, for a commercial purpose.

When reusing or sharing this work, ensure you make the licence terms clear to others by naming the licence and linking to the licence text. Where a work has been adapted, you should indicate that the work has been changed and describe those changes.

Please seek permission from the copyright holder for uses of this work that are not included in this licence or permitted under UK Copyright Law.

Ryan Yin Wai Liu

London, March 2022

ABSTRACT

Thermo-active piles have gained popularity in recent years due to their dual role of providing structural stability as foundations and exchanging heat with the ground as ground source heat exchangers to provide low carbon heating and cooling. The installation of thermo-active piles is further facilitated by the enforcement of sustainability targets, such as the Merton Rule, which requires a proportion of the energy demand of a building to be met by renewable energy generated on site. When thermo-active piles operate and are, therefore, subjected to changes in temperature, the existence of a temperature field and the resulting thermal expansion and contraction of materials induces a complex thermo-mechanical response.

The objective of the research presented in this thesis is to investigate the thermo-mechanical behaviour of thermo-active piles when they are subjected to changes in temperature, which can be due to the heat of hydration generated when they are cast, or their operation. This is achieved by performing fully coupled thermo-hydro-mechanical (THM) finite-element (FE) analyses using the Imperial College Finite Element Program (ICFEP). In order to simulate accurately the thermo-mechanical behaviour of thermo-active piles resulting from their operation, three-dimensional (3D) analyses are carried out where the heat exchanger pipes are explicitly modelled. However, these analyses are computationally expensive that render them impractical to perform in routine engineering design. A simplified method to model the problem using only two-dimensional (2D) analyses is developed. To model accurately the amount of heat generated from the hydration of concrete, a simple concrete heat of hydration model is developed, which can be readily applied in geotechnical applications.

The aforementioned developments ultimately allow the identification of whether the critical stage in terms of thermo-mechanical behaviour of a thermo-active pile is during its hydration or operation.

ACKNOWLEDGEMENTS

I would like to express my sincerest gratitude to my supervisor Dr. David Taborda for his patient and kind guidance not only throughout my PhD studies, but also during my UROP research experience and Final Year Project in my undergraduate studies. It has been my honour and pleasure to work with him throughout the years and I would have not been able to reach this far without his positive feedback, support and encouragement.

I must also thank Prof. Jamie Standing and Prof. Lidija Zdravković, who have both supervised UROP research projects during my undergraduate studies. It was these experiences which ultimately motivated me to pursue a PhD degree in the Geotechnics Section at Imperial College.

I would also like to thank Prof. David Potts who implemented the concrete heat of hydration model that I have developed into ICFEP.

I am also very grateful to Mr. Anthony Fisher from Cementation Skanska, who has provided me with field measurements of temperature within hydrating concrete piles. The validation of my heat of hydration model would not have been so successful without these data.

This research is funded by the Imperial College President's PhD Scholarship and the Engineering and Physical Sciences Research Council (EPSRC) (grant number: EP/R512540/1) and I am very grateful for this financial support.

Last but not least, I am extremely grateful to the support from my family and friends, my PhD studies would not have been so enjoyable without them.

TABLE OF CONTENTS

DECLARATION **2**

ABSTRACT **3**

ACKNOWLEDGEMENTS **4**

TABLE OF CONTENTS **5**

LIST OF FIGURES **13**

LIST OF TABLES **26**

LIST OF SYMBOLS **29**

CHAPTER 1 INTRODUCTION **37**

1.1 BACKGROUND **37**

1.2 SCOPE OF RESEARCH **38**

1.3 THESIS OUTLINE **39**

CHAPTER 2 PRELIMINARIES **42**

2.1 INTRODUCTION **42**

2.2 GEOTHERMAL ENERGY AND GROUND SOURCE HEAT PUMP SYSTEMS **42**

2.2.1 Classification of geothermal energy *43*

2.2.2 Ground source heat pump systems *47*

2.2.2.1 Heat pumps *47*

2.2.2.2 Open loop systems *49*

2.2.2.3 Closed loop systems *50*

2.3 THERMO–ACTIVE STRUCTURES **55**

2.3.1 Thermo-active piles *57*

2.3.2 Thermo-active diaphragm walls *69*

2.3.3 Thermo-active tunnels *73*

2.4 HEAT TRANSFER MECHANISMS IN SOILS **78**

2.4.1 Conduction *79*

2.4.2 Convection *79*

2.4.3 Radiation *81*

2.4.4 Vapour diffusion *81*

2.4.5 Freeze-thaw processes *81*

2.5 THERMAL AND THERMO-MECHANICAL PROPERTIES OF SOILS AND CONCRETE **82**

2.5.1 Thermal conductivity λ *82*

2.5.1.1 Laboratory testing methods *83*

2.5.1.2 In-situ testing methods *87*

2.5.1.3 Typical values for London Clay *89*

2.5.1.4 Typical values for concrete *92*

2.5.2 Specific/volumetric heat capacity C_p/c_{vol} *99*

2.5.2.1 Testing methods *99*

2.5.2.2 Typical values for London Clay *100*

2.5.2.3 Typical values for concrete *101*

2.5.3 Coefficient of thermal expansion α *102*

2.5.3.1 Water *103*

2.5.3.2 London Clay *104*

2.5.3.3 Concrete *104*

2.6 EXISTING CAPABILITIES OF ICFEP **106**

2.6.1 Coupled THM formulation *107*

2.6.2 Thermal boundary conditions *109*

2.6.2.1 Prescribed temperature *109*

2.6.2.2 Prescribed heat flux *109*

2.6.2.3 Coupled thermo-hydraulic heat flux *110*

2.6.3 Modelling of heat exchanger pipes *111*

2.7 CONCLUSIONS **118**

CHAPTER 3 THERMO-MECHANICAL BEHAVIOUR OF THERMO-ACTIVE PILES **121**

3.1 INTRODUCTION **121**

3.2 FRAMEWORK FOR UNDERSTANDING THE THERMO-MECHANICAL BEHAVIOUR OF THERMO-ACTIVE PILES **121**

3.2.1 Thermal loading *122*

3.2.2 Thermo-mechanical loading *127*

3.3 FIELD STUDIES **129**

3.3.1 Regional office of Berkel and Company Contactors, Richmond, Texas, United States *134*

3.3.2 Yongin city, Korea *137*

3.3.3 Piterm research project, Valencia, Spain *140*

3.4 LABORATORY STUDIES **143**

3.4.1 Tests at Chongqing University, Chongqing, China *149*

3.4.2 Tests at Hohai University, Nanjing, China *151*

3.5 NUMERICAL STUDIES **154**

3.5.1 Numerical study by Gawecka et al. (2017) *160*

3.5.2 Numerical study by Zito et al. (2021) *164*

3.6 CONCLUSIONS **167**

CHAPTER 4 NUMERICAL MODELLING OF THERMO-ACTIVE PILES **170**

4.1 INTRODUCTION **170**

4.2 THREE-DIMENSIONAL FINITE-ELEMENT MODELLING OF THERMO-ACTIVE PILES **170**

4.2.1 Mesh, stratigraphy and types of elements *171*

4.2.2 Pipe dimensions and arrangements *172*

4.2.3 Initial and boundary conditions *174*

4.2.4 Material models and properties *175*

4.2.5 Modelling sequence *177*

4.2.6 Results – thermal performance *179*

4.2.6.1 Evolution of the system's power with time *179*

4.2.6.2 Storage of energy within different parts of the thermo-active pile system with time *181*

4.2.7 Results – thermo-mechanical response *189*

4.2.7.1 Thermally-induced pile head displacement *189*

4.2.7.2 Thermally-induced pile axial stress *190*

4.2.7.3 Thermally-induced excess pore water pressure *199*

4.3 CONCLUSIONS 204

CHAPTER 5 A SIMPLIFIED METHOD FOR MODELLING THERMO-ACTIVE PILES 208

5.1 INTRODUCTION 208

5.2 THE METHOD 208

5.3 DEMONSTRATION OF THE METHOD 211

5.4 VALIDATION AND PERFORMANCE OF THE METHOD 213

5.4.1 Temperature changes 214

5.4.2 Thermally-induced pile head displacements 216

5.4.3 Thermally-induced pile axial stresses 218

5.4.4 Thermally-induced excess pore water pressures 219

5.5 SENSITIVITY OF THE PROPOSED METHOD TO ΔE ESTIMATE 221

5.6 CONCLUSIONS 224

CHAPTER 6 DEVELOPMENT OF A NEW HEAT OF HYDRATION MODEL FOR CONCRETE 225

6.1 INTRODUCTION 225

6.2 HEAT OF HYDRATION OF CONCRETE 226

6.3 MEASUREMENTS OF HEAT OF HYDRATION 231

6.3.1 Laboratory measurements 231

6.3.1.1 Adiabatic test 231

6.3.1.2 Semi-adiabatic test 233

6.3.1.3 Isothermal test 235

6.3.2 Field measurements 242

6.4 EXISTING HEAT OF HYDRATION MODELS FOR CONCRETE (LIST OF SYMBOLS DOES NOT APPLY TO THIS SECTION) 251

6.5 A NEW HEAT OF HYDRATION MODEL FOR CONCRETE 272

6.6 CONCLUSIONS 277

CHAPTER 7 PERFORMANCE OF THE HEAT OF HYDRATION MODEL FOR CONCRETE 278

7.1 INTRODUCTION 278

7.2 PARAMETRIC STUDY 279

7.2.1 Q_{max} 279

7.2.2 τ 280

7.2.3 β 281

7.2.4 E_a 282

7.2.5 t_n 283

7.3 IMPLEMENTATION INTO A FINITE-ELEMENT PROGRAM 284

7.4 CALIBRATION AND VALIDATION WITH ISOTHERMAL CALORIMETRY 286

7.5 CALIBRATION AND VALIDATION WITH FIELD MEASUREMENTS 290

7.5.1 A numerical technique to simulate the temperature rise within a hydrating pile using the proposed model 291

7.5.2 The field measurements 295

7.5.3 Calibration with Genetic Algorithms 297

7.6 CONCLUSIONS 304

CHAPTER 8 THE ROLE OF HEAT OF HYDRATION OF CONCRETE ON THE OPERATION OF THERMO-ACTIVE PILES 305

8.1 INTRODUCTION 305

8.2 EFFECTS OF PILE HYDRATION ON THE SURROUNDING SOIL 305

8.2.1 Details of the analyses 305

8.2.2 Results of the analyses 307

8.3 MODELLING OF HYDRATION AND OPERATION OF THERMO-ACTIVE PILES 309

8.3.1 Temperature changes 309

8.3.2 Thermally-induced pile head displacements 311

8.3.3 Thermally-induced pile axial stresses 312

8.3.4 Thermally-induced excess pore water pressure 315

8.4 CONCLUSIONS 316

CHAPTER 9 CONCLUSIONS AND FUTURE RESEARCH 318

9.1 INTRODUCTION 318

9.2 THERMO-MECHANICAL BEHAVIOUR OF THERMO-ACTIVE PILES DURING OPERATION 319

9.3 THERMO-MECHANICAL BEHAVIOUR OF PILES DUE TO CONCRETE HEAT OF HYDRATION 323

9.4 RECOMMENDATIONS FOR FUTURE RESEARCH 324

REFERENCES 327

APPENDIX A A PARAMETRIC STUDY ON THE EFFECTS OF $\lambda c/\lambda s$ TO THE SIMULATED TEMPERATURE RISE WITHIN A HYDRATING PILE 348

APPENDIX B MIX DESIGN FOR THE CONCRETE IN LP 1 355

APPENDIX C MIX DESIGN FOR THE CONCRETE IN LP 2 356

APPENDIX D FIGURES COMPARING THE MODELLED AND MEASURED TEMPERATURE RISE CURVES FOR PILES FROM LP 1 357

LIST OF FIGURES

Figure 2.1 Worldwide use of geothermal energy in different sectors between 1995 and 2020 (Lund & Toth, 2021) 43
Figure 2.2 Average measured temperatures with depth at the Royal Edinburgh Observatory on different months (Sanner, 2005) 45
Figure 2.3 (a) Locations in the United Kingdom where ground temperatures are measured and (b) mean annual temperature at $1\ m$ depth (for non-urban locations corrected to sea level) with respect to the Northings of the measured location (Busby, 2015) 46
Figure 2.4 Mean annual ground temperatures in the United States in Fahrenheit (Pauly, 2010) 46
Figure 2.5 Schematic diagram of a heat pump (Sanner, 2005) 48
Figure 2.6 The most common open loop system configuration which involves a production well and an injection well (Sanner, 2005) 49
Figure 2.7 Illustration of heat exchanger pipes connected in series and in parallel in horizontal closed loop systems (Sanner, 2005) 52
Figure 2.8 Illustration of heat exchanger pipes arranged in slinky-coils in horizontal closed loop systems (Fujii et al., 2012) 52
Figure 2.9 Illustration of (a) single U-loop configuration, (b) double U-loop configuration, (c) coaxial configuration (Sliwa et al., 2016) and (d) double-pipe configuration (Morino & Oka, 1994) 54
Figure 2.10 Temperature with depth profiles measured at a distance of $1\ m$ from the BHE in Elgg (Rybach, 2001) 55
Figure 2.11 Illustration of heat exchanger pipes being fixed to the reinforcement cage in a thermo-active pile (Soga & Rui, 2016) 57
Figure 2.12 Number of thermo-active piles installed cumulatively and the resulting $CO2$ savings in the United Kingdom from 2005 to 2016 (Sani et al., 2019) 58
Figure 2.13 Plan view of One New Change showing the locations of thermo-active piles, production and injection wells (Devriendt et al., 2012) 59
Figure 2.14 Illustration of heat exchanger pipes fixed to the reinforcement cage of a thermo-active diaphragm wall (Hofinger & Kohlböck, 2005) 69
Figure 2.15 Illustration of the typical positions of heat exchanger pipes within the cross-section of a thermo-active diaphragm wall (Soga & Rui, 2016) 70

Figure 2.16 Illustration of the typical vertical configuration of heat exchanger pipes in a diaphragm wall (Soga & Rui, 2016) 71
Figure 2.17 Illustration of a horizontal configuration of heat exchanger pipes in a diaphragm wall (Brandl, 1998) 72
Figure 2.18 Cross-section of a typical thermo-active diaphragm wall panel at the Bulgari hotel (Amis et al., 2010) 73
Figure 2.19 Illustration of heat exchanger pipes fixed to the reinforcement cage of a thermo-active tunnel lining (Nicholson et al., 2014) 74
Figure 2.20 Heat exchanger pipe connection between two precast thermo-active tunnel lining segments (Soga & Rui, 2016) 75
Figure 2.21 Illustration of heat exchanger pipes being fitted in a geotextile (Hofinger & Kohlböck, 2005) 75
Figure 2.22 A schematic diagram of the thermo-active tunnel at the LT22 section of the Lainzer Tunnel (Brandl, 2006) 76
Figure 2.23 A 'ground&air' pipe configuration for the Enertun precast thermo-active segmental tunnel lining (Barla et al., 2019) 77
Figure 2.24 Dominant heat transfer mechanism by the grain size and degree of saturation of a soil (Loveridge, 2012) 78
Figure 2.25 Configuration of the guarded hot plate test apparatus (British Standards Institution, 2001) 86
Figure 2.26 A schematic diagram of the divided bar test (Sibbitt et al., 1979) 87
Figure 2.27 The effects of water content on the thermal conductivity of concrete (Khoury, 1983) 93
Figure 2.28 The third-order polynomial function proposed by Cui et al. (2020) fitted on the data from Çengel and Ghajar (2011) on the linear coefficient of thermal expansion of water 104
Figure 2.29 The coupling between thermal, hydraulic and mechanical systems 108
Figure 2.30 Illustration of the 3×3 submatrices of the stiffness matrix in ICFEP to solve for the nodal unknowns (displacements, pore water pressures and temperatures) 108
Figure 2.31 A 1D linear element with two nodes and natural coordinate S (Gawecka, 2017) 112
Figure 2.32 A 1D quadratic element with three nodes and natural coordinate S (Gawecka, 2017) 112

Figure 2.33 Comparison between measured and modelled temperatures at different distances from the wall of BHE in the laboratory TRT from Beier et al. (2011) (Gawecka et al., 2020) 116
Figure 2.34 Comparison between measured and modelled temperatures at the monitoring point within the cross-section of the BHE at depths of (a) $13.8\ m$ and (b) $23.8\ m$ (Gawecka, 2017; Gawecka et al., 2020) 117
Figure 2.35 Comparison between measured and modelled temperatures at the pipe outlet in the laboratory TRT from Beier et al. (2011) (Gawecka et al., 2020) 118
Figure 2.36 Comparison between measured and modelled temperatures at the pipe outlet in the field TRT from Loveridge et al. (2014) (Gawecka, 2017; Gawecka et al., 2020)... 118
Figure 3.1 The profiles of $\varepsilon T - Obs$, $\varepsilon T - Free$, $\varepsilon T - Rstr$ and PT for (a) free body case when the pile is heated (b) free body case when the pile is cooled (c) perfectly restrained case when the pile is heated (d) perfectly restrained case when the pile is cooled (Bourne-Webb et al., 2013; Gawecka, 2017) 123
Figure 3.2 The profiles of $\varepsilon T - Obs$, PT and qs when a thermo-active pile surrounded by soil which is unrestrained on both pile ends is (a) heated and (b) cooled (Amatya et al., 2012; Gawecka, 2017) 124
Figure 3.3 The profiles of $\varepsilon T - Obs$, PT and qs when a thermo-active pile surrounded by soil which is (a) partially restrained at both ends, (b) partially restrained at the pile toe, and (c) partially restrained at the pile head is heated (Amatya et al., 2012; Gawecka, 2017) 126
Figure 3.4 Behaviour of a thermo-active pile surrounded by soil that is subjected to (a) mechanical loading only, (b) heating only, (c) combination of mechanical loading and heating, (d) cooling only, and (e) combination of mechanical loading and cooling (Amatya et al. (2012); Gawecka, 2017) 128
Figure 3.5 Soil profile of the test site, dimensions of the thermo-active test piles and the locations at which the VWSG were installed (Sutman et al., 2017) 135
Figure 3.6 The thermally-induced (a) axial stress and (b) shaft resistance profiles obtained during a heating cycle for TP-1 (Sutman et al., 2017) 136
Figure 3.7 The (a) axial stress and (b) shaft resistance profiles obtained during the heating cycle for TP-3 (Sutman et al., 2017) 137
Figure 3.8 Thermally-induced axial stress profiles obtained (a) during the operation stage of the cooling test (15 days), (b) during the resting stage of the cooling test (15 days), (c)

during the operation stage of the heating test (15 days), and (d) during the resting stage of the heating test (15 days) (Sung et al., 2018) 139
Figure 3.9 The scheme of Test C together with the identification of monitoring moments (de Santayana et al., 2020) 141
Figure 3.10 Pile head displacements recorded during Test C (de Santayana et al., 2020) 141
Figure 3.11 Total axial load profiles recorded during Test C (de Santayana et al., 2020) 142
Figure 3.12 Total shaft resistance profiles recorded during Test C (de Santayana et al., 2020) 143
Figure 3.13 Average temperatures measured for Pile 1, 3 and 4 over the three thermal cycles (Wang et al., 2017) 150
Figure 3.14 Pile head displacements measured for Pile 1, 3 and 4 over the three thermal cycles (Wang et al., 2017) 151
Figure 3.15 Load-displacement curves when the piles were heat up to different temperatures (Huang et al., 2018) 152
Figure 3.16 Shaft resistance profiles (shaded area represents thermally-induced shaft resistance) when the pile was (a) heated and (b) cooled (Huang et al., 2018) 153
Figure 3.17 Pile head displacement curve for the pile subjected to a thermal cycle following mechanical loading (Huang et al., 2018) 154
Figure 3.18 Illustration of the load-transfer method (Kraft et al., 1981) 155
Figure 3.19 Comparison of the evolution of maximum thermally-induced axial stress for Analyses A, B1 and B2 (Gawecka et al., 2017) 162
Figure 3.20 Comparison of temperatures at the circumference of the pile for Analyses A and C (Gawecka et al., 2017) 164
Figure 3.21 Comparison of the evolution of maximum thermally-induced axial stress for Analyses A and C (Gawecka et al., 2017) 164
Figure 3.22 The axial load and shaft resistance profiles for the pile in the (a) 30 m mesh and (b) 4 m mesh (Zito et al., 2021) 166
Figure 3.23 The (a) thermally-induced pile head displacement and (b) thermally-induced axial stress with time for the pile in both meshes (Zito et al., 2021) 167
Figure 4.1 Half of the FE mesh 171
Figure 4.2 Plan view of half of the zoomed-in FE mesh detailing the pile (shaded in grey) 172
Figure 4.3 Illustration of the 1U, 2U and 3U pipe arrangements 173
Figure 4.4 (a) Initial pore water pressure profile and (b) $K0$ profile 174

Figure 4.5 Axial stress profiles for the 600 mm and 900 mm piles just before the start of heating....178
Figure 4.6 Development of P/L with time for pile diameters of 600 mm and 900 mm and pipe arrangements of 1U, 2U and 3U....180
Figure 4.7 Average changes in temperature in different sections for the 600 mm diameter pile with 1U pipe arrangement....182
Figure 4.8 Average changes in temperature in different sections for the 600 mm diameter pile with 2U pipe arrangement....182
Figure 4.9 Average changes in temperature in different sections for the 600 mm diameter pile with 3U pipe arrangement....183
Figure 4.10 Average changes in temperature in different sections for the 900 mm diameter pile with 1U pipe arrangement....183
Figure 4.11 Average changes in temperature in different sections for the 900 mm diameter pile with 2U pipe arrangement....184
Figure 4.12 Average changes in temperature in different sections for the 900 mm diameter pile with 3U pipe arrangement....184
Figure 4.13 Evolution of $\Delta Ei/i\Delta Ei$ with time for the 600 mm diameter pile with 1U pipe arrangement....185
Figure 4.14 Evolution of $\Delta Ei/i\Delta Ei$ with time for the 600 mm diameter pile with 2U pipe arrangement....186
Figure 4.15 Evolution of $\Delta Ei/i\Delta Ei$ with time for the 600 mm diameter pile with 3U pipe arrangement....186
Figure 4.16 Evolution of $\Delta Ei/i\Delta Ei$ with time for the 900 mm diameter pile with 1U pipe arrangement....187
Figure 4.17 Evolution of $\Delta Ei/i\Delta Ei$ with time for the 900 mm diameter pile with 2U pipe arrangement....187
Figure 4.18 Evolution of $\Delta Ei/i\Delta Ei$ with time for the 900 mm diameter pile with 3U pipe arrangement....188
Figure 4.19 Thermally-induced pile head displacement for the six analyses performed....189
Figure 4.20 Distribution of (a) temperature change ℃ and (b) thermally-induced axial stresses $\sigma T\ kPa$ within the cross-section of the 600 mm pile with 1U pipe arrangement at $t = 7\ days$ and 17 m depth....192

Figure 4.21 Distribution of (a) temperature change ℃ and (b) thermally-induced axial stresses $\sigma T\ kPa$ within the cross-section of the 600 mm pile with 2U pipe arrangement at $t = 4\ days$ and 17 m depth.....192
Figure 4.22 Distribution of (a) temperature change ℃ and (b) thermally-induced axial stresses $\sigma T\ kPa$ within the cross-section of the 600 mm pile with 3U pipe arrangement at $t = 2.5\ days$ and 17 m depth.....193
Figure 4.23 Distribution of (a) temperature change ℃ and (b) thermally-induced axial stresses $\sigma T\ kPa$ within the cross-section of the 900 mm pile with 1U pipe arrangement at $t = 8\ days$ and 17 m depth.....193
Figure 4.24 Distribution of (a) temperature change ℃ and (b) thermally-induced axial stresses $\sigma T\ kPa$ within the cross-section of the 900 mm pile with 2U pipe arrangement at $t = 5\ days$ and 17 m depth.....194
Figure 4.25 Distribution of (a) temperature change ℃ and (b) thermally-induced axial stresses $\sigma T\ kPa$ within the cross-section of the 900 mm pile with 3U pipe arrangement at $t = 4\ days$ and 17 m depth.....194
Figure 4.26 Distribution of σT with depth for the analyses on the 600 mm pile 196
Figure 4.27 Distribution of σT with depth for the analyses on the 900 mm pile 197
Figure 4.28 Evolution of $\sigma Tmax$ with time for the six analyses performed.....197
Figure 4.29 Peak $\sigma Tmax$ and transient behaviour plotted with the recommended values from the design charts by GSHPA (2012) for diameters of (a) 600 mm and (b) 900 mm...198
Figure 4.30 Number of heat sources normalised by pile circumference versus time to reach peak $\sigma Tmax$ 199
Figure 4.31 Distribution of thermally-induced excess pore water pressure with θ at a radial distance of 250 mm away from the pile edge in the soil at mid-depth of the 600 mm pile with 1U pipe arrangement.....201
Figure 4.32 Distribution of thermally-induced excess pore water pressure with θ at a radial distance of 250 mm away from the pile edge in the soil at mid-depth of the 600 mm pile with 2U pipe arrangement.....202
Figure 4.33 Distribution of thermally-induced excess pore water pressure with θ at a radial distance of 250 mm away from the pile edge in the soil at mid-depth of the 600 mm pile with 3U pipe arrangement.....202

Figure 4.34 Distribution of thermally-induced excess pore water pressure with θ at a radial distance of 250 mm away from the pile edge in the soil at mid-depth of the 900 mm pile with 1U pipe arrangement.....203
Figure 4.35 Distribution of thermally-induced excess pore water pressure with θ at a radial distance of 250 mm away from the pile edge in the soil at mid-depth of the 900 mm pile with 2U pipe arrangement.....203
Figure 4.36 Distribution of thermally-induced excess pore water pressure with θ at a radial distance of 250 mm away from the pile edge in the soil at mid-depth of the 900 mm pile with 3U pipe arrangement.....204
Figure 4.37 Evolution with time of the θ-averaged thermally-induced excess pore water pressure at a radial distance of 250 mm away from the pile edge in the soil at mid-depth of the pile for the six analyses performed.....204
Figure 5.1 Illustration of the thermal boundary condition for the 2D thermal analysis 211
Figure 5.2 Illustration of θ versus temperature curve at $r = rpipes$ and $t = 8\ days$ for the 2D thermal analysis on the 900 mm pile with 1U pipe arrangement 212
Figure 5.3 Illustration of time versus $Ttbc$ for the 900 mm pile with 1U pipe arrangement 212
Figure 5.4 The axisymmetric FE mesh and the zoomed-in mesh detailing the pile (shaded in grey) and the location where the time-dependent temperature $Ttbc$ is applied within the pile (highlighted in red) for the axisymmetric analyses.....213
Figure 5.5 Evolutions of temperature changes with time computed with the proposed method and the 3D analyses at (a) centre of pile, (b) edge of pile, and (c) 250 mm away from edge of pile in the soil for the 600 mm diameter pile 215
Figure 5.6 Evolutions of temperature changes with time computed with the proposed method and the 3D analyses at (a) centre of pile, (b) edge of pile, and (c) 250 mm away from edge of pile in the soil for the 900 mm diameter pile 216
Figure 5.7 Evolutions of thermally-induced pile head displacement with time computed with the proposed method and the 3D analyses for the 600 mm diameter pile 217
Figure 5.8 Evolutions of thermally-induced pile head displacement with time computed with the proposed method and the 3D analyses for the 900 mm diameter pile 217
Figure 5.9 Evolution of $\sigma Tmax$ with time computed with the proposed method compared with those from the 3D analyses for the (a) 600 mm and (b) 900 mm piles 219

Figure 5.10 Evolutions of thermally-induced excess pore water pressure with time computed with the proposed method and the 3D analyses at $250\ mm$ away from edge of pile in the soil for the $600\ mm$ diameter pile 220
Figure 5.11 Evolutions of thermally-induced excess pore water pressure with time computed with the proposed method and the 3D analyses at $250\ mm$ away from edge of pile in the soil for the $900\ mm$ diameter pile 221
Figure 5.12 Evolution of $\sigma Tmax$ with time simulated from the proposed method using $\Delta E = 0\ W \cdot m - 1$ and $210\ W \cdot m - 1$ for the (a) $600\ mm$ and (b) $900\ mm$ piles 222
Figure 6.1 Progress of hydration of the four main cement constituents with time (Odler, 1998) and the approximate limits of the four hydration stages 227
Figure 6.2 Rate of hydration heat liberation with time for an ordinary Portland cement (Odler, 1998) 229
Figure 6.3 Adiabatic temperature rise curves for the three concrete samples tested by Lee et al. (2014) 232
Figure 6.4 Adiabatic temperature rise curves for the two concrete samples tested by Shi et al. (2015) 233
Figure 6.5 Semi-adiabatic temperature curves for the two concrete samples tested by Caggiano et al. (2012) 234
Figure 6.6 Semi-adiabatic temperature curves for the three semi-adiabatic tests conducted by Lim et al. (2016) 235
Figure 6.7 Time vs. heat of hydration power curves for cement 'Anläggningscement' at $20, 30, 40$ and $50oC$ (Wadsö, 2003) 236
Figure 6.8 Time vs. accumulated heat of hydration curves for cement 'Anläggningscement' at $20, 30, 40$ and $50oC$ 236
Figure 6.9 Time vs. accumulated heat of hydration curves for Cement A (Zayed et al., 2013) 238
Figure 6.10 Time vs. accumulated heat of hydration curves for Cement B (Zayed et al., 2013) 238
Figure 6.11 Time vs. accumulated heat of hydration curves for Cement C (Zayed et al., 2013) 239
Figure 6.12 Time vs. accumulated heat of hydration curves for Cement D (Zayed et al., 2013) 239

Figure 6.13 Time vs. accumulated heat of hydration curve for Cement E (Zayed et al., 2013) 239
Figure 6.14 Time vs. accumulated heat of hydration curve for Cement F (Zayed et al., 2013) 240
Figure 6.15 Comparison of the ranges in values of heats of hydration for different ASTM types of cement (Copeland et al., 1960) 242
Figure 6.16 Temperature vs. depth profile of a 4 ft (or 1.22 m) diameter hydrating pile (Johnson, 2016).....243
Figure 6.17 Temperature vs. depth profile of a10.7 m long, 1.2 m diameter hydrating pile (Johnson, 2016).....244
Figure 6.18 Arrangement and description of the engineered inclusions (Sun et al., 2020)...245
Figure 6.19 Temperature vs. depth profiles at (a) 2 $hours$, (b) 8 $hours$, (c) 17 $hours$ and (d) 35 $hours$ (Sun et al., 2020) 246
Figure 6.20 Time vs. temperature curves at depths of (a) 4.9 m and (b) 15.1 m (Sun et al., 2020) 246
Figure 6.21 Layout of the diaphragm wall (Liou, 1999) 247
Figure 6.22 Dimensions of the primary and secondary elements (Liou, 1999).....248
Figure 6.23 Typical time vs. temperature curves at different locations within the primary element cross-section (Liou, 1999).....248
Figure 6.24 Typical time vs. temperature curves at different locations within the secondary element cross-section (Liou, 1999).....249
Figure 6.25 Dimensions and locations of thermocouples within the cross-section of primary (left) and secondary (right) panels (Sajadi, 2020) 250
Figure 6.26 Numbering of the primary and secondary panels with respect to the entire diaphragm wall (Sajadi, 2020).....250
Figure 6.27 Time vs. temperature curves at the monitoring points in panel S01 at 24.6 m depth (Sajadi, 2020).....251
Figure 6.28 The reference rate of hydration heat liberation for each cement constituent (Kishi & Maekawa, 1995).....253
Figure 6.29 The reference rate of heat liberation due to the formation of ettringite (Kishi & Maekawa, 1995).....253
Figure 6.30 The thermal activity assumed for each cement constituent (Kishi & Maekawa, 1995) 254

Figure 6.31 The reference rate of heat liberation by slag and fly ash (Kishi & Maekawa, 1997) 257
Figure 6.32 The reference rate of heat liberation due to the formation of ettringite (Kishi & Maekawa, 1997).....258
Figure 6.33 Normalised curves of isothermal hydration test results (De Schutter & Taerwe, 1995) 261
Figure 6.34 Evolution of $Qref$ with time for the case of $Qmax = 300000\, J \cdot kgcement^{-1}$, $\tau = 70000\, s$ and $\beta = 0.7$.....274
Figure 7.1 Accumulated heat of hydration of a concrete hydrating isothermally when $Qmax$ is varied by $\pm 50\%$ from the 'base' parameters 280
Figure 7.2 Accumulated heat of hydration of a concrete hydrating isothermally when τ is varied by $\pm 50\%$ from the 'base' parameters.....281
Figure 7.3 Accumulated heat of hydration of a concrete hydrating isothermally when β is varied by $\pm 50\%$ from the 'base' parameters.....282
Figure 7.4 Accumulated heat of hydration of a concrete hydrating isothermally at $13oC$, $23oC$ and $33oC$ when Ea is varied by $\pm 50\%$ from the 'base' parameters 283
Figure 7.5 Accumulated heat of hydration of a concrete hydrating isothermally for different values of tn 284
Figure 7.6 Comparison of temperature rise curves between ICFEP and Excel analyses 286
Figure 7.7 Time vs. heat of hydration power curves for cement 'Anläggningscement' at $20, 30, 40$ and $50oC$ (from lowest to highest peaks, respectively) (Wadsö, 2003).....287
Figure 7.8 Comparison of modelled and experimental (Wadsö, 2003) accumulated heat of hydration curves at different curing temperatures ($20, 30, 40$ and $50oC$) 287
Figure 7.9 Comparison of modelled and experimental (Zayed et al., 2013) accumulated heat of hydration curves for Cement A 289
Figure 7.10 Comparison of modelled and experimental (Zayed et al., 2013) accumulated heat of hydration curves for Cement B.....289
Figure 7.11 Comparison of modelled and experimental (Zayed et al., 2013) accumulated heat of hydration curves for Cement C.....290
Figure 7.12 Discretisation of the cross-section of a hydrating pile into ILS radially and angularly, with $nr = 5$ and $n\theta = 6$.....292
Figure 7.13 Temperature rise recorded at the monitoring points for the $0.6\, m$ diameter pile 294

Figure 7.14 Temperature rise recorded at the monitoring points for the 2.4 m diameter pile 295
Figure 7.15 A typical layout of optical fibres within a pile 297
Figure 7.16 Comparison of modelled and measured temperature rise curves for Test Pile in London Project 1 301
Figure 7.17 Comparison of modelled and measured temperature rise curves for Pile P7a in London Project 1 301
Figure 7.18 Comparison of modelled and measured temperature rise curves for Pile P12 in London Project 1 302
Figure 7.19 Comparison of modelled and measured temperature rise curves for Pile P214 in London Project 2 302
Figure 7.20 Comparison of modelled and measured temperature rise curves for Pile P154 in London Project 2 303
Figure 8.1 The axisymmetric FE mesh and the zoomed-in mesh detailing the pile (shaded in grey) for the 900 mm diameter pile 306
Figure 8.2 Change in temperature and thermally-induced pore water pressures for the soil element immediately adjacent to the hydrating pile at pile mid-depth for the 900 mm diameter pile 308
Figure 8.3 Change in temperature and thermally-induced pore water pressures for the soil element immediately adjacent to the hydrating pile at pile mid-depth for the 1800 mm diameter pile 308
Figure 8.4 Evolutions of temperature change with time at various radial distances from centre of pile at pile mid-depth for the 900 mm diameter pile 310
Figure 8.5 Evolutions of temperature change with time at various radial distances from centre of pile at pile mid-depth for the 1800 mm diameter pile 310
Figure 8.6 A graphical representation of the radial distances from the pile axis for locations A to D 311
Figure 8.7 Evolutions of thermally-induced pile head displacement with time for both the 900 mm and 1800 mm diameter piles 312
Figure 8.8 Evolutions of cross-sectionally averaged maximum (compressive) and minimum (tensile) thermally-induced pile axial stress with time for both the 900 mm and 1800 mm diameter piles 313

Figure 8.9 Cross-sectionally averaged thermally-induced mechanical stress-strain path of the pile at pile mid-depth for the hydration stage 314
Figure 8.10 Evolutions of thermally-induced excess pore water pressure with time for both the 900 mm and 1800 mm diameter piles 316

Figure A.1 Temperature rise simulation at $r = 0\ m$ for the 0.6 m diameter pile 349
Figure A.2 Temperature rise simulation at $r = 0.3\ m$ for the 0.6 m diameter pile 349
Figure A.3 Temperature rise simulation at $r = 0\ m$ for the 2.4 m diameter pile 349
Figure A.4 Temperature rise simulation at $r = 0.6\ m$ for the 2.4 m diameter pile 350
Figure A.5 Temperature rise simulation at $r = 1.2\ m$ for the 2.4 m diameter pile 350
Figure A.6 Maximum temperature rise plotted against the $\lambda c \lambda s$ ratio for the 0.6 m diameter pile.....351
Figure A.7 Maximum temperature rise plotted against the $\lambda c \lambda s$ ratio for the 2.4 m diameter pile.....351
Figure A.8 Metric against $\lambda c \lambda s$ ratio for the 0.6 m diameter pile.....353
Figure A.9 Metric against $\lambda c \lambda s$ ratio for the 2.4 m diameter pile.....353
Figure D.1 Comparison of modelled and measured temperature rise curves for Pile P2 in London Project 1.....357
Figure D.2 Comparison of modelled and measured temperature rise curves for Pile P3a in London Project 1.....357
Figure D.3 Comparison of modelled and measured temperature rise curves for Pile P5 in London Project 1.....358
Figure D.4 Comparison of modelled and measured temperature rise curves for Pile P6 in London Project 1.....358
Figure D.5 Comparison of modelled and measured temperature rise curves for Pile P7 in London Project 1.....359
Figure D.6 Comparison of modelled and measured temperature rise curves for Pile P8 in London Project 1.....359
Figure D.7 Comparison of modelled and measured temperature rise curves for Pile P9 in London Project 1.....360
Figure D.8 Comparison of modelled and measured temperature rise curves for Pile P10 in London Project 1.....360

Figure D.9 Comparison of modelled and measured temperature rise curves for Pile P11 in London Project 1 361
Figure D.10 Comparison of modelled and measured temperature rise curves for Pile P13 in London Project 1 361
Figure D.11 Comparison of modelled and measured temperature rise curves for Pile P14 in London Project 1 362

LIST OF TABLES

Table 2.1 Ranges of temperature at which low, intermediate, and high enthalpy geothermal energy operate as proposed by different authors (Dickson & Fanelli, 2013) 44
Table 2.2 A summary of field studies conducted to investigate the thermal performance of thermo-active piles (includes contributions from Bourne-Webb (2013), Fadejev et al. (2017), Gawecka (2017) and Sani et al. (2019)).....62
Table 2.3 Summary of laboratory tests on the thermal conductivity of London Clay.....90
Table 2.4 Summary of TRT studies on the thermal conductivity of London Clay 91
Table 2.5 The thermal conductivity of concrete of four different types of aggregate at different water contents (Scanlon & McDonald, 1994).....94
Table 2.6 The thermal conductivity of concrete of different types of aggregate under dry state (Scanlon & McDonald, 1994).....95
Table 2.7 The thermal conductivity of concrete of different types of aggregate under saturated state (Scanlon & McDonald, 1994) 96
Table 2.8 The thermal conductivity of concrete of different types of aggregate under both saturated and dry states (Campbell-Allen & Thorne, 1963) 97
Table 2.9 The thermal conductivity of concrete of different types of aggregate under saturated states (Khoury, 1983) 97
Table 2.10 The thermal conductivity of concrete of different types of aggregate under both saturated and dry states (Khan, 2002).....98
Table 2.11 The thermal conductivity of a concrete made with crystalline and quartz aggregates at saturated, normally dry and dry states (Pagola et al., 2017) 98
Table 2.12 The volumetric and specific heat capacity of a concrete made with crystalline and quartz aggregates at saturated, normally dry and dry states (Pagola et al., 2017) 102
Table 2.13 Linear coefficient of thermal expansion of concrete made with different types of aggregates (Khoury, 1983).....105
Table 2.14 Linear coefficient of thermal expansion of concrete made with different types of aggregates (Scanlon & McDonald, 1994).....106
Table 2.15 The thermal conductivity, volumetric heat capacity and linear coefficient of thermal expansion adopted in the current research for London Clay and concrete. Values in brackets are adopted for consistency with previous research (Gawecka et al., 2017) 120

Table 3.1 A summary of field studies conducted to investigate the thermo-mechanical behaviour of thermo-active piles that had been reviewed and discussed in Gawecka (2017) 129
Table 3.2 A summary of laboratory studies conducted to investigate the thermo-mechanical behaviour of thermo-active piles that had been reviewed and discussed in Gawecka (2017) 145
Table 3.3 A summary of numerical studies conducted to investigate the thermo-mechanical behaviour of thermo-active piles, which includes contributions from Gawecka (2017) 156
Table 4.1 Material properties adopted for London Clay 176
Table 4.2 Material properties adopted for concrete thermo-active pile and TEM 177
Table 4.3 Material properties adopted for the heat exchanger pipes 177
Table 4.4 Thermally-induced pile head displacement at $t = 150\ days$ for the six analyses performed 190
Table 5.1 Magnitudes of thermally-induced pile head displacement at $t = 150\ days$ simulated by the proposed method and 3D analyses and the corresponding relative errors 218
Table 5.2 Magnitudes of peak $\sigma Tmax$ computed with the proposed method and 3D analyses and the corresponding errors 219
Table 5.3 Magnitudes of peak thermally-induced excess pore water pressure computed with the proposed method and 3D analyses and the corresponding errors 221
Table 5.4 Magnitudes of peak $\sigma Tmax$ given by the proposed method using $\Delta E = 0\ W \cdot m - 1$ and $210\ W \cdot m - 1$ and the percentage reduction of peak $\sigma Tmax$ when ΔE increases from $0\ W \cdot m - 1$ to $210\ W \cdot m - 1$ 223
Table 6.1 Heat of hydration of different cement constituents (simplified from Odler (1998)) 230
Table 6.2 Types of cement used in the three concrete samples tested by Lee et al. (2014) 232
Table 6.3 Blaine fineness of the cement samples tested by Zayed et al. (2013) 237
Table 6.4 Average accumulated heats of hydration of different ASTM types of cements cured at $21oC$ (Verbeck & Foster, 1950; Copeland et al., 1960) 241
Table 6.5 Ultimate heat liberated at the end of hydration per unit mass of different cement constituents (Swaddiwudhipong et al., 2002) 265

Table 6.6 Suggested values of specific heat capacity for different concrete components (Swaddiwudhipong et al., 2002) 265
Table 6.7 Values for model parameters A and B for different cement constituents (Swaddiwudhipong et al., 2002) 267
Table 6.8 Recommended values for $\lambda 1$, $\lambda 2$, $\lambda 3$ and $\lambda 4$ (Swaddiwudhipong et al., 2002) 268
Table 6.9 A summary of the features and capabilities for each of the reviewed models 272
Table 7.1 Arbitrarily defined 'base' model parameters 280
Table 7.2 Model parameters and thermal properties adopted for the ICFEP and Excel analyses 285
Table 7.3 The results of model calibration for cement samples A1, A2, A3, B1, B2, C1 and C2 from Zayed et al. (2013) 288
Table 7.4 Model parameters and thermal properties adopted for the MATLAB and ICFEP analyses 294
Table 7.5 A summary of the piles that Skanska has provided field measurements 296
Table 7.6 Calibrated model parameters for London Projects 1 and 2 300
Table 8.1 Critical stages for different thermo-mechanical response of both the $900\ mm$ and $1800\ mm$ diameter thermo-active piles 317

Table A.1 Model parameters and thermal properties adopted in this parametric study 348
Table A.2 Maximum temperature rise simulated at the monitoring points and the percentage difference from the case of $\lambda c \lambda s = 1.0$ for the $0.6\ m$ diameter pile 352
Table A.3 Maximum temperature rise simulated at the monitoring points and the percentage difference from the case of $\lambda c \lambda s = 1.0$ for the $2.4\ m$ diameter pile 352

LIST OF SYMBOLS

A	Area
A_c	Cross-sectional area of a pile
a	Stiffness degradation parameter
B	Non-linear permeability model parameter
b	Stiffness degradation parameter
C_p	Specific heat capacity
C_f	Specific heat capacity of fluid
C_s	Specific heat capacity of sample
C_w	Specific heat capacity of water
c_{vol}	Volumetric heat capacity
$c_{vol,a}$	Volumetric heat capacity of pore air
$c_{vol,s}$	Volumetric heat capacity of soil particles
$c_{vol,w}$	Volumetric heat capacity of pore water
c'	Cohesion
D_{pipe}	Internal pipe diameter
E	Young's modulus
E_a	Activation energy
E_d	Deviatoric strain
E_{28}	Young's modulus of concrete at 28 days

G_{min}	Minimum shear modulus
G_{ref}	Maximum shear modulus at reference mean effective stress
G_{tan}	Tangent shear modulus
g	Earth's gravitational acceleration
H	Total amount of energy transferred
h	Heat transfer coefficient
K_f	Bulk modulus of pore fluid
K_{min}	Minimum bulk modulus
K_{ref}	Maximum bulk modulus at reference mean effective stress
K_s	Bulk modulus of soil skeleton
K_{tan}	Tangent bulk modulus
K_0	Coefficient of earth pressure
k	Permeability or reaction constant
k_{TEM}	Thermal conductivity of thermally enhanced material
k_0	Non-linear permeability model parameter
L	Pile length or length
L_c	Characteristic length
m_G	Parameter defining the dependence of elastic stiffness on mean effective stress
m_K	Parameter defining the dependence of elastic stiffness on mean effective stress
m_s	Mass of sample
m_w	Mass of water

N	Nodal shape functions
N_T	Shape functions for temperature
n	Porosity or order of reaction
n_r	Number of radial discretisation in the numerical technique
$n_{U-loops}$	Number of U-loops
n_θ	Number of angular discretisation in the numerical technique
n^*	A time-dependent function within the heat of hydration model
P	Power of system or power of heat of hydration per unit volume of concrete
P_M	Mechanical axial force
P_{nodes}	Power of heat of hydration at element nodes
P_{ref}	Reference power of heat of hydration power per unit volume of concrete
P_T	Thermal axial force
P_{total}	Total axial force
Pe	Péclet number
p'	Mean effective stress
p'_{ref}	Reference mean effective stress
Q	Water flow rate
Q_{acc}	Accumulated heat of hydration per unit mass of cement
Q_{max}	Heat of hydration model parameter
Q_{ref}	Reference accumulated heat of hydration per unit mass of cement
Q_T	Field of heat flux

$Q_{T,nodes}$	Nodal heat flux
Q^T	Heat source or sink
q	Heat flux
$q_{advection}$	Advective heat flux
$q_{conduction}$	Conductive heat flux
$q_{convection}$	Convective heat flux
$q_{radiation}$	Radiative heat flux
q_s	Mobilised shaft resistance
R	Universal gas constant
$R_{G,min}$	Minimum normalised value of G_{tan}
$R_{K,min}$	Minimum normalised value of K_{tan}
r	Stiffness degradation parameter or radial distance
r_{pipes}	The radial distance measured from the pile centre at which the pipes are located within the thermo-active pile
S	Natural coordinate
S_r	Soil degree of saturation
S_u	Undrained shear strength
s	Stiffness degradation parameter or coefficient of the CEB-FIP (1990) concrete stiffness model
T	Temperature
T_b	Temperature at boundary

T_{body}	Temperature of body in contact with fluid or surface temperature of radiating body
T_f	Temperature of fluid
T_{final}	Final steady-state temperature of mixture
T_{in}	Temperature of water entering the thermo-active pile
$T_{initial}$	Initial temperature
$T_{in,mid}$	Temperature of water in the pipe going down the pile at pile mid-depth
T_{nodes}	Temperatures at element nodes
T_{out}	Temperature of water leaving the thermo-active pile
$T_{out,mid}$	Temperature of water in the pipe going up the pile at pile mid-depth
T_{ref}	Reference temperature
T_s	Temperature of sample
T_{tbc}	The temperature that is prescribed as a thermal boundary condition in the axisymmetric coupled THM analysis
T_w	Temperature of water
t	Time
t_n	Cut-off value for determining $n^*(t)$
t_{28}	28 days in the same units as t
V	Volume
v_f	Velocity of fluid
v_w	Velocity of water
W_l	Weighting functions for 1D linear elements

W_q	Weighting functions for 1D quadratic elements
X_{rand}	Random number
z	Depth below top of London Clay
α	Linear coefficient of thermal expansion or adhesion factor
α_A	Areal coefficient of thermal expansion
α_f	Linear coefficient of thermal expansion of pore fluid
α_{PG}	Petrov-Galerkin weighting factor
$\alpha_{PG,opt}$	Optimal value of Petrov-Galerkin weighting factor
α_s	Linear coefficient of thermal expansion of soil skeleton
α_{th}	Thermal diffusivity
α_V	Volumetric coefficient of thermal expansion
α_w	Linear coefficient of thermal expansion of water
β	Heat of hydration model parameter
β_{PG1}	Petrov-Galerkin weighting factor
$\beta_{PG1,opt}$	Optimal value of Petrov-Galerkin weighting factor
β_{PG2}	Petrov-Galerkin weighting factor
$\beta_{PG2,opt}$	Optimal value of Petrov-Galerkin weighting factor
γ_s	Saturated unit weight
Δ	Mutation factor
ΔE	Change in energy content or heat flux of thermo-active pile
ΔT	Change in temperature

ΔT_{av}	Average change in temperature
Δu	Excess pore water pressure
Δ_{max}	Maximum mutation factor
$\varepsilon_1, \varepsilon_2, \varepsilon_3$	Principal strains
ε_M	Mechanical axial strain
ε_{Total}	Total observed axial strain
ε_{T-Free}	Free thermal axial strain
ε_{T-Obs}	Observed axial strain
ε_{T-Rstr}	Restrained axial strain
ε_{vol}	Volumetric strain
ϵ	Emissivity factor
η	A metric to quantify error
θ	Angular coordinate
λ	Thermal conductivity
λ_a	Thermal conductivity of pore air
λ_c	Thermal conductivity of concrete
λ_{max}	Upper bound of overall thermal conductivity of soil
λ_{min}	Lower bound of overall thermal conductivity of soil
λ_s	Thermal conductivity of soil
λ_{sp}	Thermal conductivity of soil particles
λ_w	Thermal conductivity of pore water

μ	Poisson's ratio
ρ	Density
$\rho_{concrete}$	Density of concrete
ρ_f	Density of fluid
ρ_w	Density of water
σ_{S-B}	Stefan-Boltzmann constant
σ_T	Thermally-induced axial stress
$\overline{\sigma_T}$	Cross-sectionally averaged thermally-induced axial stress
$\overline{\sigma_T}_{max}$	Maximum cross-sectionally averaged thermally-induced axial stress over the pile length
τ	Heat of hydration model parameter
ϕ'	Angle of shearing resistance
χ	Mass of cement per unit mass of concrete
ψ'	Angle of dilation
Ω	Domain of a finite-element

CHAPTER 1 INTRODUCTION

1.1 BACKGROUND

Due to an ever-increasing global population, associated with an increase in energy consumption, there are increasing demands to reduce carbon emissions around the world. As a result, the United Kingdom is committed to reduce carbon emissions by 80% compared to the 1990 levels by 2050, through the 2008 Climate Change Act. In 2019, this target was made even more ambitious, which requires the country to achieve net zero emissions by 2050. In order to achieve a reduction in carbon emissions, there has been a transition to generate electricity from burning fossil fuels to using renewable resources, such as wind and solar power. To further reduce carbon emissions, local sustainability targets, such as the Merton Rule, have been enacted. The Merton Rule requires a proportion of the energy demand of a building to be generated on site using renewable sources (Merton Council, 2010; World Wide Fund For Nature, 2019). In dense urban environments such as London, designing geotechnical structures to be thermo-active and thus provide low carbon heating and cooling is perhaps the only feasible and economically viable option.

Thermo-active geotechnical structures differ from the conventional ones in a way that they can exchange heat with the ground. This is achieved by having heat exchanger pipes embedded within them to allow the circulation of a carrier fluid. When there is a heating demand in the building, cold fluid is circulated through the network of heat exchanger pipes within the thermo-active structures. The fluid absorbs heat from the ground and is returned to the building for heating purposes, while the ground is cooled. The opposite happens when there is a cooling demand in the building. As a result, the operation of these thermo-active structures means that the structure itself as well as the ground are subjected to temperature changes, resulting in complex soil-structure interactions of a thermo-hydro-mechanical nature.

The main objective of this research is to analyse the thermo-mechanical behaviour of thermo-active piles when they are subjected to temperature changes. Studies on the thermo-mechanical behaviour of thermo-active piles presented in the literature come with different levels of complexity (Bourne-Webb, 2013; Fadejev et al., 2017; Gawecka, 2017; Sani et al., 2019), leading to different interpretations and conclusions. This research aims to simulate computationally as accurately as possible the thermo-mechanical response of thermo-active

piles, using the in-house software Imperial College Finite Element Program (ICFEP) (Potts & Zdravkovic, 1999; Cui, 2015; Gawecka, 2017), which has been developed at the Geotechnics Section of Imperial College London for over 40 years. The current study involves three-dimensional (3D) fully coupled thermo-hydro-mechanical (THM) finite-element (FE) analyses of the problem, where the circulation of fluid through the heat exchanger pipes embedded within the thermo-active pile is explicitly simulated. This type of analyses, although accurate, requires significant computational resources which render them impractical to perform during routine engineering design. As a result, it is also an objective of the current research to develop a simplified approach to simulate the problem, yet producing results which are as accurate as the 3D analyses.

While significant focus has been dedicated to investigating the thermo-mechanical response of thermo-active piles due to their operation, it should be appreciated that they are made with cast-in-situ concrete, meaning that significant amount of heat of hydration is generated when they are cast, and the resulting thermo-mechanical response should not be overlooked. In order to model accurately the thermo-mechanical response of thermo-active piles due to heat of hydration, it is an objective of this research to develop a concrete heat of hydration model that can be readily applied in geotechnical applications. This model should then be validated using laboratory and field measurements, which allows it to be subsequently adopted in the simulation of temperature rise within curing thermo-active piles, and the resulting thermo-mechanical response can then be compared with that observed during operation. This would allow the identification of whether the hydration or operation stage is the critical stage in terms of thermo-mechanical response of a thermo-active pile.

1.2 SCOPE OF RESEARCH

This research consists of two main parts: (1) an in-depth investigation into the thermo-mechanical behaviour of thermo-active piles, the significance of which is highlighted by the varied interpretations and conclusions in the literature based on numerical studies involving different levels of complexity, and (2) a pioneering study on the thermo-mechanical response of piles as a result of concrete heat of hydration, due to a lack of research in the literature on this topic. The objectives of the research are, therefore, as follows:

1. To conduct 3D, fully coupled THM FE analyses on different pile diameters and heat exchanger pipe configurations, where the circulation of carrier fluid through the heat exchanger pipes is explicitly simulated. This set of complex and computationally expensive analyses provides the best approximation of the real thermo-mechanical behaviour of thermo-active piles. The thermo-mechanical response and thermal performance of the piles are analysed in order to provide a better understanding of their behaviour during their operation.
2. To propose a simplified approach which involves only two-dimensional analysis to evaluate the operation of thermo-active piles, without requiring the explicit simulation of the circulating fluid. Such an approach is needed since 3D analyses are computationally expensive to perform, and the explicit simulation of heat exchanger pipes is not available in common FE software packages. The accuracy of such a simplified approach is validated by comparing the modelled thermo-mechanical behaviour with that obtained from the 3D analyses.
3. To develop a concrete heat of hydration model that can be readily applied in geotechnical engineering applications. This model should be capable of simulating the evolution of heat of hydration from different types of concrete, while involving only a small number of parameters, allowing the model to be easily calibrated using laboratory or field heat of hydration measurements and subsequently applied. The model is validated using laboratory and field measurements of heat of hydration for different types of concrete.
4. To establish whether the hydration stage can be critical to the design of thermo-active piles. This requires the analysis of the behaviour of thermo-active piles during the hydration stage in terms of developed forces, pile displacements, temperature fields and pore water pressures in the surrounding ground. A detailed comparison with the behaviour during operation is crucial.

1.3 THESIS OUTLINE

Chapter 2 presents and explains the basic concepts underlying the current research which the subsequent chapters build upon. These include the fundamentals of geothermal energy, ground source heat pump (GSHP) systems, thermo-active structures, different types of heat transfer mechanisms in soils, definitions of different thermal and thermo-mechanical properties, as well as a literature review of these properties for London Clay and concrete. The existing

capabilities of ICFEP that are most relevant to the modelling involved in the current research are also described.

Chapter 3 presents a comprehensive literature review on field, laboratory and numerical studies dedicated to investigating the thermo-mechanical behaviour of thermo-active piles. The descriptive framework by Bourne-Webb et al. (2009), Amatya et al. (2012), and Bourne-Webb et al. (2013) to explain how thermo-active piles behave when subjected to thermal and thermo-mechanical loading is also discussed.

Chapter 4 presents a numerical study on the thermal performance and thermo-mechanical behaviour of thermo-active piles which are subjected to thermo-mechanical loads. In these simulations, fully coupled THM 3D FE analyses are undertaken, where the circulation of carrier fluid through heat exchanger pipes is explicitly modelled. Different pile diameters and heat exchanger pipe configurations are considered which allow their effects on the modelled thermo-mechanical behaviour to be investigated.

Chapter 5 proposes a simplified approach which involves only 2D analyses to model the thermo-mechanical behaviour of thermo-active piles. The 3D analyses presented in Chapter 4 are used as benchmark to gauge the accuracy of the approach.

Chapter 6 presents a comprehensive literature review on the fundamentals of concrete heat of hydration, different types of heat of hydration measurements, as well as the existing models for heat of hydration. A new concrete heat of hydration model is proposed towards the end of the chapter which involves only a small number of parameters and can be readily applied in geotechnical engineering applications.

Chapter 7 presents a parametric study of the concrete heat of hydration model proposed in Chapter 6. Implementation of the model into a FE program is discussed, followed by calibration and validation of the model using laboratory and field measurements of concrete heat of hydration.

Chapter 8 is divided into two parts. In the first part, the hydration of two individual piles with different diameters is modelled using the concrete heat of hydration model proposed in Chapter 6, and the effects on the surrounding soil are quantified. In the second part, the hydration and subsequent operation of thermo-active piles are modelled using the simplified approach

proposed in Chapter 5 which allow the assessment of the relative importance of the hydration and operation stages on their thermo-mechanical behaviour.

Chapter 9 summarises the main conclusions of this research and provides recommendations for future research.

Note that unless otherwise specified, the sign convention adopted throughout the thesis is such that positive values refer to tensile stresses and strains and upwards vertical movements.

CHAPTER 2 PRELIMINARIES

2.1 INTRODUCTION

This chapter presents and explains the basic concepts underlying the current research which the subsequent chapters build upon. First, in Section 2.2, the definition, usage and classification of geothermal energy are explained, together with how a ground source heat pump system operates and the components involved. In Section 2.3, different types of thermo-active structures are described, with an explanation of how they operate and a description of their usage. In Section 2.4, different types of heat transfer mechanisms in soils are explained, which include conduction, convection, radiation, vapour diffusion and freeze-thaw processes, as well as the associated equations. In Section 2.5, the definition of three thermal/thermo-mechanical properties – thermal conductivity, specific/volumetric heat capacity and coefficient of thermal expansion, are given, as well as how they are measured, together with a literature review of their typical values for London Clay and concrete. Finally in Section 2.6, the existing capabilities of Imperial College Finite Element Program (ICFEP) that are most relevant to the numerical modelling involved in the current research are described.

2.2 GEOTHERMAL ENERGY AND GROUND SOURCE HEAT PUMP SYSTEMS

According to Banks (2012), the term 'geothermal energy' used to only refer to high temperature energy which is derived from the heat originating from the deep interior of the Earth, harnessed by very deep boreholes or in certain specific locations in the Earth's crust. This energy mainly arises from the radioactive decay of uranium, thorium and potassium in the interior of the Earth, or from the frictional heat generated in subduction zones at tectonic plate boundaries (Lund, 2015). However, the EU Renewable Energy Directive 2009/28/EC later defined 'geothermal energy' as the energy stored in the form of heat beneath the surface of solid Earth, which means that this term now includes shallow ground source heat, which, according to Banks (2012), refers to the low enthalpy heat that occurs at 'normal' temperatures in the relatively shallow subsurface, or the energy in the subsurface that is mainly recharged by absorbing solar energy.

Geothermal energy is a low-carbon and renewable energy, and its use has been increasing over the past few decades. Figure 2.1 compares the worldwide use of geothermal energy in different sectors over the last 25 years (Lund & Toth, 2021), and, according to Lund and Toth (2021),

the worldwide total annual geothermal energy use was 1,020,887 $TJ \cdot year^{-1}$ towards the end of 2019, which is a 72.3% increase compared to that in 2015. Such a growth in use demonstrates its increasing popularity in recent years, with the authors attributing the strong growth of geothermal energy use to the rapid installations of geothermal heat pumps (which are also known as ground source heat pumps), as can be observed in Figure 2.1, which contributes to 59.2% of the energy use. Moreover, while most of the installations occurred in North America, Europe and China, there are 54 countries with installations reported.

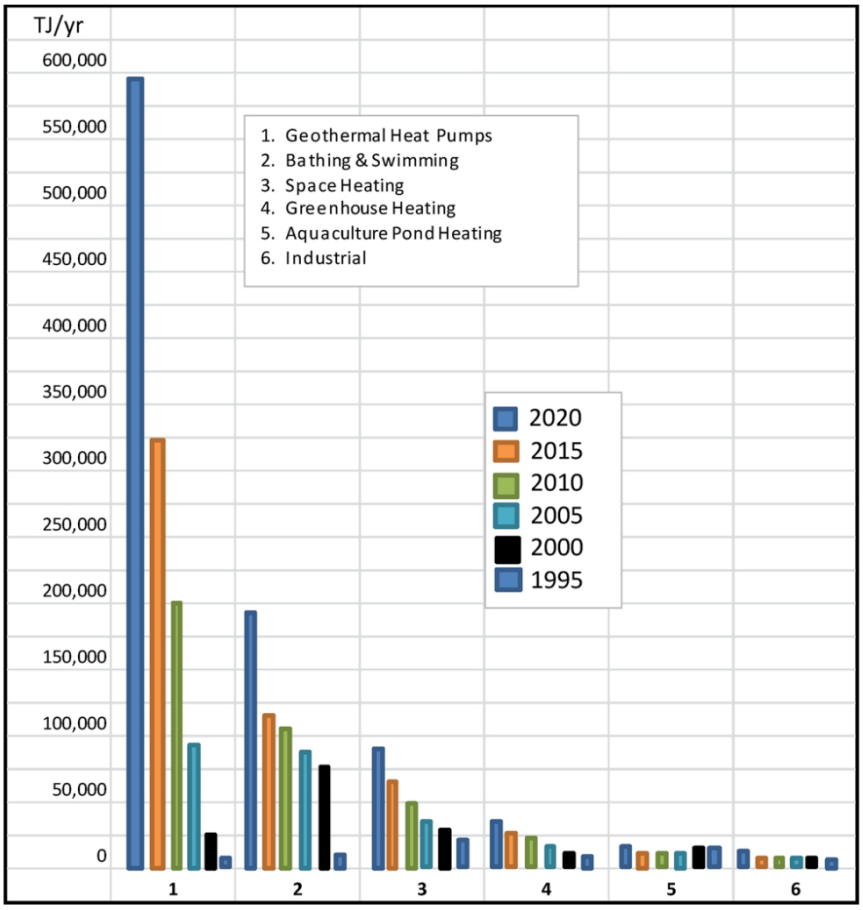


Figure 2.1 Worldwide use of geothermal energy in different sectors between 1995 and 2020 (Lund & Toth, 2021)

2.2.1 Classification of geothermal energy

According to Dickson and Fanelli (2013), there is currently no international standard on the classification of geothermal energy, but geothermal energy is usually classified based on the enthalpy (which can be considered as temperature) of the geothermal fluid (which is the fluid that carries thermal energy from and to the ground) of the system: low enthalpy, intermediate

enthalpy, and high enthalpy geothermal energy. However, the temperature ranges at which each of the above operate are not strictly defined, with different authors having proposed different ranges of temperature for each enthalpy level, which are compiled by Dickson and Fanelli (2013) in Table 2.1.

	Muffler and Cataldi (1978)	Hochstein (1990)	Benderitter and Cormy (1990)	Nicholson (1993)	Axelsson and Gunnlaugsson (2000)
Low enthalpy	$< 90^oC$	$< 125^oC$	$< 100^oC$	$\leq 150^oC$	$\leq 190^oC$
Intermediate enthalpy	$90 - 150^oC$	$125 - 225^oC$	$100 - 200^oC$	$-$	$-$
High enthalpy	$> 150^oC$	$> 225^oC$	$> 200^oC$	$> 150^oC$	$> 190^oC$

Table 2.1 Ranges of temperature at which low, intermediate, and high enthalpy geothermal energy operate as proposed by different authors (Dickson & Fanelli, 2013)

Intermediate and high enthalpy geothermal energy are not the focus of the current research and will therefore only be briefly described here. According to Lund (2015), temperature increases at about $25^oC \cdot km^{-1}$ with depth (this is also known as the geothermal gradient), so at a depth of $10\ km$, the temperature would be about 250^oC. However, intermediate and high enthalpy geothermal energy are usually exploited at volcanic areas, where the geothermal gradient is higher, which allows shallower and cheaper drilling. For example, a temperature of 280^oC can be found at $200 - 600\ m$ depth at the Hellisheiði geothermal field in Iceland (Franzson et al., 2005), and the Hellisheiði geothermal power plant makes use of this geothermal field to generate electricity and provide hot water for district heating (Hallgrímsdóttir et al., 2012). The Hellisheiði geothermal power plant, as in typical intermediate and high enthalpy geothermal power plants, operates by drawing hot water and steam at elevated pressures from geothermal wells, which are used to drive turbines and generate electricity.

According to Sanner (2005), low enthalpy geothermal energy systems, or shallow geothermal energy systems, usually operate up to a depth of $400 - 500\ m$ in areas without geothermal anomalies, therefore, ground temperatures are usually in the range of $5 - 25^oC$, which depends on the climate and solar energy absorbed. In other words, ground temperatures are dependent on the location and are subjected to seasonal variations, although seasonal variations of ground

temperatures reduce with depth. Figure 2.2 presents the average measured temperatures with depth at the Royal Edinburgh Observatory on different months (Sanner, 2005), and it can be observed that lower ground temperatures are measured during the winter months, while higher ground temperatures are measured during the summer months. Moreover, these seasonal variations of ground temperature are only significant near the ground surface since, at larger depths, the ground temperatures are more or less constant throughout the year.

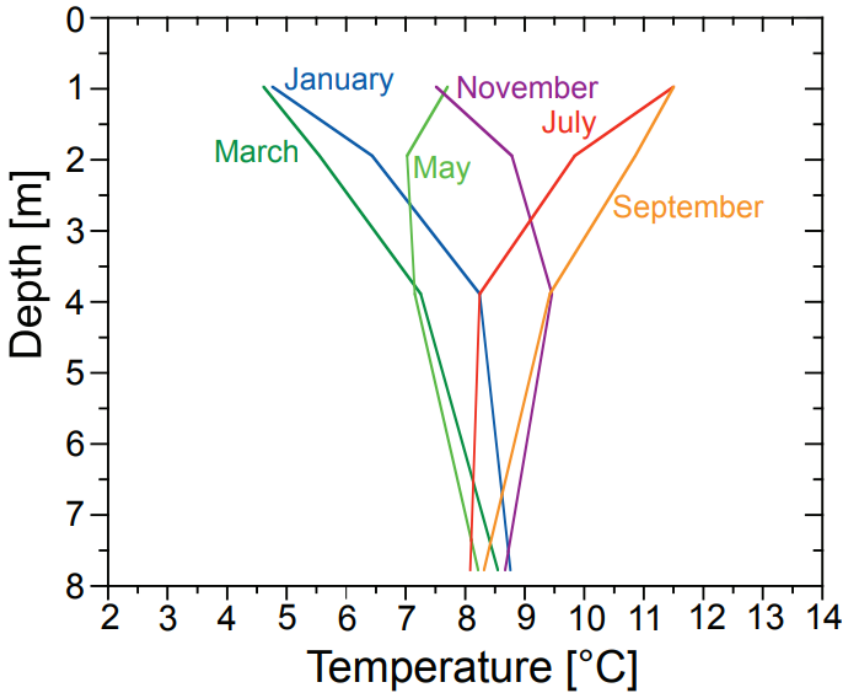


Figure 2.2 Average measured temperatures with depth at the Royal Edinburgh Observatory on different months (Sanner, 2005)

Busby (2015) reported measurements of ground temperature at different locations in the United Kingdom (see Figure 2.3(a)) and plotted the mean annual temperature at 1 m depth (for non-urban locations corrected to sea level) with respect to the northings of the measured location (see Figure 2.3(b)). Busby (2015) then fitted a linear trend to the plot in Figure 2.3(b), the equation of which is given by Equation (2.1). Figure 2.4 presents the mean annual ground temperatures in the United States in Fahrenheit (Pauly, 2010).

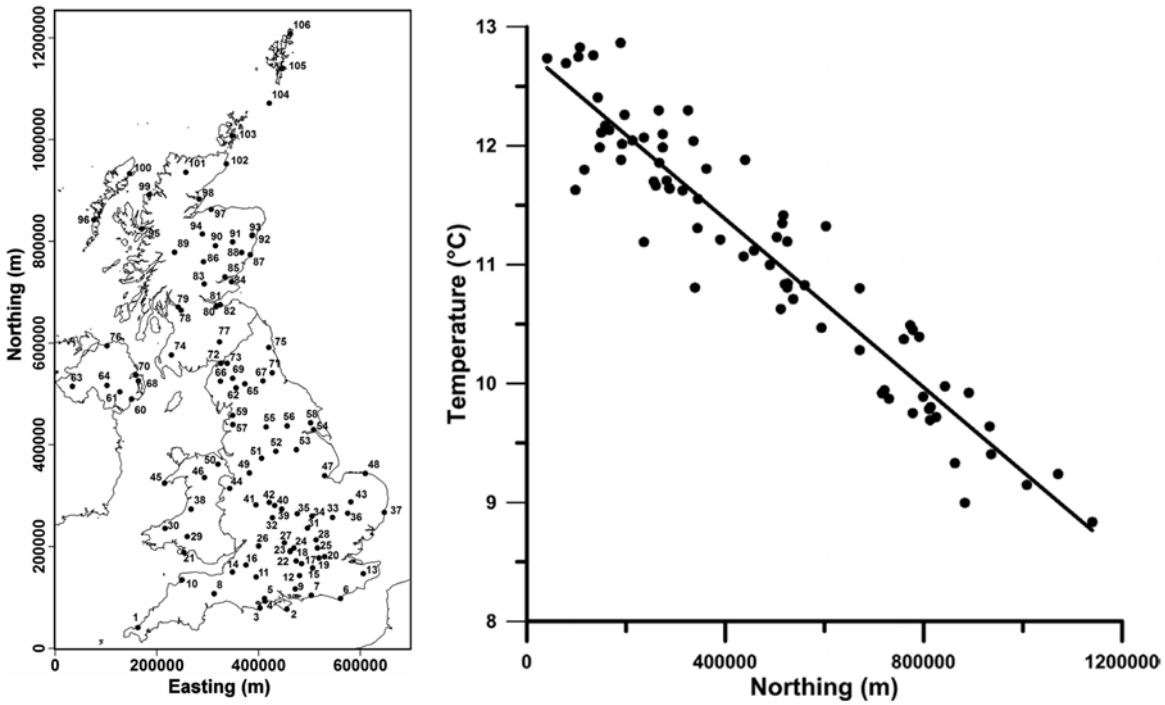


Figure 2.3 (a) Locations in the United Kingdom where ground temperatures are measured and (b) mean annual temperature at 1 m depth (for non-urban locations corrected to sea level) with respect to the Northings of the measured location (Busby, 2015)

$$Temperature\ [°C] = (-3.539 \times 10^{-6} \times northing) + 12.8 - (elevation \times 0.0065) \pm 0.3 \qquad (2.1)$$

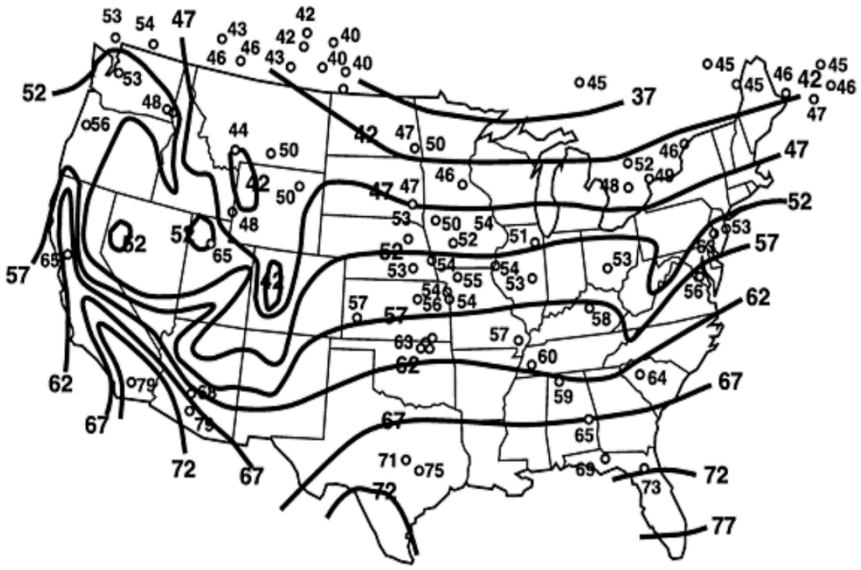


Figure 2.4 Mean annual ground temperatures in the United States in Fahrenheit (Pauly, 2010)

The shallow ground temperatures shown in Figure 2.3 and Figure 2.4 mean that the shallow ground cannot be exploited for direct heat use. However, the fact that ground temperatures remain more or less constant throughout a year at depths beyond around only $10\ m$ allows the ground to be used as a storage medium for heat, suggesting that this form of shallow geothermal energy to be exploited theoretically anywhere. In order to use heat stored in the ground, a ground source heat pump system is required.

2.2.2 Ground source heat pump systems

In order to exploit low enthalpy geothermal energy, or shallow geothermal energy, a ground source heat pump (GSHP) system is required. A GSHP system consists of two components: a heat pump and a ground source system. Heat pumps are devices that allow heat to be transported against a thermal gradient (i.e. from a medium with lower temperature to one with higher temperature) with the use of an external supply of energy. The ground source system is in contact with the ground and is responsible of transporting heat from the ground to the heat pump, or vice versa, using water or a carrier fluid. There are two types of ground source systems: open loop systems and closed loop systems.

2.2.2.1 Heat pumps

Heat pumps are used to transfer energy from the water/carrier fluid from the ground source system to the building energy system for heating or cooling purposes. The schematic diagram of a heat pump is shown in Figure 2.5 (Sanner, 2005). According to Sanner (2005), the operations that happen within a heat pump in order to extract energy from the water/carrier fluid from the ground source system to provide heating are as follows:

1. The refrigerant that circulates within the heat pump, which is a fluid with low boiling point, evaporates at the evaporator, taking energy (latent heat of vaporisation) away from the water/carrier fluid from the ground source system.
2. The refrigerant (which is now a gas) is compressed by the compressor (which requires external supply of energy) and hence heated, which then condenses in the condenser and releases the energy (latent heat of vaporisation) which can be utilised for heating purposes.
3. The refrigerant (now a liquid) then passes through the expansion valve where pressure is reduced and its temperature decreases. The refrigerant is returned to the evaporator and the above process repeats.

Note that if the heat pump is used for cooling purposes, the opposite of the above will happen, with the refrigerant flowing in the opposite direction.

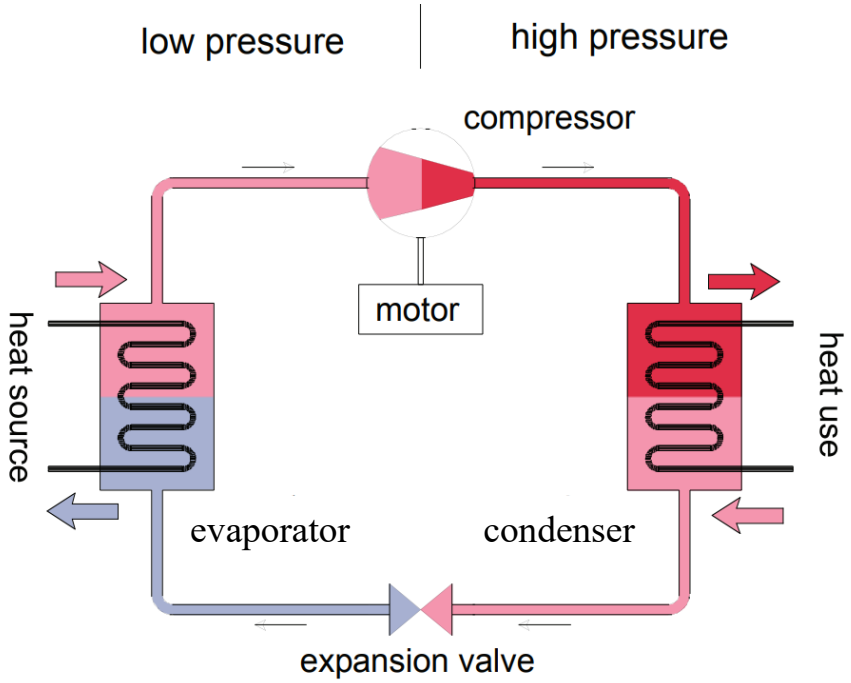


Figure 2.5 Schematic diagram of a heat pump (Sanner, 2005)

As a heat pump is a device which requires energy to operate but is capable of supplying useful thermal energy for heating or cooling purposes, its performance is usually quantified by the coefficient of performance (COP) (the expression of which is given by Equation (2.2)), which is the ratio of useful thermal energy supplied by the heat pump to the energy required for its operation (Sanner, 2005). This means that for each unit of electricity supplied to the system, the heat pump provides COP units of heating or cooling, and a higher COP means that the heat pump is more efficient.

$$COP = \frac{useful\ thermal\ energy\ supplied\ by\ heat\ pump}{energy\ required\ for\ heat\ pump\ operation} \tag{2.2}$$

According to Brandl (2006), the COP value is fundamentally dependent on the temperature difference between the water/carrier fluid from the ground source system and the fluid utilised for heating or cooling, with a larger difference resulting in a lower COP. He added that a value of $COP \geq 4$ should be achieved for the heat pump to be economically viable, which approximately translates to the fact that when the system is used for heating purposes, the temperature of the fluid utilised for heating should not exceed $35 - 45^{o}C$, and that the

temperature of the water/carrier fluid from the ground source system should not be lower than $0-5^{o}C$. Note that the COP only quantifies the efficiency of the heat pump, and that the seasonal performance factor (SPF) should be used in order to quantify the efficiency of the entire GSHP system, as there are other elements in the system that consumes energy, such as the circulation pumps (Brandl, 2006). The expression for SPF is given by Equation (2.3).

$$SPF = \frac{useful\ thermal\ energy\ supplied\ by\ GSHP\ system}{energy\ required\ for\ GSHP\ system} \tag{2.3}$$

2.2.2.2 Open loop systems

Open loop systems are not the focus of the current research and will therefore only be briefly described here, a more detailed review on open loop systems can be found in Gawecka (2017). In an open loop system, groundwater or surface water (such as lakes and ponds) are used as a carrier fluid to transfer heat to the heat pump (Self et al., 2013). This process involves the extraction of water from the source, circulation through the heat pump, and return to the source. The most common configuration of an open loop system is illustrated in Figure 2.6 (Sanner, 2005).

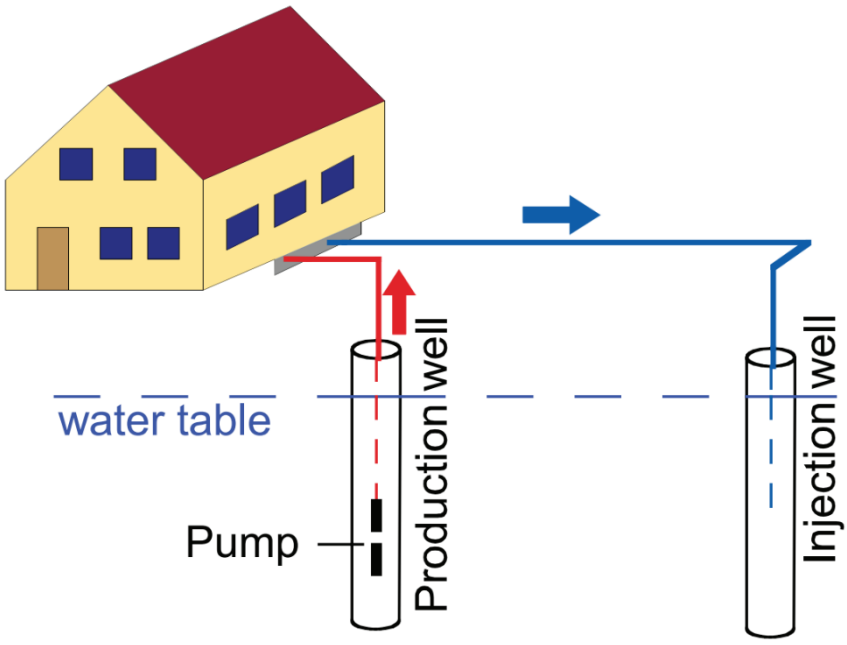


Figure 2.6 The most common open loop system configuration which involves a production well and an injection well (Sanner, 2005)

In this configuration, two wells are drilled to the water table, the well which supplies water towards the heat pump is known as the production well, and the one which returns the water that has circulated through the heat pump is known as the injection well. Note that the design of these open loop systems is subjected to the following limitations:

- The separation between the production and injection wells must be sufficiently large to avoid thermal breakthrough. According to Banks (2009), thermal breakthrough, or thermal feedback, is the phenomenon where the thermal plume from the injection well is sucked back to the production well, causing a lower temperature (when the system is used for heating purposes, i.e. the temperature of the injected water is lower than that of the natural groundwater) or higher temperature (when the system is used for cooling purposes, i.e. the temperature of the injected water is higher than that of the natural groundwater) in the water extracted from the production well, resulting in a gradual reduction in the system efficiency.
- The ground should be permeable to ensure sufficient supply of groundwater (Sanner, 2005).
- Groundwater should have a relatively neutral chemistry and low levels of minerals such as iron in order to avoid scaling, clogging and corrosion problems with the GSHP system (Sanner, 2005; Self et al., 2013).

2.2.2.3 Closed loop systems

A closed loop system involves a series of closed loop heat exchanger pipes, through which the carrier fluid circulates to transport heat between the ground and the heat pump. The carrier fluid is usually a water-based antifreeze solution, with freezing points typically between -10^oC and -20^oC to allow the fluid to be chilled below 0^oC if necessary (Banks, 2012), while the heat exchanger pipes are usually made of polyethylene or polypropylene (Self et al., 2013). In this type of systems, the carrier fluid does not have direct contact with the ground (hence the designation 'closed-loop') and heat transfer occurs through the pipe walls. The advantage of closed loop systems over open loop systems is that their installations do not rely on ground permeability or the availability of groundwater or surface water. Moreover, the absence of abstraction of groundwater in the case of closed loop systems means that the approval process from environmental protection authorities is less complex than in the case of open loop systems. Closed loop systems are mainly classified according to the layout of the heat exchanger pipes in the ground, namely horizontal closed loops and vertical closed loops.

Note that this terminology includes also thermo-active structures, in which heat exchanger pipes are embedded into the concrete used in geotechnical structures. However, these will be discussed in detail in Section 2.3 and will therefore not be covered here.

Horizontal closed loops

The installation of a horizontal closed loop system involves digging a trench, placement of heat exchanger pipes, and backfilling the trench, with the heat exchanger pipes usually located a few metres below the ground surface (Self et al., 2013). According to Self et al. (2013), the advantage of horizontal closed loop systems is that their installation is cheaper than vertical closed loop systems as it avoids drilling. However, horizontal closed loop systems require larger areas of land compared to vertical closed loop systems, which may be impractical in denser urban areas. The fact that the heat exchanger pipes are only a few metres below the ground surface means that the performance and efficiency of the system is easily affected by daily and seasonal variations of ground temperatures, which depend on the climate (as explained in Section 2.2.1). Additionally, as highlighted by Mustafa Omer (2008), horizontal closed loop systems could be subjected to fluctuations in soil thermal properties due to precipitation or drying of soil, with this interaction phenomena having to be accounted for during their design.

Horizontal closed loop systems involve two typical types of heat exchanger pipe connection: in series and in parallel, which are illustrated in Figure 2.7 (Sanner, 2005). Besides, according to Fujii et al. (2012), heat exchanger pipes can also be arranged in slinky-coils (illustrated in Figure 2.8 (Fujii et al., 2012)) as opposed to laying the pipes straight. This results in a higher installation density of heat exchanger pipes per unit ground area, which means a smaller ground area requirement for the installation and hence cheaper installation costs, though the longer total pipe length requires more energy to circulate the carrier fluid through the pipes (Mustafa Omer, 2008).

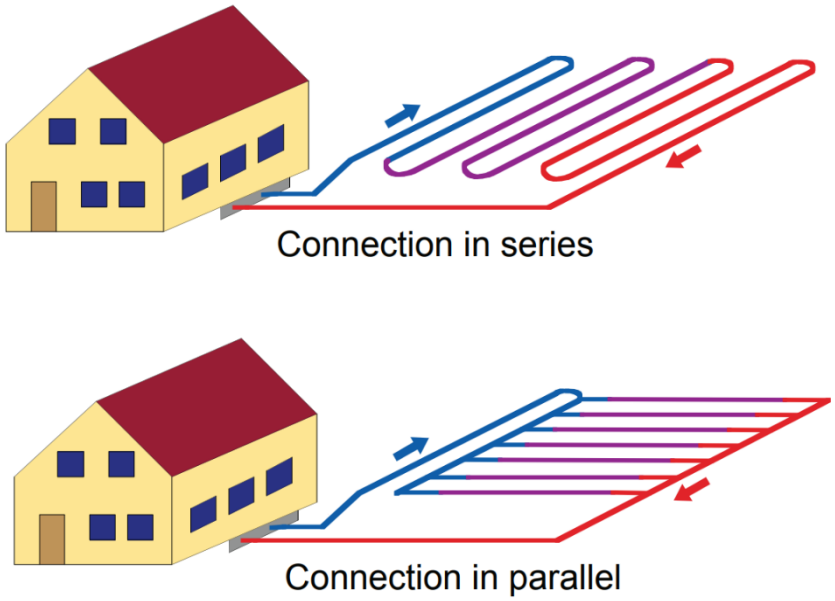


Figure 2.7 Illustration of heat exchanger pipes connected in series and in parallel in horizontal closed loop systems (Sanner, 2005)

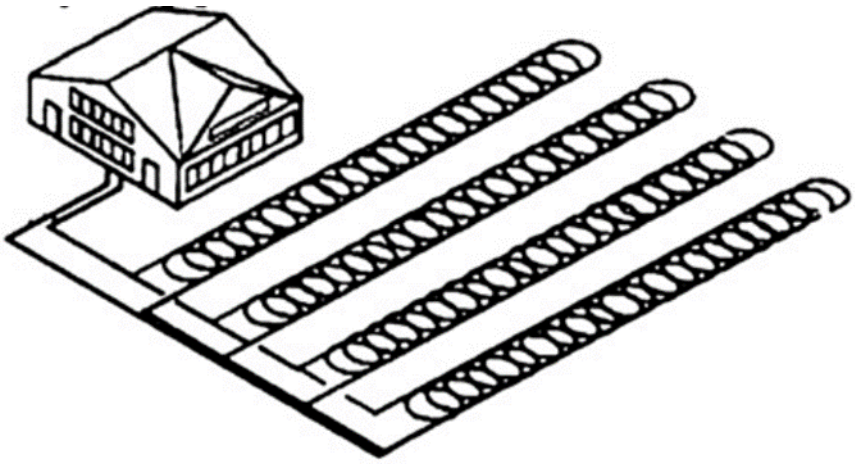


Figure 2.8 Illustration of heat exchanger pipes arranged in slinky-coils in horizontal closed loop systems (Fujii et al., 2012)

Vertical closed loops

In a vertical closed loop system, heat exchanger pipes are oriented vertically. Its installation involves drilling a borehole into the ground, which is typically $45 - 75\ m$ deep for residential and over $150\ m$ for industrial applications, lowering the heat exchanger pipes into the borehole, then filling the borehole with a pumpable grout (Self et al., 2013). The grouted borehole with heat exchanger pipes is usually referred to as a borehole heat exchanger (BHE). The advantages of vertical closed loop systems are that they do not require large areas of ground for installation,

ground temperatures are not subjected to seasonal variations (and hence are relatively constant throughout the year) for the depths they are reaching, resulting in a more reliable system performance, with borehole drilling also introducing smaller ground disturbances than the trenching required for horizontal closed loop systems (Mustafa Omer, 2008; Self et al., 2013). However, vertical closed loop systems are generally more expensive than horizontal closed loop systems as drilling is more expensive than trenching.

Vertical closed loop systems differ from one another mainly in terms of the configuration of heat exchanger pipes within the BHE. The following are a few commonly adopted basic pipe configuration designs:

- Single U-loop configuration – this is the simplest pipe configuration and consists of a pair of straight heat exchanger pipes connected by a U-shaped connector at the bottom. This is illustrated in Figure 2.9(a) (Sliwa et al., 2016).
- Double U-loop configuration – rather than having one U-loop of heat exchanger pipes in the BHE, two U-loops are installed. This is illustrated in Figure 2.9(b) (Sliwa et al., 2016).
- Coaxial configuration – a heat exchanger pipe with a centric system, where the annular space carries the carrier fluid down the BHE and the inner space circulates the fluid up the BHE. This is illustrated in Figure 2.9(c) (Sliwa et al., 2016).
- Double-pipe configuration – this configuration is mostly seen in steel thermo-active piles, where the hollow steel pile is filled with water to form a well, and heat exchange takes place by extracting/injecting hot or cold water from/into the well. This is illustrated in Figure 2.9(d) (Morino & Oka, 1994).

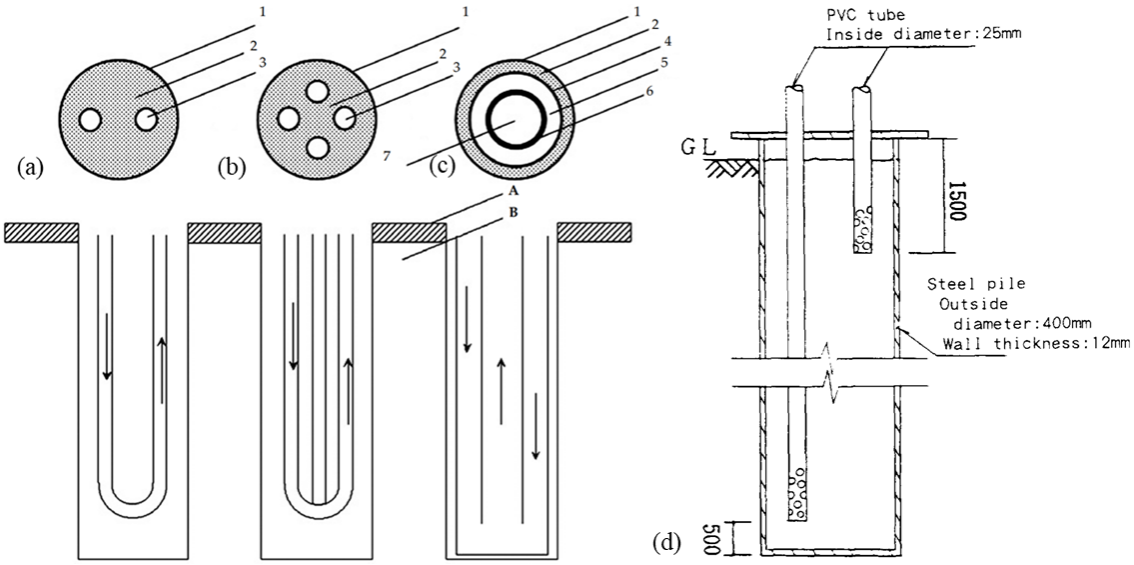


Figure 2.9 Illustration of (a) single U-loop configuration, (b) double U-loop configuration, (c) coaxial configuration (Sliwa et al., 2016) and (d) double-pipe configuration (Morino & Oka, 1994)

However, it should be noted that there exist other designs of pipe configuration (such as triple U-loop, W-loop, complex coaxial, spiral and multitube (Sanner, 2005; Gao et al., 2008; Jalaluddin et al., 2011; Fadejev et al., 2017; Zhao et al., 2018)) which will not be discussed here for brevity, as their designs would be similar to or derived from the three aforementioned basic configurations.

The performance of a $105\ m$ deep BHE with a coaxial pipe configuration installed in Elgg near Zurich, Switzerland in 1986 was reported by Rybach (2001). This BHE was utilised to provide heating for a single-family house, and it was capable of providing an average of about $13\ MWh$ per year, with a peak thermal power of $70\ W \cdot m^{-1}$. Temperature profiles with depth were measured at a distance of $1\ m$ from the BHE, and were reported every year before the heating season began and are shown in Figure 2.10 (Rybach, 2001). According to Rybach (2001), a number of observations can be made from Figure 2.10:

- The ground temperatures of the top $15\ m$ were affected by atmospheric conditions, below that geothermal effects dominate.
- As the BHE was utilised for heating purposes, heat was extracted from the ground, which resulted in lower ground temperatures (about $1 - 2^{o}C$) than the undisturbed profile.

- A stable thermal equilibrium between the BHE and the ground was reached after $2-3$ years of operation.
- The small variations between profiles of different years after $2-3$ years of operation were due to the difference in yearly heating demands.

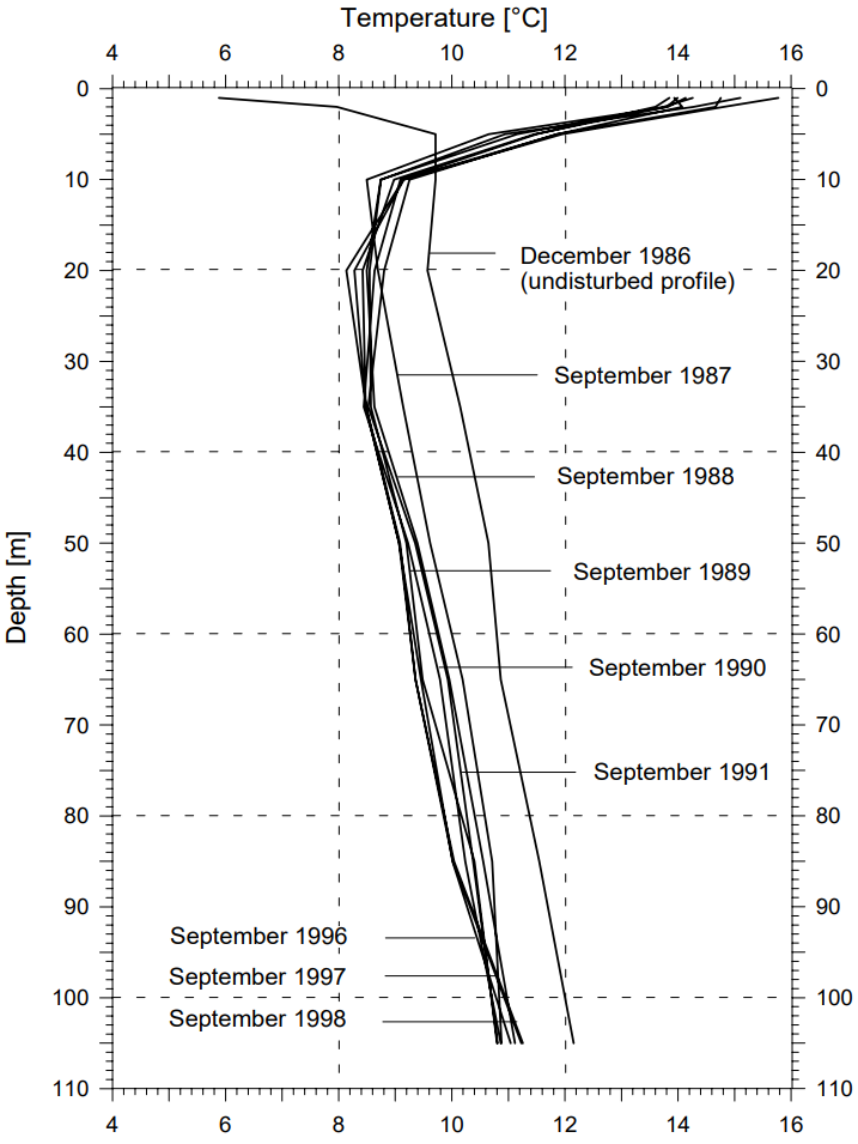


Figure 2.10 Temperature with depth profiles measured at a distance of $1\ m$ from the BHE in Elgg (Rybach, 2001)

2.3 THERMO–ACTIVE STRUCTURES

Thermo-active structures, which are also known as geothermal structures or energy geostructures, are geotechnical structures utilised as ground source systems, which form part

of the GSHP system. As a result, thermo-active structures serve two purposes: to provide structural stability, similar to conventional geotechnical structures, and to exchange heat with the ground as part of a GSHP system in order to provide renewable, low-carbon heating and cooling. As a ground source system, heat exchanger pipes are embedded within thermo-active structures to allow circulation of carrier fluid (i.e. closed loop). Also, the fact that most of the geotechnical structures are made of concrete means that their use as thermo-active structures is ideal, since concrete has good thermal conductivity and storage capacity (Soga & Rui, 2016).

There is a growing popularity in the use of thermo-active structures due to an increasing demand for renewable energy and stricter sustainability targets. For example, the Merton Rule requires that a proportion of the energy demand of a building is generated on site using renewable sources (Merton Council, 2010; World Wide Fund For Nature, 2019), and that designing geotechnical structures to be thermo-active could perhaps be the only feasible and economically viable renewable energy option in dense urban environments. According to Amis and Loveridge (2014), a building that adopts thermo-active foundation can typically meet $15\% - 25\%$ of its heating and cooling demands.

However, the fact that geotechnical structures are made thermo-active means that they are subjected to changes in temperature (they are cooled when utilised for heating purposes and heated when utilised for cooling purposes), with Loveridge and Powrie (2013) highlighting that inappropriate operation of these thermo-active structures may result in ground freezing, excessive ground deformations or additional stresses that the structures may not have been designed for. In particular, Brandl (1998) reported a thermo-active pile that has been subjected to excessive heat extraction by the circulation of carrier fluid at -5^oC, which caused the formation of ice lenses in the soil, resulting in $150\ mm$ heave at the ground surface, suggesting that the relative movement between the pile and its surrounding soil had altered the shaft skin friction. As a result, according to Loveridge and Powrie (2013), conservative design approaches have been adopted for thermo-active structures, which include applying factors of safety to ensure that thermo-active structures can withstand the additional thermally-induced stresses and displacements, and not to circulate carrier fluid below 2^oC to prevent ground freezing (NHBC, 2010).

The most common thermo-active geotechnical structures are piles, diaphragm walls and tunnels, which will be discussed in the following subsections.

2.3.1 Thermo-active piles

Thermo-active piles, which are also known as thermal piles or energy piles, are piles with heat exchanger pipes embedded within them which allow them to function both as a conventional pile to provide structural stability as foundations and as a heat exchanger to provide heating and cooling. Thermo-active piles are similar to BHEs described in Section 2.2.2.3 as they are both vertical closed loop systems, with the pipe configurations adopted in BHEs (e.g. single U-loop, double U-loop, etc.) also being applied in thermo-active piles. The main differences between thermo-active piles and BHEs are that the former usually have much smaller aspect ratios (length-to-diameter) – according to Loveridge and Powrie (2013), the aspect ratios for thermo-active piles are usually in the range of $10 - 50$, while the aspect ratios for BHEs are typically $500 - 1000$, and that the installation of heat exchanger pipes in thermo-active piles generally involves fixing the pipes to the reinforcement cage of the pile, which is illustrated in Figure 2.11 (Soga & Rui, 2016), before lowering them into the borehole and placement of concrete.



Figure 2.11 Illustration of heat exchanger pipes being fixed to the reinforcement cage in a thermo-active pile (Soga & Rui, 2016)

The concept of thermo-active piles was pioneered in Austria in the 1980s (Brandl, 2006; Amis & Loveridge, 2014), after which their use increased significantly in the 1990s and 2000s, but the rate of increase decreased after 2010 due to economic slowdown (Soga & Rui, 2016). Thermo-active pile installations have been reported in many countries, to name just a few, United Kingdom, United States, Japan, Switzerland, Netherlands, Belgium and China (Soga & Rui, 2016). However, according to Amis and Loveridge (2014), the use of thermo-active piles in the United Kingdom developed relatively slowly due to the availability of cheap gas, with the first thermo-active pile project started in 2001 for a new building at Keble College at Oxford University (Brandl, 2006). Nevertheless, due to an increase in energy prices and the implementation of the aforementioned sustainability targets (e.g. Merton Rule), the use of thermo-active piles in the United Kingdom is increasing (Amis & Loveridge, 2014), and Figure 2.12 shows the number of thermo-active piles installed and the resulting CO_2 savings in the United Kingdom from 2005 to 2016 (Sani et al., 2019).

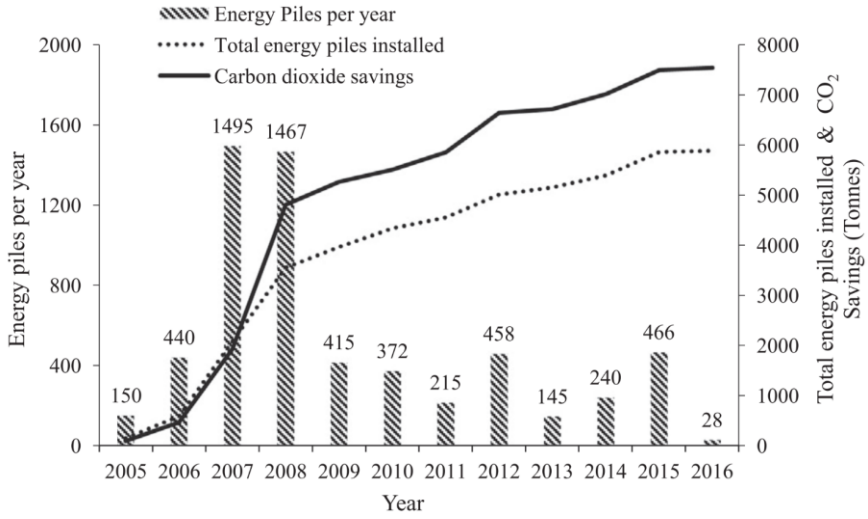


Figure 2.12 Number of thermo-active piles installed cumulatively and the resulting CO_2 savings in the United Kingdom from 2005 to 2016 (Sani et al., 2019)

The One New Change is a major office and retail development in London, which makes use of both thermo-active piles and open loop system to provide heating and cooling for its $31000\ m^2$ of office space and $21000\ m^2$ of retail space, and was the largest heat pump system in Europe when it opened (McWilliam, 2009; Devriendt et al., 2012; Garber et al., 2013; Amis & Loveridge, 2014). According to Devriendt et al. (2012), 189 out of a total of 219 load-bearing piles within the development are thermo-active, in which fluid at temperatures of 30^oC to 44^oC is circulated through the heat exchanger pipes within the piles during the summer to be

cooled by $3-5^oC$, and fluid at temperatures of -4^oC to 5^oC is circulated during the winter to be heated up by $3-5^oC$; while the open loop system consists of a production and an injection well installed to a depth of $130\ m$ into the chalk aquifer. Figure 2.13 presents the plan view of the development showing the locations of the thermo-active piles, the production (extraction) and injection (re-injection) wells (Devriendt et al., 2012). According to Amis and Loveridge (2014), the thermo-active piles at One New Change are capable of providing $2\ MW$ power of heating and cooling, which lead to annual energy savings of £65000 and CO_2 savings of 300 tonnes.



Figure 2.13 Plan view of One New Change showing the locations of thermo-active piles, production and injection wells (Devriendt et al., 2012)

According to Brandl (2006), it can generally be assumed that thermo-active piles with diameters $0.3-0.5\ m$ can achieve thermal performances of $40-60\ W$ per m of pile length, while piles with diameters $\geq 0.6\ m$ can achieve thermal performances of $35\ W$ per m^2 of earth-contact area. However, it should be noted that the actual thermal performance of a thermo-active pile is highly dependent on a number of factors, which include the site characteristics, configuration of heat exchanger pipes within the pile, flow rate of carrier fluid, temperature difference between the carrier fluid and the surrounding soil, etc., and can vary from lower than $20\ W \cdot m^{-1}$ (e.g. Henderson et al. (1998)) to higher than $250\ W \cdot m^{-1}$ (e.g. Sekine et al. (2007)). Table 2.2 shows a summary of field studies that have been conducted to

investigate the thermal performance of thermo-active piles. Alongside with the references which presented the studies, the location, ground temperature, dimensions of thermo-active piles, pipe configuration, test or monitoring duration, inlet temperatures, carrier fluid flow rate and power output are also presented in Table 2.2. It should be acknowledged that summaries of field studies on the thermal performance of thermo-active piles are also presented in Bourne-Webb (2013), Fadejev et al. (2017), Gawecka (2017) and Sani et al. (2019), the contributions of which are also included in the summary presented in Table 2.2. Note that the studies are presented in a chronological order in Table 2.2.

Based on the field studies summarised in Table 2.2, the following trends on the thermal performance of a thermo-active pile can be observed:

- The thermal performance of a thermo-active pile can be increased by increasing the difference between inlet temperature and the ground temperature, based on the studies by Nagano et al. (2005), Gao et al. (2008) and You et al. (2014). The reason is that the heat exchange between the pile and the surrounding soil takes place via conduction, which is governed by the Fourier's Law, which states that the rate of heat transfer is directly proportional to the thermal gradient.
- The thermal performance of a thermo-active pile during operation can be increased by operating the thermo-active pile intermittently, based on the studies by You et al. (2014), Faizal et al. (2016), Li et al. (2021a) and Li et al. (2021b). This is to be expected given that intermittent operation allows the temperature in the soil to recover and therefore increases the temperature difference between the heat exchanger pipes, pile and the surrounding soil. However, it has to be emphasised that the intermittent operation of a thermo-active pile can only increase its thermal performance during operation, its overall thermal performance (i.e. total energy over a year) is lower compared to the case of continuous operation (You et al., 2014).
- The thermal performance of a thermo-active pile can be increased by increasing the carrier fluid flow rate, based on the studies by Gao et al. (2008), Jalaluddin et al. (2011), You et al. (2014) and Park et al. (2017). However, it appears that the increase in thermal performance with the carrier fluid flow rate is not linear and there exists a point above which further increase of the flow rate does not yield further improvement in performance.

- The thermal performance of a thermo-active pile can be increased by increasing the number of U-loops in the pile, based on the studies by Hamada et al. (2007), Gao et al. (2008), Brettman et al. (2010) and Jalaluddin et al. (2011).

The thermal-mechanical behaviour of thermo-active piles will be reviewed in detail in Chapter 3.

References	Location	Ground temperature [℃]	Thermo-active pile details					Test or monitoring duration	Power output $[W \cdot m^{-1}]$
			Diameter $[mm]$	Length $[m]$	Pipe configuration	Inlet temperatures [℃]	Carrier fluid flow rate $[\times 10^{-6}\ m^3 \cdot s^{-1}]$		
Morino and Oka (1994)	Funabashi, Japan	15	400	20	Double-pipe (*)	30-40	1083.3	9 hours × 3	116.7-138.9 (average) and 291.7 (peak)
						3-11	500	4 hours × 3	69.4-86.1 (average) and 408.3 (peak)
Henderson et al. (1998)	Geneva, New York, United States	8	200	25.9	Single U-loop	3-30	Unspecified	2 years	18.3 for injection; 16.4 for extraction

(*) See Figure 2.9 for the geometry of double-pipe configuration.

Table 2.2 A summary of field studies conducted to investigate the thermal performance of thermo-active piles (includes contributions from Bourne-Webb (2013), Fadejev et al. (2017), Gawecka (2017) and Sani et al. (2019))

Nagano et al. (2005)	Hanamaki, Japan	13	145	8	Single U-loop	0	100	50 days	20
	Sapporo, Japan	9.3	400	40	Double-pipe (*)	2	83.3	13 days	20.4-27.2
					Double-pipe (*)	-5	166.7-500	46 days	64.6-94.9
					Single U-loop	2	166.7-500	60 days	17.0-24.3
					Single U-loop	-5	166.7-200	17 days	41.9-54.7
					Double U-loop	2	166.7-500	60 days	19.9
			165		Double-pipe (*)	2	166.7-500	42 days	14.9-19.8
					Double-pipe (*)	-5	166.7-500	46 days	45.2-61.6
					Single U-loop	2	166.7-500	60 days	13.7-14.3
					Single U-loop	-5	100-166.7	17 days	29.9-38.9
					Double U-loop	2	166.7-500	60 days	17.9-18.9
Schnürer et al. (2005); Kipry et al. (2009)	Berlin, Germany	10	Unspecified	8.5	Double U-loop	Unspecified	Unspecified	4 years	5-35 for injection; 0-30 for extraction

Table 2.2 (continued)

Li et al. (2006)	Tianjin, China	Unspecified	Unspecified	Unspecified	Single U-loop	30	222.2-333.3	1 day	130-210
						3-5			60-70
Pahud and Hubbuch (2006); Pahud and Hubbuch (2007)	Zurich Airport, Switzerland	12	900-1500	26.8	5 U-loops	3-17	238.9	2 years	16 (average) and 33 (peak) for injection; 45 (average) and 72 (peak) for extraction
Sekine et al. (2007)	Chiba, Japan	17	1500	20	8 U-loops	Unspecified	450-550	68 days	100 (average) and 158 (peak) for injection
								68 days	120 (average) and 164 (peak) for injection
								100 days	44 (average) and 119 (peak) for extraction
								100 days	52 (average) and 124 (peak) for extraction
								66 days	204 (average) and 259 (peak) for injection
								66 days	220 (average) and 278 (peak) for injection

Table 2.2 (continued)

Hamada et al. (2007)	Sapporo, Japan	6.7	302	9.0	Single U-loop	17.79	73.0	Unspecified	53.81
					Double U-loop	18.90	67.7		54.76
					Double-pipe (*)	21.07	76.7		68.71
					Single U-loop	-0.6	Unspecified	131 days	Unspecified
Gao et al. (2008)	Shanghai, China	18.2	600	25	W-loop	32/38	95	Unspecified	70/97
						35	47.5/95/190		53/82.5/93
					Single U-loop		95		58
					Double U-loop		190		90
					Triple U-loop		285		108
Kipry et al. (2009)	Germany	Unspecified	Unspecified	20	Unspecified	Unspecified	Unspecified	4 years	5-35 for injection; 0-30 for extraction
Wood et al. (2009); Wood et al. (2010)	Burton-on-Trent, United Kingdom	11	300	10	Single U-loop	Unspecified	Unspecified	200 days	36.9

Table 2.2 (continued)

Brettman et al. (2010)	Richmond, Texas, United States	22	300	18.3	Single U-loop	40-45	Unspecified	3-4 days	93.8
			300		Double U-loop				121.4
			450		Single U-loop				91.4
			450		Double U-loop				121.8
			300		Double U-loop				82.3
Jalaluddin et al. (2011)	Saga, Japan	17-18	139.8	20	Single U-loop	27	33.3/66.7/133.3	1 day	24.9/30.4/31.5
					Double-pipe (*)				36.9/49.6/54.8
					Multitube				26.6/34.8/40.2
Park et al. (2013)	Suwon, Korea	17	400	13.25	W-loop	Unspecified	250	14 hours	60.4
				13.75	Triple U-loop		283.3		72.7
You et al. (2014)	Shunyi, Beijing, China	16	420	18	W-loop	Up to 57/up to 40/up to 35	250	4 days	97.2/120.6/194.4
						35	128/250/501	2 days	84/116/94
						5/35/60	250	130 hours/50 hours/50 hours	58/116/258
						35		120 hours (intermittent mode)	139

Table 2.2 (continued)

Singh et al. (2015a)	Monash University, Melbourne, Australia	17.5-18.5	600	16.1	Single U-loop	Up to 50.5	133.3-166.7	3 days	190.4-235.6
					Triple U-loop	Up to 41		9 days	230.0
						Up to 48		52 days	181.0
Faizal et al. (2016)						5	250	20 days (24 hour mode)	79-157
								20 days (16 hour mode)	88-194
								20 days (8 hour mode)	132-213
Park et al. (2017)	Pusan, Korea	17.5	1500	60 (30 with pipes)	W-loop	30	28.0/41.0	14 days (8 hour mode)	46.9/55.7
						10-11	31.0/42.7		20.8/25.5 (normalised using the length of pile with pipes)
Zhao et al. (2018)	Jinan, China	Unspecified	1000	27	Spiral	7.5-12.5	189.2	45 hours	143.0
						3-4	162.3		53.3

Table 2.2 (continued)

Jensen-Page et al. (2019)	Parkville campue, University of Melbourne, Australia	18.1	600	30	Triple U-loop	Unspecified	750	14 days	60 for injection
								4 days	93.3 for injection
								3.5 days	120 for extraction
								19 hours	83.3 for injection
								13 hours	126.7 for extraction
								17 hours	123.3 for injection
								29 hours	140 for extraction
Li et al. (2021a); Li et al. (2021b)	Nanjing, China	19	1200	14	Triple U-loop	3.5	250	32 days (24 hour mode)	75
								46 days (16 hour mode)	115
Lou et al. (2021)	Ningbo, Zhejiang, China	20.7	650	52	Double U-loop	Up to 28.5	563	2 days	55.2

Table 2.2 (continued)

2.3.2 Thermo-active diaphragm walls

Thermo-active diaphragm walls, which are also known as energy walls or thermal walls, are not the focus of the current research and will therefore only be briefly described here, a more detailed review on thermo-active diaphragm walls can be found in Sailer (2020). Thermo-active diaphragm walls are retaining walls with heat exchanger pipes embedded within them which allow them to be load-bearing structurally and exchange heat with the ground. The installation of heat exchanger pipes in diaphragm walls is similar to that in thermo-active piles, where heat exchanger pipes are fixed to the reinforcement cage of the wall (see Figure 2.14 (Hofinger & Kohlböck, 2005)) before lowering them into the trench, followed by the pouring of concrete. However, the heat exchanger pipes are usually positioned on the side of the wall that is closer to the soil in order to facilitate heat exchange with the ground and minimise the thermal resistance of concrete, Figure 2.15 shows the typical positions of heat exchanger pipes in the cross-section of a diaphragm wall (Soga & Rui, 2016).



Figure 2.14 Illustration of heat exchanger pipes fixed to the reinforcement cage of a thermo-active diaphragm wall (Hofinger & Kohlböck, 2005)

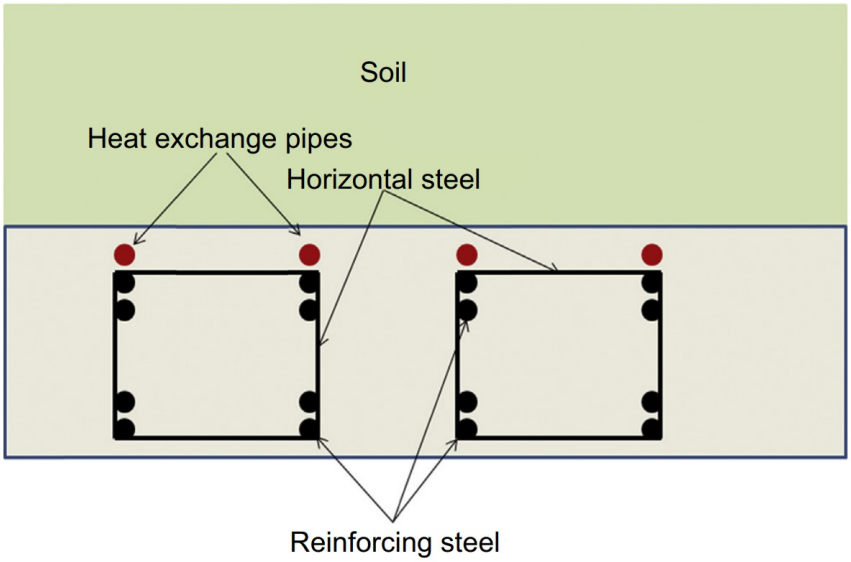


Figure 2.15 Illustration of the typical positions of heat exchanger pipes within the cross-section of a thermo-active diaphragm wall (Soga & Rui, 2016)

Similar to BHEs and thermo-active piles, different heat exchanger pipe configurations can be adopted within a thermo-active diaphragm wall. According to Sailer (2020), heat exchanger pipes are usually configured vertically within thermo-active diaphragm walls, as illustrated in Figure 2.16 (Soga & Rui, 2016), but they can also be configured horizontally, which is the case described in Brandl (1998) for an Arts Centre in Austria, and is illustrated in Figure 2.17 (Brandl, 1998). According to Brandl (2006), it can generally be assumed that thermo-active diaphragm walls can achieve thermal performances of 30 W per m^2 earth-contact area, though the actual thermal performance of a thermo-active diaphragm wall is highly dependent on the site of installation, configuration of heat exchanger pipes within the wall, and other operation parameters.

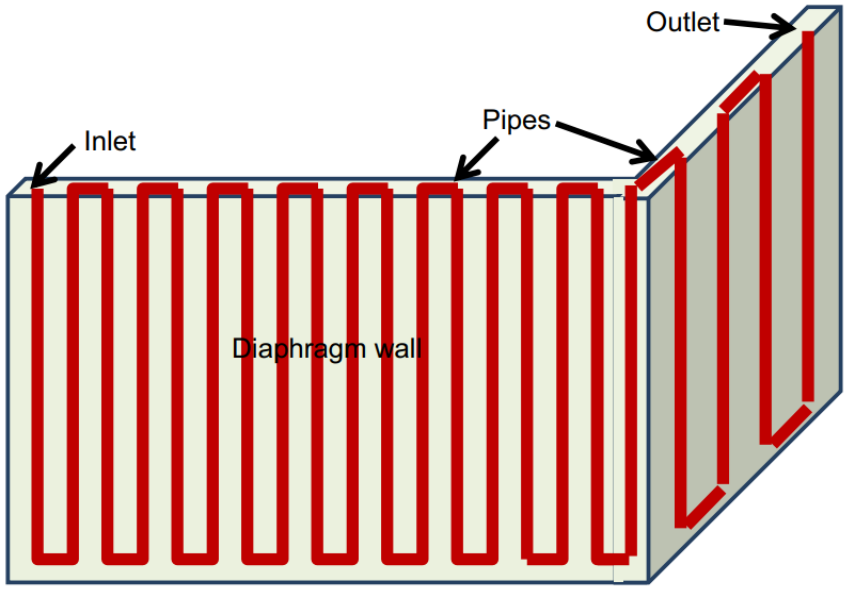


Figure 2.16 Illustration of the typical vertical configuration of heat exchanger pipes in a diaphragm wall (Soga & Rui, 2016)

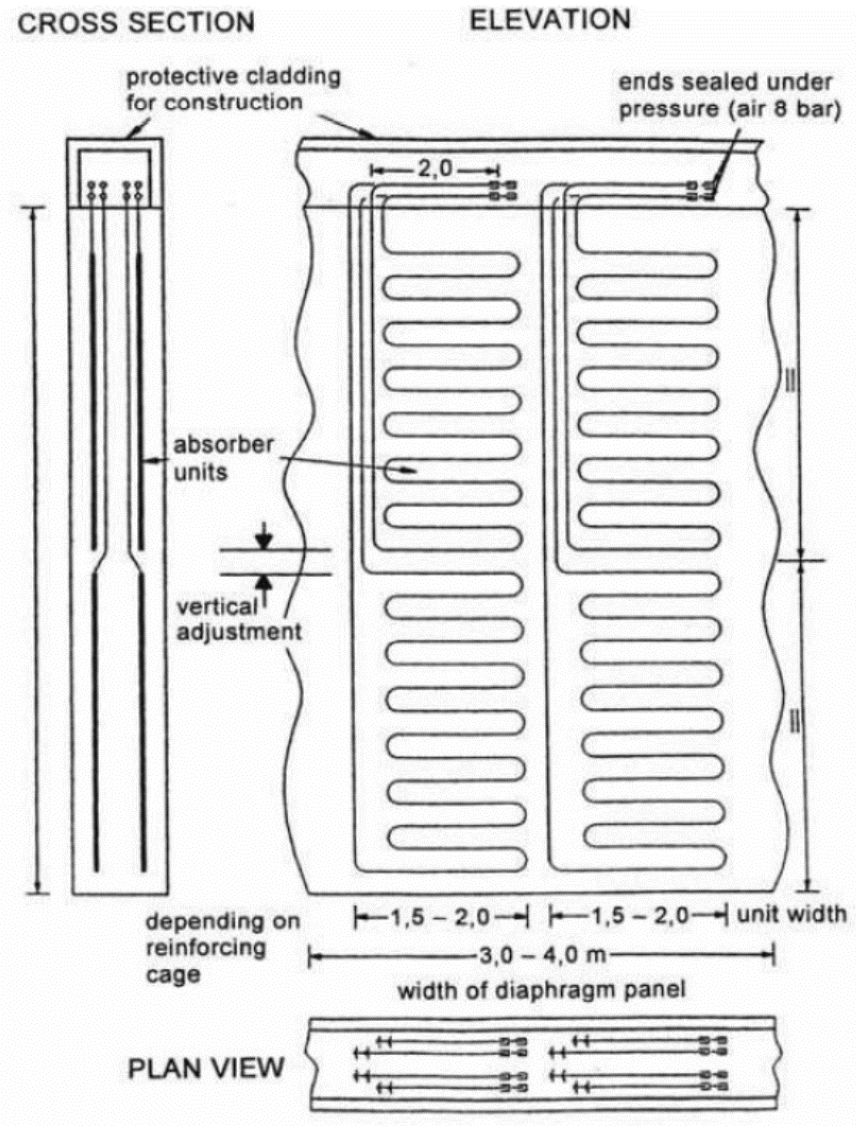


Figure 2.17 Illustration of a horizontal configuration of heat exchanger pipes in a diaphragm wall (Brandl, 1998)

The development of thermo-active diaphragm walls is not as well established as that for thermo-active piles. According to Brandl (2006), the use of thermo-active diaphragm walls started only in 1996 in Austria and Switzerland, with the first thermo-active diaphragm wall in the United Kingdom being constructed in 2010 at the Bulgari hotel in Knightsbridge, London (Amis & Loveridge, 2014). According to Amis et al. (2010), the thermo-active diaphragm walls at the Bulgari hotel are 800 mm thick and up to 36 m deep, with two U-loops of heat exchanger pipes per wall panel (Figure 2.18 presents the cross-section of a typical wall panel with the locations of heat exchanger pipes shown (Amis et al., 2010)). Amis and Loveridge (2014) reported that the use of thermo-active diaphragm walls at the Bulgari hotel, together

with thermo-active piles, which were also constructed at the site, can provide over 200 kW of heating and cooling.

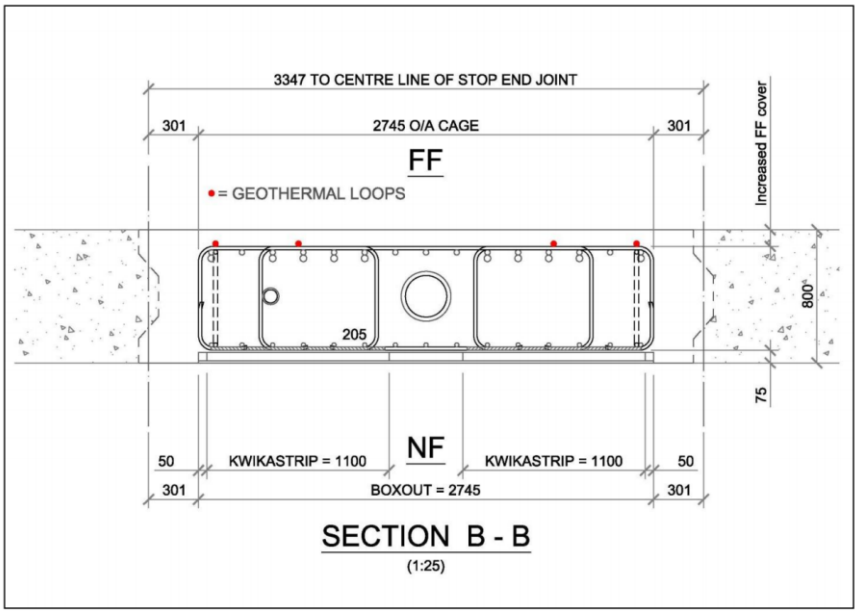


Figure 2.18 Cross-section of a typical thermo-active diaphragm wall panel at the Bulgari hotel (Amis et al., 2010)

2.3.3 Thermo-active tunnels

Thermo-active tunnels, which are also known as energy tunnels, are not the focus of the current research and will therefore only be briefly described here. Thermo-active tunnels are tunnels with heat exchanger pipes embedded within their linings which allow heat to be exchanged with the surrounding soil, or both the soil and the tunnel itself. According to Nicholson et al. (2014), underground trains generate a significant amount of heat due to the operation of their motors and braking systems, this waste heat can be extracted to provide heating in the buildings above, and at the same time, the tunnel can be cooled to provide passenger comfort, hence reducing the energy required for conventional tunnel ventilation operations. According to Soga and Rui (2016), there are two main operation modes for thermo-active tunnels, where they can be used for both heating and cooling purposes, or just for heating purposes. When a thermo-active tunnel is used for both heating and cooling purposes, an insulation layer has to be installed on the inner face of the tunnel to avoid comfort issues within the tunnel (i.e. the tunnel being heated up during the summer or cooled during winter), while if the thermo-active tunnel is used for heating purposes only, the insulation layer is unnecessary and heat is extracted from

both the soil and tunnel during the summer, but just from the soil during the winter (Soga & Rui, 2016).

There are different methods in which heat exchanger pipes can be installed into the tunnel lining. The most common method is to fix the heat exchanger pipes onto the reinforcement cage of the tunnel lining before concrete is cast, this is illustrated in Figure 2.19 (Nicholson et al., 2014). If the tunnel linings are precast in segments off-site, the end of a heat exchanger pipe in one segment is connected to the pipe in the next segment using pipe connections illustrated in Figure 2.20 (Soga & Rui, 2016). According to Soga and Rui (2016), if fibre reinforced concrete is used such that there is no reinforcement cage for the heat exchanger pipes to attach to, a simple frame structure is required to hold the pipes in place when the concrete is cast. Another method of fitting heat exchanger pipes into a tunnel lining is to fit the pipes within a geosynthetic material (Brandl, 2006), which can be geotextiles, geocomposites, or geomembranes (this is illustrated in Figure 2.21 (Hofinger & Kohlböck, 2005)). This geosynthetic layer with heat exchanger pipes can then be installed between the primary and secondary tunnel linings.



Figure 2.19 Illustration of heat exchanger pipes fixed to the reinforcement cage of a thermo-active tunnel lining (Nicholson et al., 2014)



Figure 2.20 Heat exchanger pipe connection between two precast thermo-active tunnel lining segments (Soga & Rui, 2016)

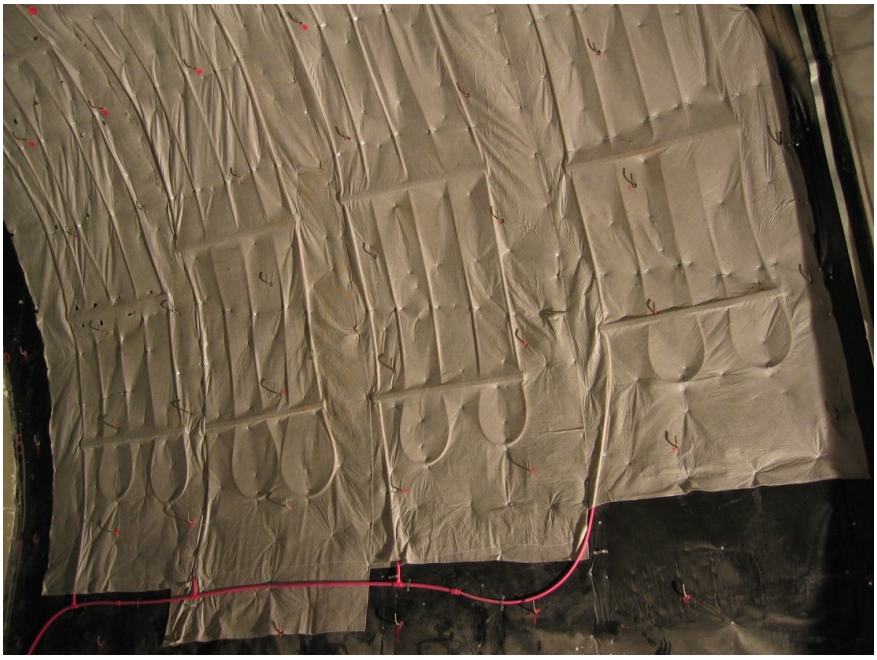


Figure 2.21 Illustration of heat exchanger pipes being fitted in a geotextile (Hofinger & Kohlböck, 2005)

The LT22 Bierhäuslberg section of the $12.8\ km$ long Lainzer Tunnel in Austria is the first tunnel that is constructed using the New Austrian Tunnelling Method (NATM) (in which a tunnel is supported by a primary lining of reinforced shotcrete, rockbolts and anchors, and a

secondary lining of reinforced concrete) to be made thermo-active (Brandl, 2006; Adam & Markiewicz, 2009). The chosen section of the tunnel was made thermo-active by installing prefabricated geocomposite with embedded heat exchanger pipes (see Figure 2.21) between the primary and secondary tunnel linings, and the schematic diagram of this thermo-active tunnel section is presented in Figure 2.22 (Brandl, 2006). Operation of this thermo-active tunnel initially began in 2004 with heat extraction, but the tunnel was designed such that it is capable of both heating and cooling operations (Adam & Markiewicz, 2009).

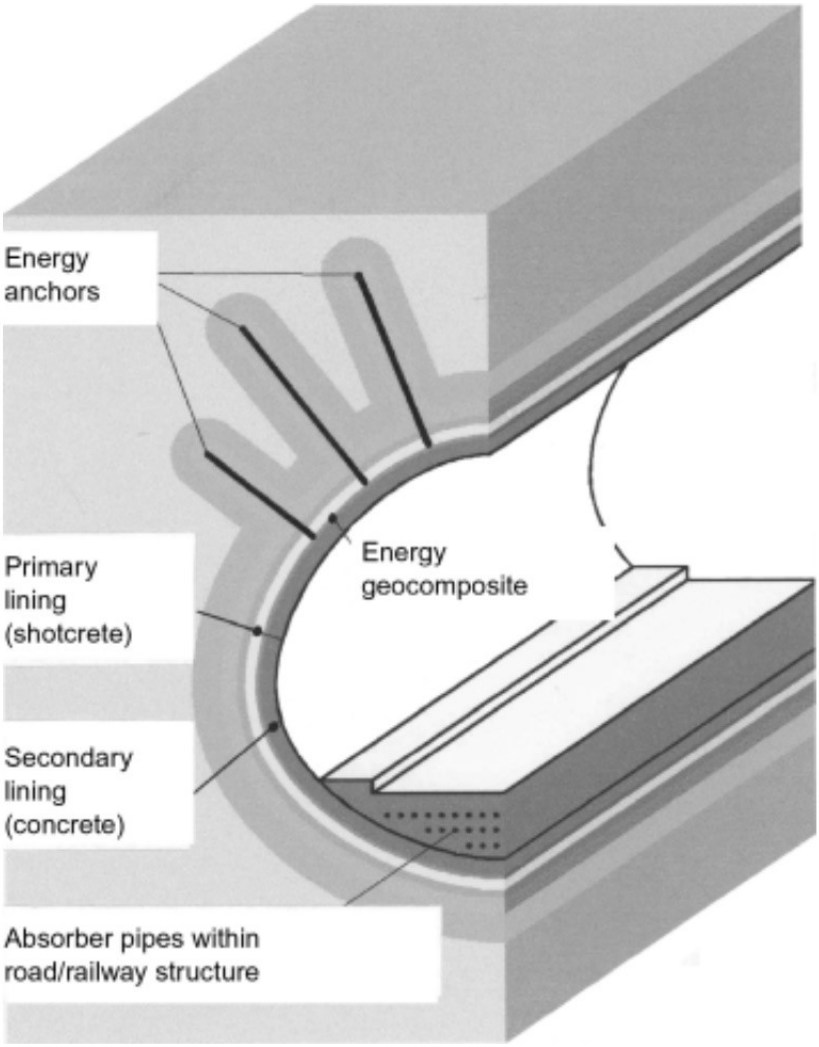


Figure 2.22 A schematic diagram of the thermo-active tunnel at the LT22 section of the Lainzer Tunnel (Brandl, 2006)

Recently, a real-scale testing of a new design of precast thermo-active segmental tunnel lining, which is known as Enertun, was conducted at the Turin Metro Line 1 South Extension in Italy (Barla et al., 2019; Insana & Barla, 2020). The Enertun lining that was tested features a

'ground&air' pipe configuration, which consists of two sets of pipe circuit, one of which is closer to the soil and is mainly responsible for exchanging heat with the soil, the other one is closer to the tunnel and is mainly responsible for exchanging heat with the air within it; this 'ground&air' pipe configuration is illustrated in Figure 2.23 (Barla et al., 2019). According to Barla et al. (2019), two rings of this Enertun segmental lining were tested at the Turin Metro Line 1 South Extension, which form a total longitudinal length of $2.8\,m$ and an internal diameter of $6.88\,m$. The thermal performance of the lining was tested and reported by Insana and Barla (2020), which shows that the tunnel is capable of delivering $47 - 66.4\,W \cdot m^{-2}$ of thermal power.

Other examples of operational thermo-active tunnels include the Viennese metro line extension U2 (Brandl, 2006; Adam & Markiewicz, 2009), Stuttgart Metro U6 (Schneider & Moormann, 2010), Crossrail Tunnel (Nicholson et al., 2014) and Linchang Tunnel (Zhang et al., 2013).

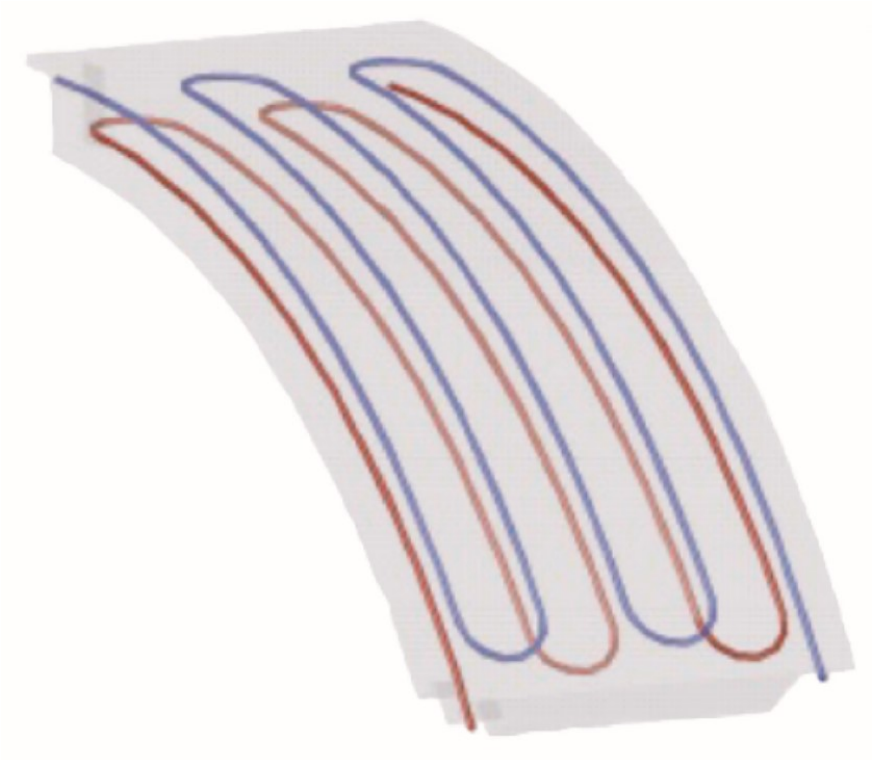


Figure 2.23 A 'ground&air' pipe configuration for the Enertun precast thermo-active segmental tunnel lining (Barla et al., 2019)

2.4 HEAT TRANSFER MECHANISMS IN SOILS

In this section, the following heat transfer mechanisms in soils will be explained:

- Conduction (Section 2.4.1)
- Convection (Section 2.4.2)
- Radiation (Section 2.4.3)
- Vapour diffusion (Section 2.4.4)
- Freeze-thaw processes (Section 2.4.5)

In soils, the mechanism that dominates the heat transfer process is mainly dependent on the grain size distribution and degree of saturation, as illustrated in Figure 2.24 (Loveridge, 2012). Referring to Figure 2.24, it can be observed that in a fine-grained fully saturated soil (i.e. a degree of saturation of 1.0), conduction is the dominant heat transfer mechanism, while for more coarse-grained fully saturated soils such as gravel, convection of water within its pores is the dominant mechanism. Note that all soils considered in the current research are fully saturated, and soil freezing will be excluded, therefore radiation and vapour diffusion, which can only be the dominant heat transfer mechanism in partly saturated soils, as well as freeze-thaw processes will only be briefly explained in the following subsections.

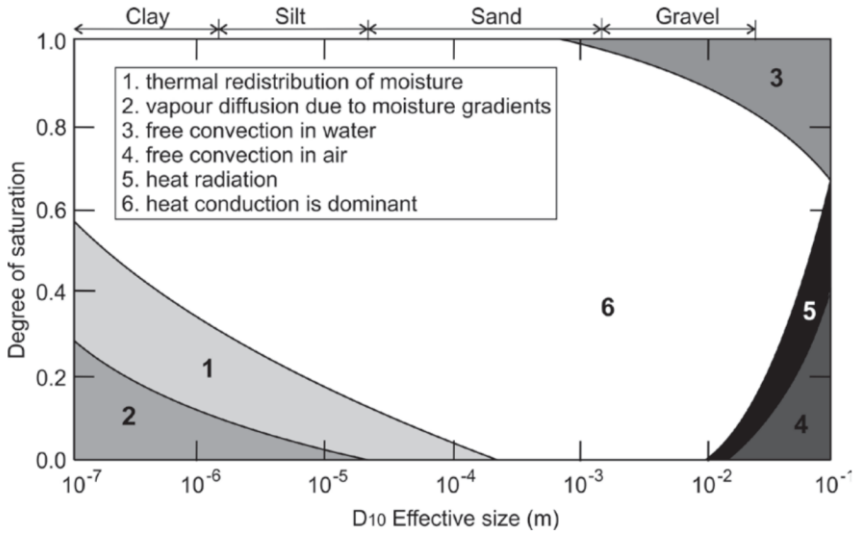


Figure 2.24 Dominant heat transfer mechanism by the grain size and degree of saturation of a soil (Loveridge, 2012)

2.4.1 Conduction

Conduction is a heat transfer mechanism that results from a thermal gradient, i.e. from a region of higher temperature to a region of lower temperature. Heat conduction occurs as particles in regions of higher temperatures vibrate more violently and are more likely to collide with neighbouring particles, causing them to vibrate more violently as well, and hence passing down the energy. As heat conduction relies on the collision of particles, it can only occur through matter (i.e. solid, liquid or gas) and not a vacuum (e.g. space). As a result, in soils, heat conduction can occur through all the three phases (i.e. soil particles, pore water and pore air). The equation describing heat conduction is given by the Fourier's law:

$$\boldsymbol{q_{conduction}} = -\lambda \boldsymbol{\nabla} T \tag{2.4}$$

In Equation (2.4), $\boldsymbol{q_{conduction}}$ $[W \cdot m^{-2}]$ is a vector of conductive heat fluxes, λ $[W \cdot m^{-1} \cdot K^{-1}]$ is the thermal conductivity of the material, $\boldsymbol{\nabla}$ $[m^{-1}]$ is the gradient operator which is a vector and T $[K]$ is temperature. Note that, in this thesis, symbols in bold represent vectors.

When Equation (2.4) is represented in transient form, the following equation can be derived by applying the conservation of energy:

$$\rho C_p \frac{\partial T}{\partial t} - \lambda \boldsymbol{\nabla^2} T = Q^T \tag{2.5}$$

In Equation (2.5), ρ $[kg \cdot m^{-3}]$ is the density of the material, C_p $[J \cdot kg^{-1} \cdot K^{-1}]$ is the specific heat capacity of the material, t $[s]$ is time and Q^T $[W \cdot m^{-3}]$ is the heat source or sink.

2.4.2 Convection

Convection is a heat transfer mechanism that occurs due to the movement of fluid, and hence can only occur in liquids and gases (i.e. pore water and pore air in soils). It can only be the dominant mechanism of heat transfer in coarse-grained soils (see Figure 2.24) where pores are sufficiently large and relatively permeable to water movement. Convection is the combined processes of heat conduction and heat advection, while heat conduction has been explained in Section 2.4.1, heat advection is the transfer of heat due to bulk fluid flow. The expression for convective heat flux is therefore given by:

$$\boldsymbol{q_{convection}} = \boldsymbol{q_{conduction}} + \boldsymbol{q_{advection}} \tag{2.6}$$

In Equation (2.6), $\boldsymbol{q_{convection}}$ $[W \cdot m^{-2}]$ is a vector of convective heat fluxes, $\boldsymbol{q_{conduction}}$ is given by Equation (2.4) and $\boldsymbol{q_{advection}}$ $[W \cdot m^{-2}]$ is a vector of advective heat fluxes, which is given by:

$$\boldsymbol{q_{advection}} = \rho_f C_f \boldsymbol{v_f}\left(T - T_{ref}\right) \tag{2.7}$$

In Equation (2.7), ρ_f $[kg \cdot m^{-3}]$ is the density of fluid, C_f $[J \cdot kg^{-1} \cdot K^{-1}]$ is the specific heat capacity of the fluid, $\boldsymbol{v_f}$ $[m \cdot s^{-1}]$ is a vector of fluid velocities and T_{ref} $[K]$ is the reference temperature. As a result, Equation (2.6) can be written as:

$$\boldsymbol{q_{convection}} = -\lambda \boldsymbol{\nabla} T + \rho_f C_f \boldsymbol{v_f}\left(T - T_{ref}\right) \tag{2.8}$$

Note that the Péclet number Pe is often used to characterise whether a convective heat flux is advection dominated or conduction dominated:

$$Pe = \frac{\rho_f C_f v_f L_c}{\lambda} \tag{2.9}$$

In Equation (2.9), L_c $[m]$ is a characteristic length. A convective heat transfer is advection dominated if $Pe \gg 1$ and conduction dominated if $Pe \ll 1$.

Equation (2.8) represents the convective heat flux in steady state condition, by applying conservation of energy, a transient form of the equation can be derived and is given by:

$$\rho_f C_f \frac{\partial T}{\partial t} - \lambda \boldsymbol{\nabla^2} T + \boldsymbol{\nabla} \cdot \left[\rho_f C_f \boldsymbol{v_f}\left(T - T_{ref}\right)\right] = Q^T \tag{2.10}$$

It should be noted that convection is also the mechanism that dominates heat transfer within heat exchanger pipes (Gawecka, 2017; Gawecka et al., 2020), as well as the heat loss of a body that is in contact with a fluid, which is defined by the Newton's law of cooling. The Newton's law of cooling states that the rate of heat loss is directly proportional to the difference in temperature between the body and the fluid:

$$q_{convection} = h\left(T_{body} - T_f\right) \tag{2.11}$$

In Equation (2.11), $h\,[W \cdot m^{-2} \cdot K^{-1}]$ is the heat transfer coefficient, $T_{body}\,[K]$ is the temperature of the body that is in contact with the fluid and $T_f\,[K]$ is the temperature of the fluid. Note that the heat transfer coefficient h is usually determined experimentally as it depends on many factors.

2.4.3 Radiation

Radiation is a mechanism of heat transfer originating from the fact that all matter with temperatures above absolute zero emit electromagnetic radiation due to the thermal motion of particles. As electromagnetic radiation can travel through vacuum, heat transfer by radiation does not have to occur through matter. The radiative heat flux that is given out by a body is given by:

$$q_{radiation} = \epsilon \sigma_{S-B} T_{body}^4 \tag{2.12}$$

In Equation (2.12), $q_{radiation}\,[W \cdot m^{-2}]$ is the radiative heat flux, ϵ is the emissivity factor, which is dimensionless and is dependent on the radiating surface, $\sigma_{S-B}\,[W \cdot m^{-2} \cdot K^{-4}]$ is the Stefan-Boltzmann constant and is equal to $5.67 \times 10^{-8}\, W \cdot m^{-2} \cdot K^{-4}$ and $T_{body}\,[K]$ is the surface temperature of the radiating body. However, referring to Figure 2.24 and according to Rees et al. (2000), heat transfer by radiation can usually be neglected, except in partly saturated, coarse, crushed-stone materials where radiation can contribute up to 10% of the total heat transfer.

2.4.4 Vapour diffusion

In partly saturated soils, water within pores can evaporate, absorbing latent heat of vaporisation (which is an energy of about $2265\ kJ \cdot kg^{-1}$) from its surroundings during this process; the vapour then diffuses through the soil down the vapour pressure gradient and condenses in regions of lower vapour pressure, releasing the same amount of energy to its surroundings, hence forming a mechanism of heat transfer (Loveridge, 2012). According to Loveridge (2012), the migration of moisture resulting from vapour diffusion can also change the degree of saturation of the soil, hence influencing its thermal properties.

2.4.5 Freeze-thaw processes

When water freezes, it releases latent heat of solidification (which is an energy of about $334\ kJ \cdot kg^{-1}$) into its surroundings. On the contrary, when ice thaws, it absorbs the same

amount of energy from its surroundings. According to Loveridge (2012), this constitutes a mechanism of heat transfer in soils in zones of freezing and thawing, adding that the freezing of soil is also associated with important mechanical effects, such as frost heave and cracking, therefore soil freezing due to the operation of GSHP systems should be avoided (Brandl, 2006).

2.5 THERMAL AND THERMO-MECHANICAL PROPERTIES OF SOILS AND CONCRETE

The rate of heat transfer and the resulting temperature change depend on the thermal properties of the material, which are thermal conductivity and specific/volumetric heat capacity, respectively. Moreover, when a material is subjected to changes in temperature, the mechanical effects (i.e. expansion or contraction) induced, which are governed by the coefficient of thermal expansion, play a significant role in the thermo-hydro-mechanical interactions observed in thermo-active structures. This section presents a review on thermal conductivity, specific/volumetric heat capacity, and coefficient of thermal expansion, as well as the typical values measured or observed for London Clay (the current research focuses on thermo-active structures founded in London Clay) and concrete.

2.5.1 Thermal conductivity λ

Thermal conductivity is a measure of the ability of a material to conduct heat and is defined as the amount of heat per unit time that can be conducted through a unit area with a unit temperature gradient, and has units of $W \cdot m^{-1} \cdot K^{-1}$. For soils, it should be appreciated that they are multiphase materials (with two phases for fully saturated soils – soil particles and pore water, and three phases for partly saturated soils – soil particles, pore water and pore air), their overall conductivities are therefore dependent on the conductivities of their phases, as well as the volume ratios and arrangements of the phases (Woodside & Messmer, 1961; Farouki, 1981). A detailed review on different theoretical models for thermal conductivity of multiphase materials can be found in Gawecka (2017). According to Loveridge et al. (2017), the simplest of those models is the Weiner bounds, where the lower and upper bounds of the overall thermal conductivity correspond to series and parallel arrangements of the material phases (Woodside & Messmer, 1961; Farouki, 1981), respectively, with the expressions for a three-phase soil given by Equations (2.13) and (2.14), respectively.

$$\frac{1}{\lambda_{min}} = \frac{1-n}{\lambda_{sp}} + \frac{nS_r}{\lambda_w} + \frac{(1-S_r)n}{\lambda_a} \tag{2.13}$$

$$\lambda_{max} = (1-n)\lambda_{sp} + nS_r\lambda_w + (1-S_r)n\lambda_a \tag{2.14}$$

In Equations (2.13) and (2.14), λ_{min} $[W \cdot m^{-1} \cdot K^{-1}]$ and λ_{max} $[W \cdot m^{-1} \cdot K^{-1}]$ are the lower and upper bounds of the overall thermal conductivity of the soil, respectively, λ_{sp} $[W \cdot m^{-1} \cdot K^{-1}]$, λ_w $[W \cdot m^{-1} \cdot K^{-1}]$ and λ_a $[W \cdot m^{-1} \cdot K^{-1}]$ are the thermal conductivities of the soil particles, pore water and pore air, respectively, n is the porosity and S_r is the degree of saturation.

The thermal conductivity of a material can be measured using many different types of laboratory tests, but they can be generally classified into two different approaches – transient and steady state. For soils, their thermal conductivities can also be measured in the field using in-situ methods.

2.5.1.1 Laboratory testing methods

Measuring the thermal conductivity of soil using laboratory testing methods has the advantage of giving results quickly and at a relatively low cost. However, compared to full-scale in-situ testing methods, these small-scale testing have scale and sampling issues (Low et al., 2015; Loveridge et al., 2017). Soils are inherently heterogeneous, and properties such as water content and density vary with depth, so when there is a localised change in property at which the soil is sampled for testing, the results can be significantly affected and do not provide a representation of the bulk thermal conductivity at the site. The study by King et al. (2012) showed that a minimum of 12 to 16 samples are required to be tested in order to give a stable estimate of the bulk thermal conductivity at the site. Large-scale soil layering cannot be taken into account by laboratory testing methods either. Besides, laboratory testing involves taking samples from the site, and this sampling process may introduce disturbances to the samples, such as a change in water content, density and structure. The stress release during the sampling process may also change the porosity of the sample, which leads to a change in thermal conductivity of the soil, as shown by Martinez Calonge (2017). As a result, it is very important to ensure that samples are either intact or reconstituted to the field conditions prior to testing. This subsection reviews some of the most common and popular laboratory tests for the measurement of thermal conductivity, while a more detailed review can be found in Gawecka (2017).

Transient approach

Laboratory testing of thermal conductivity using a transient approach involves heating the sample and monitoring the changes in temperature over time (Farouki, 1981; Low et al., 2015; Loveridge et al., 2017). The thermal conductivity can then be determined using the analytical solution to the heat diffusion equation. The needle probe (also known as hot wire method) and dual-probe heat-pulse are two common and popular methods that adopt the transient approach to measure the thermal conductivity of a sample.

- Needle probe test

The needle probe test is a quick and convenient test that measures the thermal conductivity by inserting a needle, which contains a wire heating element and temperature sensors, into the sample. The sample is then heated and the temperature change is monitored and interpreted using a line source approach (Farouki, 1981; Loveridge et al., 2017). During the test, a change in temperature of only a few degrees is involved which, for soils, minimises moisture migration effects (De Vries, 1952). The needle probe test was first used by Hooper (1950) to measure the thermal conductivity of soils, and Bloomer (1981), Low et al. (2015) and Martinez Calonge (2017) are examples where this testing method is used to measure the thermal conductivity of London Clay.

- Dual-probe heat-pulse test

The dual-probe heat-pulse test is similar to the needle probe test except that it involves a second needle which contains a thermocouple and acts as a second temperature monitoring probe that is located a few millimetres from the first needle (Campbell et al., 1991; Nusier & Abu-Hamdeh, 2003; Loveridge et al., 2017; Martinez Calonge, 2017). A short heat pulse is released and the temperature changes at both needles are monitored. The advantage of this test is that both the thermal diffusivity and volumetric heat capacity can be determined, but the drawback is that the results are very sensitive to the inter-probe spacing, which can diverge when the needles are inserted into the sample. For the determination of thermal conductivity, Martinez Calonge (2017) suggested that the simpler needle probe test should be preferred. Campbell et al. (1991), Nusier and Abu-Hamdeh (2003) and Martinez Calonge (2017) are examples where this testing method is used to measure the thermal conductivity of soils.

Steady state approach

The steady state approach involves measuring the thermal conductivity of the sample following the establishment of a thermal steady state, which may take some time after the application of temperature difference (Farouki, 1981). The guarded hot plate, divided bar and thermal cell are three common and popular methods that adopt the steady state approach to measure the thermal conductivity of a sample.

- Guarded hot plate test

The procedures for conducting a guarded hot plate test are described in Farouki (1981) and British Standards Institution (2001). The guarded hot plate test apparatus consists of two identical samples sandwiching a heater plate, which is surrounded by a guard section used to prevent horizontal heat losses and make sure that heat transfer only occurs vertically, and a pair of cooling units positioned above and below the samples, the configuration of which is illustrated in Figure 2.25 (British Standards Institution, 2001). During the test, a thermal gradient is established across the samples using the heater plate and the cooling units, the thermal conductivity of the sample can then be calculated using the Fourier's Law (Equation (2.4)) after thermal steady state is reached (Farouki, 1981). However, Farouki (1981) highlighted the drawback of applying this testing method to measure the thermal conductivity of soils: a considerable amount of time is required before thermal equilibrium can be achieved and a relatively large thermal gradient has to be applied which can lead to moisture migration in soils (Hutcheon & Paxton, 1952). Mitchell and Kao (1978), Nikolaev (2007) and Sáez Blázquez et al. (2017) are examples where this testing method is used to measure the thermal conductivity of soils.

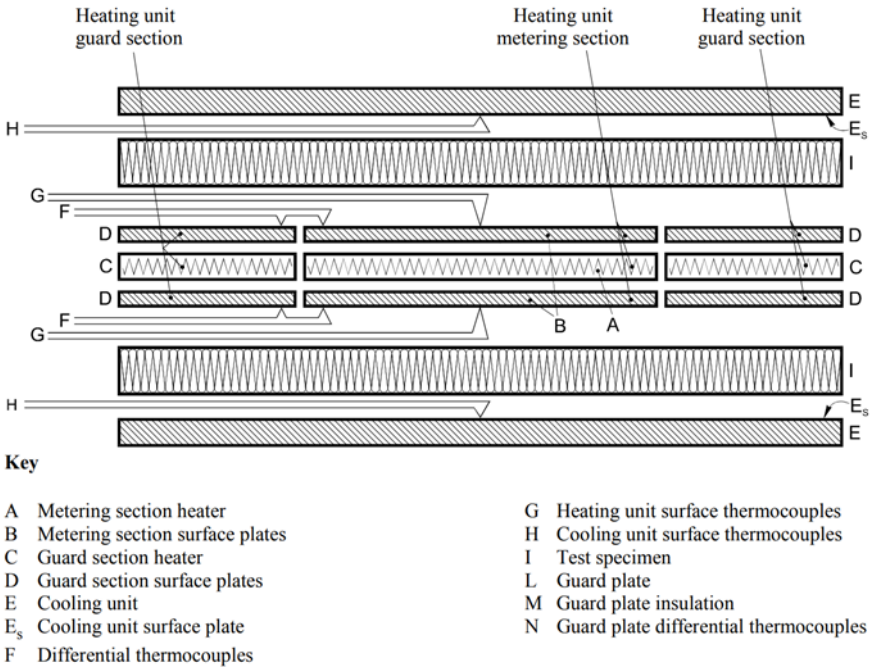


Figure 2.25 Configuration of the guarded hot plate test apparatus (British Standards Institution, 2001)

- Divided bar test

In a divided bar test, the soil sample is sandwiched between two samples of a reference material of known thermal conductivity, with a heat source and heat sink at the top and bottom of the resulting assembly, respectively (Sibbitt et al., 1979; McGuinness et al., 2014). Figure 2.26 shows a schematic diagram of the divided bar test (Sibbitt et al., 1979). A thermal gradient can be applied using the heat source and sink, and once thermal equilibrium is reached, the thermal conductivity of the sample can be calculated by comparing the heat flux through the sample with that through the reference materials (Sibbitt et al., 1979; Popov et al., 1999; McGuinness et al., 2014). The divided bar test shares similar drawbacks as the guarded hot plate test – it takes a long time before thermal equilibrium can be achieved, substantial moisture migration can result if the soil sample is unsaturated (Loveridge et al., 2017). The divided bar test is commonly used to measure the thermal conductivity of rocks (e.g. Sibbitt et al. (1979), Galson et al. (1987), Popov et al. (1999), McGuinness et al. (2014) and Bording et al. (2016)).

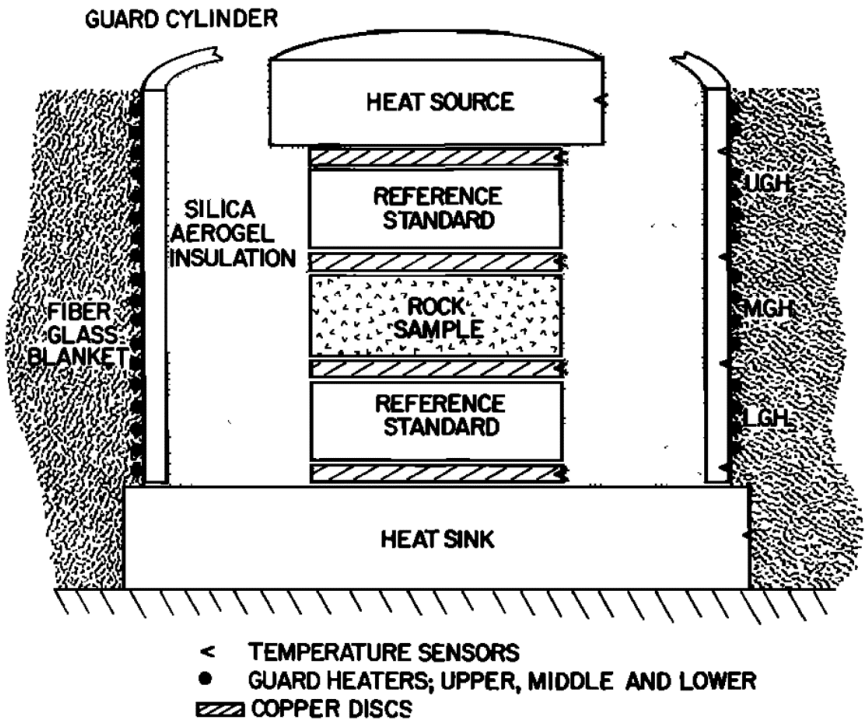


Figure 2.26 A schematic diagram of the divided bar test (Sibbitt et al., 1979)

- Thermal cell test

The thermal cell test was proposed by Clarke et al. (2008) which involves having the ends of a cylindrical sample maintained at different temperatures, and heat is allowed to flow axially through the sample, while the sample has to be insulated radially to prevent any radial loss or gain of heat. Drawbacks of this test include the long time for a thermal steady state to be reached, heat losses from the sample introduce errors to the results, and moisture migration may occur during the process (Low et al., 2015). Due to the accuracy issues associated with the thermal cell test, Low et al. (2015) concluded that the needle probe test should be preferred for the determination of the thermal conductivity of soil. Examples of using the thermal cell test to measure the thermal conductivity of soils include Clarke et al. (2008), Hamuda et al. (2010) and Low et al. (2015).

2.5.1.2 In-situ testing methods

The thermal response test (TRT) is an in-situ method to determine the thermal conductivities of soils in the field.

- Thermal response test (TRT)

The procedures for conducting a TRT can be found in Banks (2012), Loveridge et al. (2013) and Low (2016). In short, in a TRT, heat is injected into the ground at a constant and known rate using a BHE, the temperature of the fluid circulating the BHE is monitored and the results can be used to determine the thermal conductivity of the ground. TRTs can be interpreted using different approaches, though traditionally this has been done using the line source method, which assumes that the BHE is an infinitely long and infinitesimally thin heat source of constant power, and that the ground is homogeneous with uniform initial temperature (Sanner et al., 2005; Banks, 2012; Loveridge et al., 2017). There are other approaches for interpreting the results of a TRT, which includes assuming the BHE to be a cylindrical heat source instead of a line heat source, using more sophisticated models such as the Geothermal Properties Management (GPM) tool, as well as other analytical and numerical methods (Loveridge et al., 2017).

TRTs have the advantages of not having the scale and sampling issues present in laboratory testing methods (Low et al., 2015). For example, samples do not have to be removed from the ground, hence stress release-induced change in porosity does not occur and drying up of samples prior to testing is not an issue for TRTs either. Moreover, TRTs can account for the large-scale soil layering, which allows them to determine the thermal conductivity of the ground averaged over the length of the BHE, which is more representative of the conditions at the site of testing (Banks, 2012). However, the drawbacks of TRTs compared to laboratory testing methods are that they are more expensive and time-consuming to conduct.

Loveridge et al. (2017) compiled a number of studies that compare the thermal conductivity of soil measured by laboratory testing methods and TRTs, showing that the latter are, in most cases, higher than those from laboratory tests. They explained that such discrepancies could be due to the use of the line source method to interpret TRTs, but that sample quality could also contribute, as in some studies the number of laboratory tests conducted are relatively small. Moreover, for the study conducted by Low et al. (2015), they attributed the discrepancies to the sampling issues associated with the laboratory testing methods. Considering the advantages and drawbacks of laboratory tests and TRTs, as well as the results from the tests, Low et al. (2015) concluded that TRTs provide a better measurement of the in-situ soil thermal conductivity compared to the laboratory methods.

TRTs are popular and widely used to determine thermal conductivity of the ground. In the United Kingdom, for example, 61 TRTs were reported by Banks et al. (2013) which include tests throughout England, Wales, Scotland and Northern Ireland, plus a test in Isle of Man. 13 TRTs conducted throughout England during the period 2006-2010 were also reported by Underwood (2013).

2.5.1.3 Typical values for London Clay

This subsection presents a literature review on studies that measure the thermal conductivity of London Clay, which is the soil that will be modelled in subsequent chapters.

For laboratory testing methods:

- Bloomer (1981) conducted five needle probe tests on London Clay and a thermal conductivity of $2.45 \pm 0.07\ W \cdot m^{-1} \cdot K^{-1}$ was determined. Despite this value being often cited in recent literature (e.g. Headon et al., 2009; GSHPA, 2012; Banks et al., 2013), sample conditions and relevant site information were not reported.
- Low et al. (2015) conducted needle probe and thermal cell tests on six samples of London Clay from different depths and reported a thermal conductivity of $0.92 - 1.49\ W \cdot m^{-1} \cdot K^{-1}$ from the needle probe tests and $1.65 - 2.19\ W \cdot m^{-1} \cdot K^{-1}$ from the thermal cell tests. They attributed the higher values determined from the thermal cell tests to heat losses from the sample as well as moisture migration, which forms an additional mechanism of heat transfer, and concluded that the needle probe tests should be preferred.
- Martinez Calonge (2017) performed needle probe and dual-probe heat-pulse tests on seven intact samples of London Clay obtained at different depths from a borehole in Hyde Park, London. It was reported that a minimum of five tests were performed for each type of needle test on each sample. For the needle probe tests, the average thermal conductivity of the samples were determined to be $1.48 - 1.60\ W \cdot m^{-1} \cdot K^{-1}$, while for the dual-probe heat-pulse tests, the average thermal conductivity were determined to be $1.50 - 1.63\ W \cdot m^{-1} \cdot K^{-1}$. Martinez Calonge (2017) concluded that both the needle probe and dual-probe heat-pulse tests are adequate for the measurement of thermal conductivity as the results agree very well with each other. Given the small differences of results between the two methods, the simpler needle probe test is preferred.

The aforementioned laboratory tests on the thermal conductivity of London Clay are summarised in Table 2.3.

Reference	Test method	Number of samples	Thermal conductivity $[W \cdot m^{-1} \cdot K^{-1}]$
Bloomer (1981)	Needle probe	5	2.45 ± 0.07
Low et al. (2015)	Needle probe	6	$0.92 - 1.49$
	Thermal cell	6	$1.65 - 2.19$
Martinez Calonge (2017)	Needle probe	7	$1.48 - 1.60$
	Dual-probe heat-pulse	7	$1.50 - 1.63$

Table 2.3 Summary of laboratory tests on the thermal conductivity of London Clay

For in-situ testing methods:

- Banks et al. (2013) reported the results of 61 TRTs in the United Kingdom, which were carried out using closed-loop BHE since April 2005 by Geowarmth Heat Pumps Ltd., Lankelma Ltd. and Kensa Engineering Ltd. Out of the 61 TRTs, 17 of them were performed on the London Clay, Lower London Tertiary and Chalk sequence of the London Basin, and a typical thermal conductivity of $1.7 - 2.0\ W \cdot m^{-1} \cdot K^{-1}$ was reported with a range of $1.51 - 2.27\ W \cdot m^{-1} \cdot K^{-1}$. Unfortunately, details and the thermal conductivities from the individual tests were not reported.
- Underwood (2013) considered the results of 13 TRTs in the United Kingdom, most of which were obtained from commercially conducted drilling and TRT operations, the details of which were therefore confidential and unavailable. Out of the 13 TRTs reported, two of them involved testing in London Clay: one was conducted in Barnet, North London, with the actual lithology described as 100% dry London Clay, and a BHE reported to be $165mm$ in diameter and $69m$ deep, while the other one was conducted in Colchester, with the actual lithology described as 81% dry London Clay, 15% chalk and 4% sand/gravel, with a BHE that was $165mm$ in diameter and $97m$ deep. The thermal conductivities determined were $2.443\ W \cdot m^{-1} \cdot K^{-1}$ and $2.319\ W \cdot m^{-1} \cdot K^{-1}$, respectively.

- Loveridge et al. (2014) presented a TRT study at a central London development site, where the pile is $300mm$ in diameter and $26m$ deep. The thermal conductivity was interpreted to be $2.4\ W \cdot m^{-1} \cdot K^{-1} \pm 10\%$.

The aforementioned TRTs on the thermal conductivity of London Clay are summarised in Table 2.4.

Reference	Number of TRTs considered	Thermal conductivity $[W \cdot m^{-1} \cdot K^{-1}]$
Banks et al. (2013)	17	$1.5 - 2.3$ (typically $1.7 - 2.0$)
Underwood (2013)	2	2.3 and 2.4
Loveridge et al. (2014)	1	$2.4 \pm 10\%$

Table 2.4 Summary of TRT studies on the thermal conductivity of London Clay

In the context of the current research, which mainly focuses on the transfer of heat from a pile into its surrounding soil, the resulting macroscopic energy storage and temperatures (which ultimately lead to complex thermo-hydro-mechanical interactions), it has been determined that in-situ (i.e. TRTs) measurements of the thermal conductivity of London Clay are more relevant compared to the laboratory ones, as they are more representative in a macroscopic sense, and measurements are obtained in a way that is similar to what is to be simulated in the current research. This is in addition to the fact that the drawbacks of laboratory tests mentioned in Section 2.5.1.1, which include stress release, scale and sampling issues, can be avoided. Out of the three references which provided TRT thermal conductivity measurements of London Clay presented in Table 2.4, the figures provided by Underwood (2013) and Loveridge et al. (2014) are considered to be more reliable as they have provided more comprehensive details regarding the tests, in addition to agreeing closely with each other. As a result, it has been determined that, in general, a thermal conductivity of $2.4\ W \cdot m^{-1} \cdot K^{-1}$ for London Clay is to be adopted in the current research. However, it should be noted that a value of $1.79\ W \cdot m^{-1} \cdot K^{-1}$ for London Clay is still used in parts of the current research, in order to ensure consistency with previous research (Gawecka, 2017; Gawecka et al., 2017) which cited this figure from Headon et al. (2009).

2.5.1.4 Typical values for concrete

The thermal conductivity of concrete is mainly dependent on its aggregate lithology and water (or moisture) content. In terms of aggregate lithology, concrete with quartzite aggregates is amongst the ones with highest thermal conductivities (up to above 4 $W \cdot m^{-1} \cdot K^{-1}$), while concrete with basalt or dolerite aggregates is amongst the ones with lowest thermal conductivities (generally below 2 $W \cdot m^{-1} \cdot K^{-1}$) (Campbell-Allen & Thorne, 1963; Khoury, 1983; Scanlon & McDonald, 1994; Khan, 2002). In terms of water content, concrete which is saturated with water have higher thermal conductivities than samples that are oven-dry. Scanlon and McDonald (1994) explained that this is due to the fact that air replaces water within concrete upon drying, and water is a much better thermal conductor than air. Khoury (1983) showed that reducing the water content in concrete reduces its thermal conductivity in an approximately linear manner (see Figure 2.27). According to GSHPA (2012), concrete piles installed in clay soils or soils below the water table are likely to be saturated, while those installed in dry sands would experience a reduced water content. In the literature, thermal conductivities of concrete are often given under either saturated or dry (using oven) state. In the context of the current research, which mainly focuses on piles founded in London Clay, thermal conductivities of saturated concrete are therefore more relevant.

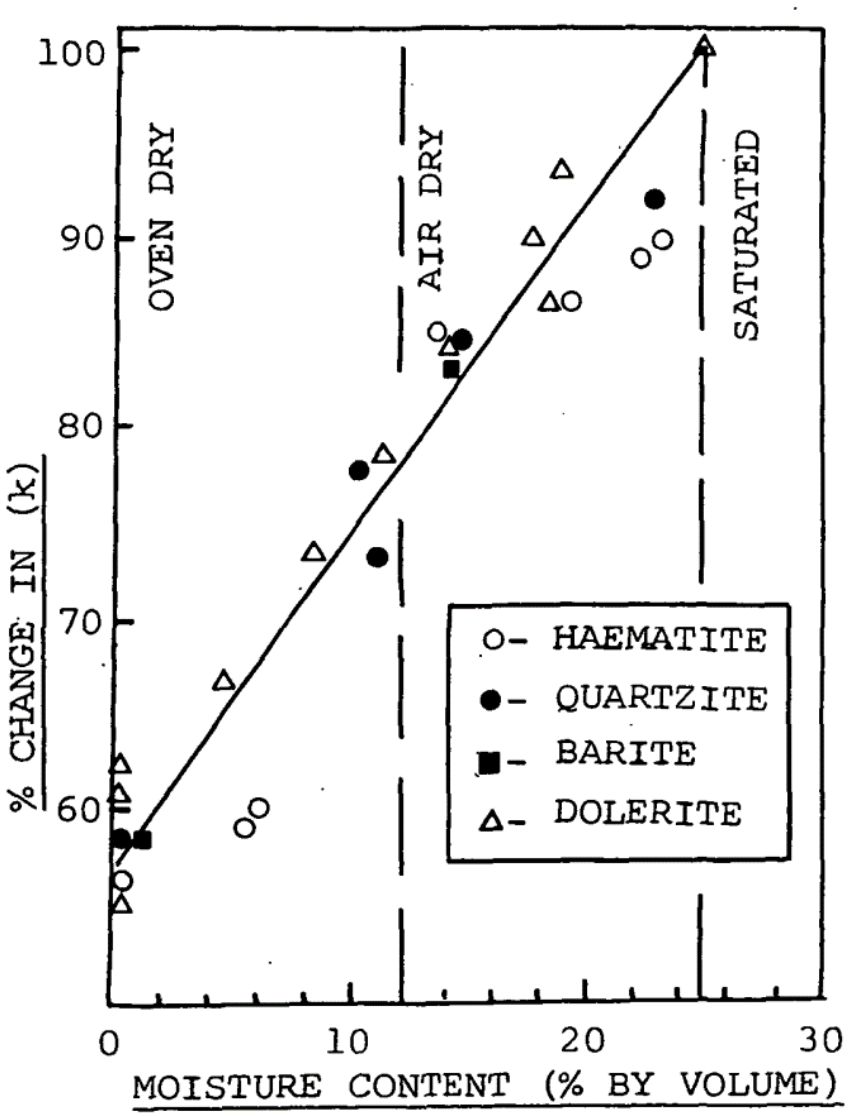


Figure 2.27 The effects of water content on the thermal conductivity of concrete (Khoury, 1983)

The following studies present measurements of thermal conductivity of concrete made with different types of aggregate and at different water contents:

- Scanlon and McDonald (1994) presented a very comprehensive study on the thermal conductivity of concrete. Table 2.5 shows the variation of thermal conductivity with the water content of concrete with four different types of aggregate. Table 2.6 and Table 2.7 present the thermal conductivity of concrete using different types of aggregate under dry and saturated states, respectively.

Water content	Thermal conductivity of concrete $[W \cdot m^{-1} \cdot K^{-1}]$
Limestone concrete	
Saturated	2.2
50% relative humidity	1.7
Dry	1.4
Sandstone concrete	
Saturated	2.9
50% relative humidity	2.2
Dry	1.4
Quartz gravel concrete	
Saturated	3.3
50% relative humidity	2.7
Dry	2.3
Expanded shale concrete	
Saturated	0.9
50% relative humidity	0.8
Dry	0.6

Table 2.5 The thermal conductivity of concrete of four different types of aggregate at different water contents (Scanlon & McDonald, 1994)

Aggregate type	Dry density $[kg \cdot m^{-3}]$	Thermal conductivity of dry concrete $[W \cdot m^{-1} \cdot K^{-1}]$
Hematite	2870	2.6
Marble	2290	1.7
Sandstone	1920	1.4
Limestone	2020	1.4
Dolerite	2180	1.2
Barite	2880	1.2
Expanded shale	1430	0.6
Expanded slag	1650	0.5
Expanded slag	960	0.2

Table 2.6 The thermal conductivity of concrete of different types of aggregate under dry state (Scanlon & McDonald, 1994)

Aggregate type	Saturated density $[kg \cdot m^{-3}]$	Thermal conductivity of saturated concrete $[W \cdot m^{-1} \cdot K^{-1}]$
Hematite	3040	4.1
Quartzite	2400	4.1
Quartzite	2440	3.5
Dolomite	2500	3.3
Quartzite	Unknown	3.3
Limestone	2450	3.2
Quartzite	2350	3.1
Sandstone	2130	2.9
Sandstone	2400	2.9
Granite	2420	2.6
Limestone	2420	2.6
Marble	2440	2.2
Limestone	2440	2.2
Basalt	2520	2.0
Rhyolite	2340	2.0
Barite	3040	2.0
Dolerite	2350	2.0
Basalt	2350	1.9
Expanded shale	1590	0.9

Table 2.7 The thermal conductivity of concrete of different types of aggregate under saturated state (Scanlon & McDonald, 1994)

- Campbell-Allen and Thorne (1963) presented the thermal conductivity of concrete made with dolerite, baryte and haematite aggregates, at both saturated and dry states (see Table 2.8). It can be observed that the conductivities in Table 2.8 match very well with those given by Scanlon and McDonald (1994) in Table 2.6 and Table 2.7.

Aggregate type	Thermal conductivity of concrete $[W \cdot m^{-1} \cdot K^{-1}]$	
	Saturated	Dry
Dolerite	1.94	1.25
Barytes	2.08	1.30
Haematite	4.39	2.56

Table 2.8 The thermal conductivity of concrete of different types of aggregate under both saturated and dry states (Campbell-Allen & Thorne, 1963)

- Khoury (1983) presented the thermal conductivity of concrete made with different types of aggregates at saturated states (see Table 2.9). It can be observed that the conductivities in Table 2.9 match very closely with those given by Scanlon and McDonald (1994) in Table 2.7, with the exception of basalt and dolerite aggregates, for which the values given by Khoury (1983) are considerably lower.

Aggregate type	Thermal conductivity of saturated concrete $[W \cdot m^{-1} \cdot K^{-1}]$
Siliceous rocks (Quartzite, sandstone, gravel)	$2.4 - 3.6$
Igneous crystalline rocks (Granite, gneiss)	$1.9 - 2.8$
Sedimentary carbonate rocks (Limestone, dolomites)	$1.9 - 2.8$
Igneous amorphous rocks (Basalt, dolerites)	$1.0 - 1.6$

Table 2.9 The thermal conductivity of concrete of different types of aggregate under saturated states (Khoury, 1983)

- Khan (2002) presented the thermal conductivity of concrete made with four different types of aggregates at both dry and saturated states (see Table 2.10). It can be observed that the conductivities for limestone and quartzite aggregates in Table 2.10 match very closely with those given by Scanlon and McDonald (1994) in Table 2.7, while the

conductivities for basalt aggregates in Table 2.10 are considerably higher than those given by Khoury (1983) in Table 2.9 and Scanlon and McDonald (1994) in Table 2.7.

Aggregate type	Thermal conductivity of concrete $[W \cdot m^{-1} \cdot K^{-1}]$	
	Saturated	Dry
Basalt	$3.24 - 3.52$	$1.97 - 2.26$
Limestone	$2.71 - 2.92$	$1.60 - 2.03$
Siltstone	$2.90 - 3.61$	$1.91 - 2.21$
Quartzite	$3.49 - 4.18$	$2.29 - 2.77$

Table 2.10 The thermal conductivity of concrete of different types of aggregate under both saturated and dry states (Khan, 2002)

- Pagola et al. (2017) presented the thermal conductivity of a concrete made with crystalline and quartz aggregates, at saturated, normally dry (under ambient air conditions) and dry states (see Table 2.11). It can be observed that the saturated conductivities shown in Table 2.11 lie within the ranges given by Khoury (1983) in Table 2.9 and Scanlon and McDonald (1994) in Table 2.7.

Sample state	Thermal conductivity of concrete $[W \cdot m^{-1} \cdot K^{-1}]$
Saturated	2.75 ± 0.15
Normally dry	2.69 ± 0.18
Dry	2.30 ± 0.28

Table 2.11 The thermal conductivity of a concrete made with crystalline and quartz aggregates at saturated, normally dry and dry states (Pagola et al., 2017)

Referring to the above studies on the thermal conductivity of concrete, it has been determined that the conductivities given by Scanlon and McDonald (1994) in Table 2.7 are to be adopted in the current research, due to the comprehensiveness of their study, and the fact that the conductivities they presented are matched by studies presented by other authors. However, it should be noted that a figure of $2.33\ W \cdot m^{-1} \cdot K^{-1}$ is adopted in parts of the current research in order to ensure consistency with previous research (Gawecka, 2017; Gawecka et al., 2017).

2.5.2 Specific/volumetric heat capacity C_p/c_{vol}

The heat capacity of an object is defined as the amount of heat that has to be supplied to it in order to produce a unit increase in its temperature and has units of $J \cdot K^{-1}$, while specific and volumetric heat capacities refer to heat capacity per unit mass (units: $J \cdot kg^{-1} \cdot K^{-1}$) and volume (units: $J \cdot m^{-3} \cdot K^{-1}$), respectively. Note that specific heat capacity is related to volumetric heat capacity by:

$$c_{vol} = \rho C_p \tag{2.15}$$

In Equation (2.15), c_{vol} $[J \cdot m^{-3} \cdot K^{-1}]$ is volumetric heat capacity, ρ $[kg \cdot m^{-3}]$ is density and C_p $[J \cdot kg^{-1} \cdot K^{-1}]$ is specific heat capacity. For soils, which are multiphase materials, their overall volumetric heat capacities can be evaluated by (Rees et al., 2000):

$$c_{vol} = (1-n)c_{vol,s} + nS_r c_{vol,w} + n(1-S_r)c_{vol,a} \tag{2.16}$$

where $c_{vol,s}$ $[J \cdot m^{-3} \cdot K^{-1}]$, $c_{vol,w}$ $[J \cdot m^{-3} \cdot K^{-1}]$ and $c_{vol,a}$ $[J \cdot m^{-3} \cdot K^{-1}]$ are the volumetric heat capacities of the soil particles, pore water and pore air, respectively, n is the soil porosity and S_r is the degree of saturation. While the volumetric heat capacities of water and air are commonly adopted as $4190\ kJ \cdot m^{-3} \cdot K^{-1}$ and $1.21\ kJ \cdot m^{-3} \cdot K^{-1}$, respectively, the volumetric heat capacities of soil particles can vary widely, from 1706 to $2488\ kJ \cdot m^{-3} \cdot K^{-1}$ according to a literature review conducted by Ren et al. (2003).

2.5.2.1 Testing methods

The specific/volumetric heat capacity of a sample can be determined using the following two methods:

- Mixture with water

The sample to be measured with known mass and temperature is mixed with water, also with known mass and temperature. The temperature of water is selected to be different from that of the sample such that a thermal equilibrium has to be reached upon mixture (Brandl, 2006; Gawecka, 2017). For the measurement of heat capacity of soils, the initial temperatures of the soil and water are usually 0^oC and 20^oC, respectively (Brandl, 2006). As the specific heat capacity of water is known ($4190\ J \cdot kg^{-1} \cdot K^{-1}$), the specific heat capacity of the sample can

be determined assuming conservation of energy by measuring the final steady-state temperature of the mixture:

$$m_s C_s T_s + m_w C_w T_w = (m_s C_s + m_w C_w) T_{final} \quad (2.17)$$

In Equation (2.17), m_s $[kg]$ and m_w $[kg]$ are the masses of the sample and water, respectively, C_s $[J \cdot kg^{-1} \cdot K^{-1}]$ and C_w $[J \cdot kg^{-1} \cdot K^{-1}]$ are the specific heat capacities of the sample (which is the unknown) and water, respectively, T_s $[K]$ and T_w $[K]$ are the temperatures of the sample and water, respectively, and T_{final} $[K]$ is the final steady-state temperature of the mixture.

- Dual-probe heat-pulse test

As explained in Section 2.5.1.1, the dual-probe heat-pulse test can be used to determine the volumetric heat capacity of a sample (Campbell et al., 1991; Nusier & Abu-Hamdeh, 2003; Ren et al., 2003; Loveridge et al., 2017; Martinez Calonge, 2017). During the test, a short heat pulse is released from the first probe and the temperature change at the second probe is monitored. The volumetric heat capacity of the sample can then be calculated from the temperature values measured, assuming that the infinite line source model is applicable (Carslaw & Jaeger, 1959) (a detailed explanation and derivation of the equations involved can be found in Campbell et al. (1991)).

2.5.2.2 Typical values for London Clay

The followings summarise the specific/volumetric heat capacity of London Clay reported in the literature:

- Headon et al. (2009) reported a volumetric heat capacity of $1820\ kJ \cdot m^{-3} \cdot K^{-1}$ for London Clay, which was subsequently adopted by Gawecka (2017) and Gawecka et al. (2017) for the numerical modelling of thermo-active piles in London Clay. This figure is therefore adopted in the current research in order to ensure consistency with previous research (Gawecka, 2017; Gawecka et al., 2017).
- A volumetric heat capacity of $2000\ kJ \cdot m^{-3} \cdot K^{-1}$ for London Clay was reported by Ground Source Consult Ltd (2015) as part of a feasibility study of a GSHP system development at 2 Holland Park in London, United Kingdom.
- Martinez Calonge (2017) made 109 and 59 measurements of volumetric heat capacity on intact and reconstituted London Clay samples, respectively, using the dual-probe

heat-pulse test. However, a range of volumetric heat capacities of 887 $kJ \cdot m^{-3} \cdot K^{-1}$ to 5389 $kJ \cdot m^{-3} \cdot K^{-1}$ are obtained, with Martinez Calonge (2017) commenting that such scatter is unacceptably high, and attributed such errors to the uncertainty in inter-probe spacing during the tests.

2.5.2.3 Typical values for concrete

The following summarises the specific/volumetric heat capacity of concrete reported in the literature, note that unlike thermal conductivity, the mineralogical character of the aggregate has little effect on the specific/volumetric heat capacity, while an increase in water content would increase the specific/volumetric heat capacity (Khoury, 1983; Scanlon & McDonald, 1994; Neville & Adam, 2002):

- Khoury (1983) reported that the specific heat capacity of a saturated concrete is typically 1000 $J \cdot kg^{-1} \cdot K^{-1}$, but may vary between 700 $J \cdot kg^{-1} \cdot K^{-1}$ and 1500 $J \cdot kg^{-1} \cdot K^{-1}$.
- Burg and Ost (1994) reported that the specific heat capacity of normally dry conventional strength concrete is typically between 790 $J \cdot kg^{-1} \cdot K^{-1}$ and 1000 $J \cdot kg^{-1} \cdot K^{-1}$, and values for high strength concrete would be in the high end of this range.
- Scanlon and McDonald (1994) reported that the specific heat capacity of concrete is typically between 920 $J \cdot kg^{-1} \cdot K^{-1}$ and 1005 $J \cdot kg^{-1} \cdot K^{-1}$.
- Neville and Adam (2002) reported that the specific heat capacity of concrete is typically between 840 $J \cdot kg^{-1} \cdot K^{-1}$ and 1170 $J \cdot kg^{-1} \cdot K^{-1}$.
- Pagola et al. (2017) presented the density and volumetric heat capacity of a concrete made with crystalline and quartz aggregates (same as that described in Section 2.5.1.4 for the same reference), at saturated, normally dry (under ambient air conditions) and dry states (see Table 2.12).

Sample state	Density $[kg \cdot m^{-3}]$	Volumetric heat capacity $[kJ \cdot m^{-3} \cdot K^{-1}]$	Specific heat capacity $[J \cdot kg^{-1} \cdot K^{-1}]$
Saturated	2405	2370	985
Normally dry	2370	2170	916
Dry	2318	1690	729

Table 2.12 The volumetric and specific heat capacity of a concrete made with crystalline and quartz aggregates at saturated, normally dry and dry states (Pagola et al., 2017)

Based on the above literature review, it has been determined that a specific heat capacity of $895\ J \cdot kg^{-1} \cdot K^{-1}$ is to be adopted in the current research for concrete, which, assuming a concrete density of $2400\ kg \cdot m^{-3}$, corresponds to a volumetric heat capacity of $2148\ kJ \cdot m^{-3} \cdot K^{-1}$. However, it should be noted that a volumetric heat capacity of $1920\ kJ \cdot m^{-3} \cdot K^{-1}$ is adopted in parts of the current research in order to ensure consistency with previous research (Gawecka, 2017; Gawecka et al., 2017).

2.5.3 Coefficient of thermal expansion α

The coefficient of thermal expansion is a thermo-mechanical property that provides a measure of the change in size of an object due to a unit change in temperature. The coefficient of thermal expansion can be expressed in terms of length, which is referred to as the linear coefficient of thermal expansion (the expression is given by Equation (2.18)), area, which is referred to as the areal coefficient of thermal expansion (the expression is given by Equation (2.19)), or volume, which is referred to as the volumetric coefficient of thermal expansion (the expression is given by Equation (2.20)).

$$\alpha = \frac{1}{L}\frac{dL}{dT} \tag{2.18}$$

$$\alpha_A = \frac{1}{A}\frac{dA}{dT} \tag{2.19}$$

$$\alpha_V = \frac{1}{V}\frac{dV}{dT} \tag{2.20}$$

In Equations (2.18) to (2.20), $\alpha\ [m \cdot m^{-1} \cdot K^{-1}]$, $\alpha_A\ [m^2 \cdot m^{-2} \cdot K^{-1}]$ and $\alpha_V\ [m^3 \cdot m^{-3} \cdot K^{-1}]$ are the linear, areal and volumetric coefficients of thermal expansion, respectively, $L\ [m]$ is length, $A\ [m^2]$ is area, $V\ [m^3]$ is volume and $T\ [K]$ is temperature. It should be appreciated

that the coefficient of thermal expansion is a thermo-mechanical property of significant importance as it plays an important role in inducing complex thermo-hydro-mechanical interactions observed in the ground. For example, due to the fact that freshly cast concrete geotechnical structures give out heat of hydration, or that heat is exchanged with the ground during the operation of thermo-active structures, thermal deformations of the structures may occur which lead to thermal cracking, and thermally-induced stresses can be induced due to restrictions from the surrounding soil (this will be discussed in detail in subsequent chapters). Moreover, due to a higher coefficient of thermal expansion in water than soil particles, in soils of low permeability (i.e. undrained conditions) such as London Clay, a change in temperature of the soil (which can be due to the casting of concrete geotechnical structures or the operation of thermo-active structures) can induce excess pore water pressure. This occurs as pore water expands/contracts more than the soil particles, but is unable to displace freely within the soil skeleton, meaning that a change in volume of water through pressurisation is necessary. Due to the multiphase nature of soils, the volumetric behaviour of soils when subjected to changes in temperature is complex and a detailed review and explanation on this, as well as the generation of excess pore water pressures in undrained soils can be found in Gawecka (2017) and Sailer (2020).

2.5.3.1 Water

The coefficient of thermal expansion of water is highly dependent on its temperature. Çengel and Ghajar (2011) described the evolution of the linear coefficient of thermal expansion of water in the temperature range of $0^oC - 100^oC$, with Cui et al. (2020) proposing a third-order polynomial function (the expression of which is given by Equation (2.21)) to fit the data (see Figure 2.28 (Cui et al., 2020)).

$$\alpha_w = 1.48 \times 10^{-10} T^3 - 3.64 \times 10^{-8} T^2 + 4.88 \times 10^{-6} T - 2.02 \times 10^{-5} \qquad (2.21)$$

In Equation (2.21), α_w $[m \cdot m^{-1} \cdot K^{-1}]$ is the linear coefficient of thermal expansion of water and T $[K]$ is temperature. In the current research, the linear coefficient of thermal expansion of water is assumed to be $6.9 \times 10^{-5}\ m \cdot m^{-1} \cdot K^{-1}$ (constant with temperature for simplicity, which corresponds to a value at around 21.5^oC according to the function from Cui et al. (2020)) in order to ensure consistency with previous research (Gawecka, 2017; Gawecka et al., 2017).

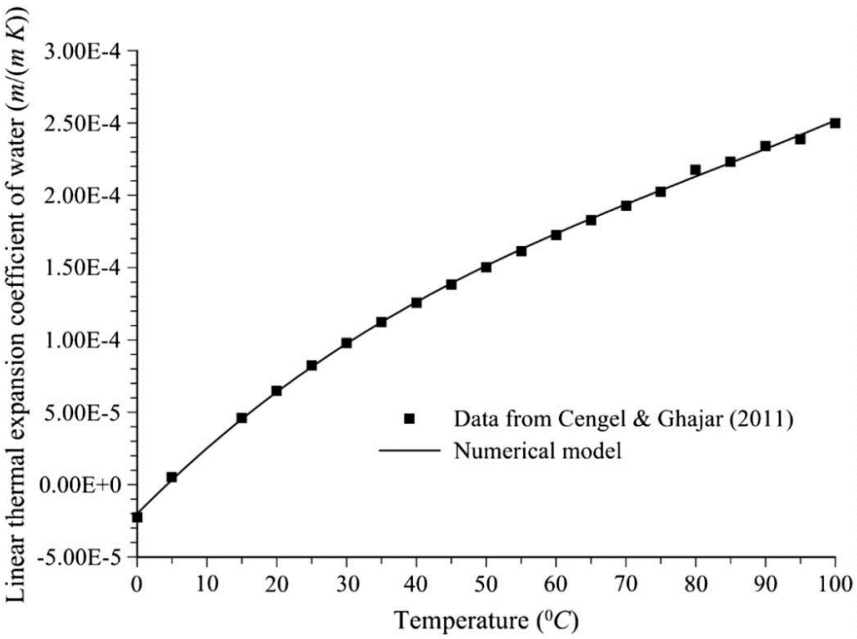


Figure 2.28 The third-order polynomial function proposed by Cui et al. (2020) fitted on the data from Çengel and Ghajar (2011) on the linear coefficient of thermal expansion of water

2.5.3.2 London Clay

Bodas Freitas et al. (2013) reported that the typical volumetric coefficients of thermal expansion of Boom and Opalinus clays (which are stiff overconsolidated clays) range from $4 \times 10^{-5}\, m^3 \cdot m^{-3} \cdot K^{-1}$ to $6 \times 10^{-5}\, m^3 \cdot m^{-3} \cdot K^{-1}$ (which correspond to linear coefficients of thermal expansion of $1.33 \times 10^{-5}\, m \cdot m^{-1} \cdot K^{-1}$ to $2 \times 10^{-5}\, m \cdot m^{-1} \cdot K^{-1}$). A linear coefficient of thermal expansion of $1.7 \times 10^{-5}\, m \cdot m^{-1} \cdot K^{-1}$ for London Clay was adopted based on this by Gawecka (2017) and Gawecka et al. (2017) for the numerical modelling of thermo-active piles. This value is also adopted in the current research in order to ensure consistency with previous research (Gawecka, 2017; Gawecka et al., 2017).

2.5.3.3 Concrete

The coefficient of thermal expansion of concrete is highly dependent on the type of aggregate used (Khoury, 1983; Scanlon & McDonald, 1994). The following summarises the coefficient of thermal expansion of concrete reported in the literature:

- Khoury (1983) presented the linear coefficient of thermal expansion of concrete made with different types of aggregates, which are shown in Table 2.13.

Aggregate type	Linear coefficient of thermal expansion of concrete $[\times 10^{-6}\ m \cdot m^{-1} \cdot K^{-1}]$
Chert	$11.4 - 12.2$
Quartzite (TRG)	$11.7 - 14.6$
Quartz	$9.0 - 13.2$
Sandstone	$9.2 - 13.3$
Marble	$4.4 - 17.4$
Siliceous limestone	$8.1 - 11.0$
Granite	$8.1 - 10.3$
Dolerite	9.6
Basalt	$7.9 - 10.4$
Limestone	$4.3 - 10.3$
Glacial gravel	$9.0 - 13.7$
Lightweight	$5.0 - 11.0$

Table 2.13 Linear coefficient of thermal expansion of concrete made with different types of aggregates (Khoury, 1983)

- Burg and Ost (1994) measured the linear coefficient of thermal expansion of five mixes of concrete which are made of dolomite coarse aggregates and fine aggregate with 60% natural sand and 40% limestone, and obtained a range of $9.4 \times 10^{-6}\ m \cdot m^{-1} \cdot K^{-1}$ to $12.3 \times 10^{-6}\ m \cdot m^{-1} \cdot K^{-1}$. These values match the corresponding one in Table 2.13 for sandstone presented by Khoury (1983).
- Scanlon and McDonald (1994) presented the linear coefficient of thermal expansion of concrete made with different types of aggregates, which are shown in Table 2.14. It can be observed that the values in Table 2.14 match very closely with those in Table 2.13 presented by Khoury (1983).

Aggregate type	Linear coefficient of thermal expansion of concrete $[\times 10^{-6}\ m \cdot m^{-1} \cdot K^{-1}]$
Quartzite	13.6
Quartz	12.1
Sandstone	11.2
Quartzite and argillite	11.0
Granite-gneiss	9.9
Limestone and granite	9.5
Basalt	7.9
Limestone and chert	7.6

Table 2.14 Linear coefficient of thermal expansion of concrete made with different types of aggregates (Scanlon & McDonald, 1994)

- Bodas Freitas et al. (2013) reported the typical range for the linear coefficient of thermal expansion of concrete to be between $6.67 \times 10^{-6}\ m \cdot m^{-1} \cdot K^{-1}$ and $13.3 \times 10^{-6}\ m \cdot m^{-1} \cdot K^{-1}$.
- Bourne-Webb et al. (2009) reported the typical range of linear coefficient of thermal expansion for concrete made with limestone aggregate to be between $6 \times 10^{-6}\ m \cdot m^{-1} \cdot K^{-1}$ and $9 \times 10^{-6}\ m \cdot m^{-1} \cdot K^{-1}$ (the range of which lie within that reported by Khoury (1983) in Table 2.13), a value of $8.5 \times 10^{-6}\ m \cdot m^{-1} \cdot K^{-1}$ was therefore adopted in their study. Note that the same figure was also adopted in GSHPA (2012) and Gawecka et al. (2017), and is therefore adopted in the current research in order to ensure consistency with previous research (Gawecka, 2017; Gawecka et al., 2017).

2.6 EXISTING CAPABILITIES OF ICFEP

The Imperial College Finite Element Program (ICFEP) (Potts & Zdravkovic, 1999) is an in-house finite-element software that has been developed within the Geotechnics Section of Imperial College London for over 40 years and most of the numerical analyses in this research are conducted using ICFEP. It is a very versatile numerical tool for geotechnical problems and, over the years, developments of the software allow it to analyse problems that are coupled hydro-mechanical (HM), dynamic and partly saturated. Recent developments include Cui

(2015), who expanded the ICFEP to allow the modelling of coupled thermo-hydro-mechanical (THM) problems, and Gawecka (2017), who incorporated the Petrov-Galerkin finite-element method into ICFEP to allow the simulation of advection dominated (high Péclet number) flows, and the coupled THM formulation of 3D beam and bar elements. Both contributions are essential for simulating the circulation of hot/cold fluid along heat exchanger pipes within thermo-active structures. Alongside with the above, the ICFEP package also includes a number of advanced constitutive models, boundary conditions, as well as different types of structural elements, which include beam, bar, shell, membrane and interface elements, with a description for each of the above structural elements available in Gawecka (2017). This section mainly focuses on giving an overview of the parts of ICFEP package that are most relevant to this research, which include the coupled THM formulation, different types of thermal boundary conditions, and the modelling of heat exchanger pipes together with the Petrov-Galerkin finite-element method, with the full details of the finite-element method that ICFEP adopts reported in Potts and Zdravkovic (1999), and in Cui (2015) for coupled THM formulation.

2.6.1 Coupled THM formulation

A coupled THM problem involves the following three systems interacting with each other, as illustrated in Figure 2.29:

- Mechanical system – governed by force equilibrium
- Hydraulic system – governed by Darcy's law and the continuity equation
- Thermal system – governed by heat transfer equations and energy conservation

The presence of the three systems above gives rise to the following interactions:

- Hydro-mechanical (HM) interactions – this is characterised by the changes in pore water pressures and water flows due to changes in stresses and strains in the soil (i.e. consolidation), or vice versa where changes in stresses and strains in the soil are induced by changes in pore water pressures (e.g. principle of effective stress) and water flows.
- Thermo-mechanical (TM) interactions – this is characterised by the changes in stresses and strains in the soil due to thermal expansion or contraction, which are more commonly referred to as thermally-induced stresses and strains.

- Thermo-hydraulic (TH) interactions – this is characterised by changes in pore water pressures and water flows due to changes in temperatures, or the heat transfer brought about by water flows (i.e. convection).

The mechanical, hydraulic and thermal systems and the three types of interactions between them make up the 3 × 3 submatrices of the stiffness matrix in ICFEP that is used to solve the nodal unknowns, which are displacements, pore water pressures and temperatures, respectively, and are illustrated in Figure 2.30.

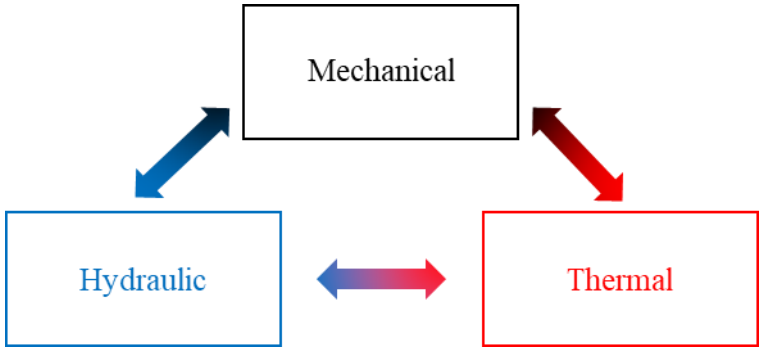


Figure 2.29 The coupling between thermal, hydraulic and mechanical systems

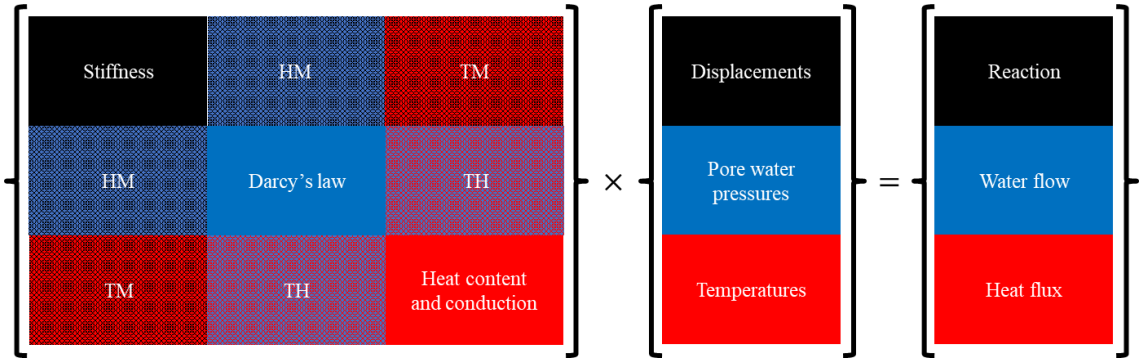


Figure 2.30 Illustration of the 3 × 3 submatrices of the stiffness matrix in ICFEP to solve for the nodal unknowns (displacements, pore water pressures and temperatures)

Note that the coupled THM formulation in ICFEP adopts the following assumptions (Cui, 2015; Cui et al., 2018b):

- The effects of heat transfer due to radiation are assumed to be negligible and are not accounted for.

- An instantaneous thermal equilibrium is assumed between soil particles and pore water, meaning that their temperatures are assumed to be the same and correspond to the overall temperature of the soil.
- A change in temperature will result in identical volumetric strain of the soil particles and the solid skeleton. This means that for a free draining and mechanically unrestrained soil, a change in temperature will not result in a change in void ratio, with changes in void ratio resulting only from changes in effective stresses.

2.6.2 Thermal boundary conditions

The coupled THM formulation in ICFEP requires the implementation of thermal boundary conditions, which can mainly be classified into three different types (Cui, 2015): prescribed temperature, prescribed heat flux and coupled thermo-hydraulic heat flux. Note that if no thermal boundary condition is specified on a mesh boundary, an adiabatic boundary condition (i.e. no heat flux across the mesh boundary) is assumed in ICFEP.

2.6.2.1 Prescribed temperature

The prescribed temperature thermal boundary condition is a Dirichlet (or first-type) boundary condition where an incremental or accumulated temperature is prescribed either at nodes or over elements.

2.6.2.2 Prescribed heat flux

There are three different types of prescribed heat flux thermal boundary condition that can be applied in ICFEP: exchange heat flux, heat sources and sinks, and convection (or also known as natural heat loss).

- Exchange heat flux

Exchange heat flux thermal boundary condition is a Neumann (or second-type) boundary condition which allows a heat flux to be applied over a line, area or volume. When a field of heat flux Q_T [$W \cdot m^{-1}$ or $W \cdot m^{-2}$ or $W \cdot m^{-3}$] is prescribed over a domain Ω [m or m^2 or m^3], which can be a line, area or volume, it is converted into equivalent nodal heat flux $\boldsymbol{Q_{T,nodes}}$ [W] using the shape functions for temperature [N_T]:

$$\boldsymbol{Q_{T,nodes}} = \int_{\Omega} [N_T]^T Q_T \, d\Omega \tag{2.22}$$

Note that the integration in Equation (2.22) is evaluated numerically using Gaussian Quadrature in ICFEP.

- Heat sources and sinks

This is a Neumann (or second-type) boundary condition where nodal heat flux $\boldsymbol{Q_{T,nodes}}$ $[W]$ is prescribed directly at the nodes.

- Convection (also known as natural heat loss)

This is a nonlinear Cauchy boundary condition which prescribes a heat flux Q_T $[W \cdot m^{-2}]$ at the surface of a body Ω $[m^2]$ that is in contact with a fluid according to the Newton's law of cooling (see Section 2.4.2 and Equation (2.11)):

$$Q_T = -h\left(T_{body} - T_f\right) \tag{2.23}$$

In Equation (2.23), h $[W \cdot m^{-2} \cdot K^{-1}]$ is the heat transfer coefficient, T_{body} $[K]$ is the temperature of the body that is in contact with the fluid and T_f $[K]$ is the temperature of the fluid. This thermal boundary condition is nonlinear as T_{body} varies over an increment.

2.6.2.3 Coupled thermo-hydraulic heat flux

The coupled thermo-hydraulic heat flux thermal boundary condition is a nonlinear thermal boundary condition that has to be prescribed in coupled TH problems (Cui et al., 2016). It prescribes a heat flux at where water enters or leaves the mesh in order to balance the energy carried by the water flow through the boundary. The heat flux Q_T $[W]$ can be evaluated as:

$$Q_T = c_{vol,w} \int_{\Omega} v_w T_b \, d\Omega \tag{2.24}$$

In Equation (2.24), $c_{vol,w}$ $[J \cdot m^{-3} \cdot K^{-1}]$ is the volumetric heat capacity of water, v_w $[m \cdot s^{-1}]$ is the velocity of water flowing perpendicular to the boundary and T_b $[K]$ is the temperature at boundary. This thermal boundary condition is nonlinear as both v_w and T_b vary over an increment.

2.6.3 Modelling of heat exchanger pipes

The heat exchanger pipes within thermo-active structures can be modelled in ICFEP using 3D bar or beam elements. These elements are one-dimensional and are fully coupled THM which allows their permeability and cross-sectional area to be defined to allow hot/cold fluid to flow through them, and their detailed coupled THM formulation can be found in Gawecka (2017). The difference between the bar and beam elements is that the beam elements involve six degrees of freedom per node (three displacements and three rotations) and allow the transmission of axial forces, shear forces, bending moments and twisting moments, whereas the bar elements involve three displacement degrees of freedom per node and allow the transmission of axial forces only. While bar and beam elements can both be used to model heat exchanger pipes, they are adopted for their capabilities of transferring heat and fluid, but not their mechanical behaviour, hence the rotational degrees of freedom offered by beam elements are redundant. Therefore, bar elements are best suited to model heat exchanger pipes.

It is highlighted by Cui et al. (2016) and Gawecka (2017) that for the conventional Galerkin finite-element method that ICFEP adopts, oscillations in nodal temperatures will occur when a heat front that is advection dominated ($Pe \gg 1$) reaches the boundary of the mesh. In order to rectify this numerical issue and solve transient advection dominated problems, the Petrov-Galerkin (PG) finite-element method is proposed and adopted for elements carrying advection dominated flows (Gawecka, 2017; Cui et al., 2018a). The PG finite-element method is an upwind finite-element method where nodal weighting factors are introduced and weighting functions are modified in order to weigh the upstream element more heavily than the downstream element, whereas the conventional Galerkin finite-element method assumes the weighting functions to be identical to the shape functions. The PG weighting factors and functions for 1D linear elements (with two nodes) (Huyakorn, 1977; Gawecka, 2017) and 1D quadratic elements (with three nodes) (Heinrich & Zienkiewicz, 1977; Gawecka, 2017) are described as follows:

- 1D linear elements

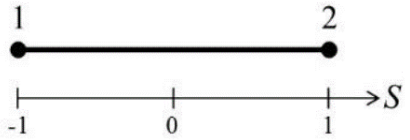


Figure 2.31 A 1D linear element with two nodes and natural coordinate S (Gawecka, 2017)

A 1D linear element with two nodes and natural coordinate S is shown in Figure 2.31 (Gawecka, 2017), with the weighting functions W_l given by:

$$W_{l,1} = N_1 - \frac{3}{4}\alpha_{PG}(1+S)(1-S)$$
$$W_{l,2} = N_2 + \frac{3}{4}\alpha_{PG}(1+S)(1-S) \tag{2.25}$$

In Equation (2.25), the subscripts represent the node numbers, N is the nodal shape function and α_{PG} is the PG weighting factor. Note that the PG weighting factor α_{PG} controls the level of upwinding and its optimal value $\alpha_{PG,opt}$ can be calculated by:

$$\alpha_{PG,opt} = \coth\left(\frac{Pe}{2}\right) - \frac{2}{Pe} \tag{2.26}$$

- 1D quadratic elements

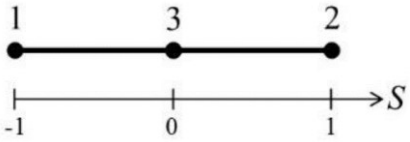


Figure 2.32 A 1D quadratic element with three nodes and natural coordinate S (Gawecka, 2017)

A 1D quadratic element with three nodes and natural coordinate S is shown in Figure 2.32 (Gawecka, 2017), with the weighting functions W_q given by:

$$W_{q,i} = N_i - \frac{5}{8}\beta_{PG1}S(S+1)(S-1) \quad (i = 1,2)$$
$$W_{q,3} = N_3 + \frac{5}{2}\beta_{PG2}S(S+1)(S-1) \tag{2.27}$$

In Equation (2.27), the subscripts represent the node numbers, N is the nodal shape function and β_{PG1} and β_{PG2} are PG weighting factors. Note that the optimal values of PG weighting factors $\beta_{PG1,opt}$ and $\beta_{PG2,opt}$ can be calculated by:

$$\beta_{PG1,opt} = 2\tanh\left(\frac{Pe}{2}\right)\left(1 + \frac{3\beta_{PG2,opt}}{Pe} + \frac{12}{Pe^2}\right) - \frac{12}{Pe} - \beta_{PG2,opt}$$
$$\beta_{PG2,opt} = \coth\left(\frac{Pe}{4}\right) - \frac{4}{Pe} \tag{2.28}$$

It is highlighted in Gawecka et al. (2020) that in order to facilitate the correct transfer of heat from the 1D bar elements to their surroundings, it is necessary to surround the bar elements with solid elements to which a 'thermally enhanced material' (TEM) is assigned. The implementation of TEM is to account for the effects of contact area and interactions between the heat exchanger pipe and its surroundings. According to Gawecka et al. (2020), the TEM should have a cross-sectional area that is equal to that of the inside of the heat exchanger pipe that is being simulated. The properties of the TEM are the same as those of the material that is surrounding the heat exchanger pipe, with the exception of the thermal conductivity of the TEM k_{TEM} which is given by Equation (2.29). This is an empirical function that relates k_{TEM} to the internal pipe diameter D_{pipe} $[mm]$, in order to account for the effects of the pipe wall. Note that if the effects of the pipe wall can be neglected, $k_{TEM} = 10\ W \cdot m^{-1} \cdot K^{-1}$ should be adopted.

$$k_{TEM} = 3.62\ln\left(D_{pipe}\right) - 7.33 \quad for \quad 10\ mm \leq D_{pipe} \leq 40\ mm \tag{2.29}$$

The aforementioned methodology of the numerical modelling of heat exchanger pipes, which includes the use of one-dimensional bar or beam elements to model the pipes and to transfer heat and fluid, the use of Petrov-Galerkin finite-element method to solve for the transient advection dominated problem, and the use of TEM to facilitate the correct transfer of heat from the heat exchanger pipes to its surroundings is validated using the results of a TRT in the laboratory from Beier et al. (2011) and a TRT in the field from Loveridge et al. (2014), both described in Gawecka (2017) and Gawecka et al. (2020).

The TRT performed in a laboratory by Beier et al. (2011) involves a BHE that is $18\ m$ long with a diameter of $126\ mm$, surrounded by saturated sand in a box that is $1.8\ m \times 1.8\ m \times 18\ m$. The BHE is made of bentonite grout mixed with water and has a single U-loop pipe configuration, with an internal pipe diameter of $27.33\ mm$, a pipe wall thickness of $3\ mm$ and

a $53\ mm$ spacing between the two legs of the U-loop. Water was circulated at a rate of $1.97 \times 10^{-4}\ m^3 \cdot s^{-1}$ and temperatures are measured at both the pipe inlet and outlet, as well as at distances of $0\ cm, 24\ cm, 44\ cm, 65\ cm$ and $85\ cm$ from the wall of the BHE, at depths of $0.9\ m, 6.4\ m, 11.9\ m, 17.4\ m$ and $18.3\ m$ (the arrangement of which is illustrated in Figure 2.33).

The TRT performed in the field by Loveridge et al. (2014) was carried out in central London, which involves a BHE with a diameter of $300\ mm$ over the top $26.8\ m$ and $200\ mm$ down to an unspecified depth. The entire BHE was installed in London Clay, with the water table at a depth of $4\ m$. The BHE is made of C35 hard pile cementitious grout and has a single U-loop pipe configuration, with an internal pipe diameter of $26.2\ mm$, a pipe wall thickness of $2.9\ mm$, a $135\ mm$ spacing between the two legs of the U-loop installed to a depth of $26\ m$ within the BHE. Water was circulated at a rate of $1.032 \times 10^{-4}\ m^3 \cdot s^{-1}$ and the flow rate, applied power and mean water temperature with time are measured, which allows the temperatures at both the pipe inlet and outlet to be calculated. Moreover, temperatures are also measured within the BHE cross-section (see Figure 2.34 regarding the location of the monitoring point within the BHE cross-section) at depths of $13.8\ m$ and $23.8\ m$, which are reported in Cecinato and Loveridge (2015).

Gawecka (2017) and Gawecka et al. (2020) conducted three-dimensional finite-element analyses with ICFEP to model both tests using the abovementioned methodology for the modelling of heat exchanger pipes, which includes the use of 2-noded one-dimensional beam elements, allowing a zone of TEM to surround the beam elements, and the Petrov-Galerkin finite-element method to solve for the transient solution. The measured temperatures at pipe inlet are prescribed as thermal boundary condition in the numerical analyses. Note that Gawecka et al. (2020) conducted three numerical analyses for each test: one with $k_{TEM} = 10\ W \cdot m^{-1} \cdot K^{-1}$ to simulate the situation where the effects of pipe walls are neglected, one with $k_{TEM} = 4.5\ W \cdot m^{-1} \cdot K^{-1}$ to account for the effects of the pipe walls (this value is calculated from Equation (2.29)), and one without the zone of TEM.

For the laboratory TRT by Beier et al. (2011), the measured temperatures at pipe outlet and the average temperature at the abovementioned distances from the wall of the BHE over depth are compared with those simulated in ICFEP in Figure 2.33 and Figure 2.35, respectively (Gawecka et al., 2020). For the field TRT by Loveridge et al. (2014), the temperatures at the pipe outlet and the temperatures measured at the monitoring point within the cross-section of

the BHE are compared with those simulated in ICFEP in Figure 2.34 and Figure 2.36, respectively (Gawecka, 2017; Gawecka et al., 2020).

Referring to Figure 2.33 to Figure 2.36, it can be observed that the modelled temperatures from analyses which include the zone of TEM match very closely with those measured in the laboratory or field, which means that the inclusion of this enhanced material around the one-dimensional bar or beam elements is necessary in order to model the transfer of heat from the bar or beam elements to their surroundings correctly. Based on Figure 2.33, Figure 2.35 and Figure 2.36, it can be concluded that whether or not to include the effects of the pipe wall is relatively unimportant as they produce similar temperature predictions; however, when temperatures within the BHE cross-section are considered (Figure 2.34), including the effects of the pipe wall produces predictions with significantly higher accuracy. To conclude, this validation exercise conducted by Gawecka (2017) and Gawecka et al. (2020) has shown that the aforementioned methodology of the numerical modelling of heat exchanger pipes can successfully simulate temperatures measured in small-scale and full-scale tests.

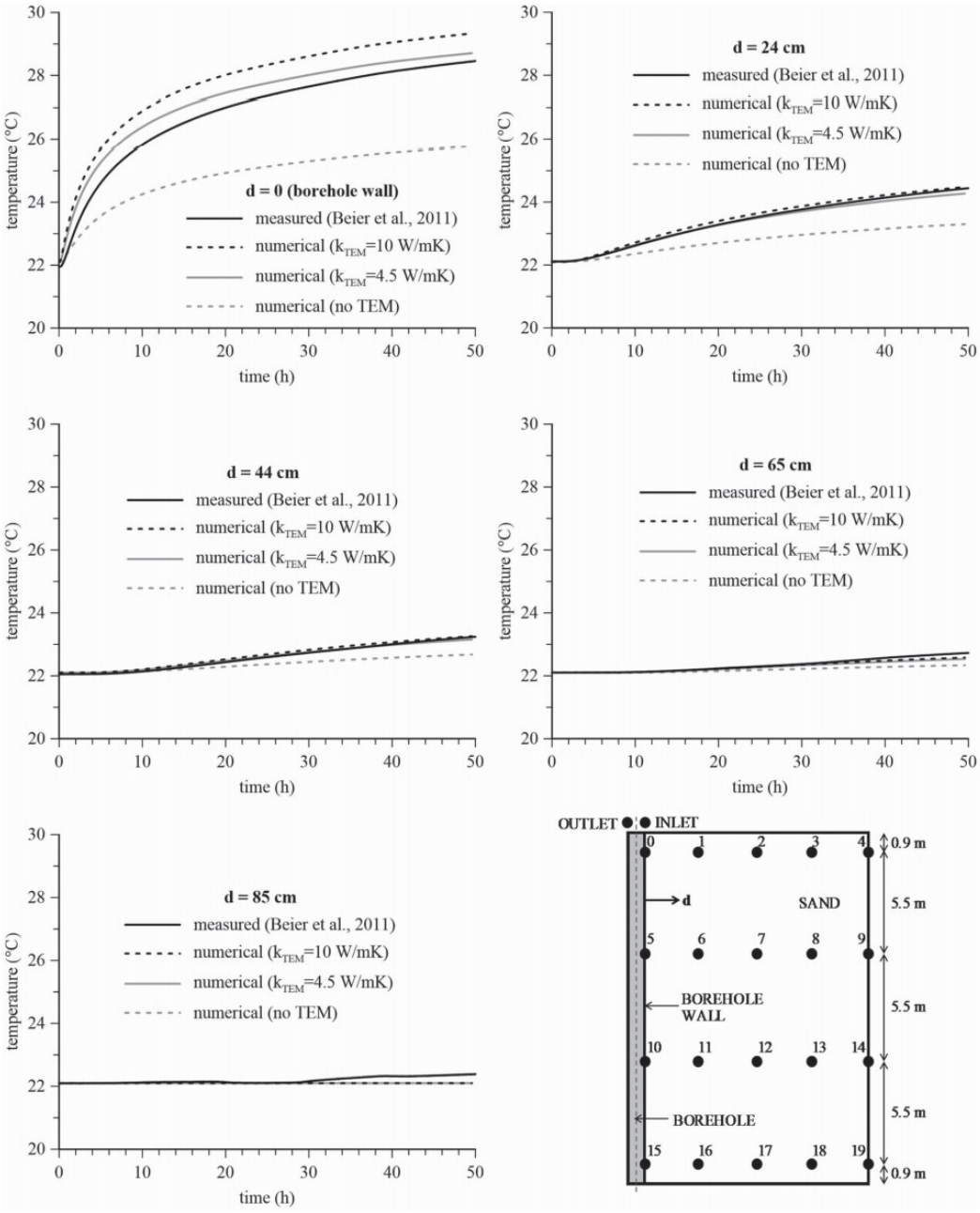


Figure 2.33 Comparison between measured and modelled temperatures at different distances from the wall of BHE in the laboratory TRT from Beier et al. (2011) (Gawecka et al., 2020)

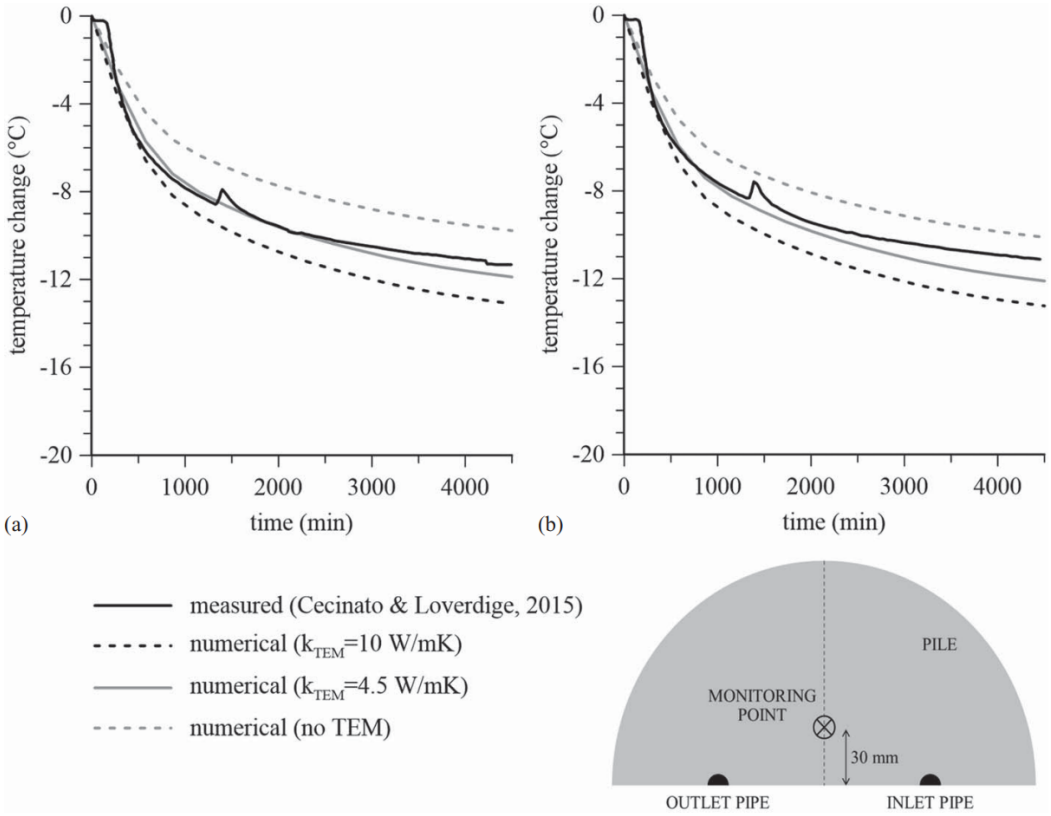


Figure 2.34 Comparison between measured and modelled temperatures at the monitoring point within the cross-section of the BHE at depths of (a) $13.8\ m$ and (b) $23.8\ m$ (Gawecka, 2017; Gawecka et al., 2020)

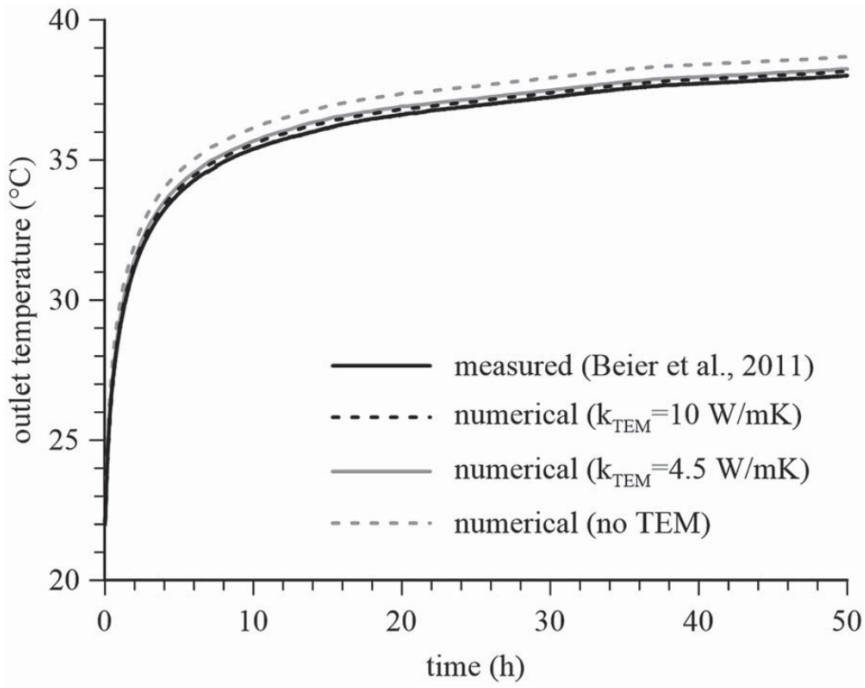


Figure 2.35 Comparison between measured and modelled temperatures at the pipe outlet in the laboratory TRT from Beier et al. (2011) (Gawecka et al., 2020)

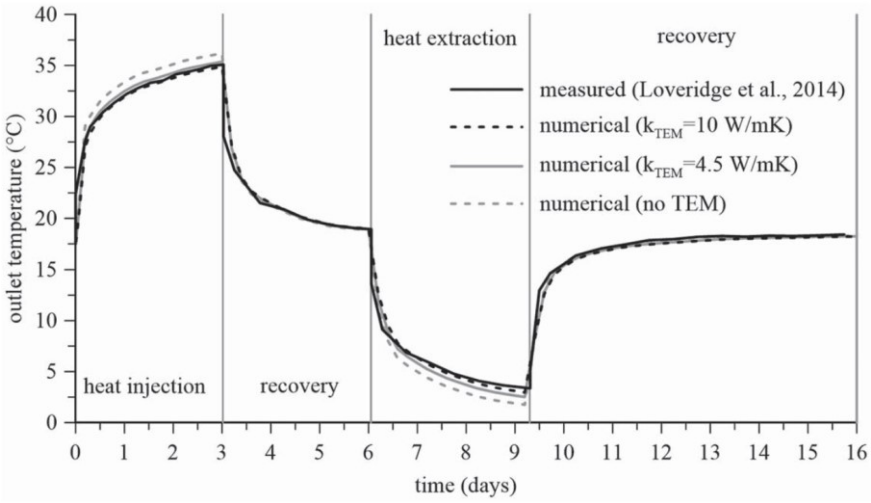


Figure 2.36 Comparison between measured and modelled temperatures at the pipe outlet in the field TRT from Loveridge et al. (2014) (Gawecka, 2017; Gawecka et al., 2020)

2.7 CONCLUSIONS

This chapter explains the basic concepts which must be understood before introducing the research shown in subsequent chapters. In Section 2.2, the definition of geothermal energy is given and its usage has been assessed, revealing a strong growth in its use in recent years,

mainly due to the rapidly increasing number of installations of ground source heat pump systems. Geothermal energy can be classified into high, intermediate and low enthalpies, which are dependent on the temperatures at which the system operates. It has been revealed that in low enthalpy geothermal energy systems, or shallow geothermal energy systems, the ground is commonly utilised as a storage medium for heat. This is achievable as ground temperatures at depth (around 10 m) remain more or less constant over a year. In order to exchange heat with the ground, a ground source heat pump system is required, which consists of a heat pump and a ground source system, which can either be open loop or closed loop. A review of the different types of closed loop ground source system has been provided, as well as the pipe arrangements that can be adopted. While thermo-active structures are also closed loop systems, they are reviewed separately in Section 2.3. Piles, diaphragm walls and tunnels are the most common geotechnical structures to be made thermo-active in order to exchange heat with the ground. The mechanism of how each of the above operate, as well as their installation and usage have been discussed.

In Section 2.4, different heat transfer mechanisms in soils have been discussed with the associated equations given. Since current research focuses on fully saturated soils and soil freezing will not be considered, conduction and convection are the dominant heat transfer mechanisms, while radiation, vapour diffusion and freeze-thaw processes would be less relevant.

In Section 2.5, reviews on two thermal properties – thermal conductivity and specific/volumetric heat capacity, as well as a thermo-mechanical property – coefficient of thermal expansion, have been provided, which include their definitions and how they are measured. Moreover, their typical values for London Clay and concrete have been given. Table 2.15 summarises the values of the above three properties for London Clay and concrete that have been determined to be adopted throughout this research.

	London Clay	Concrete
Thermal conductivity $[W \cdot m^{-1} \cdot K^{-1}]$	2.4 (1.79)	Table 2.7 (2.33)
Volumetric heat capacity $[kJ \cdot m^{-3} \cdot K^{-1}]$	1820	2148 (1920)
Linear coefficient of thermal expansion $[m \cdot m^{-1} \cdot K^{-1}]$	1.7×10^{-5}	8.5×10^{-6}

Table 2.15 The thermal conductivity, volumetric heat capacity and linear coefficient of thermal expansion adopted in the current research for London Clay and concrete. Values in brackets are adopted for consistency with previous research (Gawecka et al., 2017)

Finally in Section 2.6, a review of the existing capabilities of ICFEP that are most relevant to the current research has been provided. This includes the coupled THM formulation, the different types of thermal boundary conditions that are available to be applied, and the methodology of the numerical modelling of heat exchanger pipes. This includes the use of one-dimensional bar or beam elements to model heat exchanger pipes and to transfer heat and fluid, the use of Petrov-Galerkin finite-element method to solve for the transient advection-dominated problem, and the use of TEM to facilitate the correct transfer of heat from the heat exchanger pipes to its surroundings. A validation exercise on this methodology from Gawecka (2017) and Gawecka et al. (2020) has also been presented which shows that such methodology can successfully simulate the temperatures measured in the laboratory and field.

CHAPTER 3 THERMO-MECHANICAL BEHAVIOUR OF THERMO-ACTIVE PILES

3.1 INTRODUCTION

This chapter presents a comprehensive overview of the previous studies dedicated to investigating the thermo-mechanical behaviour of thermo-active piles. First, in Section 3.2, a descriptive framework for the behaviour of thermo-active piles when subjected to thermal or thermo-mechanical loading by Bourne-Webb et al. (2009), Amatya et al. (2012) and Bourne-Webb et al. (2013) is presented. Subsequently, a literature review on field, laboratory and numerical studies is presented in Sections 3.3, 3.4 and 3.5, respectively.

3.2 FRAMEWORK FOR UNDERSTANDING THE THERMO-MECHANICAL BEHAVIOUR OF THERMO-ACTIVE PILES

In order to understand the thermo-mechanical behaviour of thermo-active piles observed in the field, laboratory or numerical studies, a framework to explain how thermo-active piles behave when subjected to thermal or thermo-mechanical loading was proposed by Bourne-Webb et al. (2009), Amatya et al. (2012) and Bourne-Webb et al. (2013). It should be appreciated that this framework represents a simple and descriptive approach to explain the complex thermo-mechanical behaviour of thermo-active piles by adopting a number of assumptions, and therefore the thermo-mechanical response observed in reality only qualitatively resembles the one that the current framework proposes. The assumptions that the framework adopts are as follows:

- The soil surrounding the thermo-active pile has uniform strength and behaves in an idealised rigid-plastic manner. As a result, when the thermo-active pile is heated/cooled, the pile expands/contracts against the soil about a null point at mid-depth, while full and uniform shaft resistance is mobilised.
- When the thermo-active pile is subjected to a change in temperature, this temperature change is assumed to be uniform over the entire pile.
- A linear elastic thermo-active pile with constant cross-sectional area.

However, in reality, when a thermo-active pile expands/contracts against the soil, an elastic response of the latter is more likely than a plastic one. In this case, the shaft resistance that is mobilised is determined by the shear strain and shear stiffness of the soil (rather than the soil strength), which is unlikely to be uniform but dependent on a number of factors such as the confining pressure (and hence depth) and strain history. Moreover, thermo-active piles are heated/cooled by the heat exchanger pipes embedded within them, therefore the part of the pile cross-section that is in the proximity of the pipes experiences more extreme temperatures. Therefore, it must be emphasised that this framework is simply a tool that can be adopted to provide an insight into the thermo-mechanical behaviour of thermo-active piles, while the realistic thermo-mechanical behaviour of thermo-active piles subjected to thermo-mechanical loads will be discussed in detail in the following sections and in Chapter 4.

This framework considers the cases where a thermo-active pile is subjected to either thermal loading only or combined thermo-mechanical loading, together with different types and combinations of pile end restraints. The sign convention that is adopted in this framework (Section 3.2, which includes Figure 3.1 to Figure 3.4) is positive for compressive stresses and strains and for downwards acting shaft resistance.

3.2.1 Thermal loading

Consider the case where the thermo-active pile is a free body (i.e. there is no restriction to the pile, e.g. no soil surrounding the pile): when the pile is subjected to a change in temperature ΔT $[K]$, its expansion/contraction is directly proportional to its linear coefficient of thermal expansion α $[m \cdot m^{-1} \cdot K^{-1}]$ and the resulting axial strain, which is termed 'free thermal axial strain' ε_{T-Free}, is given by:

$$\varepsilon_{T-Free} = -\alpha \Delta T \tag{3.1}$$

In this case, the observed axial strain ε_{T-Obs} is equal to the free axial strain ε_{T-Free} and is uniform along the pile length as there is nothing restraining the pile.

Consider the case where the thermo-active pile is perfectly restrained at both ends such that the pile cannot expand or contract at all: the observed axial strain is zero ($\varepsilon_{T-Obs} = 0$) meaning that the restrained axial strain ε_{T-Rstr} must be equal to the free axial strain ε_{T-Free}, but in opposite direction (i.e. $\varepsilon_{T-Rstr} = -\varepsilon_{T-Free}$). This restrained strain results in a thermal axial force P_T $[N]$ developing within the pile that is uniform along the pile length:

$$P_T = EA_c\varepsilon_{T-Rstr} \tag{3.2}$$

In Equation (3.2), E $[N \cdot m^{-2}]$ is the Young's modulus and A_c $[m^2]$ is the cross-sectional area of the thermo-active pile.

The aforementioned two cases (free body case and perfectly restrained case) are illustrated in Figure 3.1 (Bourne-Webb et al., 2013; Gawecka, 2017).

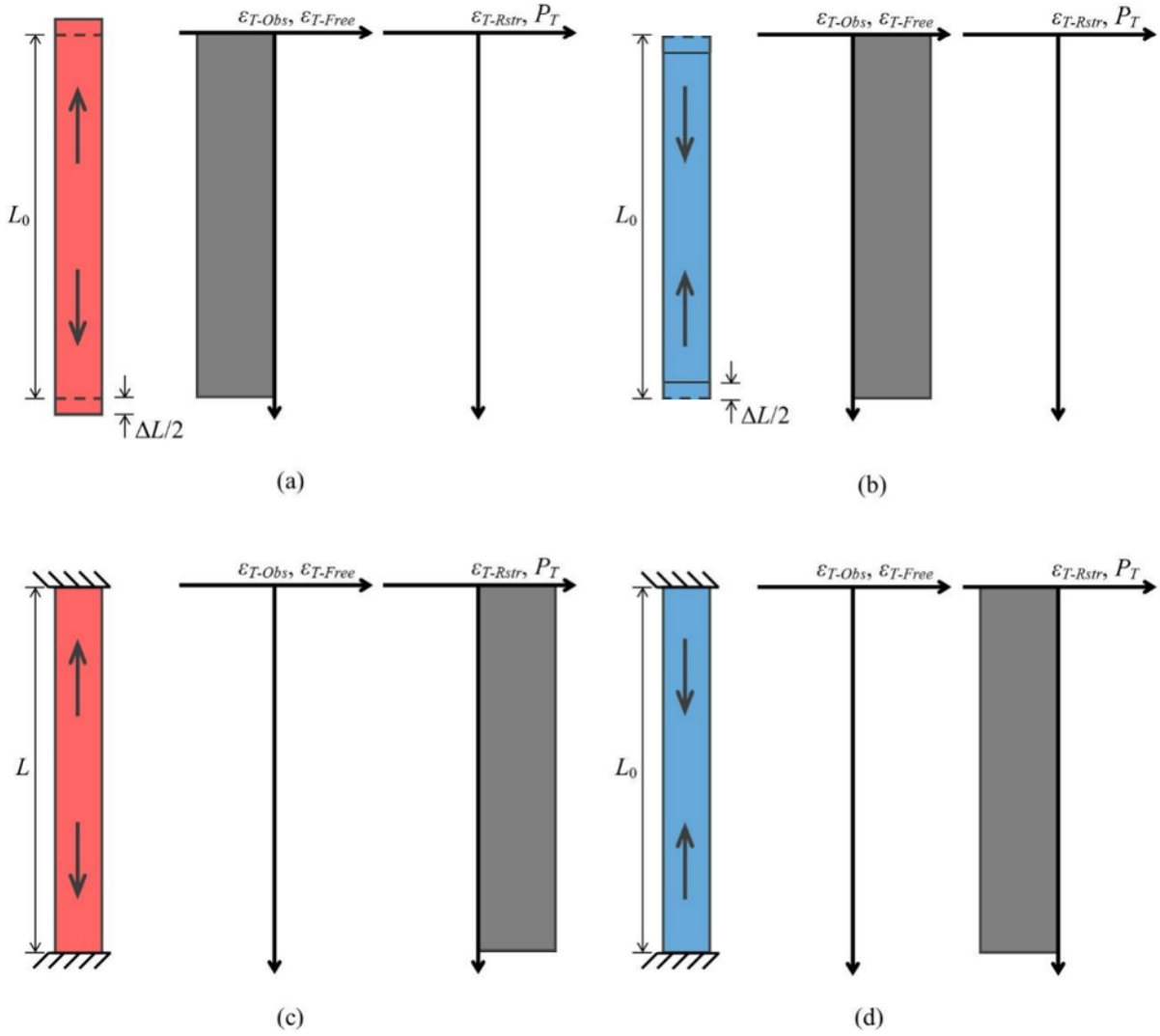


Figure 3.1 The profiles of ε_{T-Obs}, ε_{T-Free}, ε_{T-Rstr} and P_T for (a) free body case when the pile is heated (b) free body case when the pile is cooled (c) perfectly restrained case when the pile is heated (d) perfectly restrained case when the pile is cooled (Bourne-Webb et al., 2013; Gawecka, 2017)

Consider a more realistic case where the thermo-active pile is surrounded by soil. In this case, the expansion/contraction of the pile when heated/cooled is restrained by the surrounding soil

and hence the observed strain will be smaller than the free strain (i.e. $\varepsilon_{T-Obs} \leq \varepsilon_{T-Free}$). The relationship between observed strain, free strain and restrained strain can be given by:

$$\varepsilon_{T-Rstr} = \varepsilon_{T-Obs} - \varepsilon_{T-Free} \tag{3.3}$$

When both ends of the thermo-active pile are unrestrained, Figure 3.2 shows the profiles of observed strain ε_{T-Obs}, pile thermal axial force P_T and mobilised shaft resistance q_s when the thermo-active pile is heated or cooled (Amatya et al., 2012; Gawecka, 2017).

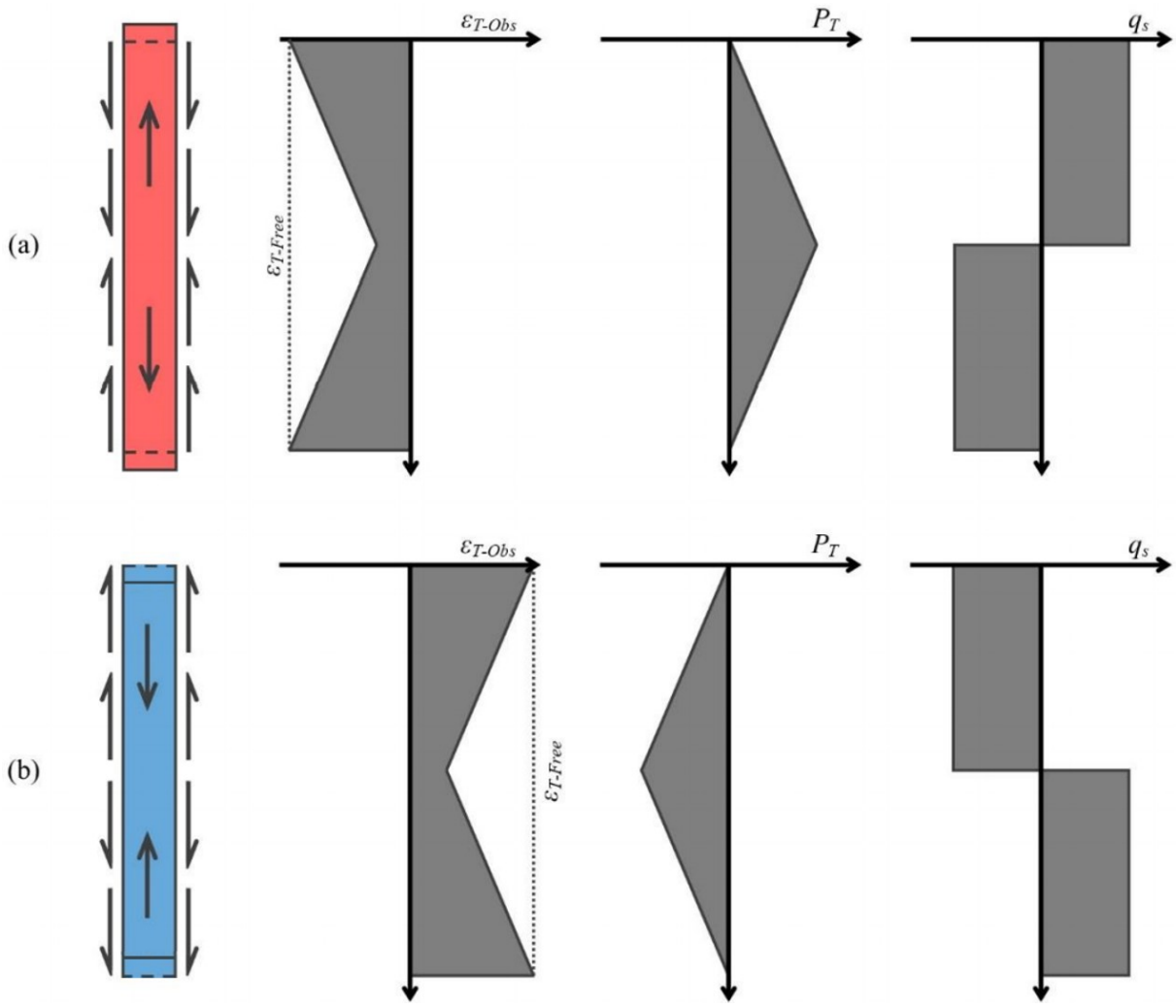


Figure 3.2 The profiles of ε_{T-Obs}, P_T and q_s when a thermo-active pile surrounded by soil which is unrestrained on both pile ends is (a) heated and (b) cooled (Amatya et al., 2012; Gawecka, 2017)

Referring to the case where the pile is heated in Figure 3.2, since the pile ends are unrestrained, the observed strains at the pile ends are equal to the free strain, which is negative for expansion. As the pile is heated and expands, it is assumed that full and uniform shaft resistance is

mobilised, which acts downwards (hence positive) for the upper part of the pile and upwards (hence negative) for the lower part of the pile. As a result, the restraint on the pile from the soil (and hence restrained strain and the pile thermal axial force from Equation (3.2)) increases with increasing distance from the pile ends and is the greatest at mid-depth, which also explains the minimum observed strain at that point. On the contrary, when the thermo-active pile is cooled, the shaft resistance acts in the opposite direction, and the resulting observed strain and pile thermal axial force profiles follow the same pattern as those for heating but in the opposite direction.

When the ends of the thermo-active pile are subjected to partial restraints (which can be due to the presence of a superstructure at the pile head, or a stiff bearing layer at the pile toe), the behaviour of a thermo-active pile surrounded by soil subjected to heating is characterised in Figure 3.3 (Amatya et al., 2012; Gawecka, 2017). Note that the response of the pile subjected to cooling is not shown here for brevity, as it will simply be opposite of that for heating. Referring to Figure 3.3, when the end of a pile is subjected to restraint, the observed strain ε_{T-Obs} at that end is reduced and become smaller than the free strain ε_{T-Free}, meaning that the pile thermal axial force at that end would be non-zero.

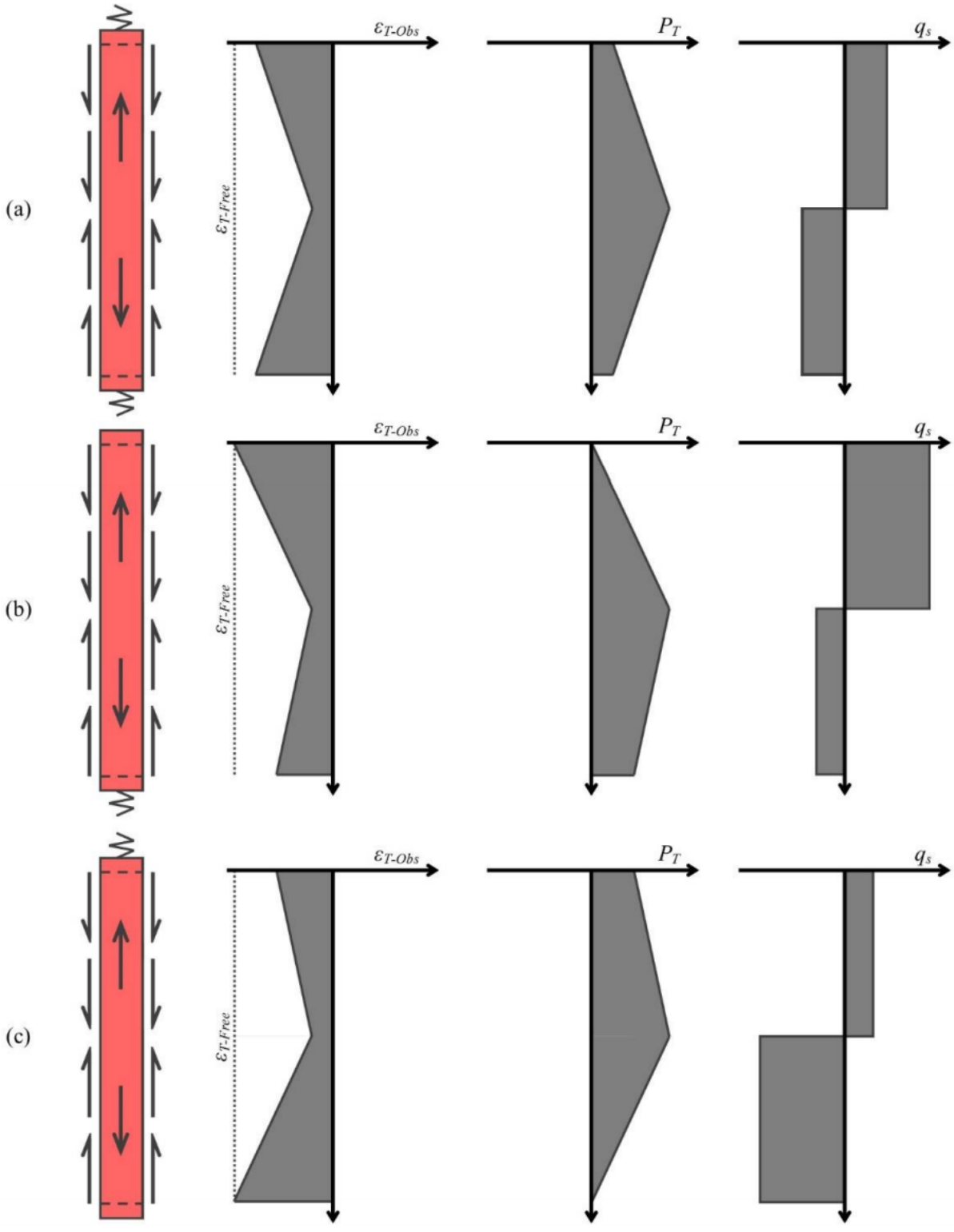


Figure 3.3 The profiles of ε_{T-Obs}, P_T and q_s when a thermo-active pile surrounded by soil which is (a) partially restrained at both ends, (b) partially restrained at the pile toe, and (c) partially restrained at the pile head is heated (Amatya et al., 2012; Gawecka, 2017)

3.2.2 Thermo-mechanical loading

When a thermo-active pile is subjected to a thermo-mechanical loading (i.e. a combination of mechanical loading and thermal loading), the total observed axial strain ε_{Total} is given by:

$$\varepsilon_{Total} = \varepsilon_M + \varepsilon_{T-Obs} \tag{3.4}$$

In Equation (3.4), ε_M is the mechanical axial strain due to the mechanical axial force P_M $[N]$:

$$\varepsilon_M = \frac{P_M}{EA_c} \tag{3.5}$$

The total axial force P_{total} acting within the pile is therefore given by the sum of thermal axial force P_T and mechanical axial force P_M:

$$P_{total} = P_T + P_M \tag{3.6}$$

Figure 3.4 illustrates the behaviour of a thermo-active pile surrounded by soil but unrestrained at both ends subjected to both mechanical and thermal (heating and cooling) loading (Amatya et al., 2012; Gawecka, 2017). Referring to Figure 3.4(a), when the pile is subjected only to a mechanical load acting at the pile head, uniform upwards acting shaft resistance is mobilised which results in a linear axial stress profile and hence a mechanical strain profile that varies linearly from a maximum value at the pile head to zero at the pile toe as the pile toe is unrestrained. While Figure 3.4(b) and Figure 3.4(d) illustrate the behaviour of the pile when subjected to heating and cooling, respectively (and are identical to Figure 3.2(a) and Figure 3.2(b)), when the pile is subjected to a combination of mechanical and thermal loads, the resulting behaviour is illustrated in Figure 3.4(c) for the case of heating and Figure 3.4(e) for the case of cooling. The axial force and shaft resistance profiles shown in Figure 3.4(c) and Figure 3.4(e) are the superposition of those due to mechanical loading only (Figure 3.4(a)) and thermal loading only (Figure 3.4(b) or Figure 3.4(d)). Note that should the pile ends be subjected to restraints, the superposition technique can also be applied to predict the total axial force and shaft resistance profiles.

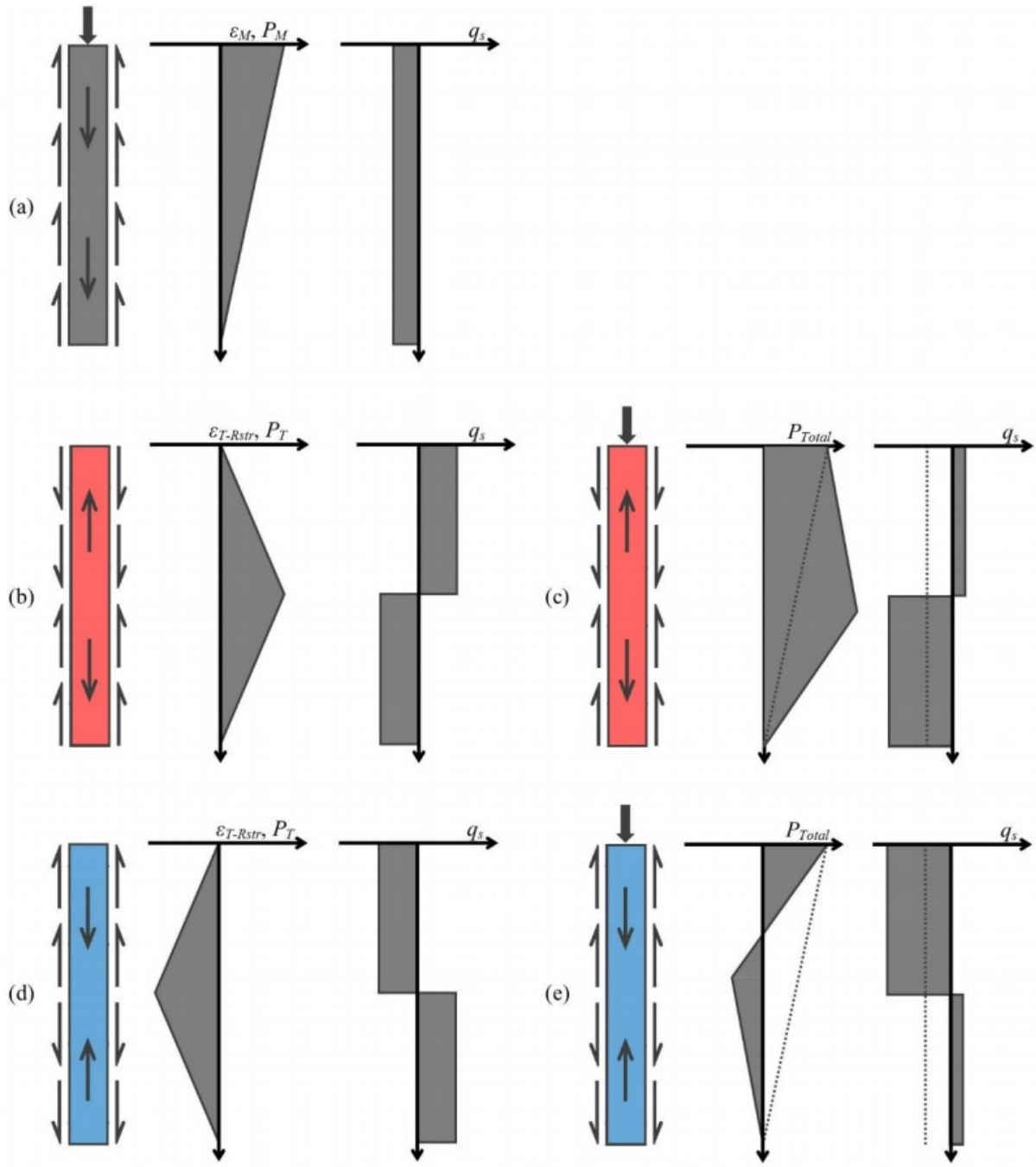


Figure 3.4 Behaviour of a thermo-active pile surrounded by soil that is subjected to (a) mechanical loading only, (b) heating only, (c) combination of mechanical loading and heating, (d) cooling only, and (e) combination of mechanical loading and cooling (Amatya et al. (2012); Gawecka, 2017)

3.3 FIELD STUDIES

This section presents a comprehensive literature review on the field studies that have been conducted on the thermo-mechanical behaviour of thermo-active piles. Since field studies that were reported before 2017 had been reviewed and discussed in Gawecka (2017), they will only be summarised briefly in Table 3.1, with the references, locations/developments and key aspects of the studies presented in a chronological order, while studies reported after 2017 are reviewed and discussed in Sections 3.3.1 to 3.3.3. Note that, unless otherwise specified, the thermally-induced axial strains (or restrained strains) presented in the literature are calculated by the difference between the free strains (i.e. those related to thermal expansion/contraction, calculated as $\alpha\Delta T$) and the observed strains due to thermal loads (see Equation (3.3)), with the latter being calculated as the difference between the measured total strains and those resulting from mechanical loading (see Equation (3.4)), as explained by the framework in Section 3.2.

References	Location/development	Key aspects of the field study
Laloui et al. (2003); Laloui et al. (2006); Amatya et al. (2012); Laloui and Di Donna (2013); Mimouni and Laloui (2013); Mimouni and Laloui (2015); Rotta Loria and Laloui (2016); Rotta Loria and Laloui (2017)	EPFL, Lausanne, Switzerland	Two studies were conducted at EPFL: a single pile study and a pile group study. In both studies, the piles were instrumented with vibrating wire and fibre optic extensometers to measure vertical and radial strains and temperatures. For the single pile study: • The pile was the only thermo-active pile out of the 97-pile foundation. • The pile was 880 mm in diameter, 25.8 m long, and the pile toe was founded in sandstone. • The pile was subjected to eight tests: Test 1 to Test 8. • Test 1 involved heating up the pile by 21℃ without any mechanical loads, while in each subsequent tests, the pile was heated up by 15℃ following the application of a mechanical load, which increased in each subsequent test to up to 1300 kN due to the construction of the building above it. • Plots of axial strains and thermally-induced axial loads were presented, and it was revealed that in Test 1, due to the absence of the overhead building, the pile head was unrestrained and expanded as a free body, whereas the pile toe was restrained by the stiff sandstone, giving rise to larger thermally-induced axial loads in the lower part of the pile.

Table 3.1 A summary of field studies conducted to investigate the thermo-mechanical behaviour of thermo-active piles that had been reviewed and discussed in Gawecka (2017)

Laloui et al. (2003); Laloui et al. (2006); Amatya et al. (2012); Laloui and Di Donna (2013); Mimouni and Laloui (2013); Mimouni and Laloui (2015); Rotta Loria and Laloui (2016); Rotta Loria and Laloui (2017)	EPFL, Lausanne, Switzerland	• In subsequent tests where the pile was subjected to increasing mechanical loads due to the construction of the building, it was found that the restraint on the pile head became larger than that at the pile toe. • It was found that thermally-induced axial loads were three times larger than the mechanical loads. For the pile group study: • A group of four thermo-active piles were studied, which formed the foundation alongside with 16 conventional piles. • The four thermo-active piles were located at the corner of the foundation, with $900\ mm$ diameter, $28\ m$ long, and design loads of $0, 800, 2100$ and $2200\ kN$, respectively. • Four tests were conducted: o In Test 1, only one of the piles was heated by $3.6℃$ prior to the construction of the overhead structure. The results showed that the pile head expanded more than the toe as it was unrestrained. o In Test 2, the piles were heated in turn by $6.5 - 10℃$ after the construction of the overhead structure. It was found that when a pile in the group was heated, the other three piles presented a decrease in compressive stresses while the heated pile presented an increase in compressive stresses. Moreover, dependent on the relative positions of the heated and unheated piles, one side of an unheated pile experienced expansion while the opposite side experienced contraction (i.e. bending). o In Test 3, all four piles were heated by $7.4 - 9.1℃$ simultaneously. The results showed that, compared to Test 2, differential displacements were significantly smaller while the overall pile displacements were larger, resulting in smaller thermally-induced axial loads. o In Test 4, one of the piles was heated for 5 months by up to $20℃$, and the results obtained were similar to those from Test 2, where heating a single pile would affect the response of the surrounding unheated piles.

Table 3.1 (continued)

Brandl (2006)	Rehabilitation Centre, Bad Schallerbach, Austria	• There were a total of 175 piles in the foundation, out of which 143 were thermo-active, with only one instrumented. • The pile was 1200 mm in diameter, 9 m long with a design load of 2000 kN. • The pile was instrumented with pressure cells at the pile head and toe, fissuremeters and thermo-elements to measure displacements and temperatures. • It was found that there was an initial reduction in base load due to cooling, hence contraction, of the pile following hydration of the concrete pile. • Subsequent application of mechanical and thermal loads had no effects on the base load, indicating that shaft friction was mobilised instead. • Plots of temperatures, mechanical and thermally-induced axial strains with depth were presented. However, Gawecka (2017) suggested that the thermally-induced axial strains presented were obtained by multiplying the temperature changes with the linear coefficient of thermal expansion of the pile (i.e. free strains), rather than from the difference between total and mechanical strains as described by the framework in Section 3.2 (i.e. restrained strain).
Bourne-Webb et al. (2009); Amatya et al. (2012)	Lambeth College, London, United Kingdom	Two thermo-active piles were studied: a main test pile and a heat sink pile. For the test pile: • The pile was 550 mm in diameter (except for the top 5 m where the diameter was 610 mm due to the presence of casing) and 23 m long. • A double U-loop of heat exchanger pipes were installed in the pile. • The pile was instrumented with vibrating wire strain gauges (VWSG), thermistors, optical fibre sensors (OFS) and linear variable differential transformers (LVDT) to measure strains, temperatures and vertical displacements of the pile head. • A load cell and hydraulic jack were used to apply mechanical loads to the pile while an 8 kW heat pump, capable of circulating fluid ranging from $-6℃$ to $56℃$, was used to apply thermal loads. • The test involved the following stages: ○ Loading to 1800 kN followed by unloading. ○ Loading to 1200 kN. ○ Cooling under constant load. ○ Intermittent heating under constant load. ○ Loading to 3600 kN followed by unloading. • During the cooling stage, the pile was cooled by $19℃$ and the recorded pile head movement was 60% of the theoretical contraction, while during the heating stage, the pile was heated by $27℃$ and the recorded pile head movement was 40% of the theoretical expansion. These suggested that the restraints from the surrounding soil were significant. • It was found that during the cooling stage, an overall tensile force was recorded in the lower part of the pile.

Table 3.1 (continued)

Bourne-Webb et al. (2009); Amatya et al. (2012)	Lambeth College, London, United Kingdom	• It was also revealed that during the heating stage, the maximum thermally-induced axial load was 675 kN, which was more than half of the applied mechanical load (1200 kN). For the heat sink pile: • The pile was 600 mm in diameter and 30 m long. • The pile was instrumented with OFS to measure strains and temperatures. • The heat sink pile was only subjected to thermal loads, where a temperature increase of 29℃ was applied. • It was found that the pile ends were subjected to very little restriction, and the maximum thermally-induced axial load was 1550 kN which occurred at mid-depth.
Bouazza et al. (2011); Singh et al. (2015a); Singh et al. (2015b); Wang et al. (2015); Faizal and Bouazza (2016); Faizal et al. (2016); Faizal et al. (2018)	Monash University, Melbourne, Australia	• A single thermo-active pile was studied which was 600 mm in diameter and 16.1 m long subjected to thermo-mechanical loads. • The mechanical loads were applied using Oesterberg Cells (O-Cells) installed at 10 m and 14 m depths. • The pile was instrumented with VWSG, vibrating wire displacement transducers and thermistors to measure strains, temperatures and displacements. • Two boreholes were also constructed at 0.5 m and 2 m away from the pile to measure soil temperatures. • Loading and unloading cycles were applied which determined the ultimate shaft resistance of the pile to be 1650 kN before the application of thermal loads. • The loading and unloading cycles were also applied after the following four heating/cooling cycles in order to determine the change in ultimate shaft resistance of the pile: o Heating by 20℃ for 9 days o Natural cooling for 47 days o Heating by 28℃ for 52 days o Natural cooling for 78 days • It was revealed that the ultimate shaft resistance of the pile following the two heating cycles increased to at least 1885 kN, which was the maximum load that the O-Cell could apply, while following the two natural cooling cycles, the ultimate shaft resistance reduced to approximately its original value, suggesting thermoelastic behaviour. • The increase in ultimate shaft resistance following the heating cycles was attributed to the increase in radial stress due to expansion of the pile and the surrounding soil.

Table 3.1 (continued)

McCartney and Murphy (2012); Murphy and McCartney (2012); Murphy and McCartney (2015); McCartney and Murphy (2017)	Denver Housing Authority Senior Living Facility, Colorado, United States	• A study of two thermo-active piles, Pile A and Pile B respectively. • Pile A was 910 mm in diameter and 14.8 m long with a design load of 3.84 MN. • Pile B was 910 mm in diameter and 13.4 m long with a design load of 3.65 MN. • Both piles were instrumented with VWSG and thermistors to measure both strains and temperatures. • Plots of thermally-induced axial stresses and strains over depth were presented. • It was found that the pile toe was more heavily restrained than the pile head, resulting in larger thermally-induced axial stresses in the lower part of the pile. • It was concluded that the thermally-induced axial stresses were not significant enough to cause structural damage.
Abdelaziz (2013); Olgun and Bowers (2016)	Virginia Tech, Blacksburg, Virginia, United States	• A study of four thermo-active piles. • All piles were 250 mm in diameter and 30.5 m long. • The upper parts of the piles were founded in silty sand while the lower parts were in shale. • All piles were subjected to thermal loads, but only one was subjected to both mechanical and thermal loads. • Strains, temperatures and head displacements were monitored throughout the test. • The pile was first loaded to its ultimate capacity of 1334 kN, then heating and cooling cycles were applied. • It was found that the lower part of the pile, which was located within the shale, showed almost no deformation and resulted in maximum thermally-induced axial loads. For the upper part of the pile, thermally-induced strains were recoverable during the first heating and cooling cycle, but residual strains were observed following subsequent cycles.
Akrouch et al. (2014)	Texas A&M University, Texas, United States	• The thermo-active pile studied was in a group of eight piles, which were 180 mm in diameter and 5.5 m long. • The pile was instrumented with strain gauges, thermocouples and dial gauges to monitor strains, temperatures and head displacements. • Five tests were performed, where tensile forces of $40, 100, 150, 200$ and 256 kN were applied, respectively, and the pile was heated up by $10 - 15^{o}C$, then cooled naturally following each load application. • It was found that the thermally-induced compressive loads were insignificant compared to the mechanical loads.
Ouyang (2014)	Waterloo Station, London, United Kingdom	• A thermal response test on a 300 mm diameter and 24 m long pile. • Short-term behaviour of the pile was investigated. • Pile was subjected to thermal cycles. • The pile ends expanded and contracted similar to a free body. • Maximum thermally-induced axial load was observed near the middle of the pile.

Table 3.1 (continued)

Ouyang (2014)	Tate Modern, London, United Kingdom	• Out of the 130 thermo-active piles in the development, two were instrumented with OFS and VWSG to measure both strains and temperatures, and one was instrumented with OFS to measure temperatures only. • All three piles were $1200\ mm$ in diameter and $30 - 50\ m$ long, with $700 - 13000\ kN$ design loads. • Temperature changes of $\pm 5℃$ were applied to the piles during the tests. • The combined mechanical and thermally-induced loads were within the designed capacities.
Murphy et al. (2014); Murphy et al. (2015)	US Air Force Academy, Colorado, United States	• A single storey building was supported by eight thermo-active piles, which were all $610\ mm$ in diameter and $15.2\ m$ long. • Each pile was instrumented with VWSG and thermistors to measure both strains and temperatures. • Thermal response tests were performed on four of the piles. • It was found that the thermally-induced axial strains (and hence thermally-induced axial stresses) obtained during the temperature-increase stages were similar to those obtained at the same temperature during the temperature-decrease stages, suggesting thermoelastic behaviour. • It was concluded that the thermally-induced stresses and strains were not significant enough to cause damage.

Table 3.1 (continued)

3.3.1 Regional office of Berkel and Company Contactors, Richmond, Texas, United States

The thermo-mechanical responses of two identical end bearing thermo-active test piles at the regional office of Berkel and Company Contactors in Richmond, Texas, United States, were studied by Sutman et al. (2017). The test site involved a total of three thermo-active piles (but only the results of two were presented), eight conventional reaction piles which were used to apply mechanical loads onto the thermo-active test piles, and three heat sink piles (which were connected to the main thermo-active piles, where heating of the thermo-active piles corresponded to the extraction of heat from the heat sink piles, and cooling of the thermo-active piles corresponded to the injection of heat from the heat sink piles). All three thermo-active piles were $457.5\ mm$ in diameter, with a single U-loop installed for heat exchange, with the two identical ones which were studied being $15.24\ m$ long and designated as TP-1 and TP-3, respectively. The thermo-active piles were instrumented with VWSG, thermistors, thermal integrity profiling (TIP) wires, OFS and LVDT to measure strains, temperatures and axial displacements. The soil profile at the test site, dimensions of the thermo-active piles and the depths at which the VWSG were installed within the thermo-active piles are shown in Figure 3.5 (Sutman et al., 2017). Note that the ground temperature of the site was measured at the start of test to be of around $22 - 23℃$ for depths greater than $5\ m$.

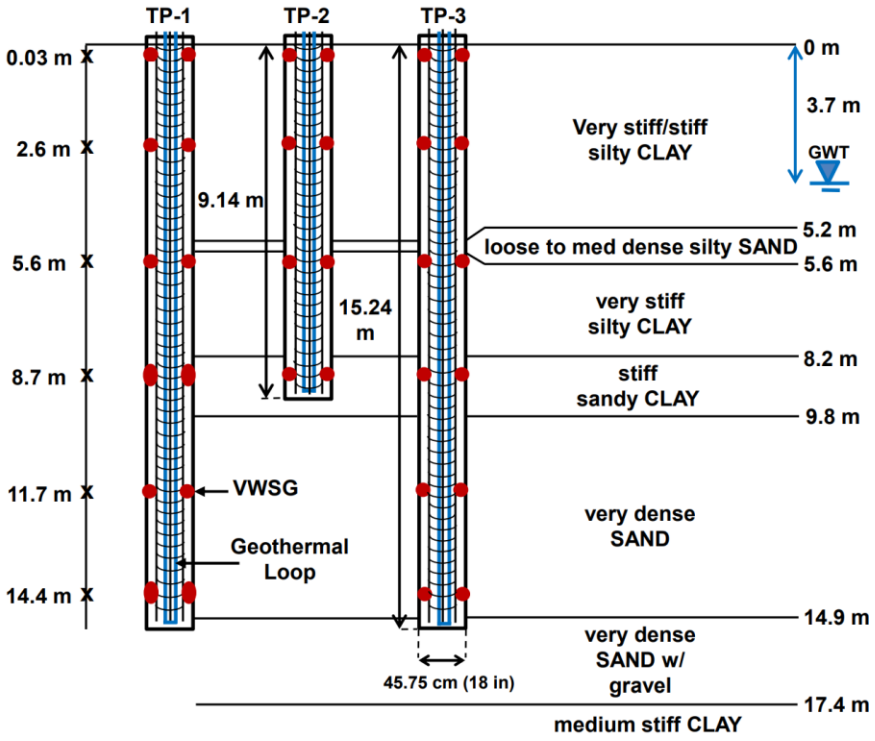


Figure 3.5 Soil profile of the test site, dimensions of the thermo-active test piles and the locations at which the VWSG were installed (Sutman et al., 2017)

In order to investigate the effects of end restraints on the thermo-mechanical responses of thermo-active piles, two tests were performed: TP-1 was subjected to five heating and cooling cycles over 38 days, with inlet temperatures ranging between 8℃ and 43℃ (the latter resulting in an average temperature rise of 7.6℃ during heating due to the transient nature of the applied thermal loads), without the application of mechanical loads; while TP-3 was mechanically loaded to a design load corresponding to a factor of safety of 2.0 (which was approximately 1110 kN). This was followed by the application of a single heating and cooling cycle over 14 days, with inlet temperatures ranging between 8 ℃ and 45 ℃ (the latter resulting in an average temperature rise of 8.4℃ during heating), during which the results reported by Sutman et al. (2017) appear to suggest that the displacement resulting from the application of the mechanical load was kept constant, hence restricting the movement of the pile head. Note that only the results from the heating cycles were presented for both piles.

The thermally-induced axial stress and shaft resistance profiles obtained during a heating cycle applied to TP-1 are presented in Figure 3.6 (Sutman et al., 2017). Note that tension and upwards acting shaft resistance are taken as positive for this case. Referring to Figure 3.6, it can be observed that:

- The maximum magnitude of thermally-induced compressive stress was 1570 kPa, which corresponds to approximately 172 $kPa \cdot ℃^{-1}$. This is relatively low compared to the figure of 284 $kPa \cdot ℃^{-1}$ observed in the main test pile from the Lambeth College test (Bourne-Webb et al., 2009), but comparable to 153 $kPa \cdot ℃^{-1}$ observed in Tests 6 and 7 of the single pile study from the Lausanne test (Laloui et al., 2006; Amatya et al., 2012).
- As no restraint was present at the pile head, it was free to expand and the thermally-induced axial stress at the pile head was zero.
- The pile toe was restrained by the very dense sand layer, resulting in significant thermally-induced axial stress (around 900 kPa) at the pile toe.
- The null point was located at a depth of 8.7 m (which was below the pile mid-depth due to the pile toe restraint), above which the downwards acting shaft resistance was approximately 2.9 $kPa \cdot ℃^{-1}$, while below the upwards acting shaft resistance was approximately 1.7 $kPa \cdot ℃^{-1}$.

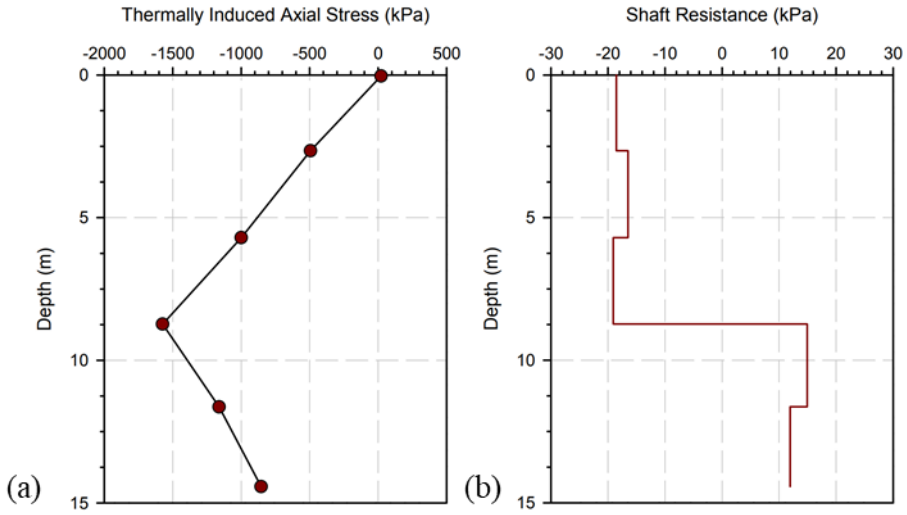


Figure 3.6 The thermally-induced (a) axial stress and (b) shaft resistance profiles obtained during a heating cycle for TP-1 (Sutman et al., 2017)

The axial stress and shaft resistance profiles obtained during the heating cycle on TP-3 are presented in Figure 3.7 (Sutman et al., 2017). In Figure 3.7, 'mechanical stresses' refer to the stresses due to the mechanical loads, 'thermo-mechanical stresses' refer to the stresses due to both mechanical and thermal loads, and 'thermal stresses' refer to the thermally-induced axial stresses, the same applies for the shaft resistance profiles. Referring to Figure 3.7, it can be observed that:

- The maximum magnitude of thermally-induced compressive stress was 1810 kPa, which corresponds to approximately 160 $kPa \cdot ℃^{-1}$, which is similar to that measured for TP-1.
- The testing control at the pile head presented a restraint, inducing approximately 1150 kPa of axial stresses at the pile head, which also means that the load applied at the pile head was not constant during the test.
- The null point was located at a depth of 5.7 m, above which the downwards acting shaft resistance was approximately 1.93 $kPa \cdot ℃^{-1}$, while below the upwards acting shaft resistance was approximately 1.9 $kPa \cdot ℃^{-1}$.

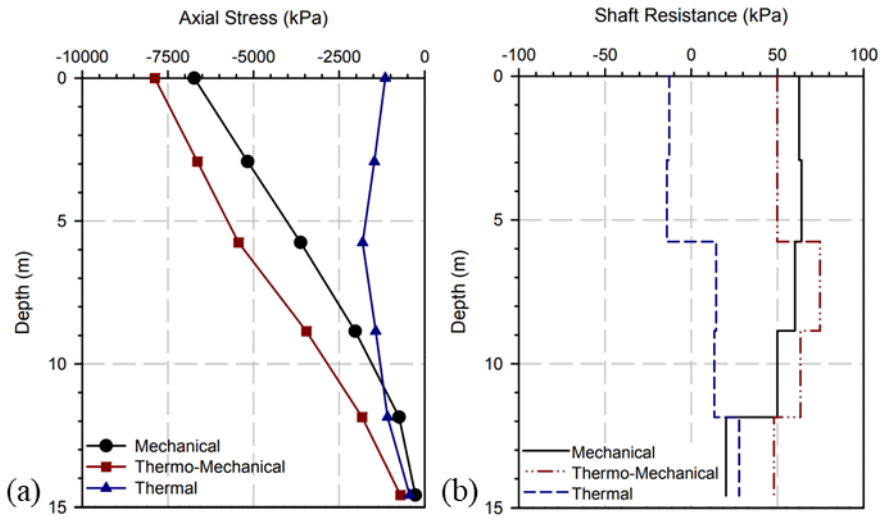


Figure 3.7 The (a) axial stress and (b) shaft resistance profiles obtained during the heating cycle for TP-3 (Sutman et al., 2017)

Comparing the results from TP-1 (no pile head restraint) and TP-3 (pile head restraint), the major observations were that the presence of a restraint at the pile head shifted the null point of the pile upwards in order to equilibrate forces. Higher thermally-induced shaft resistance was observed in TP-1 as it was freer to expand without the pile head restraint, resulting in larger axial displacements. It was also observed that the maximum thermally-induced compressive stresses achieved in TP-1 and TP-3 were 37% and 38% compared to the theoretical case of perfectly restrained conditions, respectively.

3.3.2 Yongin city, Korea

The thermo-mechanical responses of a large diameter thermo-active pile in Yongin city, Korea, was studied by Sung et al. (2018). The thermo-active pile studied was 1500 mm in diameter,

$14\ m$ long, and had five U-loops of heat exchanger pipes installed. The pile was instrumented with thermocouples and VWSG to measure temperatures and strains. The soil profile at the test site consisted of $3\ m$ of reclaimed silty sand, $11\ m$ of weathered soil and rock, followed by the hard fresh gneiss bedrock. Site investigations also revealed that the stiffness of the soils increases with depth.

Two tests were performed on the thermo-active pile, a heating test and a cooling test, both of which involved 15 days of operation followed by 15 days of resting, without the application of any mechanical load (any strains measured during the test were therefore thermally-induced). During the cooling test, fluids with inlet temperatures of $6 - 9℃$ were circulated, resulting in an average temperature drop of $6.2℃$, while during the heating test, fluids with inlet temperatures of $29 - 30℃$ were circulated, resulting in an average temperature rise of $8.8℃$ (note that this value is a change in temperature, whereas the inlet temperatures are absolute values, i.e. they include the initial ground temperature). In both cases, a carrier fluid flow rate of $7.66 \times 10^{-5}\ m^3 \cdot s^{-1}$ was adopted. The thermally-induced axial stress profiles obtained at different times from both cooling and heating tests are shown in Figure 3.8 (Sung et al., 2018). Note that tension is taken as positive for this case.

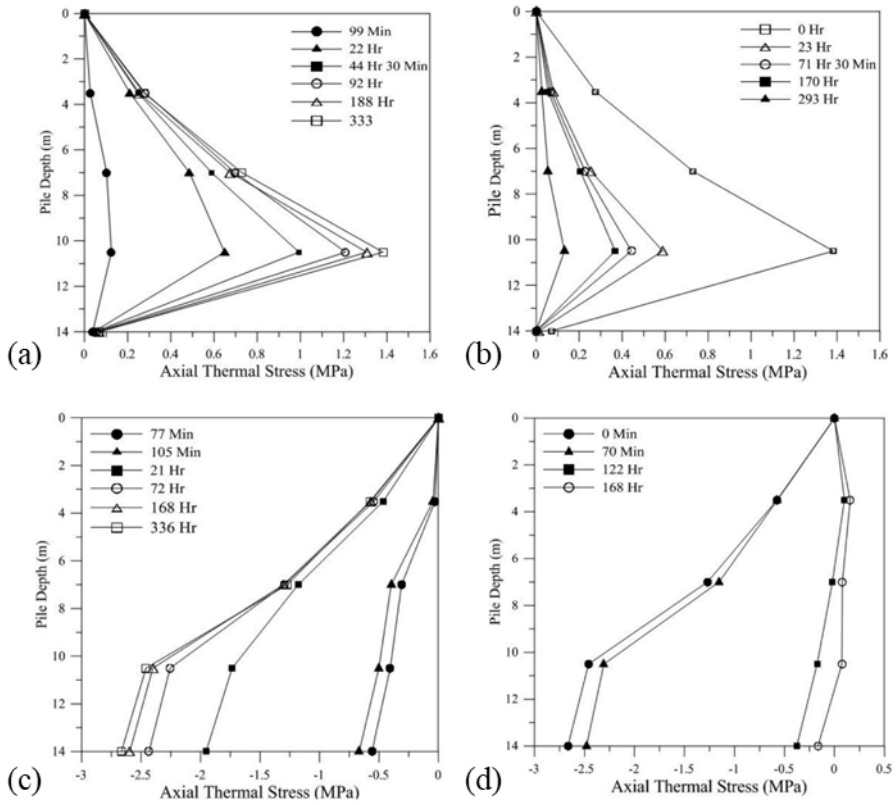


Figure 3.8 Thermally-induced axial stress profiles obtained (a) during the operation stage of the cooling test (15 days), (b) during the resting stage of the cooling test (15 days), (c) during the operation stage of the heating test (15 days), and (d) during the resting stage of the heating test (15 days) (Sung et al., 2018)

Referring to Figure 3.8, it can be observed that during the heating test, a maximum thermally-induced axial compressive stress of 2.6 MPa was achieved, which corresponds to 308.2 $kPa \cdot ℃^{-1}$ or 10% of the design compressive strength of concrete, while during the cooling test, the maximum thermally-induced axial tensile stress of 1.4 MPa was achieved, which corresponds to 223.7 $kPa \cdot ℃^{-1}$. Another observation is that during the cooling test, the null point (or the point where the maximum thermally-induced axial tensile stress occurred) was below the pile mid-depth at 10.5 m. The authors attributed this to the increase in stiffness with depth of the surrounding soil. For the heating test, the thermally-induced axial compressive stress was maximum at the pile toe, which could be explained by the restraint applied on the pile toe from the hard bedrock. On the other hand, it should be appreciated that the hard bedrock did not influence the behaviour of the pile during the cooling test (see Figure 3.8(a) and Figure 3.8(b)), as it hardly constitutes a restraint in tension. Finally, during the resting period of both cooling and heating tests, the thermally-induced axial stresses decrease with time and were eventually

almost eliminated when the pile and the surrounding soil had reached thermal equilibrium, which once again showed thermoelasticity.

3.3.3 Piterm research project, Valencia, Spain

The thermo-mechanical response of an experimental thermo-active precast driven pile as part of the Piterm research project in Valencia, Spain, was studied by de Santayana et al. (2020). The precast thermo-active pile was $17.4\ m$ long with a $350\ mm$ by $350\ mm$ cross-section. The pile was constructed of two pieces, each $8.7\ m$ long, connected by a joint. A steel pipe of $113\ mm$ diameter was used to create a circular hole at the centre of the pile cross-section, which allowed the double U-loop of heat exchanger pipes to be lowered into and filled with high thermal conductivity mortar following driving into the soil. The pile was instrumented with VWSG, thermistors, OFS, analogue dial gauges and LVDT to measure temperatures, strains and displacements, as well as a load cell to measure the actual load applied at the pile head (using a hydraulic jack and an anchored metallic frame) throughout the tests. The soil profile at the site consisted of: $1\ m$ of superficial fill of compacted sandy gravel, $1\ m$ of stiff clay, $6\ m$ of soft and black organic clays, $3\ m$ of loose sands followed by at least $16\ m$ of interlayered dense sandy gravels and stiff clays. The initial ground temperature was $18 - 20℃$. The ultimate capacity of the pile was determined to be $2511\ kN$ ($711\ kN$ of shaft resistance $+ 1800\ kN$ of base resistance) following driving tests.

A total of five tests were performed on the thermo-active pile, Tests A to E. In all the tests, a constant load of $1000\ kN$ was applied at the pile head. Tests A and B were thermal response tests which were used to characterise thermally the pile as a heat exchanger and are therefore not explained here for brevity as no mechanical response had been reported.

Test C involved heating the pile in three stages, one immediately after another (the scheme of which is illustrated in Figure 3.9 (de Santayana et al., 2020), together with the identification of monitoring moments C_0, C_a, C_b, C_c, C_d and C_e): in stage 1, a heat injection rate of $40\ W \cdot m^{-1}$ was applied for 5 days, in stage 2, a heat injection rate of $120\ W \cdot m^{-1}$ was applied for 4 days, in stage 3, a heat injection rate of $60\ W \cdot m^{-1}$ was applied for 5 days. The pile temperature was the highest at monitoring moment C_b, with an average temperature rise of around $15℃$. The recorded pile head displacements and total axial load profiles are shown in Figure 3.10 and Figure 3.11, respectively (de Santayana et al., 2020) (in Figure 3.10, V1, V3, V5 and V6 refer to four different sensors for the measurement).

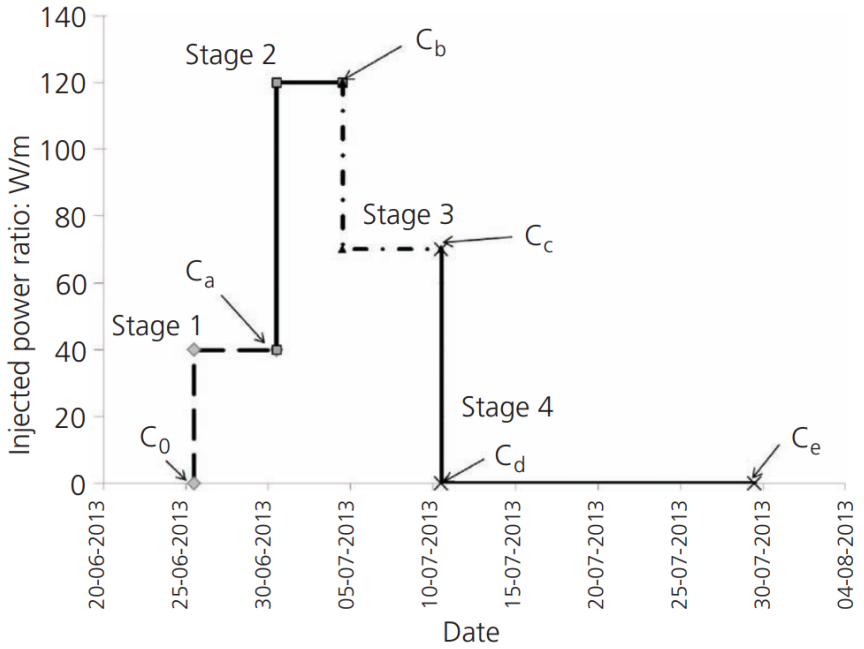


Figure 3.9 The scheme of Test C together with the identification of monitoring moments (de Santayana et al., 2020)

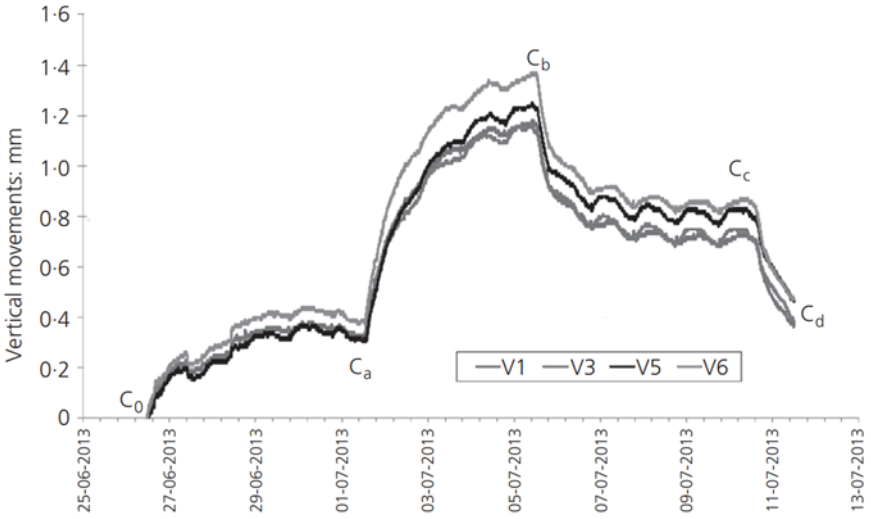


Figure 3.10 Pile head displacements recorded during Test C (de Santayana et al., 2020)

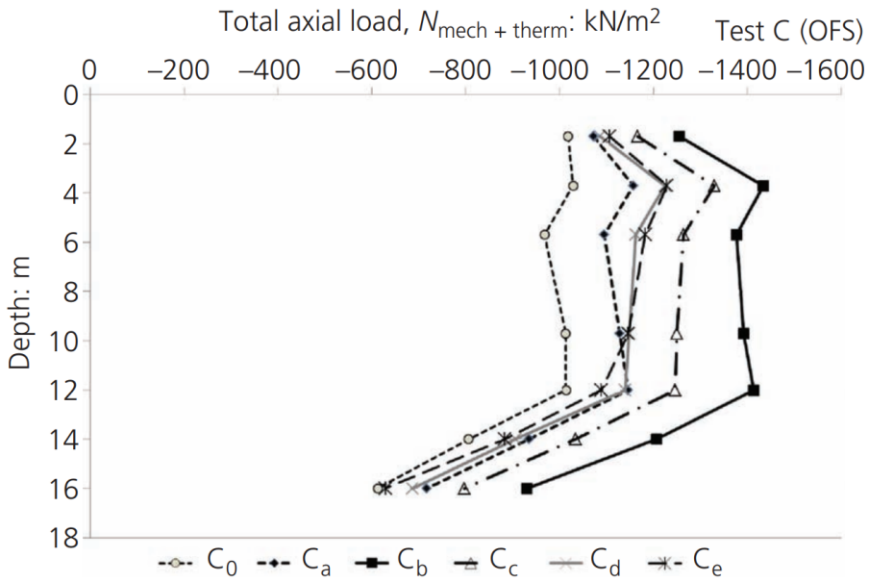


Figure 3.11 Total axial load profiles recorded during Test C (de Santayana et al., 2020)

Referring to Figure 3.10, the maximum pile head displacement was $1.23\ mm$ (which is one-third of the theoretical case of free expansion), which occurred at C_b (where the temperature change of the pile was highest). Referring to Figure 3.11, it can be observed that the maximum thermally-induced axial load was $400\ kN$ (which corresponds to $3265\ kPa$, or $218\ kPa \cdot °C^{-1}$), which is significant compared to the mechanical load of $1000\ kN$. Moreover, the maximum thermally-induced base load was $340\ kN$, which is also significant compared to the $600\ kN$ due to mechanical loads. The total shaft resistance profiles that were recorded during Test C are shown in Figure 3.12 (de Santayana et al., 2020). It can be observed that the restraints to pile expansion concentrated mainly at both ends of the pile: in the upper $2 - 3\ m$ due to the artificial fills and stiff clays, and at the base where the coarse sands and gravels were located.

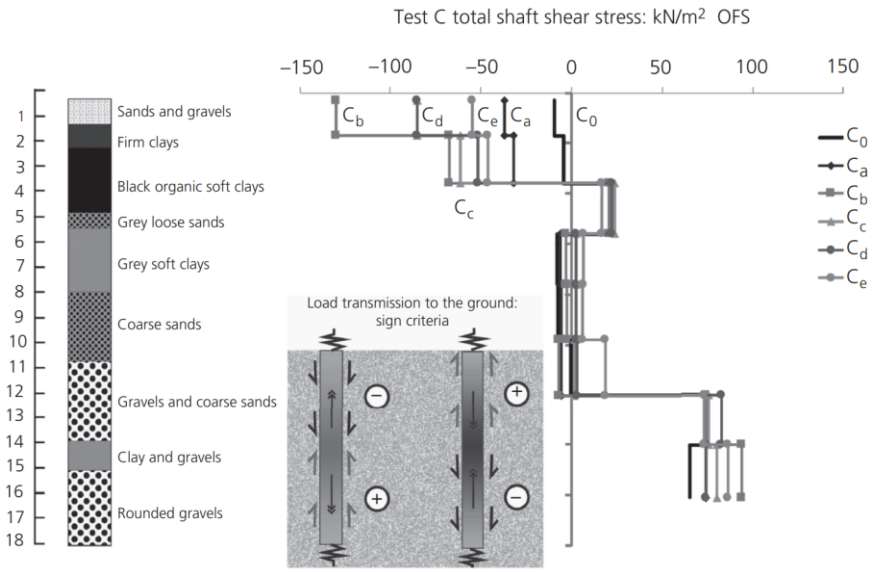


Figure 3.12 Total shaft resistance profiles recorded during Test C (de Santayana et al., 2020)

Test D is not reported as it was similar to Test C and the obtained results were 'identical', while in Test E, 14 daily cycles of heating were applied in a realistic way mimicking the operation patterns typical of cooling an office building. However, the maximum injection rate was only $80\ W \cdot m^{-1}$ (compared to the maximum of $120\ W \cdot m^{-1}$ in Test C), which resulted in a maximum temperature rise of 5℃ in the pile, a maximum pile head displacement of $0.4\ mm$ and a maximum thermally-induced axial load of $150\ kN$, the profiles of which are not shown here for brevity.

3.4 LABORATORY STUDIES

Compared to field studies, laboratory studies have the advantages of lower costs, the fact that tests are conducted under more controlled conditions, at smaller scales, with shorter timescales and higher repeatability, hence more easily allowing parametric studies to be conducted to investigate various factors that could influence pile response. Moreover, in the case of centrifuge tests, an acceleration (usually applied as N times the Earth's gravitational acceleration g) can be applied to the sample in order to replicate in the model the stresses that can be observed in the field. This is due to the fact that according to the scaling law, the scale factor for length is $1/N$, while the scale factor for gravity is N, which means that if a model that is N times smaller than the prototype tested in a gravity field that is N times the Earth's gravitational acceleration g, the stresses due to gravity will be identical in the model and prototype (Kutter, 1992). However, in the context of modelling thermo-mechanical piles, an

issue with centrifuge modelling is that, according to the scaling law, heat conducts N^2 times faster in the model than in the prototype, which means that a larger volume of soil surrounding the thermo-active pile will be affected by the heating/cooling of the pile; although from this perspective, centrifuge testing provides worst case scenario predictions (McCartney, 2013).

This section presents a comprehensive literature review on laboratory studies that have been conducted on the thermo-mechanical behaviour of thermo-active piles. Since laboratory studies that were reported before 2017 had been reviewed and discussed in Gawecka (2017), they will only be summarised briefly in Table 3.2, with the references, acceleration of the tests (which will be g for non-centrifuge tests and a multiple of g for centrifuge tests), test details and the key findings of the studies presented in a chronological order. Studies reported after 2017 are reviewed and discussed in Sections 3.4.1 and 3.4.2.

References	Acceleration of test	Test details	Key findings
McCartney et al. (2010); McCartney and Rosenberg (2011); Stewart and McCartney (2012); Goode and McCartney (2014); Goode et al. (2014); Stewart and McCartney (2014); Goode and McCartney (2015)	$24g$	Three piles of $76.2\ mm$ diameter and $381\ mm$ length were tested in Bonny Silt, which corresponded to prototypes with $1.8\ m$ diameter and $9.1\ m$ length. The testing procedures were as follows: 1. All three piles were loaded to a prototype load of $800\ kN$. 2. Pile 2 was heated up by 35℃, while Pile 3 was heated up by 35℃, then cooled by 30℃. 3. All three piles were loaded to failure.	• The pile capacity increased by 1.6 times when it was heated up by 35℃, but when the same pile was subsequently cooled by 30℃, the pile capacity was only 1.2 times the original capacity. The increase in pile capacity was due to an increase in radial stress and shaft resistance due to the expansion of pile and the surrounding soil upon heating.
		Four piles of $76.2\ mm$ diameter and $381\ mm$ length were tested in Bonny Silt, which corresponded to prototypes with $1.8\ m$ diameter and $9.1\ m$ length. The testing procedures were as follows: 1. All four piles were loaded by a displacement of $5\ mm$. 2. Pile 3 was heated up by 29℃ while Pile 4 was heated up by 41℃. 3. All four piles were loaded to failure.	• A pile that was heated up by 41℃ showed a 40% increase in shaft resistance.
		A pile of $50.8\ mm$ diameter and $533.4\ mm$ length was tested in Bonny Silt, which corresponded to a prototype with $1.2\ m$ diameter and $12.8\ m$ length. It was loaded to a prototype load of $303\ kN$, heated by 45℃, then cooled by 42℃, followed by unloading.	• For the end-bearing pile where the pile toe rested on the base of the container, maximum thermally-induced axial load was obtained near the pile toe, and the thermally-induced axial load was significantly larger than the mechanical load. Furthermore, insignificant changes in pile response were observed between the heating cycles, demonstrating thermoelasticity.
		A pile of $50.8\ mm$ diameter and $533.4\ mm$ length was tested in Bonny Silt, which corresponded to a prototype with $1.2\ m$ diameter and $12.8\ m$ length. The pile was first loaded to a prototype load of $443\ kN$, heated up by 9℃, followed by four heating cycles of 10℃.	

Table 3.2 A summary of laboratory studies conducted to investigate the thermo-mechanical behaviour of thermo-active piles that had been reviewed and discussed in Gawecka (2017)

McCartney et al. (2010); McCartney and Rosenberg (2011); Stewart and McCartney (2012); Goode and McCartney (2014); Goode et al. (2014); Stewart and McCartney (2014); Goode and McCartney (2015)	$24g$	A pile of 63.5 mm diameter and 342.9 mm length was tested in dry Nevada Sand, which corresponded to a prototype with 1.5 m diameter and 8.2 m length. It was loaded to a prototype load of 360 kN, heated by up to 18℃, followed by loading to failure. A pile of 63.5 mm diameter and 533.4 mm length was tested in dry Nevada Sand, which corresponded to a prototype with 1.5 m diameter and 12.8 m length. Two tests were performed, in Test 1, it was loaded to a prototype load of 1270 kN (load controlled), then heated up by 10℃; in Test 2, it was loaded to a prototype load of 1350 kN (stiffness controlled), then heated up by 10℃. A series of tests were conducted on two piles: Pile 1 had a diameter of 63.5 mm and a length of 342.9 mm, which corresponded to a prototype with 1.5 m diameter and 8.2 m length; Pile 2 also had a diameter of 63.5 mm, but with a length of 533.4 mm, which corresponded to a prototype with 12.8 m length. The tests involved both piles founded in Bonny Silt and Nevada, loaded to up to a prototype load of 2400 kN, and heated up by up to 18℃.	• For the friction piles founded in Nevada Sand, the strains observed upon heating were similar to the free strains suggesting that the restraints acting on the pile from the soil were limited, the increase in pile capacity hence was also limited. On the other hand, the friction piles founded in Bonny Silt showed an increase in pile capacity upon heating and larger thermally-induced axial loads were observed. The authors explained that this was caused by the larger initial radial stresses in the Bonny Silt induced by compaction. • Thermally-induced axial loads were larger in end-bearing piles than in friction piles due to the restraint imposed at the pile toe.
Wang et al. (2011); Wang et al. (2012)	g	This study involved a pile of 25.4 mm diameter tested in two different soils: silica fine sand and silica flour. The pile was subjected to displacement-controlled loading and unloading cycles before and after heating up the pile by 18℃ − 22℃ in order to assess the effects of heating on the pile capacity. This study involved a pile of 25.4 mm diameter founded in silica fine sand, which was subjected to displacement controlled load and unload cycles before and after thermal cycles of 20℃ and 40℃ heating, in order to assess the effects of heating on the pile capacity.	• The authors reported a reduction in pile capacity and shaft resistance upon heating. • The reduction in shaft resistance increases with increasing heating. • A shaft resistance reduction of up to 50% was reported as the pile was heated up. • The authors attributed the reduction in shaft resistance due to the migration of moisture away from the pile when it was heated, and back to the pile when it was cooled. However, not much evidence was provided to prove this reason.

Table 3.2 (continued)

Kalantidou et al. (2012); Yavari et al. (2014); Nguyen et al. (2016); Yavari et al. (2016); Nguyen et al. (2020)	g	This study involved a pile of $20\ mm$ diameter and $600\ mm$ length founded in dry Fontainebleau Sand. Four tests on the pile were performed, where the pile was loaded to $0, 200, 400$ and $500\ N$, respectively, then two heating and cooling cycles with amplitude of $25℃$ were applied.	• When thermal loads were applied on the pile while it was subjected to a mechanical load which was below 40% of its ultimate capacity, elastic response was reported, demonstrating thermoelasticity. • Irreversible settlements were reported when thermal cycles were applied while the pile was subjected to loads exceeding 40% of its ultimate capacity, demonstrating thermoplasticity.
		This study involved a pile of $20\ mm$ diameter and $600\ mm$ length founded in dry Fontainebleau Sand. Seven tests on the pile were performed: in Test 1, the pile was mechanically loaded to failure, in Tests 2 to 7, the pile was first loaded to $0, 100, 150, 200, 250$ and $300\ N$, respectively, then two thermal cycles of $5 - 35℃$ were applied.	
		This study involved a pile of $20\ mm$ diameter and $600\ mm$ length founded in dry Fontainebleau Sand. Two tests on the pile were performed. In Test 1, thermal cycles of $\pm 1℃$ (heating followed by cooling) were applied when the pile was loaded by $0, 100, 150, 200, 250$ and $300\ N$, while Test 2 was similar to Test 1 except that the pile was unloaded following each thermal cycle.	• The irreversible settlements associated with the application of thermal cycles were reported to be more significant than the effects of creep. • The maximum thermal cumulating settlement of the pile head was reported to be 0.25% of the pile diameter. • More than 70% of the applied mechanical load was resisted at the pile toe.
		This study involved a pile of $20\ mm$ diameter and $600\ mm$ length founded in Kaolin. Six tests on the pile were performed, in Test 1, the pile was mechanically loaded to failure, in Tests 2 to 6, the pile was first loaded to $100, 150, 200, 250$ and $300\ N$, respectively, then a thermal cycle of $\pm 5℃$ (heating followed by cooling) was applied before unloading.	
		This study involved a pile of $20\ mm$ diameter and $600\ mm$ length founded in Kaolin. Five tests on the pile were performed. In Test 1, the pile was mechanically loaded to failure in order to identify its ultimate capacity, which was determined to be $500\ N$. In Tests 2 to 5, the pile was loaded to $0\%, 20\%, 40\%$ and 60% of its ultimate capacity, respectively, then 30 thermal cycles of $\pm 1℃$ were applied before unloading.	• Irreversible settlements were induced in the first few thermal cycles, while those induced by subsequent thermal cycles were negligible.

Table 3.2 (continued)

Ng et al. (2014); Ng et al. (2015)	$40g$	Two piles of $22\,mm$ diameter and $420\,mm$ length were tested, which corresponded to prototypes with $880\,mm$ diameter and $16.8\,m$ length. Pile 1 was founded in Kaolin with an overconsolidation ratio (OCR) of 1.7, while Pile 2 was founded in Kaolin with an OCR of 4.7. The piles were loaded to a factor of safety of 2.5 (which corresponded to a prototype load of $96\,kN$ for Pile 1 and $192\,kN$ for Pile 2), then subjected to five thermal cycles between $9-36℃$. Three piles of $22\,mm$ diameter and $600\,mm$ length were tested in Toyoura Sand, which corresponded to prototypes with $880\,mm$ diameter and $24\,m$ length. Pile 1 and 2 were heated up by $15℃$ and $30℃$, respectively, followed by loading to failure, while Pile 3 was first loaded to a prototype load of $835\,kN$, then heated up by $30℃$, followed by loading to failure.	• For the two piles that were founded in Kaolin, a ratcheting settlement pattern with reducing severity was observed during the thermal cycles. After five thermal cycles, a settlement of 3.8% and 2.1% of the pile diameter were recorded for the piles founded in lightly and heavily overconsolidated Kaolin, respectively. • The authors attributed the larger settlement observed in the lightly overconsolidated clay (Kaolin) to the thermally accelerated creep and more pronounced plastic contraction at the pile-soil interface, leading to lower radial stresses and shaft resistance. On the other hand, plastic contraction is less significant in clays with higher OCR. • The ratcheting settlement pattern observed demonstrated irreversible settlements, hence thermoplasticity, which could be a serviceability issue in the long term. • For the piles that were founded in Toyoura Sand, the pile capacities increased by 13% and 30% when heated up by $15℃$ and $30℃$, respectively. For the pile that was heated up by $15℃$, the increase in pile capacity was mainly contributed by an increase in shaft resistance; whereas for the pile that was heated up by $30℃$, it was mainly contributed by an increase in base resistance, due to a larger downward thermal expansion. • As the pile temperature increased, the null point of the pile (which was below the pile mid-depth) shifted downwards due to an increasing mobilisation of base resistance.

Table 3.2 (continued)

3.4.1 Tests at Chongqing University, Chongqing, China

Wang et al. (2017) reported the physical tests performed on four model thermo-active piles at Chongqing University, China. The thermo-active piles were $104\ mm$ in diameter, $1400\ mm$ in length and founded in dry Nanjing sand. The piles differ from one another in terms of the heat exchanger pipe arrangement, where Pile 1 and 2 had a single U-loop, Pile 3 had a spiral and Pile 4 had a W-loop arrangement. Pile 2 was set up just to determine the ultimate capacity of the pile (which was $19\ kN$), therefore further tests focused on Piles 1, 3 and 4. Thermocouples, pressure transducers, dial indicators and strain gauges were installed in order to measure pile head displacements, earth pressures, strains and temperatures throughout the tests.

The tests on Piles 1, 3 and 4 consisted of mechanically loading the pile up to $10\ kN$ (which corresponded to around 50% of the ultimate capacity), followed by the application of three thermal cycles (which involved heating up the pile by circulating fluid of $55℃$ through the pipes, followed by natural recovery, cooling down the pile by circulating fluid of $4℃$, and natural recovery again). The average temperatures measured for the three piles over the three thermal cycles are shown in Figure 3.13 (Wang et al., 2017). It can be observed that Pile 4 (with W-loop pipe arrangement) was subjected to the largest temperature change, up to $+31℃$, followed by Pile 3 (with spiral pipe arrangement), up to $+24℃$, and Pile 1 (with single U-loop arrangement), up to $+21℃$.

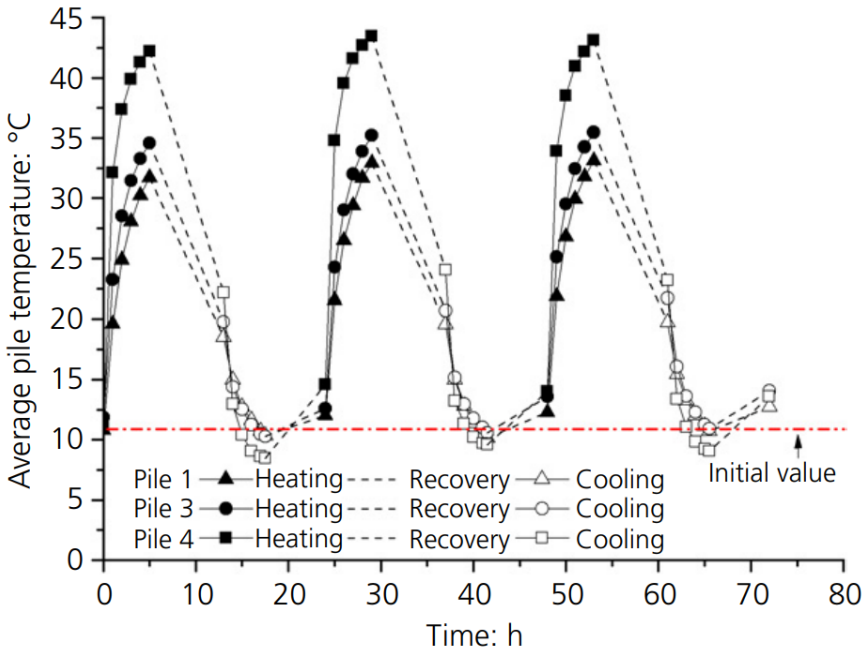


Figure 3.13 Average temperatures measured for Pile 1, 3 and 4 over the three thermal cycles (Wang et al., 2017)

The pile head displacements measured during the three thermal cycles are shown in Figure 3.14 (Wang et al., 2017), note that upwards is taken as positive. It can be observed that while heating the pile resulted in pile head heaving, cooling the pile resulted in pile head settlements. Moreover, irreversible displacements were recorded in all the tested piles following the application of each thermal cycle: after three thermal cycles, the irreversible settlements for Pile 1, 3 and 4 were 0.34%, 0.43% and 0.56% of their diameters, respectively, demonstrating thermoplasticity. The larger settlements observed in Pile 4 are consistent with the fact that it had been heated up to higher temperatures, as demonstrated in Figure 3.13. Wang et al. (2017) commented that such results are coherent with those shown by Kalantidou et al. (2012), Yavari et al. (2014), Nguyen et al. (2016), Yavari et al. (2016) and Nguyen et al. (2020), who demonstrated that when the pile was subjected to mechanical loads exceeding 40% of its ultimate capacity, irreversible displacements would be obtained. Another observation from Figure 3.14 is that the heave and settlements of the pile head measured during each thermal cycle increased progressively with the number of thermal cycles applied. The authors attributed such behaviour to the plastic contraction of the soil, but no further explanations or evidence had been provided. Moreover, Wang et al. (2017) also measured the horizontal earth pressure and the observed thermal strains during the tests, which are not shown here for brevity as both

quantities almost completely recovered to their original values following the application of each thermal cycle.

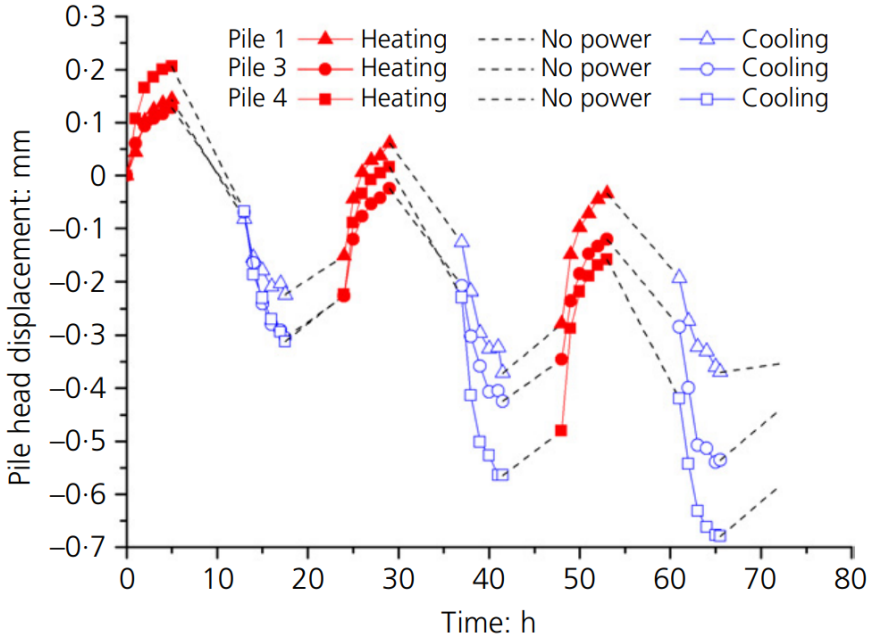


Figure 3.14 Pile head displacements measured for Pile 1, 3 and 4 over the three thermal cycles (Wang et al., 2017)

3.4.2 Tests at Hohai University, Nanjing, China

Huang et al. (2018) reported the physical tests performed on four model aluminium thermo-active piles at Hohai University, China. The piles were 50 mm in diameter, 900 mm long and founded in a saturated sandy soil. The authors highlighted that the coefficient of thermal expansion of aluminium is approximately three times higher than that of concrete and as a result, thermally-induced pile-soil interactions were likely to be overestimated. The piles were instrumented with strain gauges and thermocouples in order to measure strains and temperatures.

Four tests were carried out where fluids of 5℃, 15℃, 35℃ and 50℃, respectively, were circulated through the heat exchanger pipes followed by the application of mechanical loading. The resulting load-displacement curves are shown in Figure 3.15 (Huang et al., 2018), where it can be observed that the capacity of the piles increased with increasing temperature, and such conclusion is coherent with those suggested by most studies summarised in Table 3.2. The authors attributed this to the increase in radial stress following the heating expansion, which increased the shaft resistance.

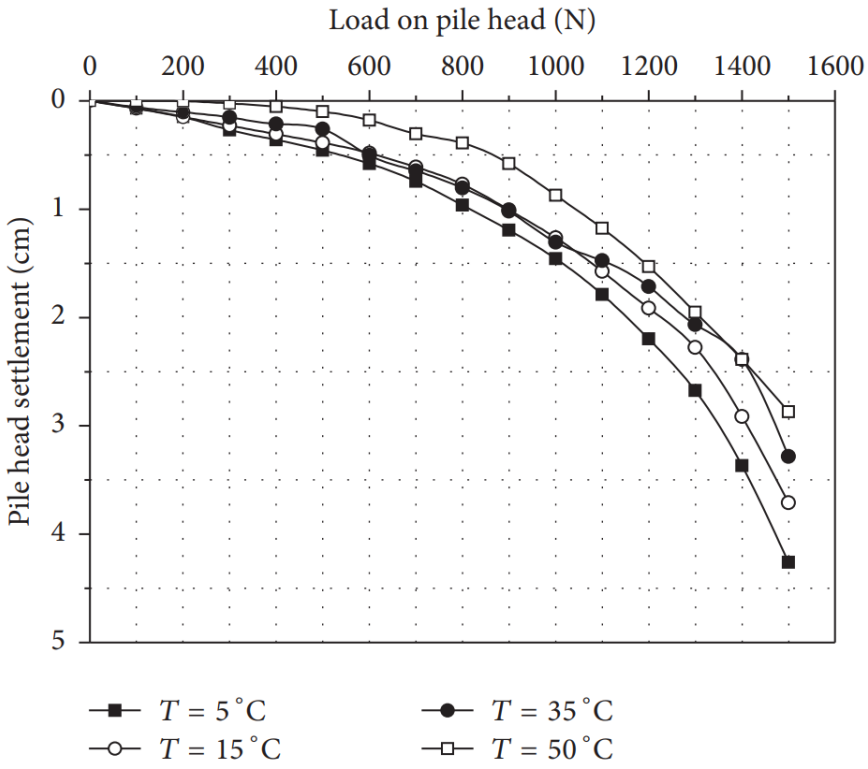


Figure 3.15 Load-displacement curves when the piles were heat up to different temperatures (Huang et al., 2018)

Figure 3.16(a) and Figure 3.16(b) show the thermally-induced shaft resistance when the piles were heated (to 50°C) and cooled (to 5°C), respectively (Huang et al., 2018). It can be observed that when the pile was heated and expanded, thermally-induced shaft resistance acted downwards in the upper part of the pile, while in the lower part, the resistance acted upwards. The opposite happened when the pile was cooled. The authors did not comment on the location of the null point, but pointed out that the observed patterns of thermally-induced shaft resistance were very similar to those observed in Bourne-Webb et al. (2009).

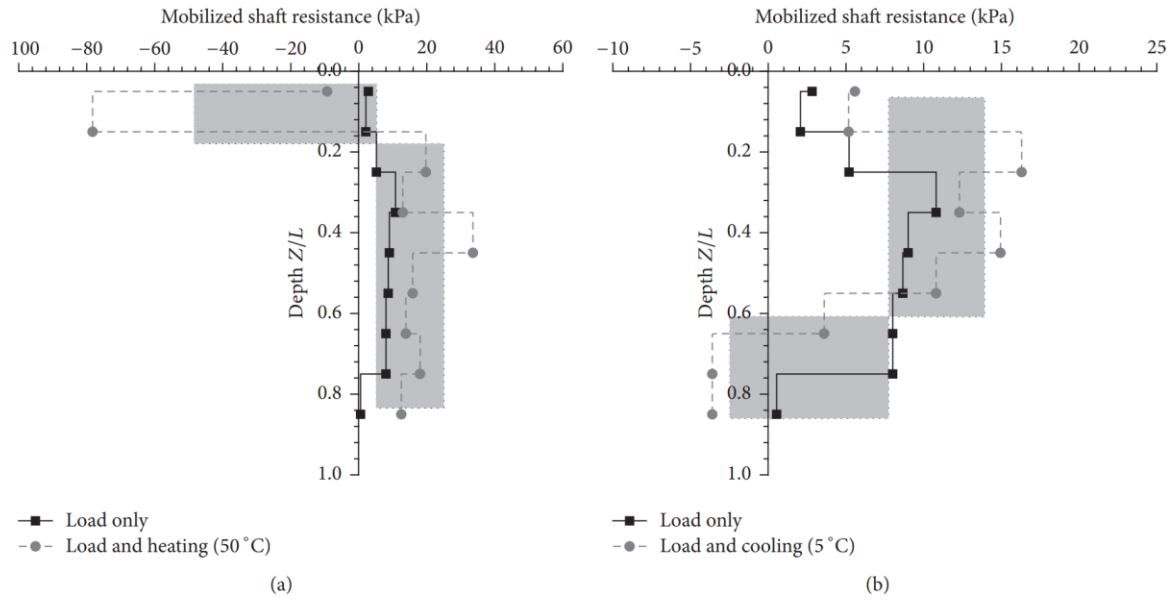


Figure 3.16 Shaft resistance profiles (shaded area represents thermally-induced shaft resistance) when the pile was (a) heated and (b) cooled (Huang et al., 2018)

Another test reported by Huang et al. (2018) involved mechanically loading the pile to a working load (the magnitude of which was not reported), followed by heating the pile to 35℃, natural recovery, cooling the pile to 5℃, and natural recovery to ambient temperature (15℃). The resulting pile head displacement curve is shown in Figure 3.17 (Huang et al., 2018), where, following the pile heaving during heating and pile settlement during cooling, irreversible settlement can be observed upon completion of the thermal cycle. This demonstrates thermoplasticity and the authors attributed this to the contraction of soil during the thermal cycles, but no further explanations or evidence were provided. As both the working load and ultimate capacity of the pile were not reported, it is not possible to conclude whether the observations agree with those made by Kalantidou et al. (2012), Yavari et al. (2014), Nguyen et al. (2016), Yavari et al. (2016) and Nguyen et al. (2020), where irreversible displacements would result should the pile be loaded beyond 40% of its ultimate capacity.

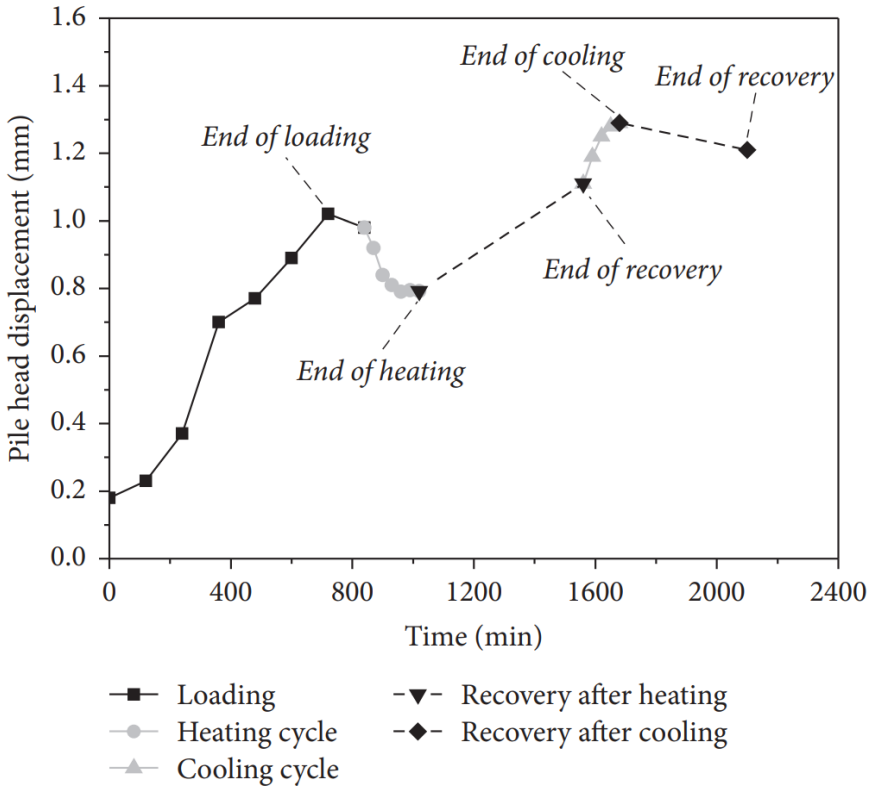


Figure 3.17 Pile head displacement curve for the pile subjected to a thermal cycle following mechanical loading (Huang et al., 2018)

3.5 NUMERICAL STUDIES

Compared to field and laboratory studies, numerical studies have the advantage that analyses can be conducted in a much shorter timescale at much lower costs. Numerical studies also allow the long-term responses of piles, as well as the effects of different variables, such as pile geometry, soil properties and boundary conditions, to be investigated. Numerical studies reported in the literature can mainly be classified into two approaches: load-transfer method (which is also known as t-z method) and finite-difference (FD)/finite-element (FE) modelling.

The load-transfer method is a simple numerical method which involves discretising the pile into elements along its length. Springs are adopted between the elements, in order to represent the pile axial stiffness, as well as attached to each element in order to model the pile-soil interaction, this is illustrated in Figure 3.18 (Kraft et al., 1981). Load-transfer (t-z) functions, which can vary in complexity, from linear elastic to nonlinear elasto-plastic (Bailie, 2013), are then prescribed to the springs which define their load (t)-displacement (z) relationship. The limitations of the load-transfer method are that, firstly, the load-transfer relationship is

dependent on many factors, such as pile geometry and soil profile, and are therefore empirically based. However, the empirical data available for thermo-active piles are limited. Secondly, the load-transfer method inherently assumes that the soil surrounding the pile is thermally inert (i.e. its behaviour is independent of temperature) (Gawecka, 2017).

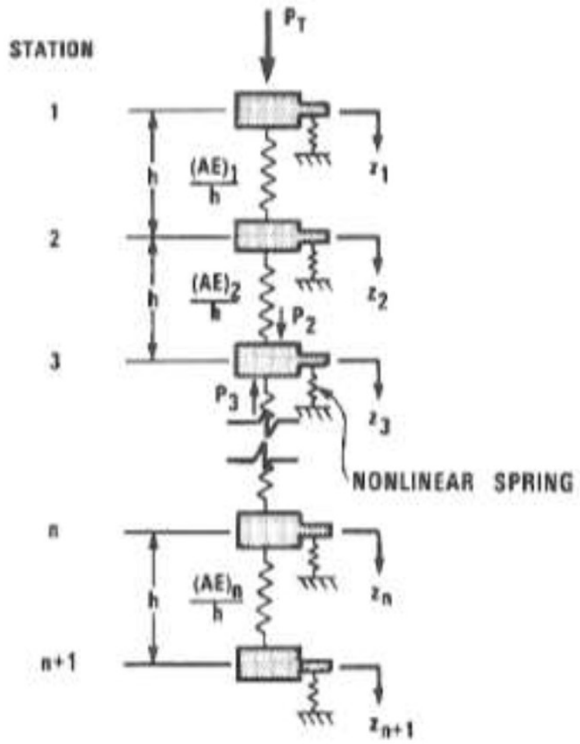


Figure 3.18 Illustration of the load-transfer method (Kraft et al., 1981)

On the other hand, finite-difference (FD) or finite-element (FE) modelling involve discretising both the pile and its surrounding soil, and allow analyses with different levels of complexity, from simple mechanical analyses to fully coupled thermo-hydro-mechanical (THM) analyses, which allow the simulation of the complex THM interactions between the thermo-active pile and the surrounding soil. Advanced soil models can also be adopted in order to simulate the behaviour of soil when subjected to changes in temperatures. Moreover, recent developments (e.g. Rotta Loria and Laloui (2016) and Gawecka et al. (2020)) allow the explicit modelling of the circulation of a hot/cold fluid through heat exchanger pipes, and the associated heat transfer to the surrounding thermo-active pile and soil.

Table 3.3 shows a summary of the numerical studies that were conducted to investigate the thermo-mechanical behaviour of thermo-active piles, with the references, type of numerical analyses (load-transfer method, FD or FE modelling), pile geometry and soil type presented in

a chronological order. Note that, from the studies presented in Table 3.3, those that were conducted before 2017 had been reviewed and discussed in Gawecka (2017), while the studies by Gawecka et al. (2017) and Zito et al. (2021) are selected to be reviewed in detail in Sections 3.5.1 and 3.5.2, respectively.

References	Type of numerical analyses	Pile geometry	Soil type
Knellwolf et al. (2011); Péron et al. (2011); Mimouni and Laloui (2014)	Load-transfer method	Pile diameter: $500\ mm$ Pile length: $10\ m$	Unspecified
Ouyang et al. (2011); Ouyang (2014)	Load-transfer method	Pile diameter: $600\ mm$ Pile length: $23\ m$	$2\ m$ of made ground, followed by $2\ m$ of River Terrace Deposits, then London Clay
GSHPA (2012)	Load-transfer method	Pile diameter: $600\ mm, 900\ mm$ and $1200\ mm$ Pile length: $10 - 30\ m$	London Clay
Suryatriyastuti et al. (2012); Suryatriyastuti (2013); Suryatriyastuti et al. (2014a); Suryatriyastuti et al. (2014b); Suryatriyastuti et al. (2016)	FD modelling	A pile with a square cross-section with $600\ mm$ sides Pile length: $15\ m$	Very loose sandy soils
Abdelaziz (2013); Abdelaziz and Ozudogru (2016)	Load-transfer method and FE modelling	Pile diameter: $250 - 500\ mm$ Pile length: $10\ m$	Homogeneous, isotropic saturated clay

Table 3.3 A summary of numerical studies conducted to investigate the thermo-mechanical behaviour of thermo-active piles, which includes contributions from Gawecka (2017)

Bailie (2013)	Load-transfer method	Pile diameter: 600 mm Pile length: 23 m	2 m of made ground, followed by 2 m of River Terrace Deposits, then London Clay
Bodas Freitas et al. (2013)	FE modelling	Pile diameter: 1000 mm Pile length: 30 m	Moderately overconsolidated clay
Burlon et al. (2013)	Load-transfer method	A pile with a square cross-section with 600 mm sides Pile length: 15 m	12 m of fine soil followed by 3 m of granular soil
Suryatriyastuti et al. (2013)	FD modelling	Pile diameter: 600 mm Pile length: 15 m	Fully saturated sandy soil
Suryatriyastuti (2013); Suryatriyastuti et al. (2014b)	Load-transfer method	A pile with a square cross-section with 600 mm sides Pile length: 15 m	Very loose sandy soils
Dupray et al. (2014)	FE modelling	A 7×15 pile group with pile diameters of 800 mm and pile lengths of 20 m	Low permeability clayey soil
Hassani Nezhad Gashti et al. (2014)	FE modelling	Pile diameter: 220 mm Pile length: 20 m	Clay
Jeong et al. (2014)	FE modelling	3×3 and 5×5 pile groups with pile diameters of 500 mm and pile lengths of 20 m	Sand and clay

Table 3.3 (continued)

Olgun et al. (2014a)	FE modelling	Pile diameter: $600\ mm$ Pile length: $20\ m$	Unspecified
Olgun et al. (2014b)	FE modelling	Pile diameter: $600\ mm$	Clay
Pasten and Santamarina (2014)	Load-transfer method	Pile diameter: $1000\ mm$ Pile length: $20\ m$	Unspecified
Batini et al. (2015)	FE modelling	Pile diameter: $900\ mm$ Pile length: $9\ m, 18\ m$ and $36\ m$	$12\ m$ of soft clay, followed by $9.6\ m$ of soft sandy gravelly clay, then $3.6\ m$ of stiff sandy gravelly clay and $0.6\ m$ of moderately weak sandstone
Di Donna and Laloui (2015)	FE modelling	Pile diameter: $800\ mm$ Pile length: $20\ m$	Normally consolidated clay
		A 7×3 pile group with pile diameters of $800\ mm$ and pile lengths of $20\ m$	
Ozudogru et al. (2015)	FE modelling	Pile diameter: $600\ mm$ Pile length: $20\ m$	Unspecified
Rotta Loria et al. (2015)	FE modelling	Pile diameter: $880\ mm$ Pile length: $19.6\ m$	Saturated Toyoura sand

Table 3.3 (continued)

Salciarini et al. (2015)	FE modelling	Pile groups with $8-9$ piles with pile diameters of $1000\ mm$ and pile lengths of $25\ m$	$4\ m$ of medium-dense sand, followed by $11\ m$ of overconsolidated clay, then dense sand with gravel
Bourne-Webb et al. (2016)	FE modelling	Pile diameter: $1000\ mm$ Pile length: $15\ m, 30\ m$ and $45\ m$	Moderately overconsolidated clay
Di Donna et al. (2016)	FE modelling	A pile group with 4 piles with pile diameters of $900\ mm$ and pile lengths of $28\ m$	$8.6\ m$ of alluvial soil, followed by $8\ m$ of sandy-gravelly moraine, then $3.5\ m$ of bottom moraine and molasse
Fuentes et al. (2016)	FD modelling	Pile diameter: $1000\ mm$ Pile length: $25\ m$	Low permeability clay
Gawecka et al. (2016)	FE modelling	Pile diameter: $1000\ mm$ Pile length: $30\ m$	London Clay
Ng et al. (2016)	FE modelling	Pile diameter: $600-1750\ mm$ Pile length: $20-35\ m$	Dry Toyoura sand
Tsetoulidis et al. (2016)	FE modelling	A 3×3 pile group with pile diameters of $600\ mm$ and pile lengths of $23\ m$	$1.5\ m$ of made ground, followed by $4\ m$ of River Terrace Deposits, then London Clay

Table 3.3 (continued)

Gawecka et al. (2017)	FE modelling	Pile diameter: 600 mm Pile length: 23 m	1.5 m of made ground, followed by 2.5 m of Terrace Gravel, then London Clay
Vieira and Maranha (2017)	FD modelling	Pile diameter: 600 mm Pile length: 20 m	Normally consolidated saturated Kaolin
Adinolfi et al. (2018)	FE modelling	Pile diameter: 600 mm and 800 mm Pile length: 23 m and 11.4 m	4 m of made ground and river deposits, followed by London Clay; 3.55 m of pozzolanas, followed by saturated Neapolitan yellow tuff
Rammal et al. (2018)	FE modelling	A pile with a square cross-section with 410 mm sides Pile length: 12 m	2.7 m of silty soil, followed by sandy soil
Georgiadis et al. (2020)	FE modelling	Pile diameter: 750 − 1500 mm Pile length: 10 − 40 m	Sand
Bourne-Webb et al. (2020); Zito et al. (2021)	FE modelling	Pile diameter: 1000 mm Pile length: 30 m	Moderately overconsolidated clay

Table 3.3 (continued)

3.5.1 Numerical study by Gawecka et al. (2017)

The numerical study conducted by Gawecka et al. (2017) involved employing coupled thermo-hydro-mechanical (THM) finite-element (FE) analyses to analyse the thermo-mechanical behaviour of thermo-active piles using the Imperial College Finite Element Program (ICFEP) (Potts & Zdravkovic, 1999; Potts & Zdravkovic, 2001; Cui, 2015). The study consisted of two

parts: the first part consisted of a back-analysis of the Lambeth College thermo-active pile test (Bourne-Webb et al., 2009), which demonstrated the capability of the modelling method by closely reproducing the measured temperatures, displacements, strains and stresses, and are therefore not explained here in detail for brevity; the second part of the study involved a parametric study which investigated the effects of:

- employing coupled thermo-mechanical (TM) or pure mechanical (M) analyses rather than coupled THM analyses (Analyses B1 and B2);
- applying a heat flux rather than a uniform temperature change over the volume of the pile (Analysis C);
- soil thermal conductivity (Analyses D1 and D2); and
- soil permeability (Analyses E1 and E2).

Following successful back-analysis of the Lambeth College pile test in the first part of the numerical study, the same modelling techniques were employed in the parametric study, where the pile geometry and soil profile from the Lambeth College pile test were adopted, with the pile modelled to have a constant diameter of $550\ mm$ and a length of $23\ m$, while the ground profile consisted of $1.5\ m$ of made ground, $2.5\ m$ of Terrace Gravel, $60\ m$ of London Clay, $15\ m$ of Lambeth Group Clay, $5\ m$ of Lambeth Group Sand and $10\ m$ of Thanet Sand. The concrete pile was modelled as a linear elastic material, the made ground as a linear elasto-plastic material with a Mohr-Coulomb failure surface, and the rest of the soil layers as nonlinear elasto-plastic materials, coupled with the Imperial College Generalised Small-Strain Stiffness (IC.G3S) model (Measham et al., 2014; Taborda et al., 2016). Appropriate parameters were prescribed to each soil layer, and the London Clay and Lambeth Group Clay were modelled as consolidating materials. The modelling procedures involved loading the pile to $1200\ kN$, followed by six months of pile cooling by $-15℃$ (to $4.5℃$), then six months of pile heating by $15℃$ (to $34.5℃$). Unless otherwise specified, heating/cooling of the pile was achieved by applying a uniform temperature change over the volume of the pile at a rate of $0.05℃$ per day. Note that only Analyses B1, B2 and C are selected to be discussed in detail here, with the remaining being described in detail, together with the associated thermal, hydraulic and displacement boundary conditions, in Gawecka et al. (2017).

The set of analyses in the parametric study which involved Analyses A, B1 and B2 (Analysis A was the reference analysis, which was coupled THM) investigated the effects of decoupling consolidation (Analysis B1), and both consolidation and heat transfer (Analysis B2),

respectively. Figure 3.19 compares the evolution of maximum thermally-induced axial stress for the three analyses (Gawecka et al., 2017) – note that compression was taken as positive. Referring to the results from Analysis A, when the pile was cooled, tensile stresses were induced as the surrounding soil restricted the contraction of the pile. However, with time, as the surrounding soil cooled down as well and contracted, the restriction acting on the pile reduced, which explained the observed decrease in thermally-induced tensile stresses with time. Very similar behaviour can be observed when the pile was heated. For Analysis B1 where consolidation was not simulated, the modelled thermally-induced axial stresses were very similar to those from Analysis A initially, but as time progressed and a larger volume of soil was cooled/heated and contracted/expanded, the restriction acting on the pile reduced by a larger extent compared to the situation in Analysis A. This was because excess pore water pressure was responsible for the contraction/swelling of the London Clay, and in Analysis B1, although excess pore water pressures were generated (which led to the contraction/swelling of soil to reduce the restriction acting on the pile), no dissipation was allowed (which could reduce the extent to which the soil contracts/swells, and hence the reduction in restriction). For Analysis B2, where neither consolidation nor heat transfer were modelled, the thermally-induced axial stresses obtained were overestimated by up to 78%. The reason for that was that the soil was not cooled/heated, so no volume change took place and the restriction acting on the contracting/expanding pile did not reduce. This set of analyses therefore demonstrated the importance of the coupling between the thermal, hydraulic and mechanical systems in a numerical analysis.

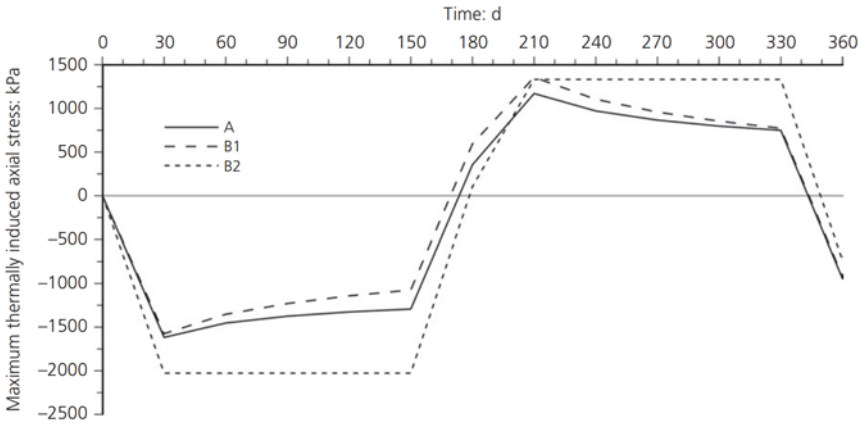


Figure 3.19 Comparison of the evolution of maximum thermally-induced axial stress for Analyses A, B1 and B2 (Gawecka et al., 2017)

The set of analyses in the parametric study which involved Analyses A and C investigated the effects of the method of thermal loading application. In Analysis C, rather than prescribing a uniform temperature change to the pile, a heat flux over the volume of the pile was prescribed, and the magnitude of heat flux chosen was such that the temperature at the circumference of the pile at the end of both cooling and heating (corresponding to 150 and 330 days, respectively) were equal to those in Analysis A, which is illustrated in Figure 3.20 (Gawecka et al., 2017). Figure 3.21 compares the evolution of maximum thermally-induced axial stress for both analyses (Gawecka et al., 2017), where it can be observed that the thermally-induced axial stress was larger in Analysis C, but remained relatively constant with time compared to those obtained in Analysis A. Not much explanation was given in Gawecka et al. (2017) for such behaviour, but it is expected that the larger thermally-induced axial stress obtained in Analysis C was due to the fact that the average temperature change of the pile in Analysis C was larger than that in Analysis A, hence the pile in Analysis C was subjected to greater contraction and expansion. This is because when the pile was heated up by the application of a uniform heat flux over the volume of the pile, the centre of the pile should be subjected to larger temperature changes compared to its circumference (which in the current case was used to match with those from Analysis A to determine the applied heat flux). On the other hand, since the applied heat flux was constant from 0 to 150 days, and from 150 to 330 days, the temperature changes, and hence pile contraction/expansion, were continuously varying within both periods, as reflected in Figure 3.20. The continuous pile contraction/expansion and the resulting thermally-induced axial stresses could have balanced the reduction in restriction from the soil as heat transfer took place with time, which explained why the thermally-induced axial stresses appeared to remain constant with time in Analysis C. This set of analyses demonstrated that the choice of the modelling technique in numerical studies is very important and could have a significant impact on the modelled results.

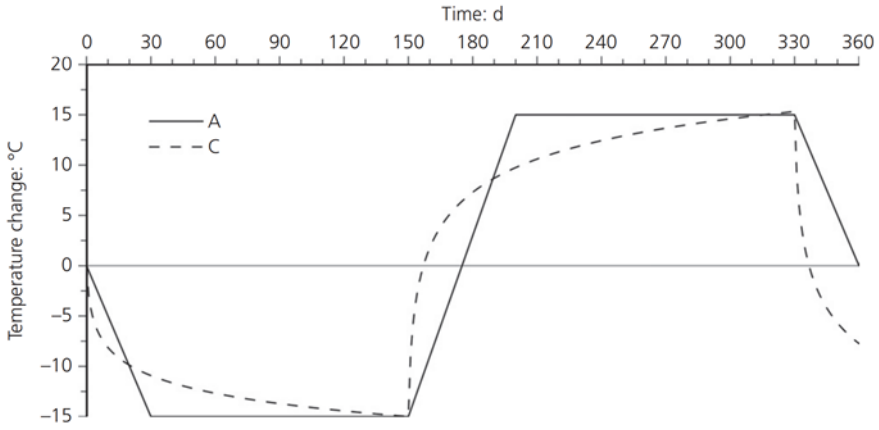


Figure 3.20 Comparison of temperatures at the circumference of the pile for Analyses A and C (Gawecka et al., 2017)

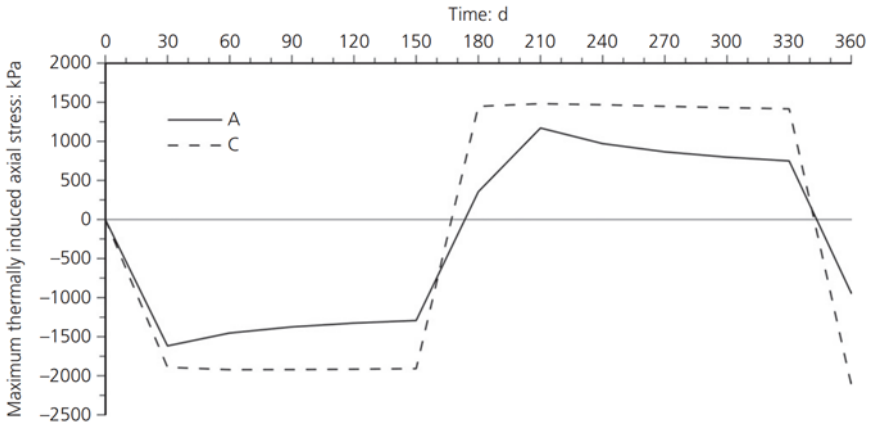


Figure 3.21 Comparison of the evolution of maximum thermally-induced axial stress for Analyses A and C (Gawecka et al., 2017)

3.5.2 Numerical study by Zito et al. (2021)

The numerical study conducted by Zito et al. (2021) involved performing axisymmetric thermo-mechanical (TM) finite-element (FE) analyses using ABAQUS on a single thermo-active pile, but using different mesh (or domain) sizes, with the aim of highlighting the importance of choosing the correct mesh size when conducting FE analyses in order to avoid interactions with the mesh boundaries.

The pile modelled was 1000 mm in diameter and 30 m long, and two different mesh sizes were considered: one with its vertical boundary located 30 m from the pile centre-line, while the other one was located at only 4 m from the pile centre-line, both meshes were 90 m deep. For both meshes, the bottom boundary was restricted in both vertical and horizontal directions,

while the cylindrical boundary was only restricted in the horizontal direction. A constant temperature of 14℃ was prescribed at the bottom boundary while an adiabatic condition was prescribed at the cylindrical boundary. A harmonic temperature T given by Equation (3.7) with $\Delta T = 11℃$ was prescribed at the ground surface. The pile was modelled as a linear elastic material, while the soil was modelled as a linear elastic perfectly plastic material with a Tresca type failure surface. Note that the Young's modulus of the soil was modelled to be increasing with depth. For the modelling procedures, the pile was mechanically loaded to $3500\ kN$, then 10 years of thermal loading was applied, where the harmonic temperature given by Equation (3.7) with $\Delta T = 12℃$ was prescribed to the pile.

$$T = 14℃ + \Delta T \cdot \sin\left(2\pi t - \frac{\pi}{2}\right) \tag{3.7}$$

Figure 3.22 shows the axial load and shaft resistance profiles for the pile in both meshes (or domains) (Zito et al., 2021), where it can be observed that for the pile in the $30\ m$ mesh, the thermally-induced axial stress and shaft resistance due to heating and cooling were almost identical, with the null point located at a depth of $19\ m$ (which is below the pile mid-depth, as expected since the soil stiffness was modelled to be increasing with depth). On the other hand, for the pile in the $4\ m$ mesh, due to the proximity of the cylindrical boundary, the pile settled together with the soil upon mechanical loading, causing reduced relative movement at the pile-soil interface and therefore reduced shaft resistance mobilisation in the upper part of the pile. This led to full mobilisation of both base and shaft resistance in the lower part of the pile. As a result, when the pile was heated, no additional resistance can be mobilised and there was a change in mobilised shaft resistance in the lower part of the pile only upon cooling. This also led to the fact that the null point for heating and cooling were at different depths.

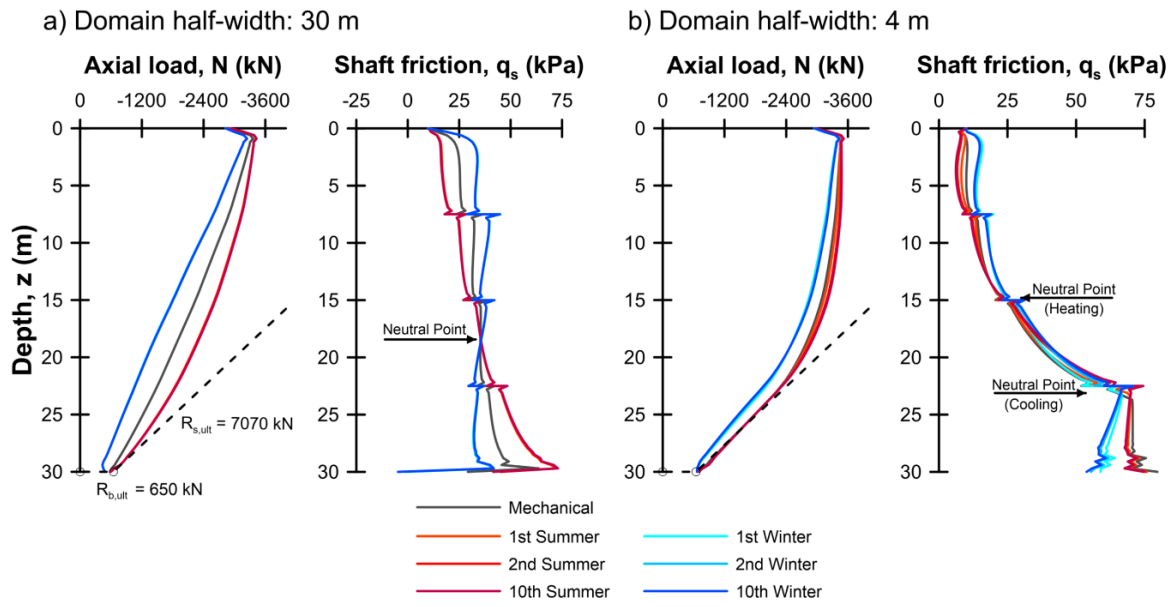


Figure 3.22 The axial load and shaft resistance profiles for the pile in the (a) 30 m mesh and (b) 4 m mesh (Zito et al., 2021)

Figure 3.23 shows the thermally-induced pile head displacement and maximum thermally-induced axial stress with time for the pile in both meshes (Zito et al., 2021). In Figure 3.23(a), it can be observed that for the pile in the 30 m mesh, a regular oscillation of $\pm 2.1\ mm$ was obtained, while for the pile in the 4 m mesh, a ratcheting pattern was observed in the first few cycles, which subsequently stabilised at $+2.6\ mm$ when the pile was heated and $-3.6\ mm$ when the pile was cooled. Similar patterns were displayed on Figure 3.23(b) for maximum thermally-induced axial stress, where for the pile in the 30 m mesh, 460 kN of tension and 400 kN of compression were regularly induced in each thermal cycle, but for the pile in the 4 m mesh, a ratcheting pattern was observed in the first few cycles, followed by stabilisation at 350 kN of tension and 130 kN compression, which was a much more asymmetric response compared to the case in the 30 m mesh.

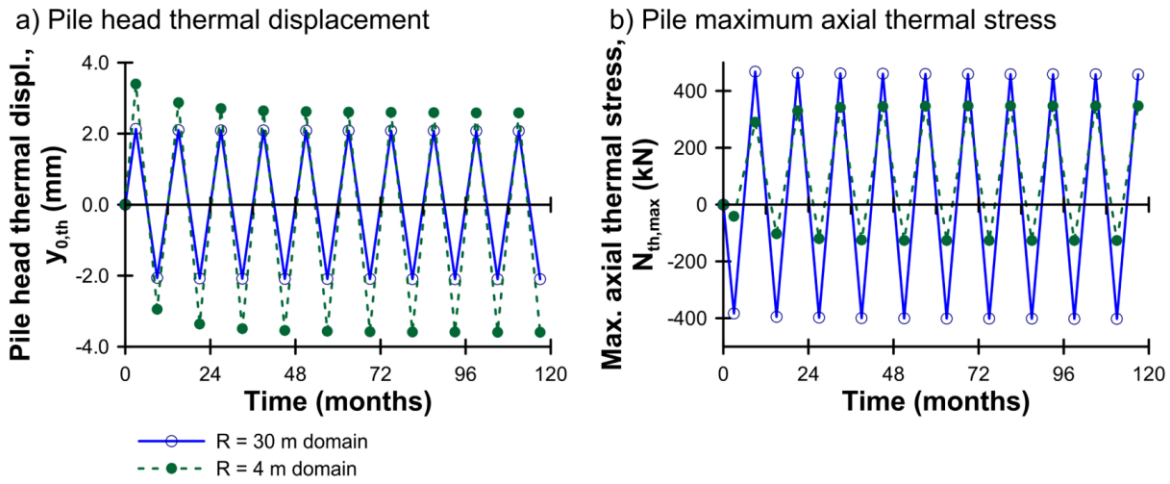


Figure 3.23 The (a) thermally-induced pile head displacement and (b) thermally-induced axial stress with time for the pile in both meshes (Zito et al., 2021)

This numerical study highlighted the fact that it is very important to choose the mesh size for FE analyses carefully, and that the mesh size should be sufficiently large to ensure that there are no interactions between the pile and the mesh boundary; otherwise, the obtained results could be erroneous and would never be representative of an isolated pile.

3.6 CONCLUSIONS

A comprehensive literature review on the thermo-mechanical behaviour of thermo-active piles has been presented in this chapter. First, a simple descriptive framework by Bourne-Webb et al. (2009), Amatya et al. (2012) and Bourne-Webb et al. (2013) to explain the qualitative thermo-mechanical behaviour of thermo-active piles when subjected to thermal and thermo-mechanical loads is presented. The concepts suggested by this framework, which include free thermal axial strain ε_{T-Free}, observed axial strain ε_{T-Obs}, restrained axial strain ε_{T-Rstr}, pile end restraints, and the relationship between them provide a unique insight into predicting the thermal axial force P_T and mobilised shaft resistance q_s profiles when a pile is heated or cooled. It has been found that the thermo-mechanical behaviour of thermo-active piles observed in reviewed field, laboratory and numerical studies are generally coherent with the framework. However, it should be appreciated that this framework has made assumptions which do not reflect how real soils behave, which is where observations from reviewed studies diverge from the framework. For example, the framework assumes that the soil has uniform strength and behaves in an idealised rigid-plastic manner, which means that when the pile is heated or cooled,

it expands or contracts around a null point located at pile mid-depth. In reality, as observed or modelled in various studies reported in the literature (e.g. Gawecka et al. (2017) and Sung et al. (2018)), the null point is usually located below pile mid-depth as the stiffness of soil increases with depth, or due to the presence of a restraint at pile toe.

A comprehensive literature review on field studies on the thermo-mechanical behaviour of thermo-active piles has been conducted. These studies represent very valuable data as they are most representative of reality. The review reveals that the significance of thermally-induced pile axial loads can vary compared to mechanical loads. In Akrouch et al. (2014), the thermally-induced axial loads were insignificant; in Bourne-Webb et al. (2009) and Sutman et al. (2017), they were larger than half of the mechanical loads; while in Laloui et al. (2006), they were three times that of mechanical loads. In addition to that, Bourne-Webb et al. (2009) reported an overall tensile force within the thermo-active pile upon cooling, highlighting the importance of taking thermally-induced loads into account when designing thermo-active piles. It is also found that the presence of stiff bedrock (hence presenting an end restraint to the pile toe) could increase the thermally-induced axial loads in the lower part of the thermo-active pile (Laloui et al., 2006; McCartney & Murphy, 2012; Sutman et al., 2017; Sung et al., 2018). On the other hand, Bouazza et al. (2011) showed that the ultimate capacity of a thermo-active pile is increased after application of heating cycles, as the expansion increases the radial stresses and hence the ultimate shaft resistance. All the thermo-active piles reported in the field studies behave thermo-elastically when subjected to thermal loads, with the exception of the one presented by Abdelaziz (2013), where thermoplasticity was observed, but this is expected as the pile was first loaded to its ultimate capacity before the application of thermal loads. Finally, no thermally-induced structural damage of thermo-active piles has ever been reported, with Sung et al. (2018) reporting that the maximum thermally-induced axial compressive stress observed corresponds to only 10% of the design compressive strength of concrete.

Laboratory studies have also been conducted to study the thermo-mechanical behaviour of thermo-active piles. Compared with field studies, they have the advantages of lower costs, and the fact that tests can be conducted under more controlled conditions, in smaller scales and with shorter timescales. Conclusions from laboratory tests presented in the literature are generally coherent with the observations from field studies. In particular, McCartney et al. (2010), Ng et al. (2014) and Huang et al. (2018) reported increase in pile capacity when the pile is heated, due to an increase in shaft resistance (as a result of the increased radial stresses

associated with pile expansion), which agree with the observations made by Bouazza et al. (2011). However, as opposed to field studies, thermoplastic response following the application of thermo-mechanical loads appears to be more commonly observed in laboratory studies, with Kalantidou et al. (2012) suggesting that thermoplasticity occurs when thermal cycles are applied to piles subjected to mechanical loads exceeding 40% of their ultimate capacities, with such conclusion agreed by Wang et al. (2017).

Finally, a literature review on the numerical studies that have been performed to study the thermo-mechanical behaviour of thermo-active piles has been conducted. Numerical studies can be classified into two main approaches, the load-transfer method and finite-difference (FD)/finite-element (FE) modelling. It has been revealed that the load-transfer method is a simple numerical method that can hardly be accurate in modelling the thermo-mechanical behaviour of thermo-active piles, as the method relies on the load-transfer relationship that is applied to the springs, which is heavily dependent on the limited empirical data for thermo-active piles. FD and FE modelling, on the other hand, allow much more complex fully coupled thermo-hydro-mechanical (THM) analyses, and in addition to that, models with different levels of complexity can be adopted to simulate the behaviour of soils, and recent developments (Rotta Loria & Laloui, 2016; Gawecka et al., 2020) even allow the explicit modelling of heat exchanger pipes. The numerical study conducted by Gawecka et al. (2017) has shown that the heating or cooling of a thermo-active pile is a coupled THM problem. In the study, the effects of decoupling the consolidation and heat transfer components from the analyses were studied, and it has been revealed that the modelled thermally-induced axial stresses can be up to 78% different from those obtained from a coupled THM analysis, highlighting the importance of the coupling between the three systems (thermal, hydraulic and mechanical systems) in a numerical analysis. As a result, the fact that load-transfer method is unable to allow these coupled analyses render the method inferior in simulating this type of problem. On the other hand, it is important to highlight that results obtained from numerical analyses are heavily dependent on the modelling techniques, applied boundary conditions, chosen domain size and other input parameters. It has been shown in Zito et al. (2021) that having an incorrect domain size chosen for an FE analysis can lead to erroneous results.

CHAPTER 4 NUMERICAL MODELLING OF THERMO-ACTIVE PILES

4.1 INTRODUCTION

This chapter presents a numerical study on the thermal performance and thermo-mechanical behaviour of thermo-active piles which are subjected to thermo-mechanical loads. Three-dimensional, fully coupled thermo-hydro-mechanical finite-element analyses are carried out, with the details of the analyses provided in Sections 4.2.1 to 4.2.5. Following the analyses, the thermal performance of the thermo-active piles is analysed and discussed in Section 4.2.6, while the thermo-mechanical behaviour of the thermo-active piles is discussed in Section 4.2.7. Note that the contents of this chapter were published in part or whole in Liu et al. (2019), Liu et al. (2020a), Liu et al. (2020b) and Zdravković et al. (2021).

4.2 THREE-DIMENSIONAL FINITE-ELEMENT MODELLING OF THERMO-ACTIVE PILES

In order to model accurately the thermo-mechanical response when a thermo-active pile is subjected to thermo-mechanical loads, three-dimensional (3D), coupled thermo-hydro-mechanical (THM) finite-element (FE) analyses are conducted using the Imperial College Finite Element Program (ICFEP) (Potts & Zdravkovic, 1999; Potts & Zdravkovic, 2001; Cui, 2015). Moreover, the application of thermal loads (only pile heating is considered in this numerical study) is modelled by the explicit simulation of the circulation of hot water through heat exchanger pipes within the thermo-active pile (see Section 2.6.3 and Gawecka et al. (2020)) .

In order to assess the impacts of pile diameter and arrangement of heat exchanger pipes on the thermo-mechanical behaviour of thermo-active piles, as well as to establish a set of analyses for the verification of the performance of a proposed simplified method to analyse thermo-active piles using axisymmetric analyses (to be introduced in Chapter 5), two different pile diameters ($600\ mm$ and $900\ mm$) and three different pipe arrangements (single U-loop, double U-loop and triple U-loop, which are abbreviated as 1U, 2U and 3U, respectively) are considered, while a pile length of $25\ m$ is adopted.

4.2.1 Mesh, stratigraphy and types of elements

The thermo-active pile modelled is founded in a homogeneous stratigraphy of London Clay, which is similar to that adopted in Gawecka et al. (2016). The size of the adopted domain is 80 m in diameter (which is determined to be sufficient and appropriate based on a parametric study on mesh sizes) and 64 m deep (which corresponds to the bottom of London Clay in the stratigraphy adopted in Gawecka et al. (2017)). The discretisation of the domain is illustrated in Figure 4.1 while the detailed discretisation of the pile cross-section is illustrated in Figure 4.2, note that only half of the mesh is shown in both Figure 4.1 and Figure 4.2 for clarity. It is appreciated that the soil elements adjacent to the pile are quite large to distribute stresses from the pile, smaller elements could have been used which could improve the accuracy of the analyses. Also note that a full section of the mesh is required for the cases of 2U and 3U pipe arrangements, as the heat exchange that takes place through the heat exchanger pipes at discrete locations within the pile cross-section leads to non-symmetric temperature fields, despite the fact that there exists a plane of symmetry in the geometry (see Olgun et al. (2014a)).

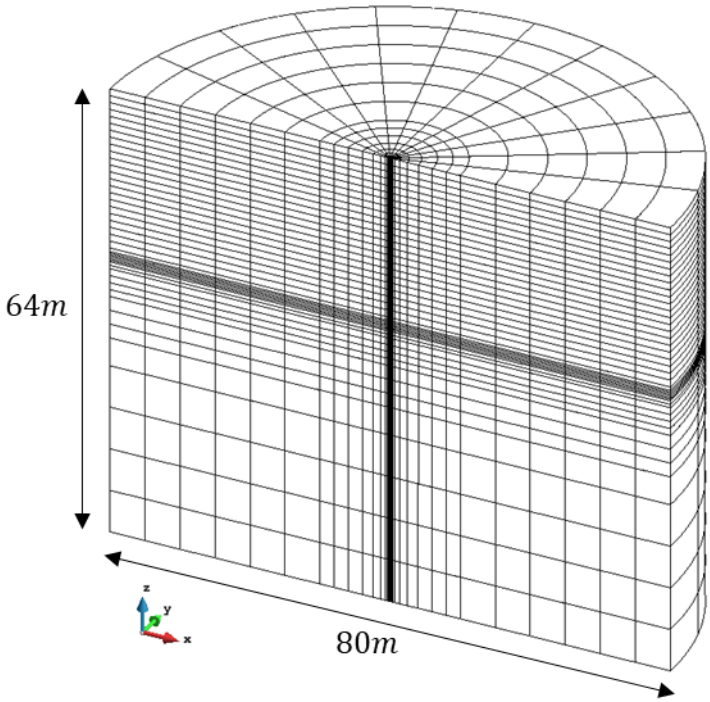


Figure 4.1 Half of the FE mesh

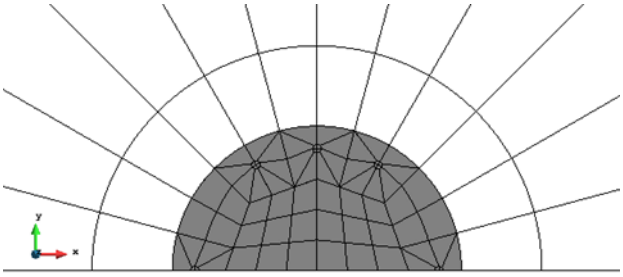


Figure 4.2 Plan view of half of the zoomed-in FE mesh detailing the pile (shaded in grey)

The thermo-active pile and London Clay are discretised using 20-noded isoparametric elements, while the heat exchanger pipes are discretised using one-dimensional (1D) quadratic (3-noded) bar elements (see Section 2.6.3 and Gawecka et al. (2020)). There are three displacement and one temperature degrees of freedom at each node, while a pore water pressure degree of freedom also exists at the corner nodes of the London Clay elements and the end nodes of the bar elements. As explained in Section 2.6.3, in order to model correctly the heat transfer that takes place from the one-dimensional pipes to the surrounding medium, the pipes are surrounded by a thermally enhanced material (TEM), which in this case is modelled in the same way as the pile elements, except that its thermal conductivity is calculated using Equation (2.29) and the volumetric heat capacity is equal to $1\ kJ \cdot m^{-3} \cdot K$, with its cross-sectional area corresponding to that of the inside of the pipe that is simulated ($5.39 \times 10^{-4}\ m^2$ in this case as the internal pipe diameter is $26.2\ mm$, which will be explained in Section 4.2.2). Note that interface elements are not adopted such that full adhesion is modelled between the pile and the soil.

4.2.2 Pipe dimensions and arrangements

The heat exchanger pipes that are modelled in this study are adopted from the ones employed in the thermal response test reported in Loveridge et al. (2014) (which are also adopted in Gawecka et al. (2020)). The adopted concrete cover (the distance between the pipes and the edge of pile) is $70\ mm$, the internal pipe diameter is $26.2\ mm$ (which corresponds to a cross-sectional area of $5.39 \times 10^{-4}\ m^2$) with a pipe wall thickness of $2.9\ mm$, carrying a flow rate of $1.032 \times 10^{-4}\ m^3 \cdot s^{-1}$ for each U-loop (which corresponds to a flow velocity of $0.191\ m \cdot s^{-1}$).

Three different pipe arrangements (1U, 2U and 3U) are considered in this numerical study. The arrangements of the pipes and the way water is circulated in each case are illustrated in Figure

4.3. Note that the pipe that carries water up the pile is always diametrically opposite to that carrying water down the pile (i.e. for the case of 3U pipe arrangement, the pipes at $\theta = 120^o$ and $\theta = 300^o$ form one of the U-loops).

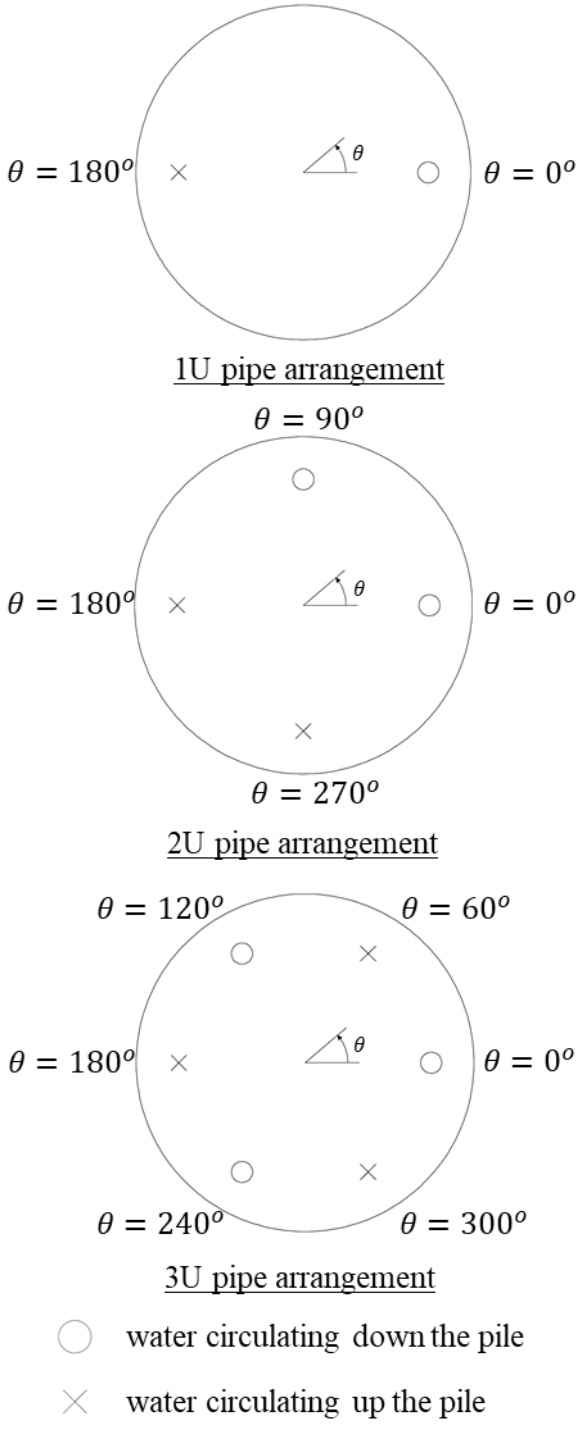


Figure 4.3 Illustration of the 1U, 2U and 3U pipe arrangements

4.2.3 Initial and boundary conditions

As coupled THM analyses are performed, displacement, hydraulic and thermal boundary conditions have to be specified:

- Displacement boundary conditions:
    - The bottom of the mesh is restricted from moving in any direction.
    - The far cylindrical boundary of the mesh is restricted from moving in the radial direction.
- Hydraulic boundary conditions:
    - No change in pore water pressure from the initial conditions on both the top and bottom boundaries of the mesh.
    - No water flow across the far cylindrical boundary of the mesh.
- Thermal boundary conditions:
    - No change in temperature from the initial conditions at all the mesh boundaries, except the top of the pile which is modelled as adiabatic.

As for initial conditions, it is assumed that the ground water table is at the ground surface, with an underdrained pore water pressure profile (which is typical in London and consistent with the adopted nonlinear permeability model (Equation (4.5))), as shown in Figure 4.4(a). An initial ground temperature of 19.5℃ is assumed and the adopted K_0 profile, as shown in Figure 4.4(b), is similar to that adopted in Gawecka et al. (2017).

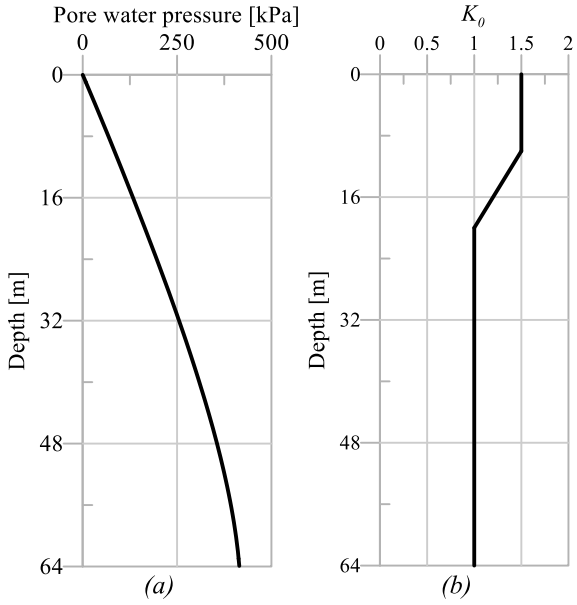


Figure 4.4 (a) Initial pore water pressure profile and (b) K_0 profile

4.2.4 Material models and properties

The London Clay is modelled as a nonlinear elasto-plastic material, with a Mohr-Coulomb failure surface coupled with the Imperial College Generalised Small-Strain Stiffness (IC.G3S) model (Measham et al., 2014; Taborda et al., 2016), which models the reduction of tangent shear modulus G_{tan} with deviatoric strain E_d according to Equation (4.1), and tangent bulk modulus K_{tan} with volumetric strain ε_{vol} according to Equation (4.3), respectively. In Equations (4.1) to (4.4), p' is mean effective stress, p'_{ref} is a reference mean effective stress, G_{ref} is the maximum shear modulus at the reference mean effective stress, $R_{G,min}$ is the minimum normalised value of G_{tan}, $\varepsilon_1, \varepsilon_2$ and ε_3 are the principal strains, K_{ref} is the maximum bulk modulus at the reference mean effective stress, $R_{K,min}$ is the minimum normalised value of K_{tan}, a, b, r and s are stiffness degradation parameters while m_G and m_K are parameters defining the dependence of elastic stiffness on mean effective stress. For the hydraulic behaviour, a nonlinear permeability model given by Equation (4.5) (where k_0 and B are model parameters) is adopted. The material properties adopted for London Clay are reported in Table 4.1, which are identical to those adopted in Gawecka et al. (2017). In Table 4.1, c' is the cohesion, ϕ' is the angle of shearing resistance, ψ' is the angle of dilation, G_{min} is the minimum shear modulus, K_{min} is the minimum bulk modulus, γ_s is the saturated unit weight, α_s is the linear coefficient of thermal expansion of soil skeleton, α_f is the linear coefficient of thermal expansion of pore fluid, K_f is the bulk modulus of pore fluid, ρC_p is the volumetric heat capacity and λ is thermal conductivity.

$$G_{tan} = G_{ref}\left(\frac{p'}{p'_{ref}}\right)^{m_G}\left[R_{G,min} + \frac{1 - R_{G,min}}{1 + \left(\frac{E_d}{a}\right)^b}\right] \tag{4.1}$$

where

$$E_d = \frac{2}{\sqrt{6}}\sqrt{(\varepsilon_1 - \varepsilon_2)^2 + (\varepsilon_2 - \varepsilon_3)^2 + (\varepsilon_1 - \varepsilon_3)^2} \tag{4.2}$$

$$K_{tan} = K_{ref}\left(\frac{p'}{p'_{ref}}\right)^{m_K}\left[R_{K,min} + \frac{1 - R_{K,min}}{1 + \left(\frac{|\varepsilon_{vol}|}{r}\right)^s}\right] \tag{4.3}$$

where

$$\varepsilon_{vol} = \varepsilon_1 + \varepsilon_2 + \varepsilon_3 \tag{4.4}$$

$$k = k_0 e^{-Bp'} \tag{4.5}$$

Mohr-Coulomb strength properties	
c'	$5.0\ kPa$
ϕ'	25.0^o
ψ'	12.5^o
Small-strain stiffness properties	
G_{ref}	$51744\ kPa$
p'_{ref}	$100\ kPa$
m_G	1.0
m_K	1.0
a	0.000056
b	0.9
$R_{G,min}$	0.06450
G_{min}	$2667\ kPa$
K_{ref}	$26693\ kPa$
r	0.000127
s	1.8
$R_{K,min}$	0.13275
K_{min}	$5000\ kPa$
Thermal and thermo-mechanical properties	
γ_s	$20.0\ kN \cdot m^{-3}$
α_s	$1.7 \times 10^{-5}\ m \cdot m^{-1} \cdot K^{-1}$
α_f	$6.9 \times 10^{-5}\ m \cdot m^{-1} \cdot K^{-1}$
K_f	$2.2\ GPa$
ρC_p	$1820\ kJ \cdot m^{-3} \cdot K^{-1}$
λ	$1.79\ W \cdot m^{-1} \cdot K^{-1}$
Hydraulic properties	
k_0	$1.0 \times 10^{-10}\ m \cdot s^{-1}$
B	$0.0023\ kPa^{-1}$

Table 4.1 Material properties adopted for London Clay

The concrete thermo-active pile, as well as the TEM surrounding the pipes, are modelled as linear-elastic materials, with the material properties given in Table 4.2 (the properties adopted for concrete are identical to those adopted in Gawecka et al. (2017)). In Table 4.2, μ is the Poisson's ratio. As mentioned in Section 4.2.1, the material properties for the TEM are identical to those of the concrete pile, except that its volumetric heat capacity is equal to $1\ kJ \cdot m^{-3} \cdot K^{-1}$ and the thermal conductivity is evaluated using Equation (2.29). With an internal pipe diameter of $26.2\ mm$, a thermal conductivity of $4.5\ W \cdot m^{-1} \cdot K^{-1}$ should be adopted for the TEM.

Linear material properties	
E	$40 \times 10^6\ kPa$
μ	0.3
Thermal and thermo-mechanical properties	
γ_s	$24.0\ kN \cdot m^{-3}$
α_s	$8.5 \times 10^{-6}\ m \cdot m^{-1} \cdot K^{-1}$
ρC_p	$1920\ kJ \cdot m^{-3} \cdot K^{-1}$ for concrete $1\ kJ \cdot m^{-3} \cdot K^{-1}$ for TEM
λ	$2.33\ W \cdot m^{-1} \cdot K^{-1}$ for concrete $4.5\ W \cdot m^{-1} \cdot K^{-1}$ for TEM

Table 4.2 Material properties adopted for concrete thermo-active pile and TEM

The heat exchanger pipes are also modelled as a linear-elastic material and the material properties are given in Table 4.3. Note that pipes have a very small stiffness so they do not contribute to the stiffness of the pile (i.e. they do not act as reinforcement). They also have a linear coefficient of thermal expansion which is identical to that of the concrete pile so that they expand/contract to the same extent when subjected to temperature changes. The volumetric heat capacity of water $\rho_w C_w$ is taken as $4190\ kJ \cdot m^{-3} \cdot K^{-1}$ in this numerical study.

Linear material properties	
E	$1 \times 10^3\ kPa$
Thermal and thermo-mechanical properties	
α_s	$8.5 \times 10^{-6}\ m \cdot m^{-1} \cdot K^{-1}$
ρC_p	$4190\ kJ \cdot m^{-3} \cdot K^{-1}$
λ	$0.6\ W \cdot m^{-1} \cdot K^{-1}$

Table 4.3 Material properties adopted for the heat exchanger pipes

4.2.5 Modelling sequence

In this numerical study, the thermo-active pile is first mechanically loaded before applying heating (which is simulated by the circulation of hot water through the heat exchanger pipes), in order to replicate the conditions that a thermo-active pile is likely to be subjected to in reality. The pile is mechanically loaded to a service load of $1800\ kN$ for the $600\ mm$ diameter pile and $2900\ kN$ for the $900\ mm$ diameter pile, which correspond to a factor of safety of 2.6 applied to their ultimate capacities, which are evaluated using the α-method with $\alpha = 0.5$ and $S_u = 60 + 8z$ (as adopted in GSHPA (2012)). Following the application of mechanical loads, full dissipation of pore water pressures is allowed before it is heated in order to isolate the effects of pile heating from those due to pile loading. As a result, when the term 'thermally-induced' is used to describe a quantity, it refers to the change in that quantity since the start of heating. Just before the start of heating, the axial stress profiles for the $600\ mm$ and $900\ mm$

piles are shown in Figure 4.5, with a pile head displacement of $-2.8\,mm$ and $-3.0\,mm$ (upwards positive) having been obtained for the $600\,mm$ and $900\,mm$ piles, respectively.

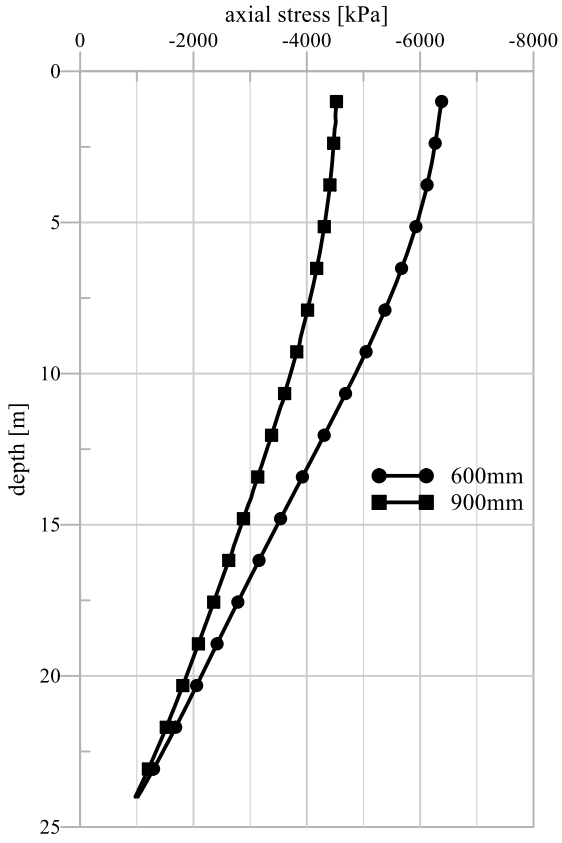


Figure 4.5 Axial stress profiles for the $600\,mm$ and $900\,mm$ piles just before the start of heating

After pore water pressures are fully dissipated, the pile is heated up by circulating water at 39.5℃ (which corresponds to 20℃ above the initial ground temperature) through the pipes at a flow rate of $1.032 \times 10^{-4}\,m^3 \cdot s^{-1}$ per U-loop for a duration of five months. It should be appreciated that such duration of pile heating (which corresponds to provision of cooling demands), which follows Gawecka et al. (2017), should have covered typical realistic durations of cooling demand. Furthermore, as will be shown in the following sections, modelling five months of heating would be long enough to allow the critical cases of thermally-induced pile axial stress, pile head displacement and pore water pressure in the soil to be simulated, which happen within the first month of heating, as well as the subsequent transient response. Note that the circulation of hot water is achieved by prescribing a constant temperature boundary condition of $T = 39.5℃$ at the pipe inlet(s) and a coupled thermo-hydraulic boundary condition (see Section 2.6.2.3 (Cui et al., 2016)) at the pipe outlet(s), which allow the removal

of the energy corresponding to the water leaving the mesh. Due to the presence of an advection dominated flow, the Petrov-Galerkin finite-element method is adopted for the pipes (see Section 2.6.3, Cui et al. (2016) and Gawecka (2017)). It should be noted that prescribing a constant inlet temperature is likely to be a simplified representation of a realistic thermal load, but this approach allows comparisons between the results of the analyses and the current design charts, which are based on a fixed temperature change being applied to a pile; also, this ensures that any obtained transient response is exclusively due to the transient soil response resulting from the associated heat transfer. It should also be noted that just before hot water is injected into the pile, the stiffness of London Clay is reset to its maximum value by setting the deviatoric strain (E_d) and volumetric strain (ε_{vol}) used to calculate the tangent shear (G_{tan}) and bulk (K_{tan}) stiffnesses, respectively, to zero. This is to account for the increase in stiffness upon reversal of the loading direction induced by the pile expansion due to increase in temperature (Gawecka et al., 2017). However, it should be appreciated that the reset of stiffness of the entire London Clay soil mass is an approximation as there are locations within the soil that do not experience reversal of loading direction. Such approximation (which would result in an overall overestimation of soil stiffness) is conservative for stresses, but non-conservative for displacements simulation.

4.2.6 Results – thermal performance

The thermal performance of the thermo-active piles considered in this study is quantified by:

- Evolution of the system's power with time (Section 4.2.6.1).
- Storage of energy within different parts of the thermo-active pile system with time (Section 4.2.6.2).

4.2.6.1 Evolution of the system's power with time

The system's power P $[W]$ refers to the rate of energy transfer from the heat exchanger pipes to the surrounding pile and soil mass and can be calculated using Equation (4.6), where $n_{U-loops}$ is the number of U-loops in the thermo-active pile, Q_i $[m^3 \cdot s^{-1}]$ is the water flow rate in U-loop i, while $T_{in,i}$ [℃] and $T_{out,i}$ [℃] are temperatures of water entering and leaving the pile in U-loop i, respectively. The development of P with time normalised by the length of the pile L $[m]$ for the six analyses performed (pile diameters of 600 mm and 900 mm with pipe arrangements of 1U, 2U and 3U) are shown in Figure 4.6.

$$P = \sum_{i=1}^{n_{U-loops}} \rho_w C_w \cdot Q_i \cdot \left(T_{in,i} - T_{out,i}\right) \tag{4.6}$$

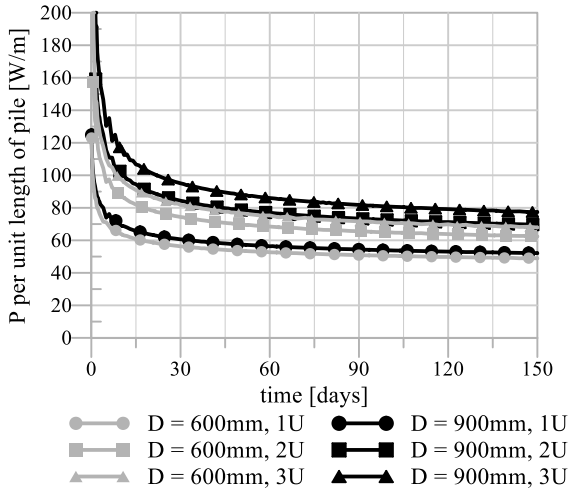


Figure 4.6 Development of P/L with time for pile diameters of 600 mm and 900 mm and pipe arrangements of 1U, 2U and 3U

It can be observed from Figure 4.6 that for all the analyses considered, the power is larger during the initial stages of heating. This is due to the large thermal gradient between the hot heat exchanger pipes and the cold pile. However, as time progresses, the power reduces significantly and stabilises towards the end of 5 months: as the pile is heated up and its temperature increases, the thermal gradient between the pipes and the surrounding concrete reduces. Towards the end of the 5 months period, or in the long-term, when the power has stabilised, this essentially means that the rate of energy transfer from the pipes into the pile is more or less equal to that from the pile into the surrounding soil. It should be noted that this pattern of power evolution with time was also observed in Jalaluddin et al. (2011) and Lu et al. (2017).

Moreover, it can be observed in Figure 4.6 that for both 600 mm and 900 mm diameter piles, both short-term and long-term power increase with the number of U-loops. However, it should be appreciated that doubling or tripling the number of U-loops in the pile does not result in a proportional increase in the power of the system. In particular, for the 600 mm pile at $t = 150\ days$, the power is 49.0 $W \cdot m^{-1}$ for 1U pipe arrangement, while powers of 62.4 $W \cdot m^{-1}$ (27% increase from the case of 1U) and 67.9 $W \cdot m^{-1}$ (39% increase from the case of 1U) are obtained for 2U and 3U pipe arrangements, respectively. For the 900 mm pile at $t = 150\ days$, the power is 52.1 $W \cdot m^{-1}$ for 1U pipe arrangement, while powers of 69.6 $W \cdot m^{-1}$ (34% increase from the case of 1U) and 77.4 $W \cdot m^{-1}$ (49% increase from the case of

1U) are modelled for 2U and 3U pipe arrangements, respectively. Note that this finding agrees with the conclusions presented in Gao et al. (2008), Cecinato and Loveridge (2015) and Lu et al. (2017).

Lastly, it can also be observed from Figure 4.6 that, for the same pipe arrangement, the power of the $900\ mm$ diameter pile is always slightly larger than that of the $600\ mm$ diameter pile, with the difference increasing with the number of U-loops. This is related to the fact that the concrete pile is modelled to have a higher thermal conductivity than the London Clay surrounding it. Therefore, in the $900\ mm$ diameter pile, there is a larger volume of material which is more thermally conductive (i.e. the concrete pile) surrounding the pipes, allowing a more efficient removal of energy from the water in the pipes. Note that this finding agrees with the conclusions presented in Nagano et al. (2005).

4.2.6.2 Storage of energy within different parts of the thermo-active pile system with time

The change in energy content within different parts of the thermo-active pile-soil system with time is evaluated in order to quantify their relative contribution towards the storage of energy at different times. In the current study, the system is divided into the following sections, which are defined based on element boundaries:

1. The pile
2. The $250\ mm$ thick soil annulus around the pile
3. The next $600\ mm$ thick soil annulus
4. The next $1100\ mm$ thick soil annulus
5. The next $1600\ mm$ thick soil annulus
6. The rest of the soil

The change in energy content of section i, ΔE_i $[J]$ is calculated using Equation (4.7), where $\rho C_{p,i}$ $[J \cdot m^{-3} \cdot K^{-1}]$ is the volumetric heat capacity of the material in section i, V_i $[m^3]$ is the volume of section i and $\Delta T_{av,i}$ [°C] is the average change in temperature of section i.

$$\Delta E_i = \rho C_{p,i} \cdot V_i \cdot \Delta T_{av,i} \tag{4.7}$$

The average changes in temperature in the six abovementioned sections for the six analyses performed (pile diameters of $600\ mm$ and $900\ mm$ with pipe arrangements of 1U, 2U and 3U) are shown in Figure 4.7 to Figure 4.12. It can be observed that the patterns of average changes in temperature for the six analyses are very similar, with the largest temperature changes occurring at the pile, as it is closest to the pipes which are the heat sources. As expected, as the

distance from the pipes increases, the changes in temperature reduce progressively, reaching negligible values in the far-field ('rest of soil' section). Comparing the changes in temperature between analyses of 1U, 2U and 3U pipe arrangements for piles of the same diameter, increasing the number of U-loops in the pile increases the changes in temperature, as having more heat sources means transferring a larger amount of energy into the pile. It can also be observed that the average changes in temperature are higher in the 600 mm diameter pile than those in the 900 mm diameter pile for the same pipe arrangement, this is due to the fact that smaller volumes of concrete or soil are to be heated up in the 600 mm cases.

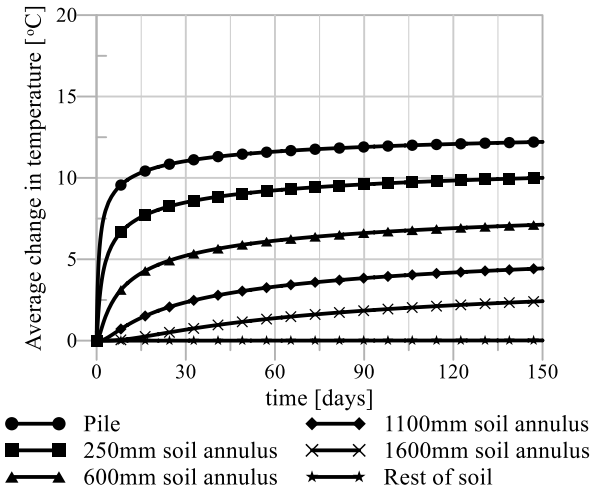


Figure 4.7 Average changes in temperature in different sections for the 600 mm diameter pile with 1U pipe arrangement

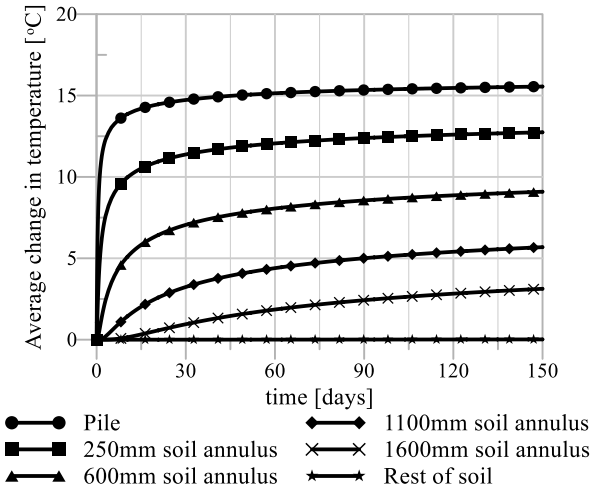


Figure 4.8 Average changes in temperature in different sections for the 600 mm diameter pile with 2U pipe arrangement

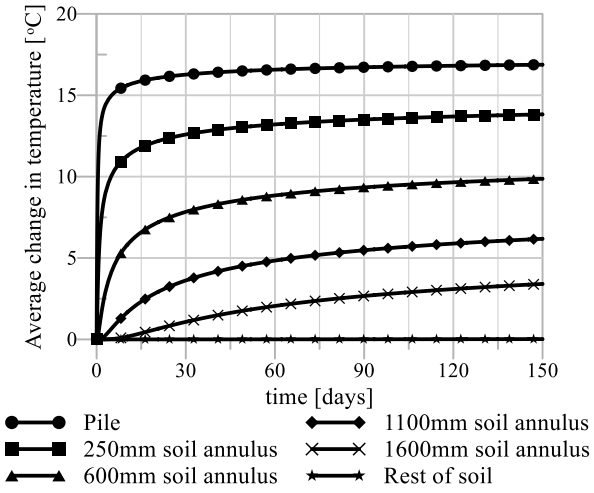


Figure 4.9 Average changes in temperature in different sections for the 600 mm diameter pile with 3U pipe arrangement

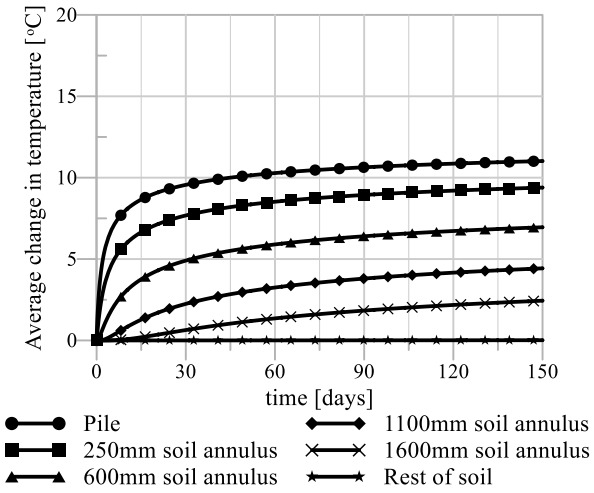


Figure 4.10 Average changes in temperature in different sections for the 900 mm diameter pile with 1U pipe arrangement

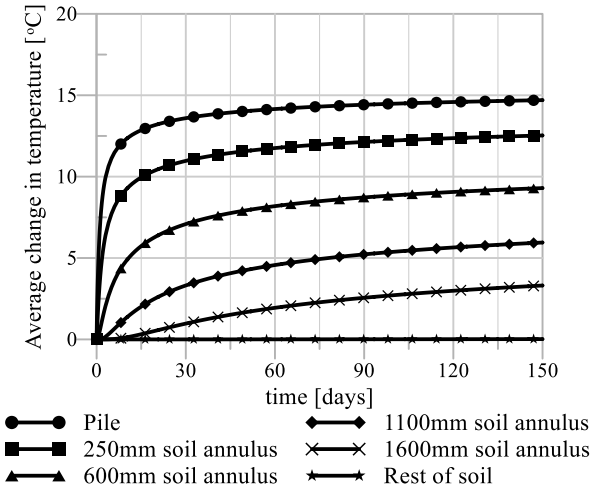


Figure 4.11 Average changes in temperature in different sections for the 900 mm diameter pile with 2U pipe arrangement

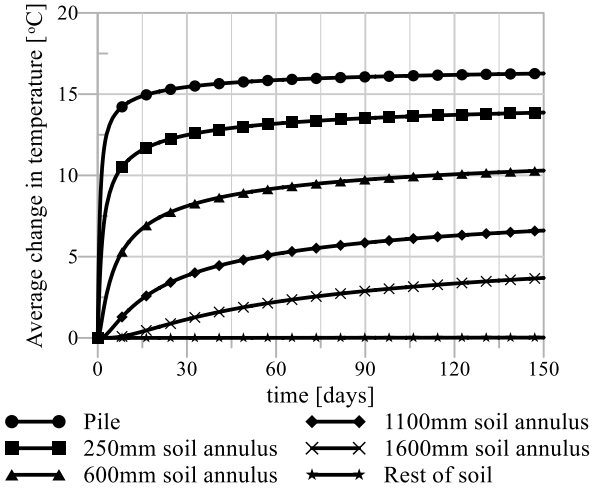


Figure 4.12 Average changes in temperature in different sections for the 900 mm diameter pile with 3U pipe arrangement

Based on the average changes in temperature with time in different sections presented in Figure 4.7 to Figure 4.12, the changes in energy content of each section with time ΔE_i can be evaluated using Equation (4.7). It is worth noting that the change in energy content of the entire system (i.e. $\sum_i \Delta E_i$) at any time is always smaller than the total amount of energy that has been transferred into the system ($H = \int Pdt$), due to energy losses through the mesh boundaries which are set at a constant temperature (see Section 4.2.3 on thermal boundary conditions of the analyses). In the current analyses, comparing the energy content of the entire system and the energy that has been transferred into the system at $t = 150\ days$, it is found that $16 - 18\%$ of the energy transferred into the system has been lost. However, it should be emphasised

that the modelling of this energy loss is highly uncertain and heavily dependent on the boundary conditions adopted. For example, the modelled energy loss would be significantly different if the top boundary (i.e. ground surface) is modelled with a seasonal change in temperature, or prescribed with a convection/natural heat loss boundary condition (see Section 2.6.2.2). Therefore, in the current study, the contribution of each section to the entire pile-soil system in terms of energy storage is quantified using $\Delta E_i / \sum_i \Delta E_i$, which is the change in energy content of the section normalised by the change in energy content of the entire system. The normalised change in energy content of each section with time for the six analyses performed (pile diameters of $600\ mm$ and $900\ mm$ with pipe arrangements of 1U, 2U and 3U) are shown in Figure 4.13 to Figure 4.18.

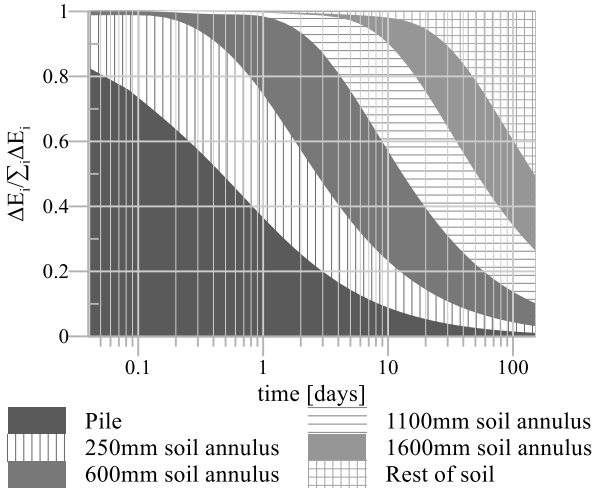


Figure 4.13 Evolution of $\Delta E_i / \sum_i \Delta E_i$ with time for the $600\ mm$ diameter pile with 1U pipe arrangement

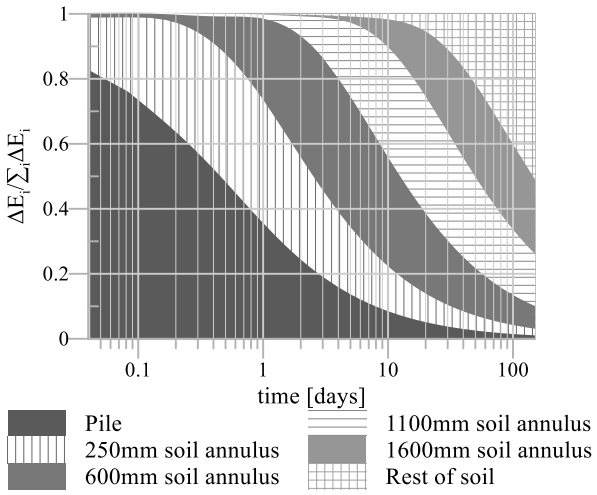


Figure 4.14 Evolution of $\Delta E_i / \sum_i \Delta E_i$ with time for the 600 mm diameter pile with 2U pipe arrangement

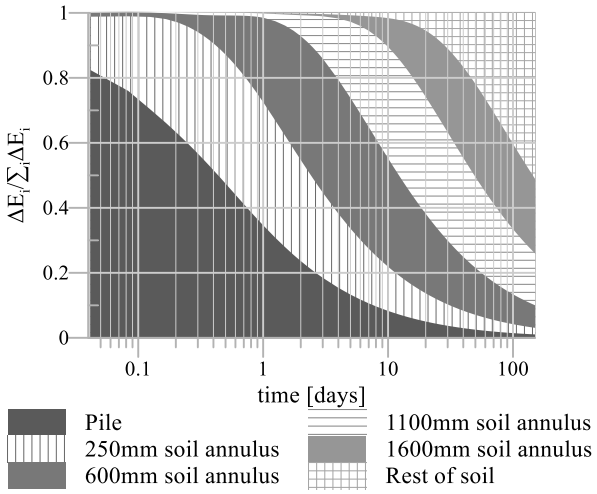


Figure 4.15 Evolution of $\Delta E_i / \sum_i \Delta E_i$ with time for the 600 mm diameter pile with 3U pipe arrangement

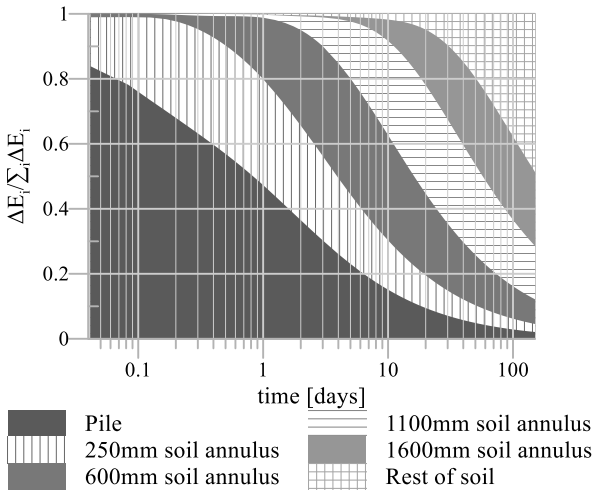


Figure 4.16 Evolution of $\Delta E_i / \sum_i \Delta E_i$ with time for the 900 mm diameter pile with 1U pipe arrangement

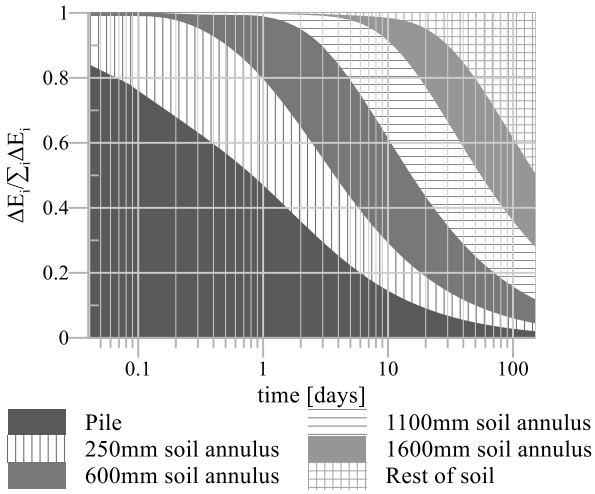


Figure 4.17 Evolution of $\Delta E_i / \sum_i \Delta E_i$ with time for the 900 mm diameter pile with 2U pipe arrangement

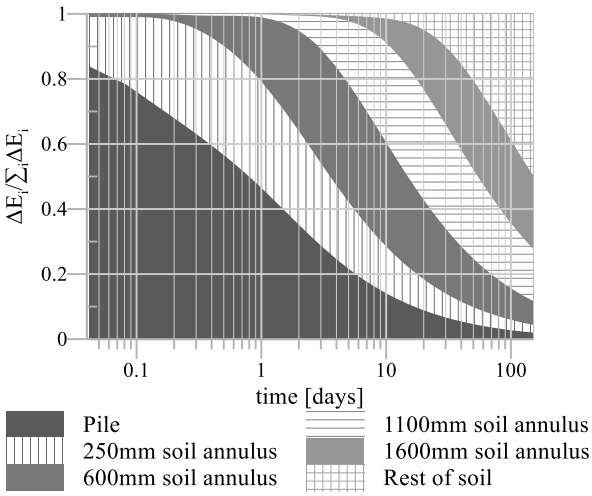


Figure 4.18 Evolution of $\Delta E_i / \sum_i \Delta E_i$ with time for the $900\ mm$ diameter pile with 3U pipe arrangement

Comparing the evolutions of $\Delta E_i / \sum_i \Delta E_i$ with time between analyses with 1U, 2U and 3U pipe arrangements in both pile diameters from Figure 4.13 to Figure 4.18, it can be observed that although a larger amount of energy is transferred into the system when the number of U-loops increases, the patterns of where the energy is stored within the system are almost the same. It can therefore be concluded that the transient storage of energy in different parts of the pile-soil system is largely independent of the amount of energy transferred into the system. On the other hand, comparing the patterns of energy storage obtained between the $600\ mm$ diameter pile (Figure 4.13 to Figure 4.15) and the $900\ mm$ diameter pile (Figure 4.16 to Figure 4.18), while the patterns look very similar, the main difference is that a larger proportion of energy in the system is stored within the pile for the $900\ mm$ case, which is expected as it has a larger volume than the $600\ mm$ diameter pile, despite the fact that the average changes in temperature within the $900\ mm$ diameter pile are slightly lower than those of the $600\ mm$ diameter pile considering the same pipe arrangement (see Figure 4.7 to Figure 4.12). Referring to the patterns of energy storage in Figure 4.13 to Figure 4.18, it can be observed that in all the cases, more than 80% of the system's energy is stored within the pile when heating begins. As time progresses and energy is transferred outwards from the pile into the surrounding soil, the section that contributes most to energy storage moves outwards progressively. At $t = 150\ days$, around 50% of the total energy transferred into the system is stored in the far-field soil, and only $1 - 2\%$ within the pile. It should be appreciated that despite the fact the far-field soil stores about 50% of the total energy transferred into the system at $t = 150\ days$, its average change in temperature is negligible (see Figure 4.7 to Figure 4.12) due to its large

volume. As a result, it is important to take into account the entire pile-soil system with sufficient domain size when analysing long-term energy storage and thermal performances of thermo-active piles.

4.2.7 Results – thermo-mechanical response

As heat is injected into the pile, the temperature of the pile, and subsequently its surrounding soil increases and expands, inducing thermo-mechanical responses. In this study, the following thermo-mechanical responses are investigated:

- Thermally-induced pile head displacement (Section 4.2.7.1).
- Thermally-induced pile axial stress (Section 4.2.7.2).
- Thermally-induced excess pore water pressure (Section 4.2.7.3).

4.2.7.1 Thermally-induced pile head displacement

When heat is injected into the pile, its temperature increases and thermal expansion takes place. This causes heaving at the pile head as reported in the literature on previous field, laboratory and numerical studies (see Sections 3.3 to 3.5). In the current numerical study, the thermally-induced pile head displacement is monitored throughout the analyses for the six analyses performed (pile diameters of 600 mm and 900 mm with pipe arrangements of 1U, 2U and 3U) and are shown in Figure 4.19, while Table 4.4 reports the thermally-induced pile head displacement at $t = 150\ days$ for each analysis. Note that upwards is taken as positive.

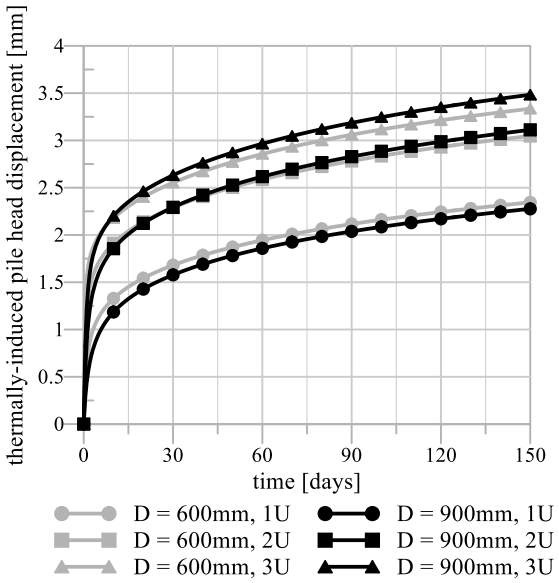


Figure 4.19 Thermally-induced pile head displacement for the six analyses performed

		Pipe arrangement		
		1U	2U	3U
Pile diameter	600 mm	2.3 mm	3.0 mm	3.3 mm
	900 mm	2.3 mm	3.1 mm	3.5 mm

Table 4.4 Thermally-induced pile head displacement at $t = 150\ days$ for the six analyses performed

It can be observed in Figure 4.19 that the pattern of evolution of thermally-induced pile head displacement with time is, as expected, similar to the pattern of average temperature change of the pile with time (see Figure 4.7 to Figure 4.12), as heaving of the pile head is driven by the thermal expansion of the pile. Moreover, increasing the number of U-loops in the pile increases the thermally-induced pile head displacement, as more heat sources are present in the pile, meaning that higher temperatures are obtained (see Figure 4.7 to Figure 4.12) and, thus, larger pile expansion and displacements.

Comparing the thermally-induced pile head displacements at $t = 150\ days$ from Table 4.4 with those due to mechanical loading ($-2.8\ mm$ and $-3.0\ mm$ for the $600\ mm$ and $900\ mm$ diameter piles, respectively), it is found that for the case of 2U and 3U pipe arrangements on both piles, the thermally-induced pile head displacements are more significant than the settlements due to mechanical loading. This means that in such cases, there is a net heave of the pile head. The presented results highlight a potential issue that, should the piles be cooled instead of heated, there would be thermally-induced pile head settlement rather than heaving, and this thermally-induced settlement would further increase the settlement due to mechanical loading. Therefore, it is important to anticipate additional settlements if a thermo-active pile is designed to be cooled (i.e. to provide heating for the building).

4.2.7.2 Thermally-induced pile axial stress

Compressive axial stresses develop within the pile when it heats up and expands, due to the restraint acting on it from the surrounding soil, which is subjected to lower temperature changes (see Figure 4.7 to Figure 4.12) and therefore expands less. As the pile is heated up by heat exchanger pipes (via the circulation of hot water through them) which are at discrete locations within the pile cross-section, the temperature field, and hence the thermally-induced axial stresses σ_T within the pile is not only a function of time, but also non-uniform over the cross-section and depth. In order to simplify the presentation and interpretation of thermally-induced

axial stresses, the cross-sectionally averaged σ_T, denoted by $\overline{\sigma_T}$, is used. This quantity is obtained by integrating σ_T over the pile cross-section, thus obtaining an axial force, which is subsequently divided by the cross-sectional area. Note that $\overline{\sigma_T}$ is a function of time and depth, and the maximum $\overline{\sigma_T}$ over the pile length is denoted by $\overline{\sigma_T}_{max}$, which is then only a function of time.

Figure 4.20 to Figure 4.25 show the distributions of temperature change and thermally-induced axial stresses within the pile cross-section for the six analyses performed (pile diameters of $600\ mm$ and $900\ mm$ with pipe arrangements of 1U, 2U and 3U). Note that the small circles surrounding the pipes define the areas of the cross-section occupied by the TEM (see Section 4.2.1). Furthermore, the pile cross-sections are plotted at the time instants and depths where the value of $\overline{\sigma_T}$ is largest over the pile length (i.e. the position where $\overline{\sigma_T}_{max}$ occurs). It is found that for all the cases, this correspond to a depth of around $17\ m$ (see Figure 4.26 and Figure 4.27), which is below mid-depth of the pile due to the modelled increase in stiffness of London Clay with depth due to its proportionality with mean effective stress (see Section 4.2.4). This pattern is also reported in the literature on previous field, laboratory and numerical studies (see Sections 3.3 to 3.5).

Referring to Figure 4.20 to Figure 4.25, it can be observed that the temperature distributions are highly non-uniform, as expected, with higher temperatures in the regions closer to the heat exchanger pipes. The larger thermal expansion of concrete in these regions leads to the resulting spatial distribution of thermally-induced axial stresses, which follows similar patterns as those of the temperature changes. As the number of U-loops increase, the temperature field within the cross-section becomes more uniform with larger average temperatures, and hence larger thermally-induced axial stresses. It can also be observed that increasing the number of U-loops reduces the time at which the peak stress occurs, due to the faster increase in pile temperature.

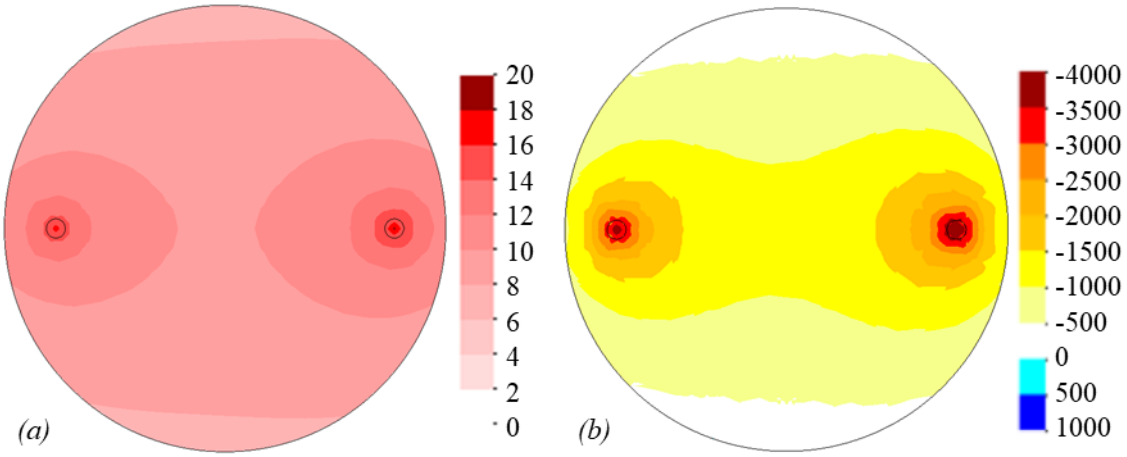


Figure 4.20 Distribution of (a) temperature change [℃] and (b) thermally-induced axial stresses σ_T $[kPa]$ within the cross-section of the 600 mm pile with 1U pipe arrangement at $t = 7$ $days$ and 17 m depth

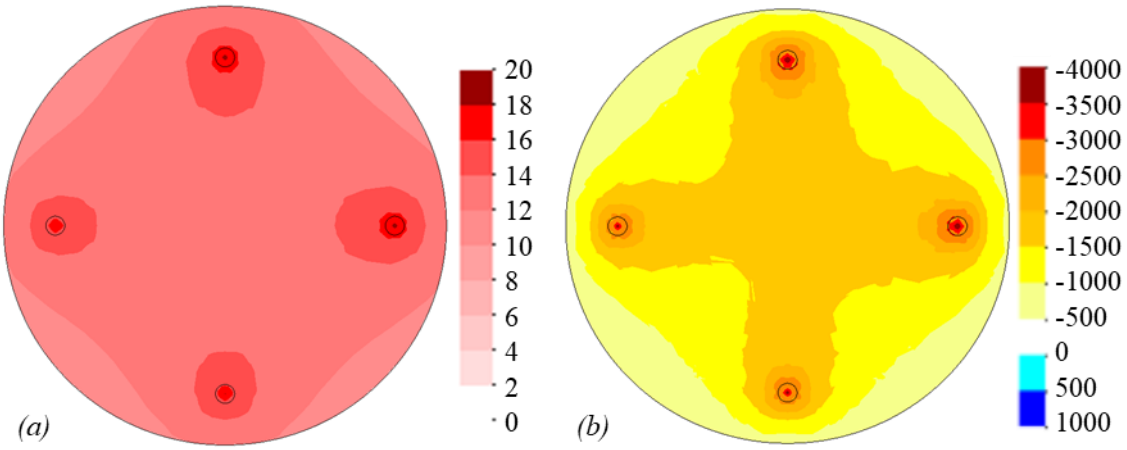


Figure 4.21 Distribution of (a) temperature change [℃] and (b) thermally-induced axial stresses σ_T $[kPa]$ within the cross-section of the 600 mm pile with 2U pipe arrangement at $t = 4$ $days$ and 17 m depth

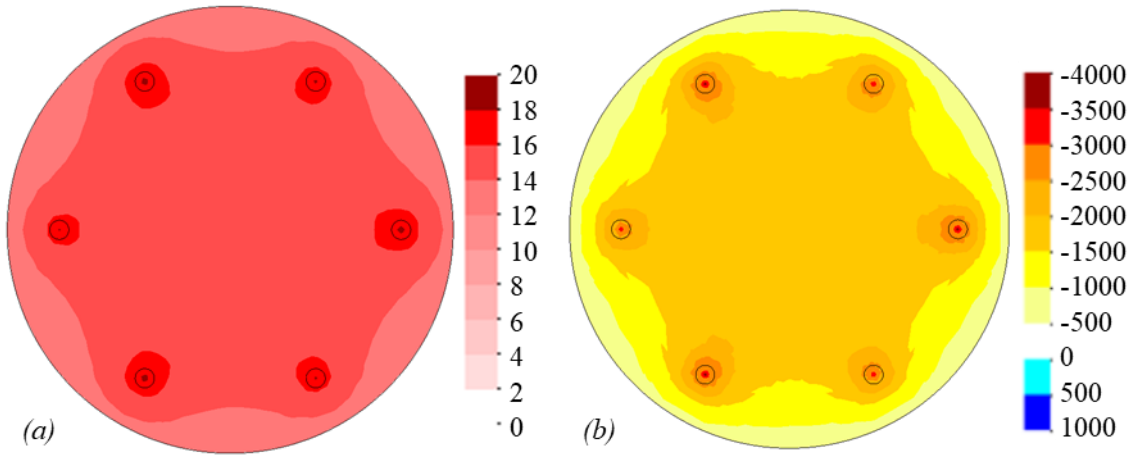


Figure 4.22 Distribution of (a) temperature change [℃] and (b) thermally-induced axial stresses σ_T $[kPa]$ within the cross-section of the 600 mm pile with 3U pipe arrangement at $t = 2.5$ $days$ and 17 m depth

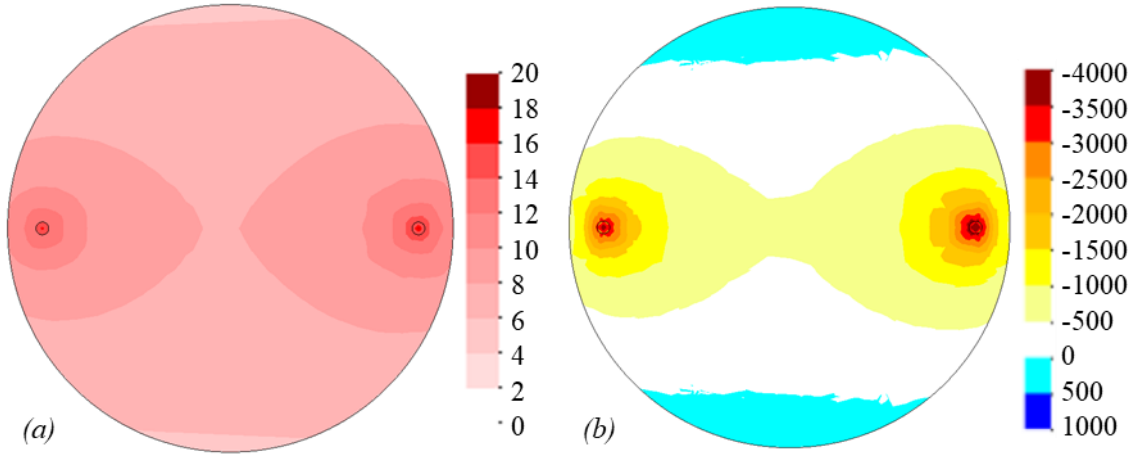


Figure 4.23 Distribution of (a) temperature change [℃] and (b) thermally-induced axial stresses σ_T $[kPa]$ within the cross-section of the 900 mm pile with 1U pipe arrangement at $t = 8$ $days$ and 17 m depth

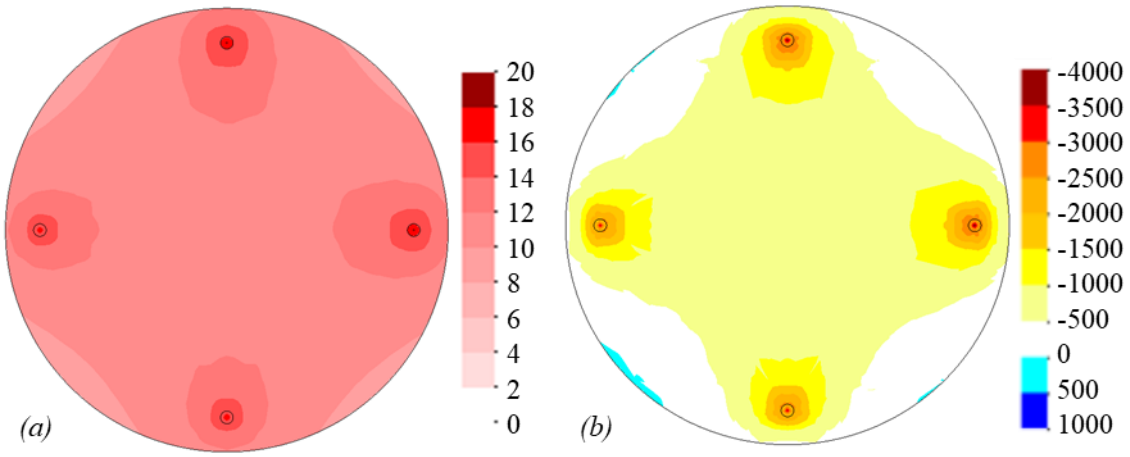


Figure 4.24 Distribution of (a) temperature change [℃] and (b) thermally-induced axial stresses σ_T $[kPa]$ within the cross-section of the 900 mm pile with 2U pipe arrangement at $t = 5$ $days$ and 17 m depth

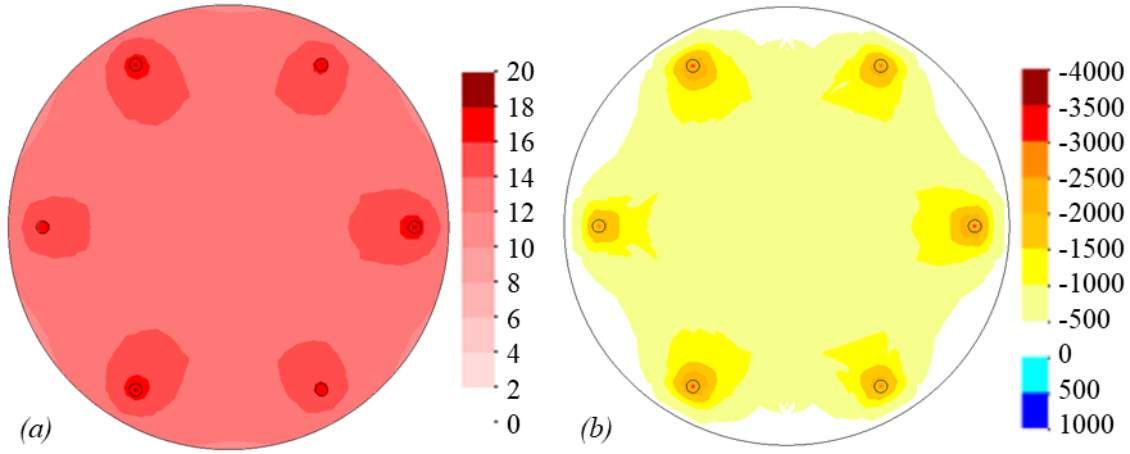


Figure 4.25 Distribution of (a) temperature change [℃] and (b) thermally-induced axial stresses σ_T $[kPa]$ within the cross-section of the 900 mm pile with 3U pipe arrangement at $t = 4$ $days$ and 17 m depth

Figure 4.26 and Figure 4.27 plot the distribution of $\overline{\sigma_T}$ with depth for the analyses on the 600 mm and 900 mm diameter piles, respectively, at the time instants when the corresponding values of $\overline{\sigma_T}_{max}$ are largest over the five months of heating, while Figure 4.28 shows the evolutions of $\overline{\sigma_T}_{max}$ with time for all the six analyses performed. Clearly, as previously concluded, increasing the number of U-loops increases the thermally-induced axial stresses due to the higher temperatures involved. For the 600 mm diameter pile, the peak $\overline{\sigma_T}_{max}$ increases by 34% and 49% when the number of U-loops is doubled and tripled, respectively, while for the 900 mm diameter pile, the equivalent figures are 39% and 61%,

respectively. This means that increasing the number of U-loops does not result in directly proportional increase in thermally-induced axial stresses. This is expected as heat transfer from the heat exchanger pipes to the pile is dependent on the thermal gradient between these two elements, which is reduced by a higher average pile temperature when the number of U-loops increases.

In Figure 4.28, for the same pipe arrangement, when the pile diameter reduces from $900\ mm$ to $600\ mm$, the peak $\overline{\sigma_T}_{max}$ increases significantly (by $107\%, 100\%$ and 92% for 1U, 2U and 3U pipe arrangements, respectively). The reason is that in the $600\ mm$ diameter pile, the smaller distance between the heat exchanger pipes leads to higher average pile temperatures (see Figure 4.7 to Figure 4.12 and Figure 4.20 to Figure 4.25), and hence, larger thermally-induced axial stresses. Figure 4.28 also highlights that the magnitudes of peak $\overline{\sigma_T}_{max}$ are significant, which correspond to $30\% - 50\%$ (for the $600\ mm$ diameter pile) and $20\% - 30\%$ (for the $900\ mm$ diameter pile) of the axial stresses due to mechanical loading at the same depth ($17\ m$). This further demonstrates the importance of accounting for thermal loads when designing thermo-active piles.

Moreover, Figure 4.28 also demonstrates that this problem is highly transient in nature. When the pile is heated, it expands and axial stresses increase due to the restraint from the surrounding soil. As time progresses and heat propagates into the surrounding soil, the soil temperature increases and compressive excess pore water pressures are induced (see Section 4.2.7.3) as the coefficient of thermal expansion of pore fluid is greater than that of the soil. These thermally-induced compressive excess pore water pressures reduce the effective stresses, causing tensile mechanical volumetric strains, or swelling, in the soil, in addition to its thermal expansion due to heating. This expansion reduces the restraint acting on the pile, causing a reduction of axial stresses with time after reaching a peak. Referring to the transient stage shown in Figure 4.28, the initial rate of $\overline{\sigma_T}_{max}$ reduction increases with the number of U-loops, as faster heat transfer to the surrounding soil leads to greater thermal expansion in the soil. As time progresses, the rate of $\overline{\sigma_T}_{max}$ reduction decreases, and after five months of heating, the values of $\overline{\sigma_T}_{max}$ have roughly stabilised. In all the analyses considered, the reduction in $\overline{\sigma_T}_{max}$ during the transient stage increases with the peak $\overline{\sigma_T}_{max}$, and the $\overline{\sigma_T}_{max}$ after five months of heating are only around half of peak $\overline{\sigma_T}_{max}$. It should be appreciated that this transient phenomenon can only be simulated by performing coupled THM analyses, as it requires the time-dependent temperature and pore water pressure changes within the soil to be modelled, together with the

effects of differential thermal expansion between the soil skeleton and the pore fluid. Note that this transient behaviour was also reported in Gawecka et al. (2017) for thermo-active pile foundations and in Sailer et al. (2019) for thermo-active retaining walls.

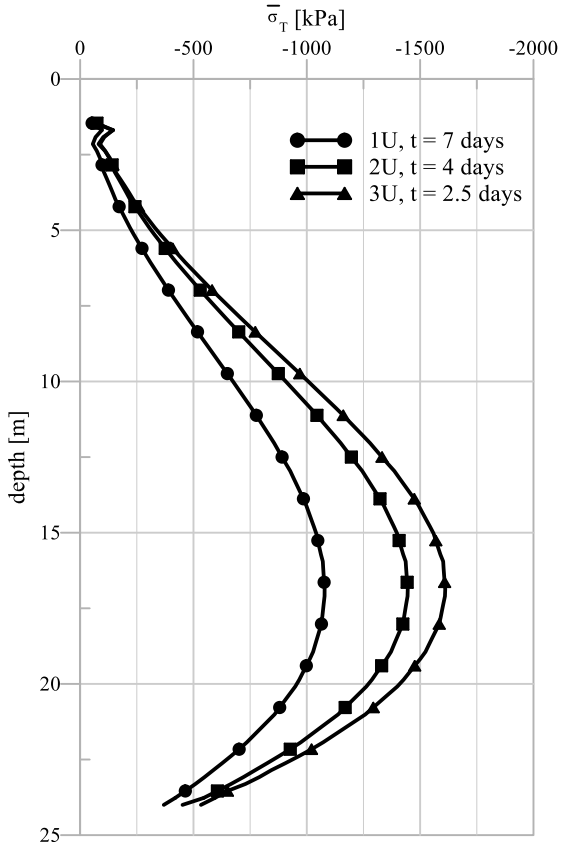


Figure 4.26 Distribution of $\overline{\sigma_T}$ with depth for the analyses on the 600 mm pile

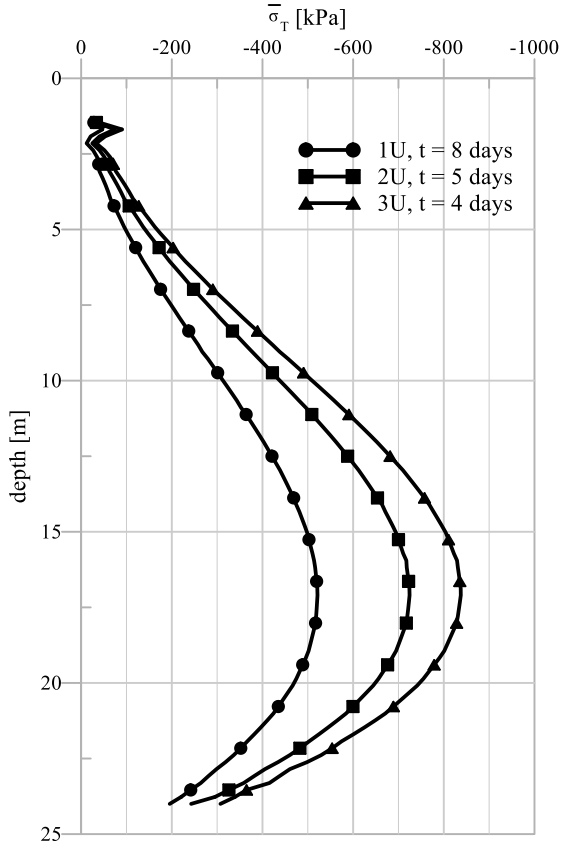


Figure 4.27 Distribution of $\overline{\sigma_T}$ with depth for the analyses on the 900 mm pile

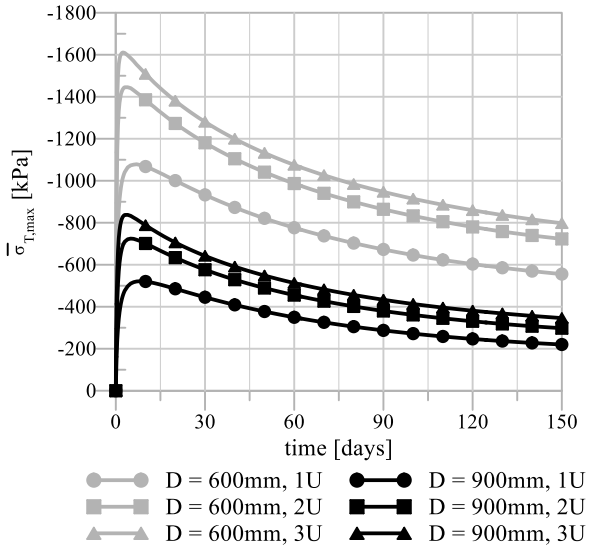


Figure 4.28 Evolution of $\overline{\sigma_T}_{max}$ with time for the six analyses performed

The importance of the transient behaviour is further demonstrated in Figure 4.29, where the peak values of $\overline{\sigma_T}_{max}$ together with its reduction during the transient stage are compared with the recommended values from the current design charts proposed by GSHPA (2012) for the same pile diameters ($600\,mm$ and $900\,mm$, respectively), pile length ($25\,m$), the soil

surrounding the pile (London Clay), loading condition (mechanically loaded to a factor of safety of 2.6) and temperature change (+20℃). In Figure 4.29, it can be observed that the peak values of $\overline{\sigma_T}_{max}$ obtained from the 3D coupled THM FE analyses in the current study are significantly larger (up to 282%) than those recommended by the design charts, though the differences reduce significantly to a maximum of 58% towards the end of the simulation period. The large differences are likely due to the different modelling approaches adopted. The design charts in GSHPA (2012) were developed using the load-transfer method, which is unable to model the non-isothermal response of soil (see Section 3.5) and, hence, account for the transient response of the thermo-active pile.

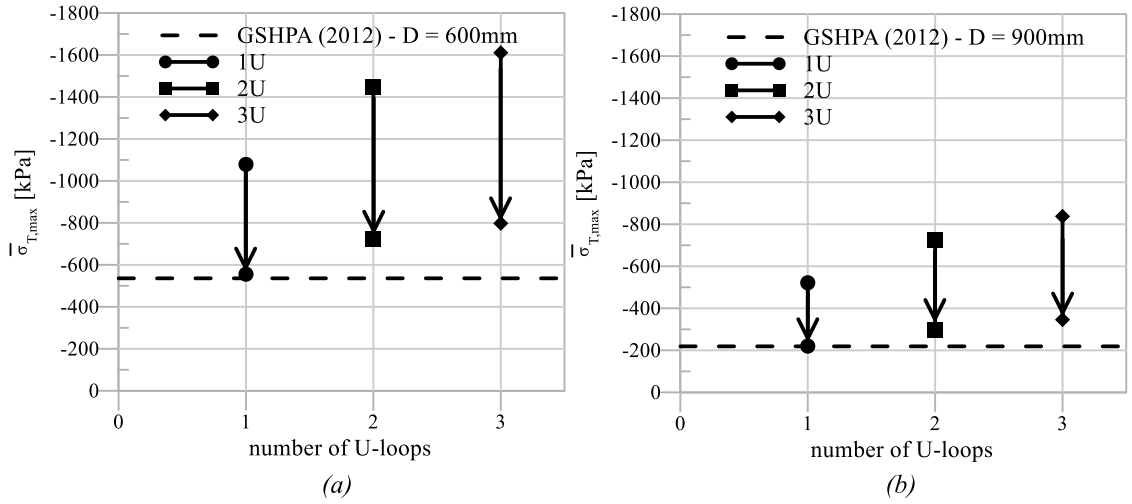


Figure 4.29 Peak $\overline{\sigma_T}_{max}$ and transient behaviour plotted with the recommended values from the design charts by GSHPA (2012) for diameters of (a) 600 mm and (b) 900 mm

When comparing the time to reach peak $\overline{\sigma_T}_{max}$ from different analyses, it is found that it is related to the volume of concrete that each heat source is required to heat up and the rate of heat transfer from the pile into the surrounding soil. This is represented here as the number of heat sources normalised by the pile circumference. Indeed, Figure 4.30 shows that for all the cases considered, a unique relationship exists between these two quantities. Note that each U-loop is considered as two heat sources.

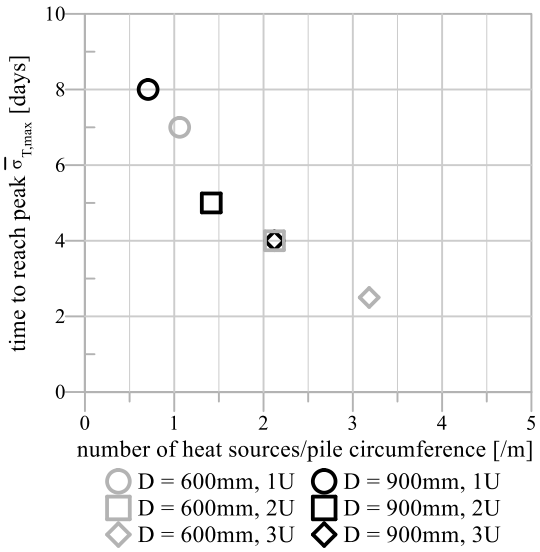


Figure 4.30 Number of heat sources normalised by pile circumference versus time to reach peak $\overline{\sigma_T}_{max}$

4.2.7.3 Thermally-induced excess pore water pressure

As mentioned in Section 4.2.7.2, when heat propagates from the pile into its surrounding soil and the soil temperature increases, compressive excess pore water pressures are induced. The reason is that the coefficient of thermal expansion of pore fluid ($\alpha_f = 6.9 \times 10^{-5}\, m \cdot m^{-1} \cdot K^{-1}$ is adopted in this numerical study) is significantly greater than that of the soil skeleton ($\alpha_s = 1.7 \times 10^{-5}\, m \cdot m^{-1} \cdot K^{-1}$ is adopted in this numerical study), and when a fully saturated soil is heated under undrained conditions (which is the case for London Clay due to its low permeability), the pore fluid expands more than the soil skeleton does, but is unable to displace freely within it, hence inducing compressive excess pore water pressure Δu, which is a function of porosity n, difference in coefficient of thermal expansion between the pore fluid and the soil skeleton $(\alpha_f - \alpha_s)$, change in temperature ΔT, bulk modulus of pore fluid K_f and bulk modulus of soil skeleton K_s, given by Equation (4.8) (Cui, 2015; Cui et al., 2020):

$$\Delta u = \frac{3n(\alpha_f - \alpha_s)\Delta T}{n/K_f + 1/K_s} \tag{4.8}$$

These compressive excess pore water pressures reduce the effective stresses and therefore the stiffness and shear strength in the soil, leading to tensile mechanical volumetric strains, or swelling, ultimately driving the transient behaviour observed in Figure 4.28. It is therefore important to consider the generation of thermally-induced excess pore water pressures when

examining the thermo-mechanical behaviour of a thermo-active pile subjected to thermo-mechanical loads.

Figure 4.31 to Figure 4.36 show the distribution of thermally-induced excess pore water pressure with θ (θ is defined in Figure 4.3) at a radial distance of $250\ mm$ away from the pile edge in the soil at $t = 1\ day, 5\ days, 30\ days$ and $150\ days$ at mid-depth of the pile for the six analyses performed. Figure 4.37 shows the evolution with time of the θ-averaged thermally-induced excess pore water pressure at a radial distance of $250\ mm$ away from the pile edge in the soil at mid-depth of the pile for the six analyses performed. Note that compression is taken as negative in Figure 4.31 to Figure 4.37.

It can also be observed in Figure 4.31 to Figure 4.36 that for the 1U pipe arrangement at $t = 1\ day$, there are obvious peaks of thermally-induced excess pore water pressures at $\theta = 0^c$ and π^c. This is because these positions in the soil are closest to the pipes (i.e. sources of heating), and after such a short period of heating considered (1 day), these are the regions in the soil where the heat front can only reach at that time, and hence the observed patterns of thermally-induced excess pore water pressures. Considering the cases of 2U pipe arrangement at $t = 1\ day$, it can be observed that the thermally-induced excess pore water pressure distributions are much more uniform over θ (matching those of the temperatures) compared to the cases of 1U pipe arrangement, due to the fact that having more heat sources in the pile means faster heat transfer from the pile into the soil, and by $t = 1\ day$, the heat front from the pile has reached pretty much the entire circumference of the soil annulus. It can be observed, however, that the thermally-induced excess pore water pressures between $\theta = 0^c$ and $\pi/2^c$ are slightly larger than those between $\theta = \pi^c$ and $3\pi/2^c$. This can be explained by the way how the pipes that carry hot water down and those up the pile are positioned within the pile cross-section (see Figure 4.3). Pipes that carry hot water down the pile are slightly hotter than those that carry hot water up the pile (see temperature distributions within the pile cross-sections in Figure 4.20 to Figure 4.25), especially during the initial stages of heating when the thermal gradient between the pipes and pile are steep and a large amount of energy is extracted from the water as it moves along the pipes (see Figure 4.6). Considering the cases of 3U pipe arrangement at $t = 1\ day$, it can be observed that, having more heat sources within the pile cross-section, the heat transfer is fast enough such that the soil annulus surrounding the pile is heated up evenly over θ by $t = 1\ day$, resulting in a uniform distribution of thermally-induced excess pore water pressure over θ. As time progresses, considering $t = 5\ days$, $30\ days$ and

$150\ days$, it can be observed that distributions of thermally-induced excess pore water pressure become uniform over θ for all the analyses considered.

Referring to Figure 4.37 which shows the evolution with time the θ-averaged thermally-induced excess pore water pressure, it can be observed that the patterns obtained from the six analyses are similar, where excess pore water pressures build up quickly during the initial stages of heating, and reduce with time after reaching a peak due to dissipation of the thermally-induced excess pore water pressures. As expected, higher peaks of thermally-induced excess pore water pressures are reached when the number of U-loops increases as the soil is heated to higher temperatures.

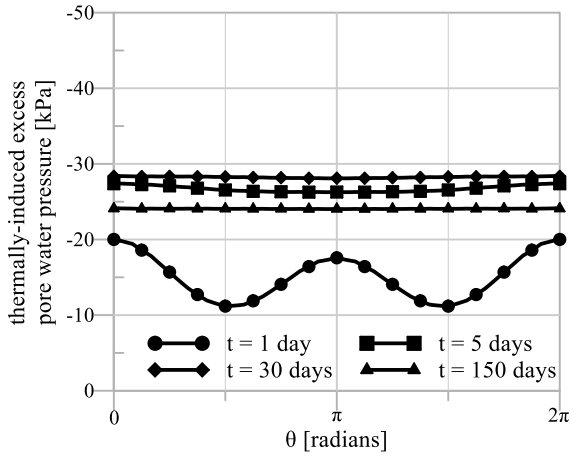


Figure 4.31 Distribution of thermally-induced excess pore water pressure with θ at a radial distance of $250\ mm$ away from the pile edge in the soil at mid-depth of the $600\ mm$ pile with 1U pipe arrangement

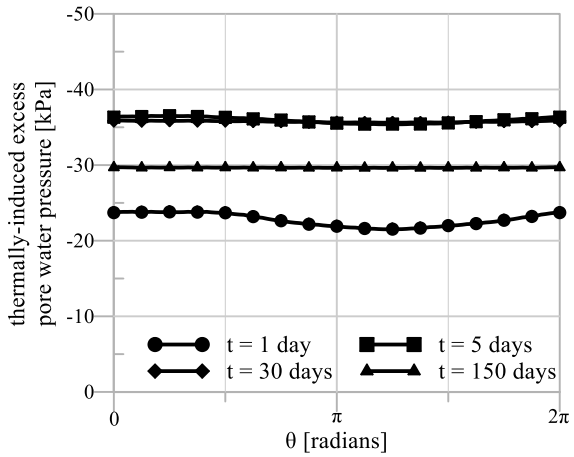


Figure 4.32 Distribution of thermally-induced excess pore water pressure with θ at a radial distance of $250\ mm$ away from the pile edge in the soil at mid-depth of the $600\ mm$ pile with 2U pipe arrangement

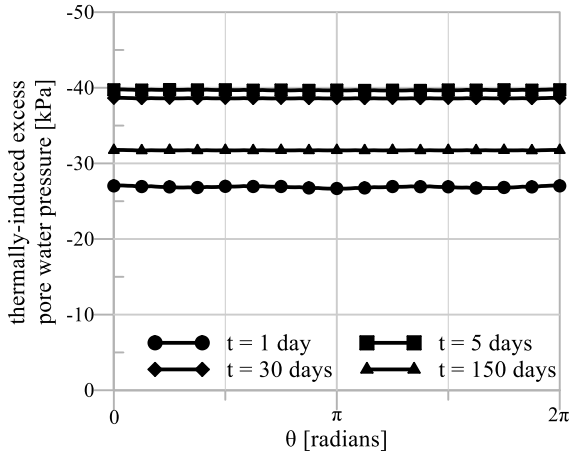


Figure 4.33 Distribution of thermally-induced excess pore water pressure with θ at a radial distance of $250\ mm$ away from the pile edge in the soil at mid-depth of the $600\ mm$ pile with 3U pipe arrangement

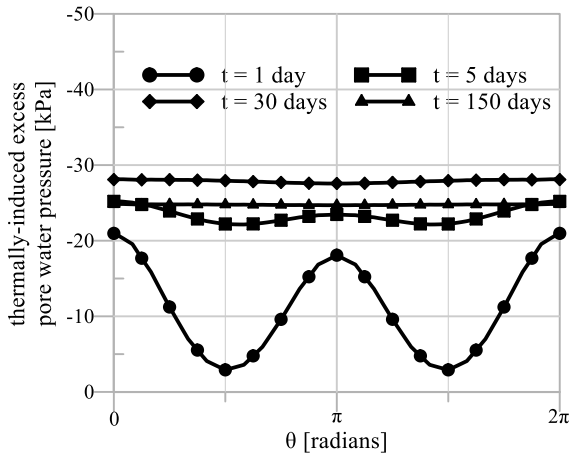


Figure 4.34 Distribution of thermally-induced excess pore water pressure with θ at a radial distance of 250 mm away from the pile edge in the soil at mid-depth of the 900 mm pile with 1U pipe arrangement

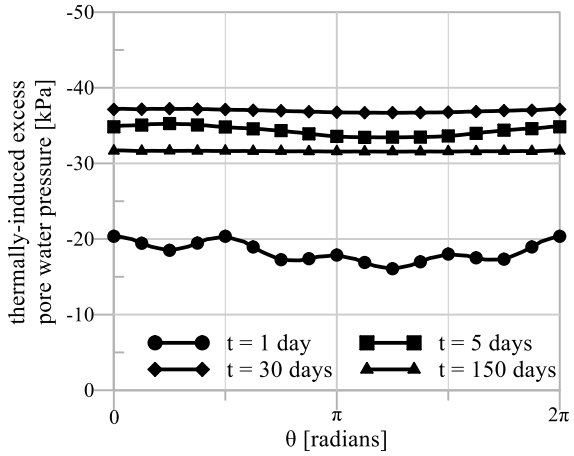


Figure 4.35 Distribution of thermally-induced excess pore water pressure with θ at a radial distance of 250 mm away from the pile edge in the soil at mid-depth of the 900 mm pile with 2U pipe arrangement

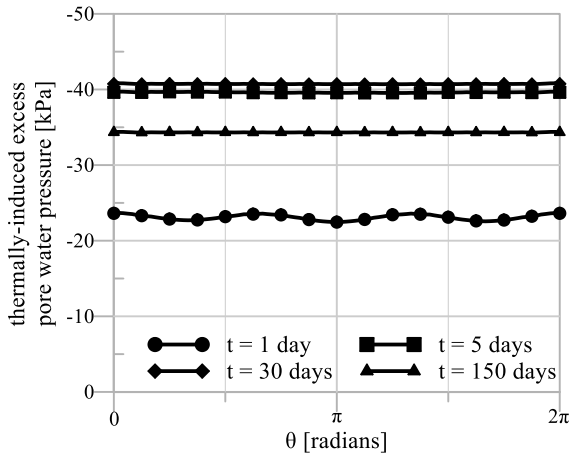


Figure 4.36 Distribution of thermally-induced excess pore water pressure with θ at a radial distance of 250 mm away from the pile edge in the soil at mid-depth of the 900 mm pile with 3U pipe arrangement

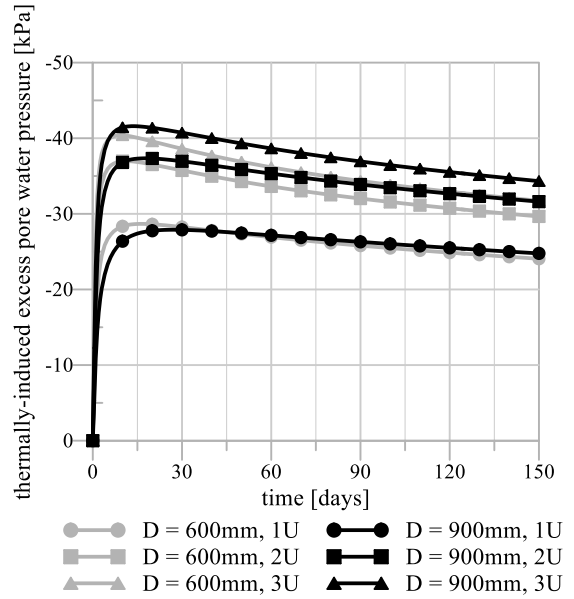


Figure 4.37 Evolution with time of the θ-averaged thermally-induced excess pore water pressure at a radial distance of 250 mm away from the pile edge in the soil at mid-depth of the pile for the six analyses performed

4.3 CONCLUSIONS

A numerical study on the thermal performance and thermo-mechanical behaviour of thermo-active piles which are subjected to thermo-mechanical loads has been presented in this chapter. In order to simulate accurately the thermo-mechanical responses of thermo-active piles when subjected to thermo-mechanical loads, 3D fully coupled THM FE analyses are conducted using

ICFEP, where heating of the piles is modelled by the explicit simulation of the circulation of hot water through heat exchanger pipes. In order to quantify the effects of pile diameter and pipe arrangement on the thermal performance and thermo-mechanical behaviour of thermo-active piles, two pile diameters, $600\ mm$ and $900\ mm$, and three pipe arrangements, single U-loop (1U), double U-loop (2U) and triple U-loop (3U), are considered.

The thermal performances of the thermo-active piles have been analysed, which shows that increasing the number of U-loops means having more heat sources in the thermo-active pile, leading to faster and larger amount of heat transfer from the pipes into the pile, and subsequently into the surrounding soil. For all the analyses considered, the powers of the systems are large during the initial stages of heating, due to the large thermal gradient between the hot heat exchanger pipes and the cold pile; with time, the powers reduce significantly and stabilise towards the end of the simulation period (i.e. five months). While increasing the number of U-loops in the pile increases the power of the system, the increase in not proportional (i.e. doubling or tripling the number of U-loops in the pile does not result in doubled or tripled system power). At $t = 150\ days$, the powers of the system range between $49.0\ W \cdot m^{-1}$ and $77.4\ W \cdot m^{-1}$ for the analyses considered, which agree with the figures observed in the field studies in the literature (see Section 2.3.1). When the storage of energy within the pile-soil system with time is analysed, it has been revealed that the patterns of where energy is stored within the system are almost the same for the analyses considered, which means that the relative transient storage of energy in different parts of the system is independent of the amount of energy transferred into the system. It has also been revealed that more than 80% of the system's energy is stored within the pile during the initial stages of heating, but in the long-term, around 50% of the total energy transferred into the system is stored in the far-field soil, and only $1 - 2\%$ within the pile. This highlights the importance of accounting for the entire pile-soil system with sufficient domain size when analysing long-term energy storage and thermal performances of thermo-active piles.

The thermally-induced pile head displacement, pile axial stress and excess pore water pressure are investigated when examining the thermo-mechanical behaviour of the thermo-active piles. It is found that for the cases of 2U and 3U pipe arrangements for both the $600\ mm$ and $900\ mm$ diameter piles, the thermally-induced pile head displacements (heaving) at $t = 150\ days$ are more significant than the pile head settlements due to mechanical loadings, resulting in a net heave of the pile head. This raises a concern that, should the thermo-active pile be cooled rather than heated, there would be thermally-induced pile head settlements rather

than heaving, which are additional to the settlement due to mechanical loading. This highlights the importance to take thermal loadings into account when designing thermo-active piles, and to anticipate additional settlements if a thermo-active pile is designed to be cooled (i.e. to provide heating for the building).

When the thermo-active piles are heated, non-uniform distributions of temperature, and hence axial stresses, develop within the pile cross-section due to the thermal expansion of materials. These stresses increase rapidly during the initial stages of heating. Upon reaching a peak, there is a transient reduction in these stresses with time due to the swelling of soil surrounding the pile caused by the thermally-induced compressive excess pore water pressures. Towards the end of the simulation, the stresses are stabilised in all the analyses considered. It is found that, as expected, thermally-induced axial stresses increase with the number of U-loops, due to the higher average and more uniformly distributed temperatures associated. Stresses are also larger in the 600 mm diameter pile than in the 900 mm diameter pile, due to the higher average temperatures reached in the former, where each U-loop is required to heat up a smaller volume of concrete. The modelled peak values of thermally-induced axial stress range from 20% to 50% of the axial stresses due to mechanical loading at the same depth, which demonstrates the significance of thermal loading. It is also found that the modelled thermally-induced axial stresses are significantly larger than those suggested by the current design charts (GSHPA, 2012), although such differences reduce significantly with time, highlighting the importance of modelling accurately the transient response of thermo-active piles.

When hot water is circulated through the heat exchanger pipes, heat is transferred into the pile, and subsequently into the surrounding soil. When the soil heats up, compressive excess pore water pressures are induced as the coefficient of thermal expansion of pore fluid is greater than that of the soil. These excess pore water pressures reduce the effective stresses in the soil, causing tensile mechanical volumetric strains in the soil, eventually driving the transient response of the pile. Investigation into these thermally-induced excess pore water pressures reveals that during the initial stages of heating, there is an uneven distribution of these pressures with θ, due to the way the pipes are positioned within the pile cross-section. With time, when the heat front from the pile reaches the entire circumference of the soil annulus surrounding the pile, the thermally-induced excess pore water pressures become uniform with θ. When these pressures are averaged over θ and plotted with time, the patterns obtained are similar to those for thermally-induced pile axial stresses, where larger pressures are reached when the number of U-loops increases due to the soil being heated to higher temperatures. The evolution

of the excess pore water pressure with time also confirms that dissipation of the pressure is successfully modelled during the transient stage.

Although the presented 3D fully coupled THM FE analyses are capable of simulating the thermo-mechanical behaviour of thermo-active piles subjected to thermo-mechanical loads effectively and with high degrees of detail, they require significant computational resources, which may render them impractical for routine engineering design. A simplified method to predict thermo-mechanical behaviour of thermo-active piles is therefore proposed in the following chapter (Chapter 5), where its accuracy can be validated using the results from the analyses presented in this chapter.

CHAPTER 5 A SIMPLIFIED METHOD FOR MODELLING THERMO-ACTIVE PILES

5.1 INTRODUCTION

The three-dimensional (3D) fully coupled thermo-hydro-mechanical (THM) finite-element (FE) analyses presented in Chapter 4 allow the thermo-mechanical behaviour of thermo-active piles to be simulated accurately. However, they are very computationally expensive to run, and the explicit simulation of the circulation of hot water through heat exchanger pipes is not widely available in common FE packages. The above constraints render the analyses presented in Chapter 4 impractical to perform during routine engineering design. As a result, a simplified method to predict thermo-mechanical behaviour of thermo-active piles is proposed in this chapter, which only involves a two-dimensional (2D) thermal analysis combined with a 2D axisymmetric coupled THM analysis. The 3D analyses presented in Chapter 4 are used as a benchmark to demonstrate the excellent accuracy of the method. Note that the contents of this chapter were published in part or whole in Liu et al. (2020b) and Zdravković et al. (2021).

5.2 THE METHOD

The fundamental idea behind this method is to simulate the thermo-mechanical behaviour of a thermo-active pile using an axisymmetric coupled THM analysis, where heating or cooling of the pile is modelled using a time-dependent prescribed temperature (T_{tbc}) thermal boundary condition. This temperature T_{tbc} is applied at a radial distance equal to that of the heat exchanger pipes (i.e. $r = r_{pipes}$), and is equal to the time-dependent average temperature at $r = r_{pipes}$ which is obtained from a 2D thermal analysis of the pile cross-section where the discrete nature and precise location of the heat exchanger pipes are modelled. This method involves the following four steps:

Step 1 – Determine the thermal boundary condition for the 2D thermal analysis

A 2D thermal analysis is conducted to approximate the time-dependent temperature field of the thermo-active pile cross-section. A constant temperature thermal boundary condition is applied at the locations where the pipes are realistically located, and the constant temperatures that are applied, $T_{in,mid}$ [℃] for the case of a pipe where the fluid circulates downwards and

$T_{out,mid}$ [°C] for pipes where the fluid circulates upwards, are determined from the inlet temperature T_{in} [°C] and outlet temperature T_{out} [°C] of each U-loop. In this context, T_{in} is the design inlet temperature for a given U-loop, while T_{out} can be evaluated using Equation (5.1), where ΔE $[W \cdot m^{-1}]$ is an assumed power injected or extracted from the pile per unit pile length, L $[m]$ is the pile length, $n_{U-loops}$ is the number of U-loops in the pile, $\rho_w C_w$ $[J \cdot m^{-3} \cdot K^{-1}]$ is the volumetric heat capacity of water and Q $[m^3 \cdot s^{-1}]$ is the water flow rate within a U-loop.

$$T_{out} = T_{in} - \frac{\Delta E \cdot L}{n_{U-loops} \cdot \rho_w C_w \cdot Q} \tag{5.1}$$

Obviously, the real power injected or extracted from the pile is unknown without conducting a field test or a 3D FE analysis similar to those presented in Chapter 4, where circulation of water through heat exchanger pipes is explicitly modelled. To avoid these complex and costly field and numerical studies, a constant injection or extraction rate is assumed. As suggested by Brandl (2006) and discussed in Section 2.3.1, rates of 35 W per m^2 of earth-contact area can be assumed for piles with diameters $\geq 600\ mm$, while for piles with diameters of $300\ mm$ to $500\ mm$, $40 - 60\ W$ per m pile length can be assumed. This means for example, that for the $600\ mm$ diameter pile considered in Chapter 4, a heat injection rate per unit length ΔE of $66\ W \cdot m^{-1}$ can be estimated, while for the $900\ mm$ diameter pile, this figure would rise to $99\ W \cdot m^{-1}$. Both values are well within the range of power outputs of thermo-active piles reported in the literature, as summarised in Table 2.2. It should however be noted that in the context of this 2D thermal analysis, ΔE is solely used to estimate T_{out} (using Equation (5.1)), and subsequently $T_{in,mid}$ and $T_{out,mid}$ (using Equations (5.2) and (5.3)), and is not an actual measure of the transferred energy, which will depend on many other factors such as pipe arrangements, thermal properties of the pile and those of the soil. Therefore, it should be noted that the adoption of ΔE is justified solely as a form of obtaining more realistic temperature profiles along the pipes that can be used to establish the thermal boundary conditions in the 2D thermal analysis. It will be shown in Section 5.5 that the outputs of the proposed method are relatively unaffected by the adopted value of ΔE, provided reasonable values are used. It should also be noted that it is not a requirement of the proposed method to have a fixed inlet temperature T_{in}. Transient inlet temperatures T_{in} can be adopted instead to model cycles of heating and cooling, and T_{out} (which would then be transient) would still be evaluated using Equation (5.1). By assuming that temperatures vary linearly with depth within the pipes, $T_{in,mid}$ and $T_{out,mid}$ can be determined using Equations (5.2) and (5.3), respectively:

$$T_{in,mid} = T_{in} - (T_{in} - T_{out}) \times \frac{1}{4} \tag{5.2}$$

$$T_{out,mid} = T_{in} - (T_{in} - T_{out}) \times \frac{3}{4} \tag{5.3}$$

Step 2 – Conduct the 2D thermal analysis

By adopting constant temperature thermal boundary conditions $T_{in,mid}$ and $T_{out,mid}$ as evaluated from Step 1, a 2D thermal analysis is conducted to simulate the evolution of the temperature field of the thermo-active pile cross-section over the entire duration of thermal loading. Note that TEM should be adopted at the locations where the pipes are positioned (see Section 2.6.3).

Step 3 – Determine T_{tbc} that is used as a prescribed temperature boundary condition for the axisymmetric coupled THM analysis

A time-dependent temperature field of the thermo-active pile cross-section is obtained following the 2D thermal analysis in Step 2. The average temperature along the circumference with $r = r_{pipes}$ is calculated (using the mean value theorem for integrals) for each time step, generating the time-dependent temperature T_{tbc}, which is to be applied as a thermal boundary condition in the axisymmetric coupled THM analysis, thus simplifying significantly the complexity of the simulated problem by removing the need to conduct 3D analyses and explicitly model heat exchanger pipes.

Step 4 – Conduct the axisymmetric coupled THM analysis

An axisymmetric coupled THM analysis is conducted by applying the time-dependent temperature T_{tbc} obtained in Step 3 at $r = r_{pipes}$. Appropriate material properties for the pile and the surrounding soil, as well as initial and boundary conditions are adopted (e.g. if a restraint to the pile head exists due to the existence of a superstructure, then an appropriate boundary condition should be applied at the pile head to reflect this). Note that the simulation of TEM is not necessary in axisymmetric analyses since the application of the boundary condition T_{tbc} at a given value of the radius corresponds in 3D to a heated or cooled cylindrical shell, which easily transfers heat to/from the surrounding material. The thermo-mechanical responses of the thermo-active pile can then be determined from the results of this axisymmetric analysis.

5.3 DEMONSTRATION OF THE METHOD

The proposed method is demonstrated using the case of the 900 mm thermo-active pile with a single U-loop pipe arrangement simulated in Chapter 4 using 3D analysis. For the 2D thermal analysis, the adopted FE mesh features the same discretisation and dimensions as used in the 3D analysis for the pile and London Clay, using eight-noded quadrilateral elements with one temperature degree of freedom at each node. With a design inlet temperature T_{in} of 39.5℃, a T_{out} of 33.8℃ is evaluated from Equation (5.1) for $\Delta E = 99\ W \cdot m^{-1}$ (as mentioned in Section 5.2, this is based on the assumption of 35 W per m^2 of earth-contact area), $L = 25\ m$, $n_{U-loops} = 1$, $\rho_w C_w = 4190\ kJ \cdot m^{-3} \cdot K^{-1}$ and $Q = 1.032 \times 10^{-4}\ m^3 \cdot s^{-1}$ (i.e. the value adopted in the 3D analyses in Chapter 4). $T_{in,mid}$ and $T_{out,mid}$ are then determined to be 38.1℃ and 35.2℃ using Equations (5.2) and (5.3), respectively. The 2D thermal analysis is then conducted to simulate the evolution of the temperature field of the pile cross-section over the 150 days of heating by applying the constant temperature thermal boundary conditions $T_{in,mid}$ and $T_{out,mid}$ at the locations where the pipes are located in the 3D analysis, which are illustrated in Figure 5.1. Note that the adopted thermal properties for the pile concrete, TEM and London Clay are the same as those adopted in the 3D analyses (see Table 4.1 and Table 4.2).

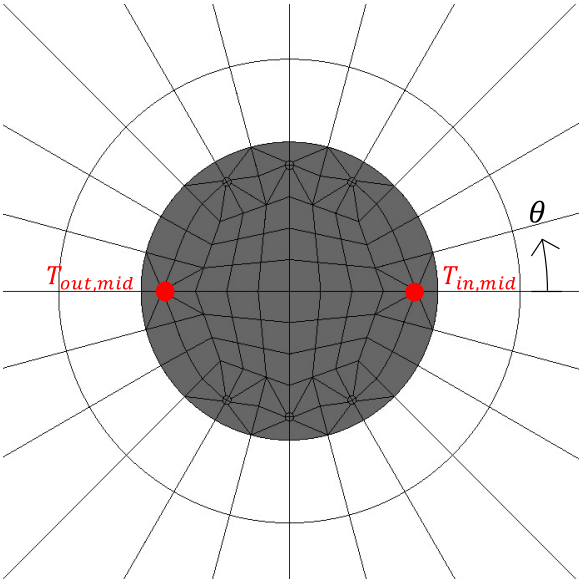


Figure 5.1 Illustration of the thermal boundary condition for the 2D thermal analysis

For each time step of the 2D thermal analysis, the temperature distribution along the circumference with $r = r_{pipes}$ is extracted, and Figure 5.2 illustrates such a curve at $t =$

8 $days$ with the angle θ being measured in an anti-clockwise direction from the positive horizontal semi-axis, as defined in Figure 5.1. As expected, for 1U pipe arrangement, two peaks exist at $\theta = 0^o$ (repeated at 360^o, corresponding to water circulating down the pile) and $\theta = 180^o$ (water circulating up the pile), with the temperature being highest in the former as it represents the inlet branch of the U-loop. The average temperature at $r = r_{pipes}$ is then evaluated using the mean value theorem for integrals for each time step, generating the time-dependent temperature T_{tbc} given in Figure 5.3.

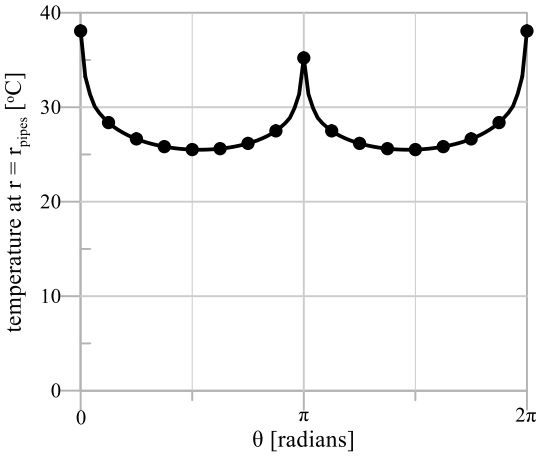


Figure 5.2 Illustration of θ versus temperature curve at $r = r_{pipes}$ and $t = 8\ days$ for the 2D thermal analysis on the 900 mm pile with 1U pipe arrangement

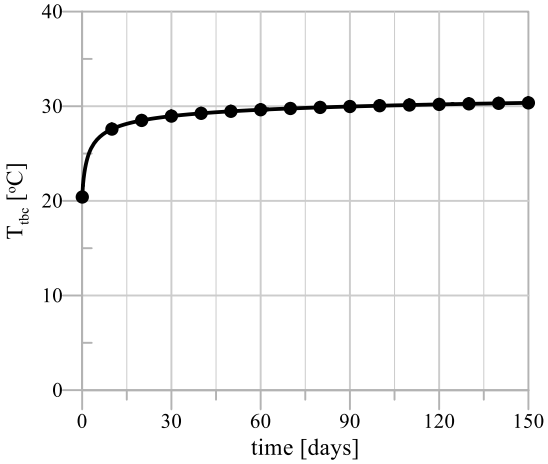


Figure 5.3 Illustration of time versus T_{tbc} for the 900 mm pile with 1U pipe arrangement

The axisymmetric coupled THM analysis is then conducted by applying the time-dependent temperature T_{tbc} as a thermal boundary condition at $r = r_{pipes}$ (see Figure 5.4). The discretisation of the mesh in this analysis (see Figure 5.4) is identical to that adopted in the 3D analyses (see Figure 4.1) in the $x - z$ plane, using eight-noded quadrilateral elements with two

displacement and one temperature degrees of freedom at each node. For elements discretising the London Clay, a pore water pressure degree of freedom also exists at corner nodes. The applied initial and boundary conditions are in accordance with those adopted in the 3D analyses (see Section 4.2.3) and the material properties adopted for the concrete pile and London Clay are also the same as those used in the 3D analyses (see Table 4.1 and Table 4.2).

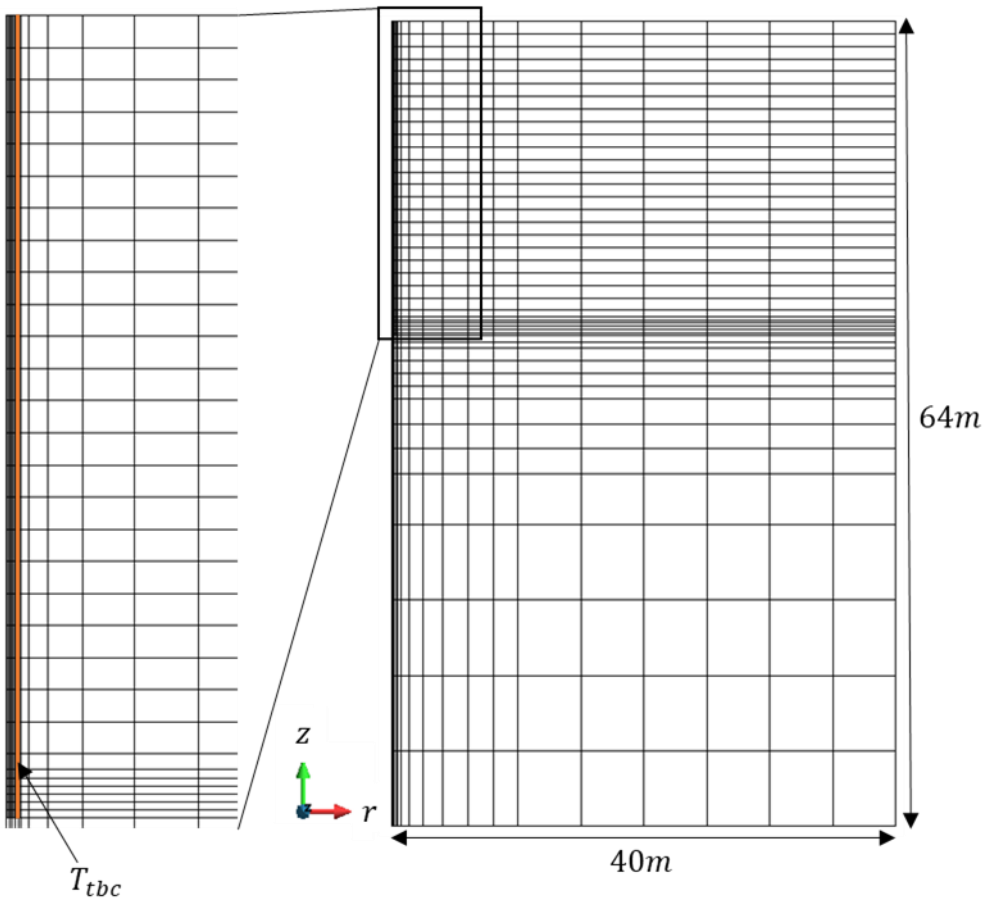


Figure 5.4 The axisymmetric FE mesh and the zoomed-in mesh detailing the pile (shaded in grey) and the location where the time-dependent temperature T_{tbc} is applied within the pile (highlighted in red) for the axisymmetric analyses

5.4 VALIDATION AND PERFORMANCE OF THE METHOD

The performance of the proposed method is assessed by comparing the results computed using the proposed method with those obtained from the 3D analyses described in Chapter 4. In the comparisons, the evolutions with time of the following quantities are considered:

- Temperature changes (Section 5.4.1)

- Thermally-induced pile head displacements (Section 5.4.2)
- Thermally-induced pile axial stresses (Section 5.4.3)
- Thermally-induced excess pore water pressures (Section 5.4.4)

5.4.1 Temperature changes

Figure 5.5 ($600\ mm$ diameter pile) and Figure 5.6 ($900\ mm$ diameter pile) compare the evolution of temperature changes with time at pile mid-depth computed with the proposed method against those obtained from the 3D analyses (averaged at the corresponding radial distance from the centre of the pile using the mean value theorem for integrals) at the centre of the pile, edge of pile and $250\ mm$ away from the pile edge in the soil. It can be observed from Figure 5.5 and Figure 5.6 that the proposed method is capable of simulating the temperature changes accurately, which means that it should also be capable of simulating other thermo-mechanical responses with good accuracy (to be demonstrated in Sections 5.4.2 to 5.4.4) as they are driven by temperature changes.

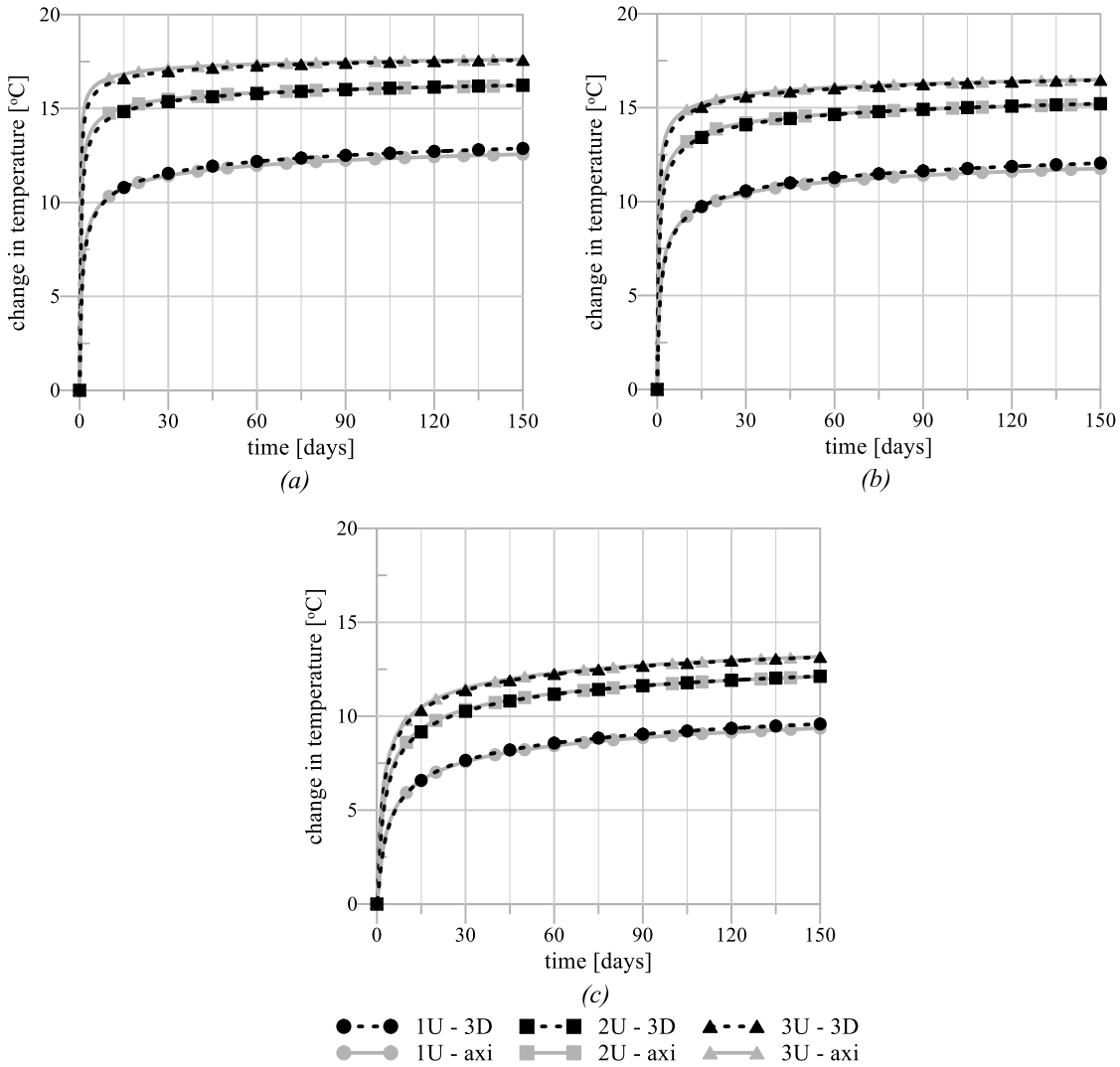


Figure 5.5 Evolutions of temperature changes with time computed with the proposed method and the 3D analyses at (a) centre of pile, (b) edge of pile, and (c) 250 mm away from edge of pile in the soil for the 600 mm diameter pile

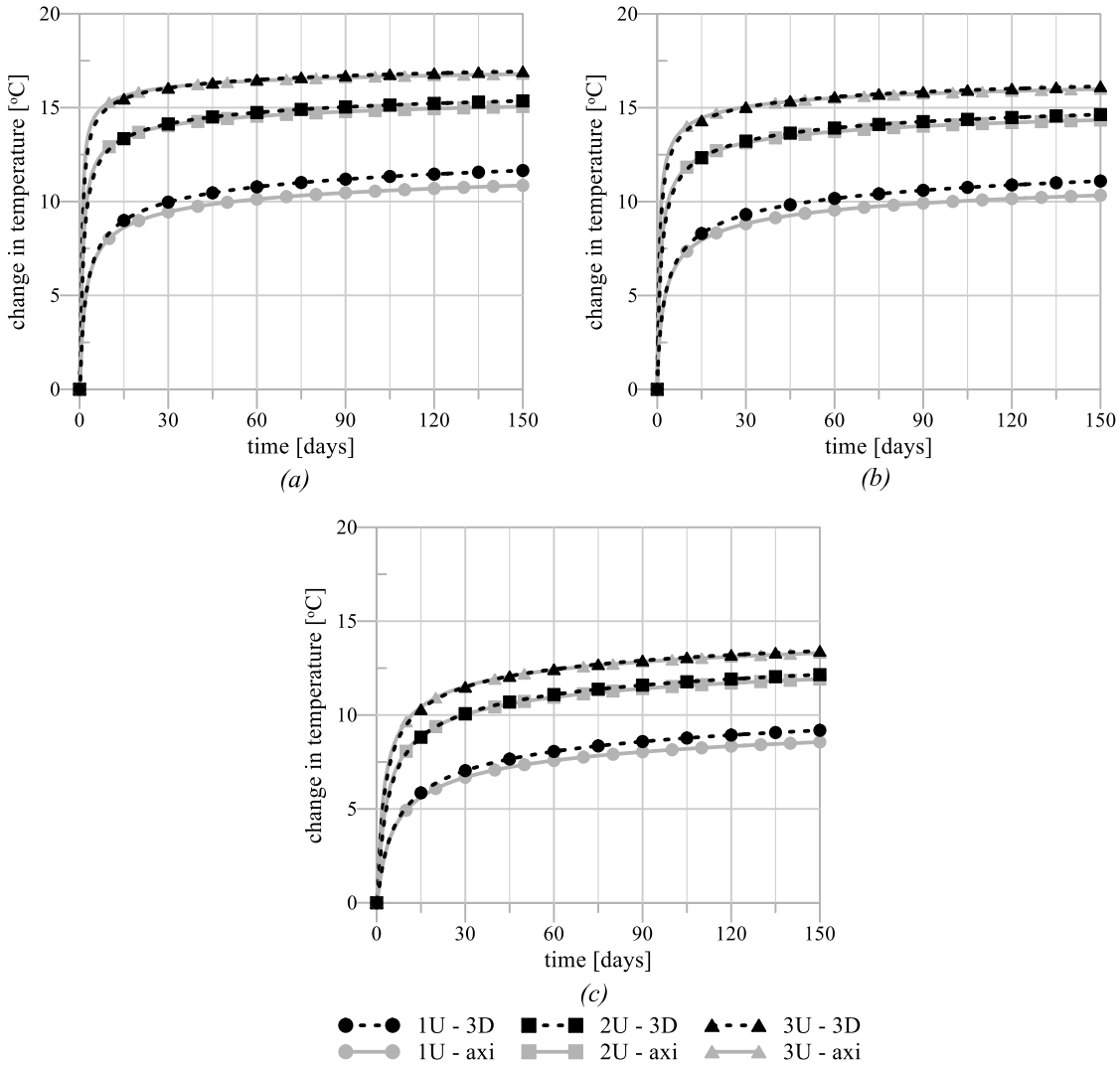


Figure 5.6 Evolutions of temperature changes with time computed with the proposed method and the 3D analyses at (a) centre of pile, (b) edge of pile, and (c) 250 mm away from edge of pile in the soil for the 900 mm diameter pile

5.4.2 Thermally-induced pile head displacements

Figure 5.7 and Figure 5.8 compare the evolutions of thermally-induced pile head displacement with time computed with the proposed method against those obtained from the 3D analyses for the 600 mm and 900 mm diameter piles, respectively. Clearly, it can be seen that the proposed method is capable of predicting with good accuracy the evolution of thermally-induced pile head displacement. This is expected as thermally-induced pile head displacement arises due to temperature changes, which are correctly modelled by the proposed method as demonstrated in Section 5.4.1. Table 5.1 reports the magnitudes of thermally-induced pile head displacements at $t = 150\ days$ given by the proposed method and 3D analyses and the

corresponding relative errors. It can be observed that for all the analysed cases, the maximum difference in thermally-induced pile head displacement at $t = 150\ days$ is less than 3% of the one modelled in the 3D analysis, demonstrating high degree of accuracy of the proposed method. Moreover, it is interesting to note that, with the exception of the 900 mm diameter pile with single U-loop, this approximate methodology yields conservative results.

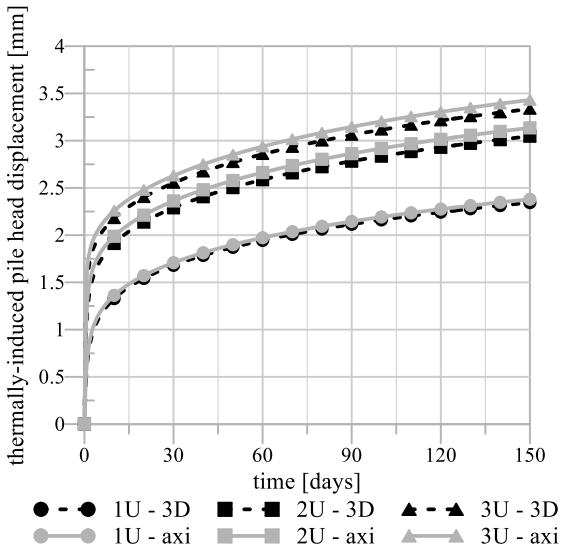


Figure 5.7 Evolutions of thermally-induced pile head displacement with time computed with the proposed method and the 3D analyses for the 600 mm diameter pile

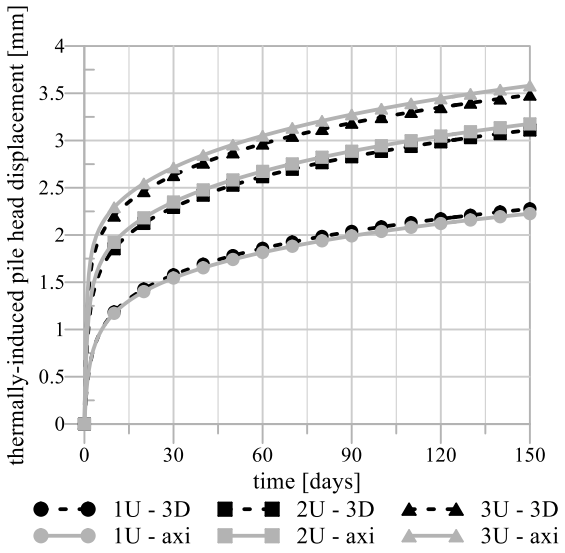


Figure 5.8 Evolutions of thermally-induced pile head displacement with time computed with the proposed method and the 3D analyses for the 900 mm diameter pile

Pile diameter $[mm]$	Pipe arrangement	Thermally-induced pile head displacement $[mm]$		Relative error [%]
		Proposed method	3D analysis	
600	1U	2.4	2.3	1.5
	2U	3.1	3.0	2.9
	3U	3.4	3.3	2.9
900	1U	2.2	2.3	−2.2
	2U	3.2	3.1	2.1
	3U	3.6	3.5	2.8

Table 5.1 Magnitudes of thermally-induced pile head displacement at $t = 150\ days$ simulated by the proposed method and 3D analyses and the corresponding relative errors

5.4.3 Thermally-induced pile axial stresses

Figure 5.9 compares, for both pile geometries and the three different pipe configurations, the evolution with time of the cross-sectionally averaged maximum thermally-induced pile axial stress $\overline{\sigma_T}_{max}$ computed with the proposed method to those obtained from the 3D analyses, while Table 5.2 reports the magnitudes of peak $\overline{\sigma_T}_{max}$ given by the proposed method and 3D analyses and the corresponding relative errors. Referring to Figure 5.9, it can clearly be observed that the proposed method is capable of simulating with good accuracy the value of peak $\overline{\sigma_T}_{max}$, the time instants at which it occurs, as well as the overall transient behaviour of each pile. This is again expected as thermally-induced pile axial stresses are driven by temperature changes, which are correctly modelled by the proposed method as demonstrated in Section 5.4.1. Referring to Table 5.2, for all the analysed cases, the maximum difference in peak $\overline{\sigma_T}_{max}$ is less than 7% of the one recorded in the 3D analysis, demonstrating the high degree of accuracy of the proposed method. Moreover, despite the low values of error, it is still important to highlight that conservative estimates have been returned by the proposed method for all the considered cases.

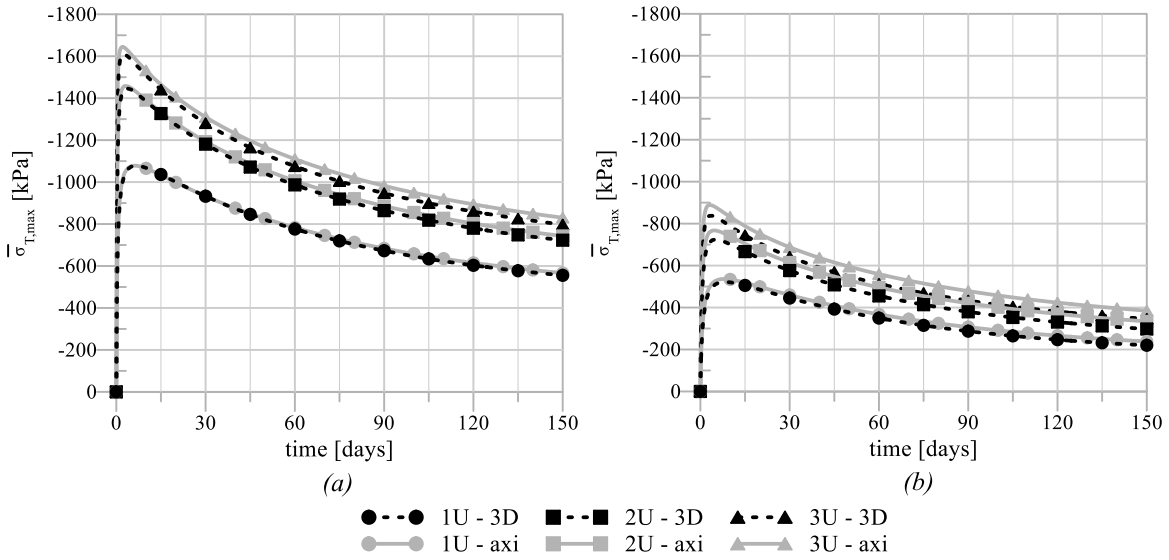


Figure 5.9 Evolution of $\overline{\sigma_T}_{max}$ with time computed with the proposed method compared with those from the 3D analyses for the (a) 600 mm and (b) 900 mm piles

Pile diameter [mm]	Pipe arrangement	Peak $\overline{\sigma_T}_{max}$ [kPa]		Relative error [%]
		Proposed method	3D analysis	
600	1U	1078.5	1078.6	0.0
	2U	1458.6	1445.3	0.9
	3U	1644.5	1610.7	2.1
900	1U	536.3	521.4	2.9
	2U	767.5	724.5	5.9
	3U	889.3	837.5	6.2

Table 5.2 Magnitudes of peak $\overline{\sigma_T}_{max}$ computed with the proposed method and 3D analyses and the corresponding errors

5.4.4 Thermally-induced excess pore water pressures

Figure 5.10 and Figure 5.11 compare the evolution with time of the thermally-induced excess pore water pressures at 250 mm away from the pile edge in the soil computed with the proposed method against those obtained from the 3D analyses (averaged at the corresponding radial distance from the centre of the pile using the mean value theorem for integrals) at pile mid-depth, for the 600 mm and 900 mm diameter piles, respectively. Table 5.3 reports the

magnitudes of peak thermally-induced excess pore water pressure given by the proposed method and 3D analyses and the corresponding relative errors. Referring to Figure 5.10 and Figure 5.11, it can be observed that the proposed method is capable of simulating with good accuracy the value of peak thermally-induced excess pore water pressures, the time instants at which they occur, as well as the long-term dissipation of excess pore water pressures taking place around each pile. This is expected due to the correct simulation of the drainage conditions (permeability and drainage paths), temperature changes within the pile and the surrounding soil (as demonstrated in Section 5.4.1), as well as the transient reduction in thermally-induced pile axial stresses (as demonstrated in Section 5.4.3). On the other hand, Table 5.3 shows that for all the analysed cases, the maximum difference in peak thermally-induced excess pore water pressure is less than 8% of the one recorded in the 3D analysis, demonstrating the high degree of accuracy of the proposed method.

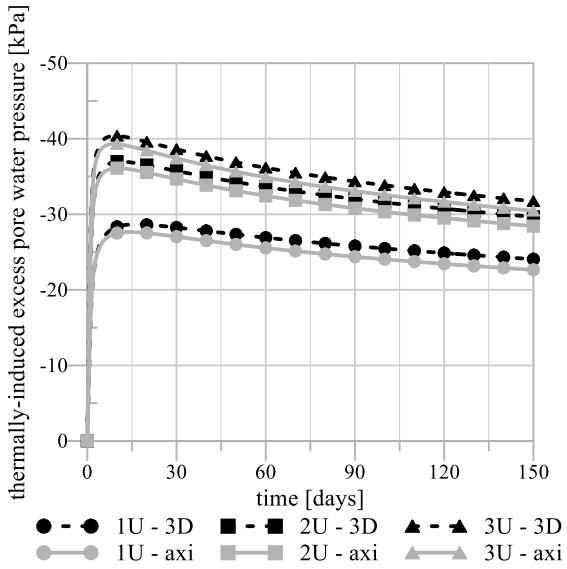


Figure 5.10 Evolutions of thermally-induced excess pore water pressure with time computed with the proposed method and the 3D analyses at 250 mm away from edge of pile in the soil for the 600 mm diameter pile

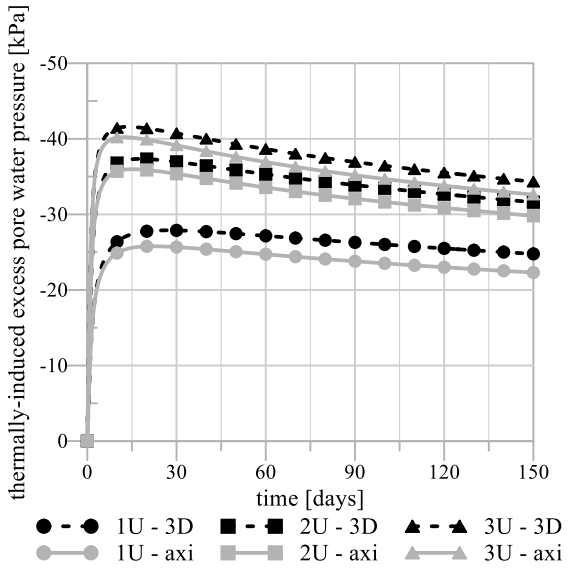


Figure 5.11 Evolutions of thermally-induced excess pore water pressure with time computed with the proposed method and the 3D analyses at 250 mm away from edge of pile in the soil for the 900 mm diameter pile

Pile diameter [mm]	Pipe arrangement	Peak thermally-induced excess pore water pressure [kPa]		Relative error [%]
		Proposed method	3D analysis	
600	1U	27.7	28.7	−3.5
	2U	36.1	37.0	−2.4
	3U	39.3	40.4	−2.7
900	1U	25.8	27.9	−7.6
	2U	36.0	37.3	−3.7
	3U	40.2	41.6	−3.3

Table 5.3 Magnitudes of peak thermally-induced excess pore water pressure computed with the proposed method and 3D analyses and the corresponding errors

5.5 SENSITIVITY OF THE PROPOSED METHOD TO Δ*E* ESTIMATE

Referring to the description of the proposed method in Section 5.2, the only source of uncertainty in its application arises from the need to estimate the temperature profiles along the

heat exchanger pipes, which is based on an assumed power ΔE injected or extracted from the pile, in order to apply Equation (5.1). Given that alternative approaches could be used to estimate the value of ΔE (e.g. using local knowledge on the performance of thermo-active structures), the sensitivity of the proposed method to this quantity has to be assessed. In this sensitivity study, only the evolution of $\overline{\sigma_T}_{max}$ with time is considered for brevity.

The proposed method is applied to the six piles considered in Chapter 4 and Section 5.4 (pile diameters of 600 mm and 900 mm and pipe arrangements of 1U, 2U and 3U) by assuming two extreme values for ΔE, 0 $W \cdot m^{-1}$ and 210 $W \cdot m^{-1}$. It should be appreciated that $\Delta E = 0\ W \cdot m^{-1}$ represents the most conservative case, as it leads to the highest applied temperatures in the 2D thermal analysis (i.e. $T_{in,mid} = T_{out,mid} = T_{in}$) and are also independent of the number of U-loops, while $\Delta E = 210\ W \cdot m^{-1}$ represents a typical upper bound value found in the literature (e.g. Bourne-Webb (2013), see Table 2.2 in Chapter 2).

The evolutions of $\overline{\sigma_T}_{max}$ with time from the analyses are given in Figure 5.12, while Table 5.4 outlines the magnitudes of peak $\overline{\sigma_T}_{max}$ and the relative reduction in the predicted values of peak $\overline{\sigma_T}_{max}$ when ΔE increases from 0 $W \cdot m^{-1}$ to 210 $W \cdot m^{-1}$.

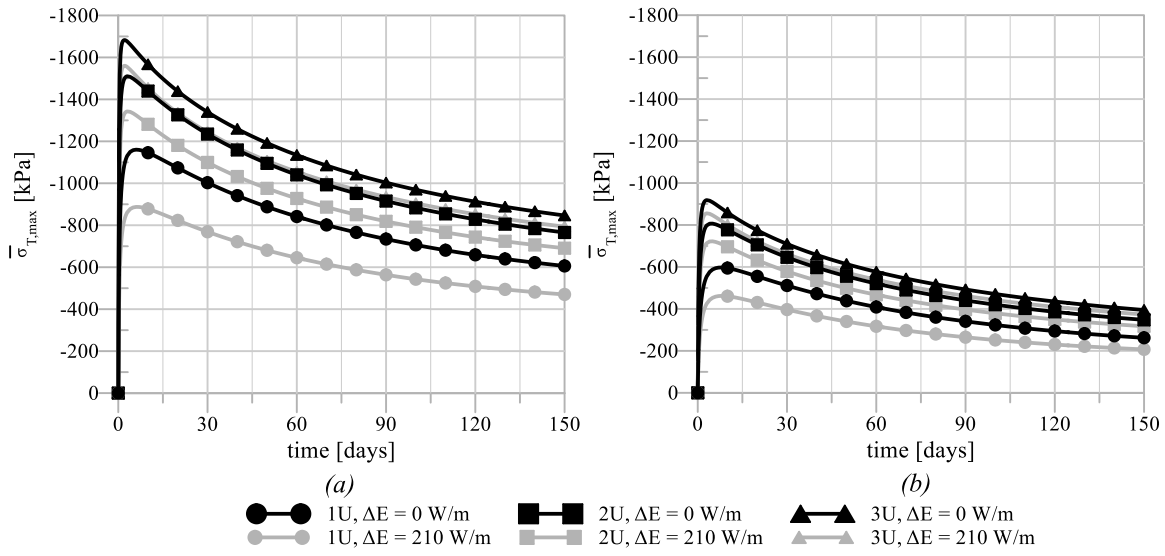


Figure 5.12 Evolution of $\overline{\sigma_T}_{max}$ with time simulated from the proposed method using $\Delta E = 0\ W \cdot m^{-1}$ and 210 $W \cdot m^{-1}$ for the (a) 600 mm and (b) 900 mm piles

Pile diameter $[mm]$	Pipe arrangement	Peak $\overline{\sigma_{T}}_{max}$ [kPa]		Variation of peak $\overline{\sigma_{T}}_{max}$ when ΔE increases from $0\ W \cdot m^{-1}$ to $210\ W \cdot m^{-1}$ [%]
		Proposed method using $\Delta E = 0\ W \cdot m^{-1}$	Proposed method using $\Delta E = 210\ W \cdot m^{-1}$	
600	1U	1160.3	887.4	−23.5
	2U	1510.1	1342.5	−11.1
	3U	1682.5	1559.9	−7.3
900	1U	597.5	462.1	−22.7
	2U	806.6	722.1	−10.5
	3U	918.6	855.6	−6.9

Table 5.4 Magnitudes of peak $\overline{\sigma_{T}}_{max}$ given by the proposed method using $\Delta E = 0\ W \cdot m^{-1}$ and $210\ W \cdot m^{-1}$ and the percentage reduction of peak $\overline{\sigma_{T}}_{max}$ when ΔE increases from $0\ W \cdot m^{-1}$ to $210\ W \cdot m^{-1}$

Referring to Figure 5.12 and Table 5.4, it can be observed that there are relatively limited changes in the simulated evolution of $\overline{\sigma_{T}}_{max}$ when ΔE increases from $0\ W \cdot m^{-1}$ to $210\ W \cdot m^{-1}$, particularly when compared to the very large range of possible temperature profiles within the heat exchanger pipes (represented in the proposed method by $T_{in,mid}$ and $T_{out,mid}$) considered in this study, which are determined based on the assumed thermal performance (ΔE). The results presented suggest that the sensitivity of the proposed method to ΔE, while relatively independent of the pile diameter, varies significantly with pipe arrangement. However, it should be appreciated that as the number of U-loops increases, for example, from one to three, ΔE per U-loop reduces from $210\ W \cdot m^{-1}$ to $70\ W \cdot m^{-1}$. As a result, the estimated drop in temperature between the pipes' inlets and outlets is smaller when a larger number of U-loops is used and becomes more similar to the case of $\Delta E = 0\ W \cdot m^{-1}$. This explains the smaller difference in $\overline{\sigma_{T}}_{max}$ obtained for the two extreme cases considered when the number of U-loops increase. As expected, maximum thermally-induced axial stresses are determined for $\Delta E = 0\ W \cdot m^{-1}$, suggesting that this value can be used when either a conservative design is required or when considerable uncertainty surrounds the assumed temperature profiles along the heat exchanger pipes.

5.6 CONCLUSIONS

Although the thermo-mechanical behaviour of thermo-active piles can be simulated accurately with the 3D analyses presented in Chapter 4, these analyses are computationally expensive to perform, rendering these analyses impractical in routine engineering design. As a result, a simplified method to predict the thermo-mechanical behaviour of thermo-active piles is presented in this chapter. This simplified method involves the modelling of thermo-mechanical behaviour of thermo-active piles using simpler axisymmetric analysis, where the modelling of heat exchanger pipes is replaced by the use of a prescribed temperature thermal boundary condition. This applied temperature is determined from a 2D thermal analysis which models the discrete nature and precise location of the heat exchanger pipes within the pile cross-section. The thermal boundary conditions to be applied in this 2D thermal analysis are determined based on an assumed power of the thermo-active pile, which forms the only uncertainty of this method. It is found that an assumption of $35\ W$ per m^2 of earth-contact area, as suggested by Brandl (2006) for piles with diameter $\geq 600mm$, yields accurate thermo-mechanical responses (with temperature changes, thermally-induced pile head displacements, pile axial stresses and excess pore water pressures considered) in both $600mm$ and $900mm$ piles. However, in scenarios where the thermal performance is uncertain, it is recommended that the design inlet temperature is to be prescribed at all the heat sources in the 2D thermal analysis (i.e. assuming $\Delta E = 0\ W \cdot m^{-1}$). It should be appreciated that other thermally-induced quantities that are not considered (e.g. thermally-induced shear stresses, radial stresses, pile toe displacement, etc.) should be able to be modelled with high degree of accuracy with the simplified method as well, as these thermally-induced quantities are all temperature driven and the 2D axisymmetric analysis captures the true geometry of the problem on the soil side.

CHAPTER 6 DEVELOPMENT OF A NEW HEAT OF HYDRATION MODEL FOR CONCRETE

6.1 INTRODUCTION

Significant research has been dedicated to investigating the response of thermo-active structures, such as piles, retaining walls and tunnels, and their effects on soil due to their operation. However, it has to be appreciated that the construction of these structures, which are often made with cast-in-situ concrete, involves the generation of significant heat due to concrete hydration, and as a result it is imperative to consider the effects of the resulting temperature changes. In effect, it is possible that, at least for larger pile diameters, the maximum temperature reached during the hydration of concrete is of the same order of magnitude of that observed during the operation of thermo-active structures. Indeed, a temperature of 63^oC (about 50^oC above ambient ground temperature) was recorded at the reinforcement cage of a $1.2\ m$ diameter pile (Johnson, 2016), with temperatures at the centre of the pile expected to be even larger. High temperatures developing within concrete create large thermal gradients, which can induce thermal stresses and strains that lead to the development of thermal cracking. For instance, Liou (1999) reported thermal cracking on the inner face of a $100\ m$ diameter, $2.8\ m$ thick and $119\ m$ deep cylindrical, cast-in-place concrete diaphragm wall in Japan, and the author concluded that the thermal stresses resulting from the heat of hydration of concrete are as significant as the soil and water pressures acting on the outside of the wall. As a result, a model that can simulate the evolution of heat of hydration from concrete, which can be coupled with geotechnical engineering software (such as ICFEP), is necessary in order to capture any potential mechanical response associated with the heat of hydration of concrete.

In parallel, the evolution of heat of hydration from hydrating concrete inspired the development of a new non-destructive technique for evaluating the post-construction integrity of piles, which is known as thermal integrity profiling (TIP). In a TIP operation, the temperature field within a pile is measured during and after the casting, and the appearance of local variations in temperature indicate the presence of anomalies within the concrete pile. When the temperature measurements from a TIP operation are back-analysed with a heat of hydration model, an estimate of pile diameter variation with depth can be provided, which can then be compared to the one assumed during the design stage. In the context of the current research, such

temperature measurements would allow a heat of hydration model coupled with a geotechnical engineering software which is capable of analysing such a boundary value problem to back-calculate the model parameters associated with the concrete measured, and forward predict the temperature fields resulting from subsequent casts using the same concrete mix, hence allowing its effects in the surrounding soil to be assessed.

This chapter begins with an introduction to the nature of heat of hydration of concrete, which includes an in-depth review of the exothermic chemical reactions between cement and water that lead to the release of heat, together with the factors that influence the amount and rate of hydration heat liberation. Subsequently, in Section 6.3, heat of hydration measurements from the field and different types of laboratory tests available in the literature are reviewed in order to characterise the amount of heat or temperatures that should be anticipated resulting from hydrating concrete. In Section 6.4, a review of the existing heat of hydration models for concrete is provided, together with a rationale for the development of a new concrete heat of hydration model for geotechnical engineering applications. Finally in Section 6.5, a new heat of hydration model for concrete is derived and introduced, including a summary of the required input parameters. Note that contents of this chapter were published in part or whole in Liu et al. (2022).

6.2 HEAT OF HYDRATION OF CONCRETE

The hydration of concrete can be referred to as the hydration reaction between Portland cement and water. Portland cement is a multi-component system, and its hydration reaction with water is highly complex which involves chemical reactions taking place both in parallel and successively (Odler, 1998). The main components (referred to in concrete technology as phases) of Portland cement which are responsible for the hydration heat generation are tricalcium silicate (C_3S), dicalcium silicate (C_2S), tricalcium aluminate (C_3A) and tetracalcium aluminoferrite (C_4AF) and their reactions with water can be briefly described by Equations (6.1) to (6.4) (Sedaghat, 2016):

$$2C_3S + 11H_2O \longrightarrow C_3S_2H_8 + 3CH \tag{6.1}$$

$$2C_2S + 9H_2O \longrightarrow C_3S_2H_8 + CH \tag{6.2}$$

$$C_3A + 3C\hat{S}H_2 + 26H \longrightarrow 26H_2O + C_6A\hat{S}_3H_{32} \tag{6.3}$$

$$C_4AF + 3C\hat{S}H_2 + 21H_2O \longrightarrow C_6(A,F)\hat{S}_3H_{32} + (F,A)H_3 \tag{6.4}$$

where C is CaO, S is SiO_2, A is Al_2O_3, F is Fe_2O_3, M is MgO, $\hat{S}$ is SO_3, H is H_2O, $C\hat{S}H_2$ is gypsum, $C_3S_2H_8$ is commonly known as the C-S-H gel and is primarily responsible for the strength of concrete, and $C_6A\hat{S}_3H_{32}$ is ettringite (which together with $C_6(A,F)\hat{S}_3H_{32}$, are alumina, ferric oxide, tri-sulphate (AFt) phases). When all available gypsum is consumed, the AFt phases then react with C_3A and C_4AF to form alumina, ferric oxide, mono-sulphate (AFm) phases, and the reaction between ettringite and C_3A to form a calcium aluminate monosulphate hydrate ($C_4A\hat{S}H_{12}$) (which is an AFm phase) is given by Equation (6.5) (Odler, 1998).

$$C_6A\hat{S}_3H_{32} + 2C_3A + 4H \longrightarrow 3C_4A\hat{S}H_{12} \tag{6.5}$$

According to Odler (1998), the hydration reaction between cement and water can be characterised by four stages: pre-induction period (Stage I), induction period (Stage II), acceleration stage (Stage III) and post-acceleration period (Stage IV). A brief description of the reactions taking place in each of the four stages are summarised from van Breugel (1991), Odler (1998) and Sedaghat (2016) in the following paragraphs, with Figure 6.1 showing the progress of hydration of the four main cement constituents with time (Odler, 1998) and the approximate limits of the four hydration stages.

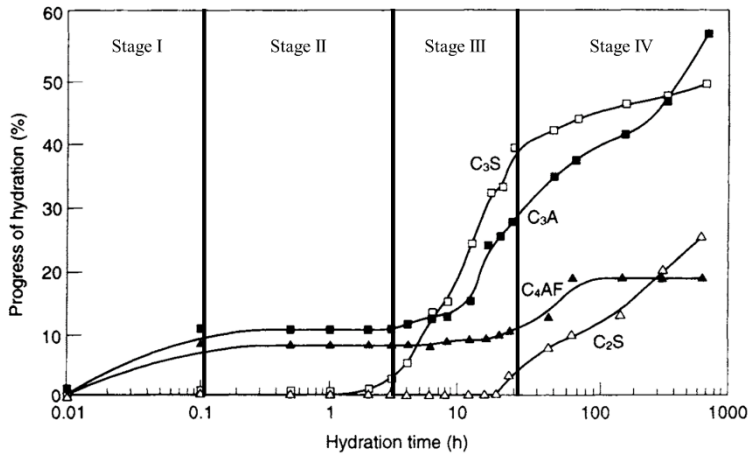


Figure 6.1 Progress of hydration of the four main cement constituents with time (Odler, 1998) and the approximate limits of the four hydration stages

Stage I – the pre-induction period only lasts for a few minutes. This stage is characterised by the dissolution of various cement phases, together with gypsum, ionic compounds and alkali

sulphates, to form hydrate phases. Around 2-10% of C_3S is hydrated during this stage, forming a layer of C-S-H on the cement particles. C_3A reacts with gypsum to form ettringite, which precipitates on the cement particles, with around 5-25% of C_3A hydrated during this stage. Similar to C_3A, C_4AF reacts to form an AFt phase, while a very small fraction of C_2S also reacts during this stage to form the C-S-H gel. Note that this stage occurs rapidly but is short-lived as the process is quickly slowed down by the deposition of hydrated products on the surface of cement particles.

Stage II – the induction period, which is also known as the dormant period and follows the pre-induction period, only lasts for a few hours. This stage is characterised by the slow rate of hydration of all phases and, as a result, the liberation of hydration heat is very limited.

Stage III – the acceleration stage, which follows the induction period, lasts for 3 to 12 hours after mixing. This stage is characterised by the accelerated rate of hydration of C_3S, forming more C-S-H gel, and by the start of hydration of C_2S. Moreover, gypsum becomes completely dissolved as it is continuously consumed to form the AFt phases, which include ettringite.

Stage IV – The post-acceleration period follows the acceleration stage, where the hydration rate slows down gradually as the amount of unreacted material declines. C-S-H is still continuously formed from the hydration of C_3S and C_2S, but the contribution of C_2S increases with time. When all gypsum is consumed, the formed AFt phases then react with C_3A and C_4AF to form AFm phases. If the concrete water-to-cement ratio (w/c, which is the mass ratio of water to cement in a concrete mix) is sufficiently high, the hydration process will continue until all the unhydrated materials are consumed. On the other hand, if the w/c is low, the hydration process will stop, leaving a significant amount of unhydrated materials due to a lack of water for the hydration reactions.

The hydration of cement constituents is an exothermic process (i.e. heat is given out during the process), and the hydration of different cement constituents gives out different amounts of heat (see Table 6.1, which is simplified from Odler (1998)). As a result, the power given out from the concrete mix at a particular instant is dependent on the power of the cement constituents at that instant. Figure 6.2 shows the evolution with time of the rate of hydration heat liberation $[J \cdot s^{-1} \cdot kg_{cement}^{-1}]$ for an ordinary Portland cement (Odler, 1998). Odler (1998) has provided explanations to the observations in Figure 6.2, which are summarised as follows:

- there is a negative rate of hydration heat liberation at the beginning of the hydration process (indicated by '1' in Figure 6.2). This is due to the dissolution of potassium sulphate, which is an endothermic process.
- the rapid hydration of C_3S and C_3A during the pre-induction period gives rise to the first peak of rate of hydration heat liberation (indicated by '2' in Figure 6.2).
- as the rate of hydration slows down during the induction period, the rate of hydration heat liberation drops as well (indicated by '3' in Figure 6.2).
- during the acceleration stage, a second peak of rate of hydration heat liberation is reached due to the hydration of C_3S (indicated by '4' in Figure 6.2).
- following this peak, the rate of hydration heat liberation reduces gradually to very low values. However, two more local peaks may be observed (indicated by '5' and '6' in Figure 6.2), which are due to the formation of AFt phases and AFt-AFm conversion respectively.

Note that the negative and first peaks of rate of hydration heat liberation, which occur within minutes of mixing, may not be very relevant to geotechnical engineering applications. Indeed, in practice, concrete is not cast immediately after mixing, meaning that the negative and first peaks of rate of hydration heat liberation occur within the mixer rather than after casting or within the soil, which leads to slightly higher initial temperature and can be considered implicitly in the casting temperature (De Schutter & Taerwe, 1995).

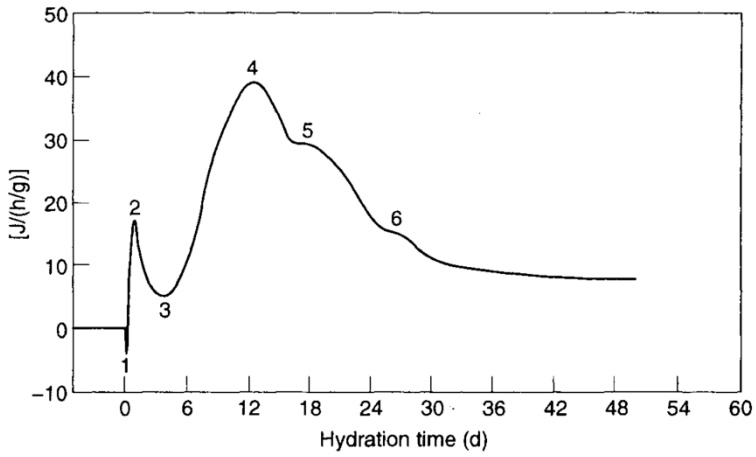


Figure 6.2 Rate of hydration heat liberation with time for an ordinary Portland cement (Odler, 1998)

Reactant	Main reaction product	Heat of hydration $[kJ \cdot kg^{-1}]$
C_3S	C-S-H gel	520
C_2S	C-S-H gel	260
C_3A	$C_6A\hat{S}_3H_{32}$	1670
C_3A	$C_4A\hat{S}H_{12}$	1140
C_4AF	$C_3(A,F)H_6$	420

Table 6.1 Heat of hydration of different cement constituents (simplified from Odler (1998))

According to van Breugel (1991) and Odler (1998), the hydration of cement, and hence the amount and rate of hydration heat liberation, is influenced by a number of factors, which include, but are not limited to:

- the composition of cement – cements with different proportions of constituents behave differently in terms of both the total amount of heat liberated at the end of hydration and the rate of hydration at early ages (hence rate of hydration heat liberation). For example, cements with higher contents of C_3S and C_3A generate more heat and have higher rates of hydration heat liberation (Portland Cement Association, 1997).
- the fineness of cement – cements with higher fineness provide a larger surface area for reaction with water, and hence have higher rates of hydration heat liberation at early ages (Portland Cement Association, 1997; Bentz et al., 1999; Schindler & Folliard, 2005; Sedaghat et al., 2015). However, the total amount of heat liberated at the end of hydration is unaffected by cement fineness (Portland Cement Association, 1997; Bentz et al., 1999).
- the water to cement ratio, w/c – when the w/c is not sufficiently high, incomplete hydration will occur as there is not enough water to sustain the hydration reaction. In such situation, the total amount of hydration heat liberated will be reduced. However, the heat of hydration experiments conducted by Bentz et al. (2009) have shown that the influence of w/c on heat of hydration begins to diminish when w/c approaches 0.425.
- the curing temperature – an increase in curing temperature leads to a higher rate of hydration heat liberation at early ages, however the total amount of heat liberated at the end of hydration appears to be unaffected by the curing temperature (Carlson & Forbrich, 1938). Moreover, Copeland et al. (1960) suggested that the dependence of the

rate of hydration on the curing temperature is related to the Arrhenius equation, as a linear relationship is obtained by plotting the log of rate of hydration and the reciprocal of temperature using the experimental data (the same cement hydrated at different temperatures) provided by Carlson and Forbrich (1938).

- the presence of any admixtures – for example, the use of fly ash can reduce both the total amount of heat liberated from the hydration reaction, as well as the rate of hydration heat liberation (Portland Cement Association, 1997).

As a result, in order to model correctly the amount and rate of heat liberated due to the hydration of concrete, the above factors have to be taken into account by the model.

6.3 MEASUREMENTS OF HEAT OF HYDRATION

This section aims to provide a few examples from the literature where heat of hydration is measured, both in the laboratory during different types of heat of hydration tests (Section 6.3.1) and in the field (Section 6.3.2), thus characterising the magnitude of heat fluxes and temperatures that can be anticipated from and within hydrating concrete.

6.3.1 Laboratory measurements

Laboratory testing for determining concrete heat of hydration can broadly be classified into three different types according to the thermal boundary conditions imposed during the test: adiabatic, semi-adiabatic, and isothermal.

6.3.1.1 Adiabatic test

In an adiabatic test, no heat loss is allowed from the hydrating sample to the surroundings, such that all the heat of hydration liberated by the concrete is used to heat up the hydrating concrete itself, resulting in a monotonic temperature rise. According to Caggiano et al. (2012) and Lim et al. (2016), this is achieved by casting the concrete in an apparatus, where the thermal boundary conditions are controlled by a computer and a cryostat unit, which ensure that the temperature of the chamber of the apparatus matches that of the concrete: with no thermal gradient between the concrete and the apparatus, heat loss is prevented. However, the test equipment for adiabatic test is expensive and not many laboratories can perform the test (Lim et al., 2016). The adiabatic test results by Lee et al. (2014) and Shi et al. (2015) are presented.

Lee et al. (2014)

Lee et al. (2014) conducted adiabatic tests on three concrete samples, PSLB-352, PSLB-442 and Type IV, with the types of cement used for each sample presented in Table 6.2. Note that all samples have a w/c of 0.45, a specific heat capacity of $1046\ J \cdot kg^{-1} \cdot K^{-1}$, a density of $2300\ kg \cdot m^{-3}$ and an initial placement temperature of 20^oC. Figure 6.3 shows the measured adiabatic temperature rise curves for the samples (Lee et al., 2014). In the adiabatic tests, the Type IV concrete sample reaches the highest temperature rise of 37.5^oC, followed by the PSLB-442 and PSLB-352 samples, reaching 30.0^oC and 24.5^oC respectively.

Concrete sample	Types of cement used
PSLB-352	• $114\ kg \cdot m^{-3}$ Ordinary Portland cement • $190\ kg \cdot m^{-3}$ blast-furnace slag • $76\ kg \cdot m^{-3}$ fly ash
PSLB-442	• $152\ kg \cdot m^{-3}$ Ordinary Portland cement • $152\ kg \cdot m^{-3}$ blast-furnace slag • $76\ kg \cdot m^{-3}$ fly ash
Type IV	• $380\ kg \cdot m^{-3}$ Type IV low heat cement

Table 6.2 Types of cement used in the three concrete samples tested by Lee et al. (2014)

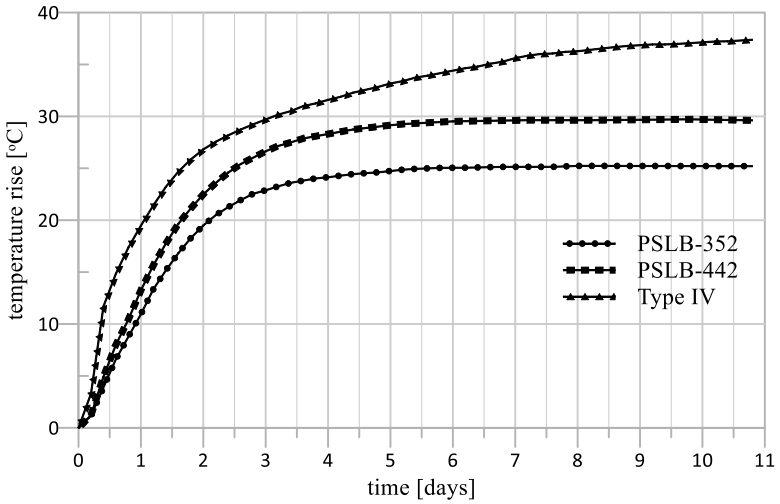


Figure 6.3 Adiabatic temperature rise curves for the three concrete samples tested by Lee et al. (2014)

Shi et al. (2015)

Shi et al. (2015) conducted adiabatic tests on two concrete samples, which are designated as Sample A and Sample B, respectively, in this thesis. Sample A consists of $220\ kg \cdot m^{-3}$

Ordinary Portland cement and 180 $kg \cdot m^{-3}$ fly ash, while Sample B consists of 220 $kg \cdot m^{-3}$ Ordinary Portland cement and 180 $kg \cdot m^{-3}$ slag. The w/c for both samples are 0.42. Figure 6.4 shows the measured adiabatic temperature rise curves for both samples (Shi et al., 2015). In the adiabatic tests, the temperature rise for Samples A and B are $41.85^{o}C$ and $39.46^{o}C$, respectively, after 9 days.

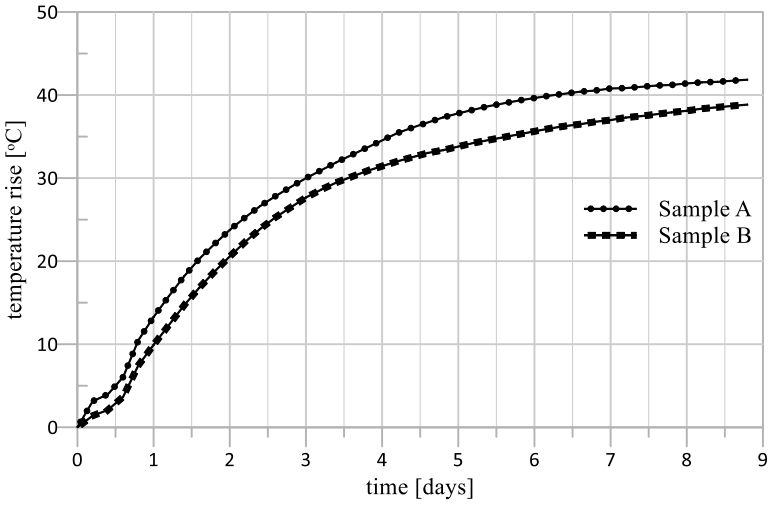


Figure 6.4 Adiabatic temperature rise curves for the two concrete samples tested by Shi et al. (2015)

6.3.1.2 Semi-adiabatic test

In a semi-adiabatic test, some heat loss is allowed from the hydrating sample to the surroundings. This test is simpler than an adiabatic test (Lim et al., 2016) and is conducted by measuring the temperature rise within a hydrating sample, which is surrounded by an insulating material (e.g. expanded polystyrene). No effort is made to change the thermal boundary condition of the sample to compensate for any heat losses. Therefore, the results from a semi-adiabatic test exhibit a very characteristic pattern, whereby the temperature of the sample first increases because of heat of hydration, reaches a peak, then decreases when the rate of heat loss becomes larger than the rate of hydration heat generation. There are different ways in which the semi-adiabatic test can be analysed. For example, the heat losses through the insulating material can be monitored by heat flux sensors, eventually allowing the total heat generated by the hydrating sample to be determined (Wadsö, 2003); or by using finite-element analyses to simulate as closely as possible the experimental set-up and back-calculate the heat flux from the concrete based on the measured semi-adiabatic temperature curves (Lim et al.,

2016). The semi-adiabatic test results by Caggiano et al. (2012) and Lim et al. (2016) are presented.

Caggiano et al. (2012)

Caggiano et al. (2012) performed semi-adiabatic tests on two concrete samples, Mixture 3 and Mixture 4. Mixture 3 consists of $450\ kg \cdot m^{-3}$ CEM I 32.5 cement and 5% of silica-fume, while Mixture 4 consists of $450\ kg \cdot m^{-3}$ CEM II/A cement, with both samples having a w/c of 0.4. Moreover, the samples' dimensions are $750\ mm \times 150\ mm \times 100\ mm$, and are thermally insulated during the test. Temperature is measured at the centre of the sample, at half the sample height. Figure 6.5 shows the semi-adiabatic temperature curves for both samples (Caggiano et al., 2012). In the semi-adiabatic tests, the peak temperature rises for Mixtures 3 and 4 are $20.2^{o}C$ and $17.8^{o}C$, respectively. Clearly, the obtained results adhere to a pattern identical to that described before.

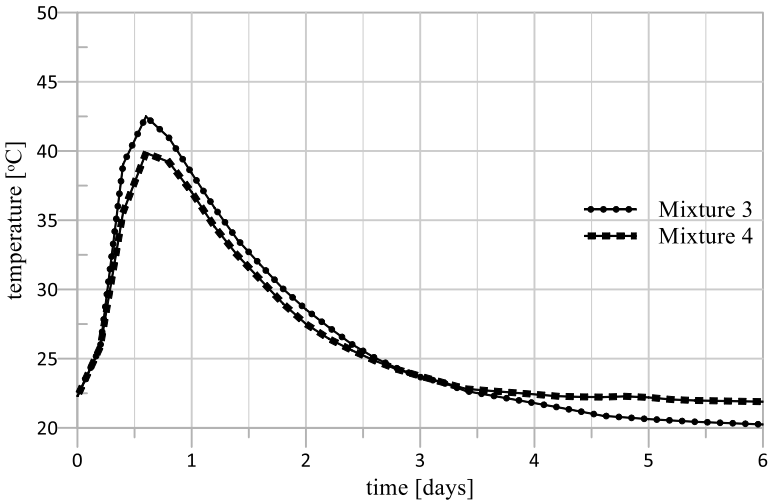


Figure 6.5 Semi-adiabatic temperature curves for the two concrete samples tested by Caggiano et al. (2012)

Lim et al. (2016)

Lim et al. (2016) performed semi-adiabatic tests on a concrete which consists of $226\ kg \cdot m^{-3}$ Ordinary Portland cement, $72\ kg \cdot m^{-3}$ ground granulated blast-furnace slag (GGBS), $61\ kg \cdot m^{-3}$ fly ash and has a w/c of 0.46. Three semi-adiabatic tests were conducted on this concrete, where the samples were $20\ cm$, $30\ cm$ and $40\ cm$ cubes respectively, with $35 - 40\ cm$ thick of expanded polystyrene surrounding the samples as insulation. Temperatures are measured at the centre of the samples and the semi-adiabatic temperature curves are presented in Figure 6.6

(Lim et al., 2016). In the semi-adiabatic tests, the observed peak temperature rises for the $40\ cm, 30\ cm$ and $20\ cm$ cube samples are $32.5^oC, 27.4^oC$ and 20.4^oC, respectively. As expected, larger temperatures correspond to larger volumes of concrete, despite the increase in area through which heat losses take place.

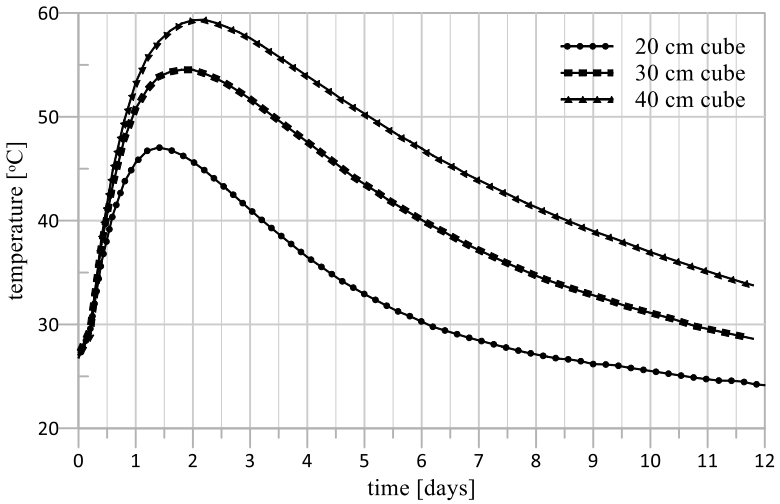


Figure 6.6 Semi-adiabatic temperature curves for the three semi-adiabatic tests conducted by Lim et al. (2016)

6.3.1.3 Isothermal test

In an isothermal test, the hydrating sample is kept at a constant temperature. There are two different types of isothermal tests: isothermal calorimetry and heat of solution. In an isothermal calorimetry test, the heat that is generated from the sample is conducted away to a heat sink through a heat flux sensor, which essentially measures the heat generated by the sample, while keeping the sample temperature constant (Wadsö, 2003). The heat of solution test, on the other hand, measures the total amount of heat produced after a certain period of hydration. This is accomplished by comparing the difference in heat produced between the hydrating sample and an unhydrated one, when they are dissolved in an acid (Wadsö, 2003). The isothermal calorimetry test results by Wadsö (2003) and Zayed et al. (2013) and the heat of solution test results by Verbeck and Foster (1950) and Copeland et al. (1960) are presented.

Isothermal calorimetry tests by Wadsö (2003)

Wadsö (2003) performed isothermal calorimetry tests on the cement 'Anläggningscement', which is a CEM I 42.5 BV/SR/LA cement, at four curing temperatures: $20, 30, 40$ and 50^oC. The results of the isothermal tests are presented in Figure 6.7 as time vs. heat of hydration

power (in power per unit mass of cement $[J \cdot s^{-1} \cdot kg_{cement}^{-1}]$) curves (Wadsö, 2003), which are converted into time vs. accumulated heat of hydration (in energy per unit mass of cement $[J \cdot kg_{cement}^{-1}]$) curves in Figure 6.8. Clearly, it can be observed that an increase in curing temperature leads to a higher rate of hydration heat liberation at early ages, as explained in Section 6.2.

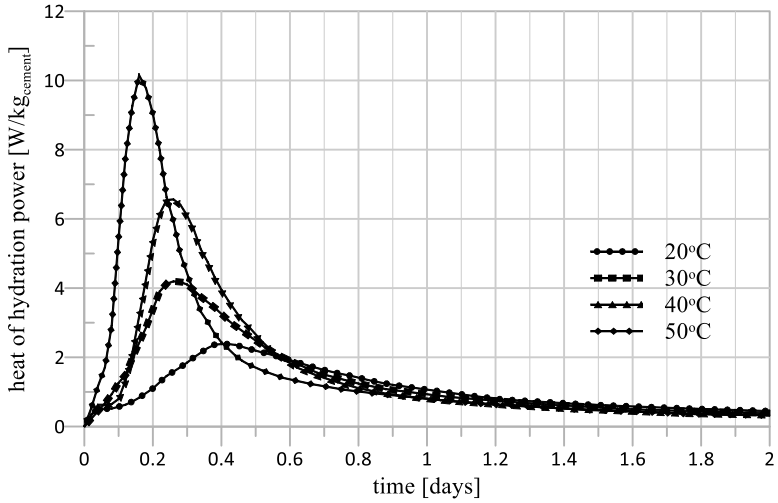


Figure 6.7 Time vs. heat of hydration power curves for cement 'Anläggningscement' at $20, 30, 40$ and $50^{o}C$ (Wadsö, 2003)

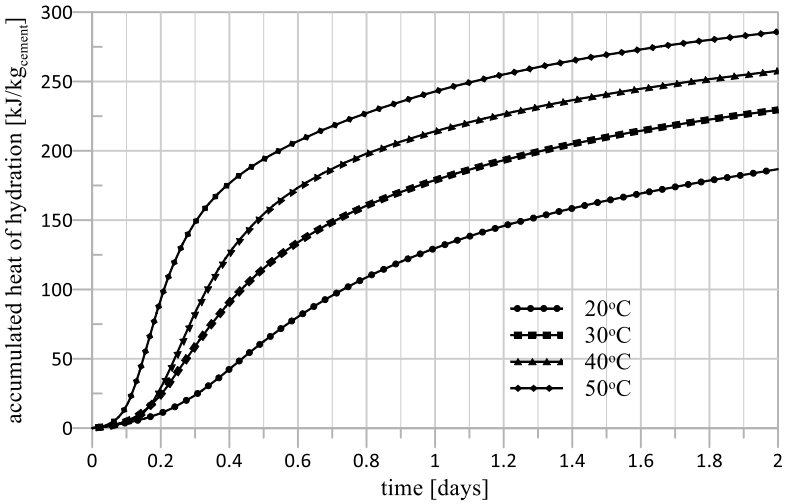


Figure 6.8 Time vs. accumulated heat of hydration curves for cement 'Anläggningscement' at $20, 30, 40$ and $50^{o}C$

Isothermal calorimetry tests by Zayed et al. (2013)

Zayed et al. (2013) conducted 11 isothermal calorimetry tests on six cement samples, which are designated as Cement A, B, C, D, E and F, respectively. Cement A was tested at three fineness levels (designated as Cement A1, A2 and A3 respectively), while Cements B, C and D were tested at two fineness levels (designated as Cement B1, B2, C1, C2, D1 and D2, respectively). Note that all the cements apart from Cement D are Type II (MH) cements (the classification of Cement D was not reported), and that all the samples were isothermally cured at 23^oC during the tests. Table 6.3 reports the Blaine fineness $[m^2 \cdot kg^{-1}]$ of each cement sample and Figure 6.9 to Figure 6.14 show the time vs. accumulated heat of hydration curves for Cements A, B, C, D, E and F, respectively (Zayed et al., 2013). Referring to Figure 6.9 to Figure 6.12, it can be observed that samples with higher fineness levels have higher rates of hydration heat liberation at early ages, which is in accordance with the discussion presented in Section 6.2.

Cement sample	Blaine fineness $[m^2 \cdot kg^{-1}]$
Cement A1	325
Cement A2	414
Cement A3	575
Cement B1	417
Cement B2	617
Cement C1	402
Cement C2	590
Cement D1	405
Cement D2	530
Cement E	426
Cement F	494

Table 6.3 Blaine fineness of the cement samples tested by Zayed et al. (2013)

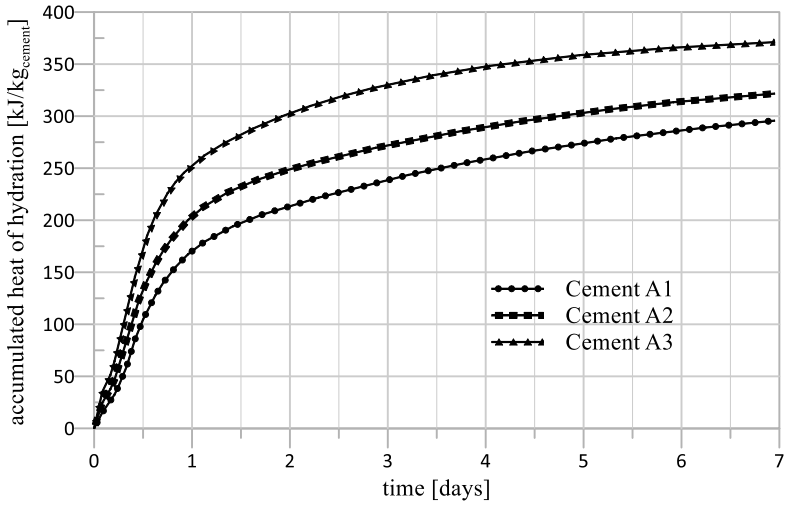


Figure 6.9 Time vs. accumulated heat of hydration curves for Cement A (Zayed et al., 2013)

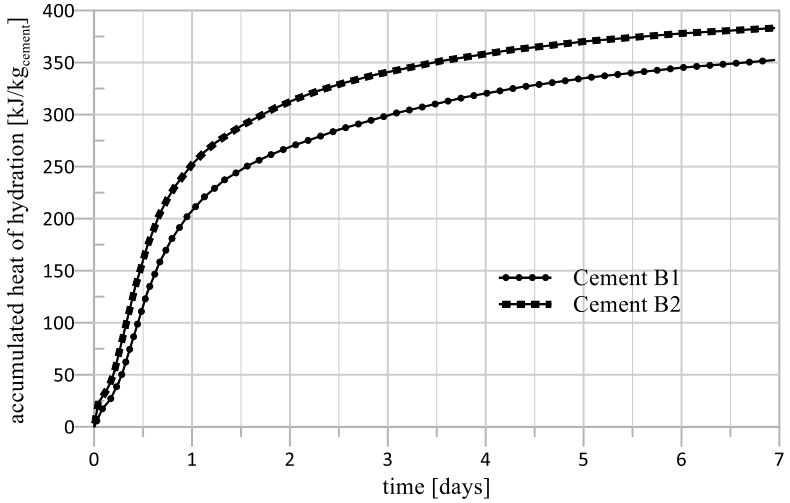


Figure 6.10 Time vs. accumulated heat of hydration curves for Cement B (Zayed et al., 2013)

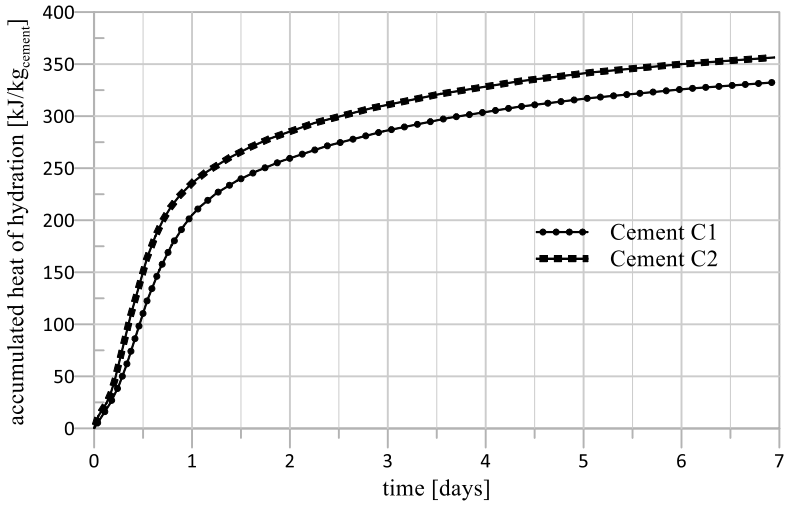


Figure 6.11 Time vs. accumulated heat of hydration curves for Cement C (Zayed et al., 2013)

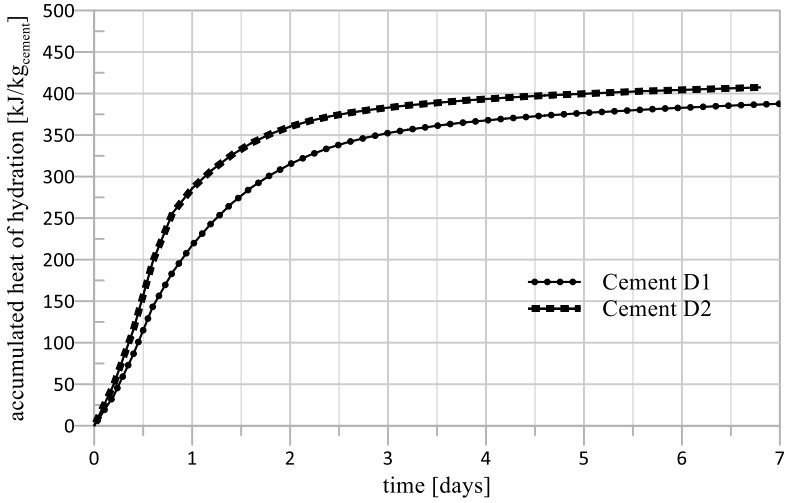


Figure 6.12 Time vs. accumulated heat of hydration curves for Cement D (Zayed et al., 2013)

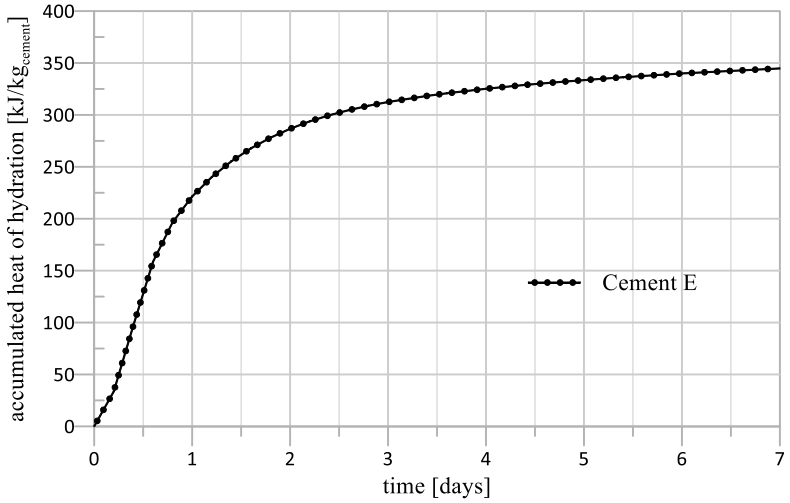


Figure 6.13 Time vs. accumulated heat of hydration curve for Cement E (Zayed et al., 2013)

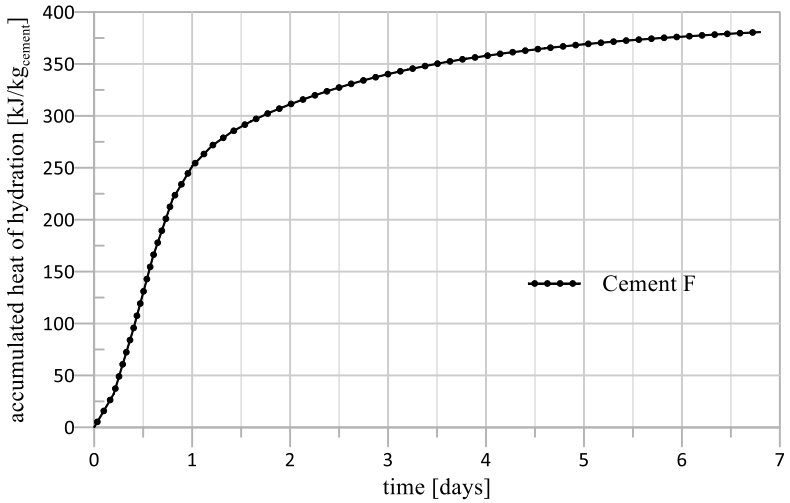


Figure 6.14 Time vs. accumulated heat of hydration curve for Cement F (Zayed et al., 2013)

Heat of solution tests by Verbeck and Foster (1950) and Copeland et al. (1960)

Verbeck and Foster (1950) performed extensive heat of solution tests to investigate the liberation of hydration heat from different ASTM types of cement at w/c of 0.4, and presented results with up to 6.5 years of data. Copeland et al. (1960) then continued their tests and presented up to 13 years of data for these samples, and at the same time started new tests on samples with w/c of 0.6 and 0.8 and presented up to 6.5 years of data for these samples. Table 6.4 reports the results they provided (Verbeck & Foster, 1950; Copeland et al., 1960). Note that Verbeck and Foster (1950) and Copeland et al. (1960) performed the heat of solution tests on a number of samples within each cement type (8 samples for Type I, 5 samples for Type II, 3 samples for Type III and 4 samples for Type IV), therefore the data shown in Table 6.4 represent an average of their samples for the corresponding cement type and w/c, while Figure 6.15 shows a comparison of the ranges in values of heat of hydration obtained for different ASTM types of cement (Copeland et al., 1960). Note that all the samples were cured at an isothermal temperature of 21^oC. Referring to Table 6.4 and Figure 6.15, it can be observed that hydration heat continues to be liberated all the way up to 13 years, and possibly beyond that. However, the small amount of hydration heat being liberated at such a long timescale after the early ages means that the rate of hydration heat liberation after the early ages is negligibly small, which makes it irrelevant in the context of comparing it with those arising from the operation of thermo-active structures, or geotechnical engineering in general. It can therefore be concluded that, in the context of the current research, it is appropriate to consider heat of hydration measurements during the early ages only, when the rates of hydration heat liberation

and resulting temperature changes are significant when compared to other heat sources in the ground (e.g. thermo-active structures).

ASTM cement type	w/c	Accumulated heat of hydration at age indicated $[kJ \cdot kg_{cement}^{-1}]$						
		3 days	7 days	28 days	90 days	1 year	6.5 years	13 years
I	0.4	254.81	331.37	399.99	434.30	454.38	488.69	494.55
	0.6	275.31	366.94	448.11	479.90	502.08	515.05	
	0.8	277.40	374.05	466.93	499.99	511.28	523.00	
II	0.4	196.23	254.81	333.05	368.61	399.15	411.71	421.33
	0.6	207.53	256.48	349.36	396.64	427.19	437.65	
	0.8	206.27	269.03	354.38	415.05	446.85	443.92	
III	0.4	317.57	379.07	425.09	446.85	477.81	504.59	504.17
	0.6	360.24	433.46	501.66	520.49	532.62	532.20	
	0.8	362.75	439.32	506.26	528.44	543.92	546.43	
IV	0.4	171.13	209.62	274.47	311.29	337.23	356.90	365.26
	0.6	180.75	223.84	278.65	329.28	378.23	387.02	
	0.8	174.47	220.92	292.04	345.18	396.64	403.34	

Table 6.4 Average accumulated heats of hydration of different ASTM types of cements cured at $21^{o}C$ (Verbeck & Foster, 1950; Copeland et al., 1960)

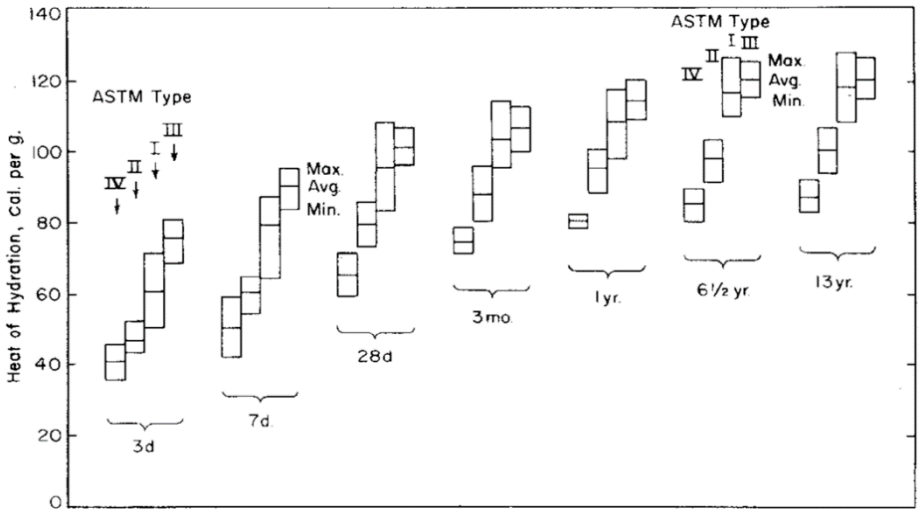


Figure 6.15 Comparison of the ranges in values of heats of hydration for different ASTM types of cement (Copeland et al., 1960)

6.3.2 Field measurements

Heat of hydration of concrete is not only measured in the laboratory, but also in the field, within geotechnical structures. This section presents selected studies published in the literature where temperature rise due to heat of hydration from hydrating concrete is measured within instrumented geotechnical structures. This includes a rise in temperature within hydrating piles which are detected during TIP operations (Johnson, 2016; Sun et al., 2020), as well as within hydrating diaphragm walls (Liou, 1999; Sajadi, 2020).

Johnson (2016)

According to Johnson (2016), more than 200 bored piles (which are referred to as drilled shafts in the paper) were constructed for the widening of the Lee Roy Selmon Expressway in Tampa, Florida, United States, and as part of the TIP operations on the piles, a temperature vs. depth profile is presented for one of the $4\ ft$ (or $1.22\ m$) diameter piles, as shown in Figure 6.16 (Johnson, 2016). It is understood that in Figure 6.16, Tubes 1 to 4 represent four temperature sensors which were attached to the reinforcement cage of the pile, 'Avg' represents the average of the measurements of Tubes 1 to 4, while TOS, BOS and BOC represent top of pile, bottom of pile and bottom of casing, respectively. Clearly, although the time after pouring that the measurements correspond to was not reported, it can be seen that temperatures within the pile can reach up to $55^{o}C$ due to heat of hydration, with the temperature at the centre of the pile expected to be even higher. It can also be observed that a range of temperatures were measured

both within the same depth and along the pile, which may be due to eccentricity of the reinforcement cage (and hence the temperature sensors), anomalies in the casting, or spatial variation of thermal properties in the surrounding soil due to stratigraphy.

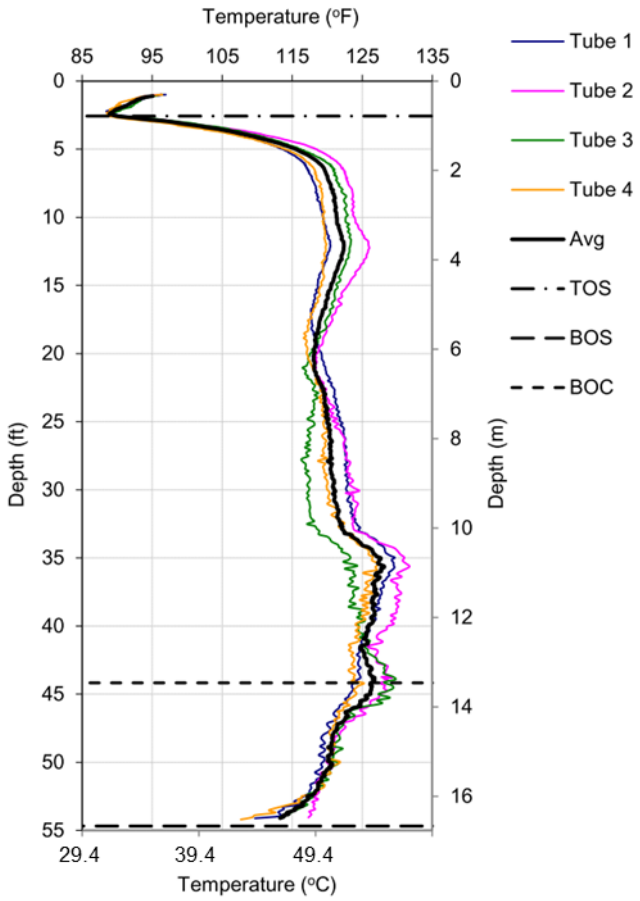


Figure 6.16 Temperature vs. depth profile of a 4 ft (or 1.22 m) diameter hydrating pile (Johnson, 2016)

Apart from the aforementioned 4 ft diameter pile, Johnson (2016) also presented the temperature vs. depth profile of a 10.7 m long, 1.2 m diameter pile, at 18 $hours$ after pouring (when peak temperatures were observed), which is shown in Figure 6.17 (Johnson, 2016). These measurements were taken also as part of a TIP operation. Referring to Figure 6.17, five temperature sensors were attached to the reinforcement cage, with measurements correspond to Wire 1 to 5 respectively. In this case, a peak temperature of around 63^oC was measured, which was around 50^oC above the initial ground temperature. Johnson (2016) explained that the elevated measured temperatures up to a depth of around 3.5 m was due to two reasons: borehole records indicate that the water table was at a depth of 3.4 m, and at the same depth, there is an interface of clay overlying sand, which causes a change in soil conductivity at this

depth; on the other hand, a small annular air gap formed around the pile due to predrilling in the clay layer to install the casing, which provided a thermal insulation for the pile.

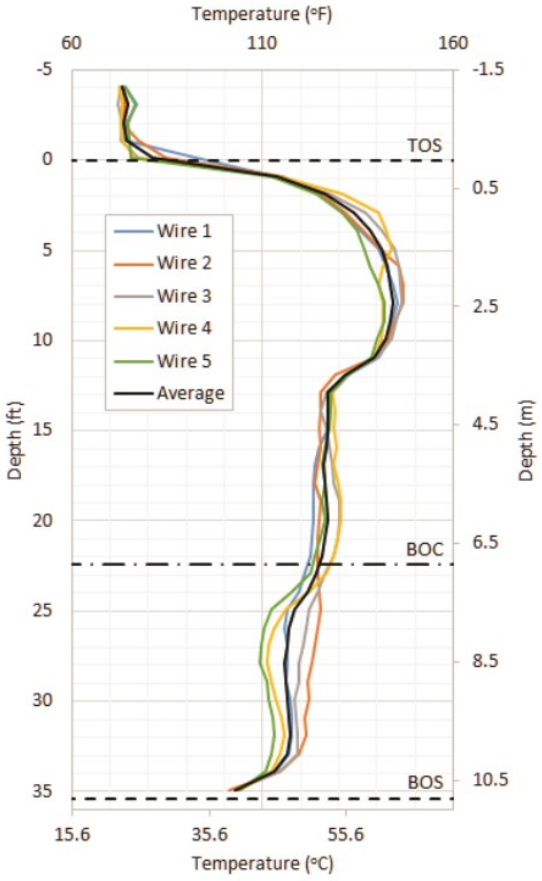


Figure 6.17 Temperature vs. depth profile of a10.7 m long, 1.2 m diameter hydrating pile (Johnson, 2016)

Sun et al. (2020)

Sun et al. (2020) performed a TIP operation on a pile where engineered inclusions were intentionally left within the pile in an attempt to investigate alternative interpretation approaches to TIP operations. The pile considered was 20 m long, 900 mm in diameter with a 750 mm diameter reinforcement cage. Temperatures were measured using thermal wire cables attached to the reinforcement cage, which were positioned 120^o apart from each other in the cross-section. Three engineered inclusions were introduced into the pile at three different locations within the cross-section and positioned at three different levels, with the arrangement shown in Figure 6.18 (Sun et al., 2020). The temperature vs. depth profiles of the pile at 2 $hours$, 8 $hours$, 17 $hours$ and 35 $hours$ are presented in Figure 6.19 (Sun et al., 2020), and

the time vs. temperature curves at 4.9 m and 15.1 m depths are presented in Figure 6.20 (Sun et al., 2020). In Figure 6.19 and Figure 6.20, TIP-1, TIP-2 and TIP-3 represent the measurements from the three thermal wire cables, respectively, Avg represents an average of the three measurements, and Theor represents the theoretical development of temperature (assuming a perfect pile), which was obtained through numerical analyses. Referring to Figure 6.19 and Figure 6.20, it can be observed that a maximum temperature rise of around $11.5^{o}C$ was recorded, as well as a clear trend indicating that smaller temperatures were indeed measured around the engineered inclusions. Note that the initial drop in temperature observed in Figure 6.19(a) and Figure 6.20 is due to the fact that the initial concrete temperature was higher than the ground temperature, so there was a loss of heat to the cooler ground upon casting.

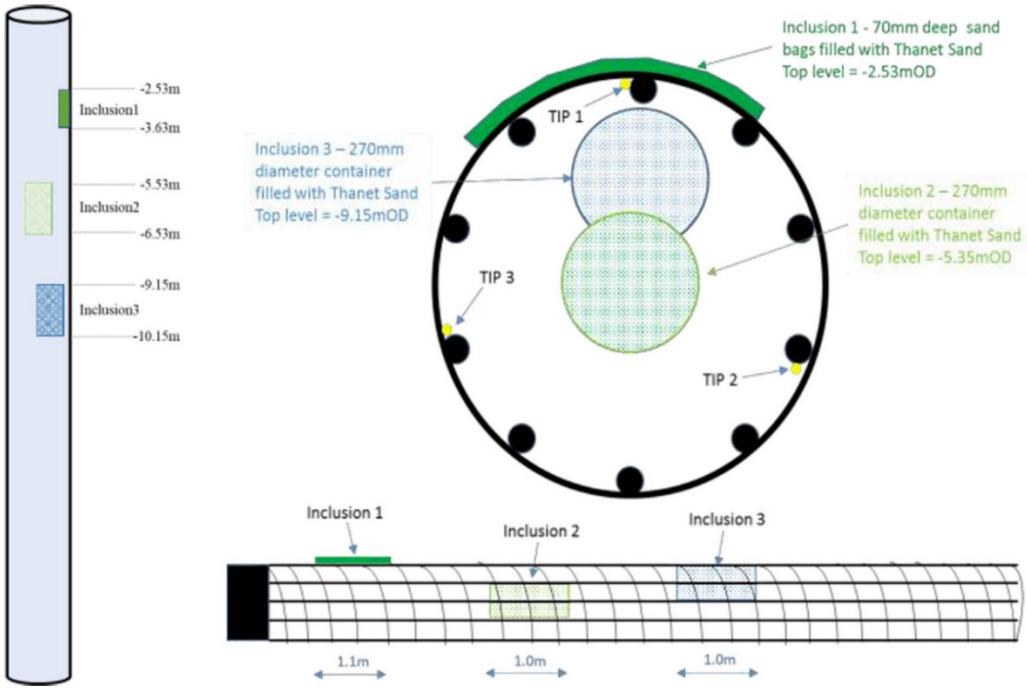


Figure 6.18 Arrangement and description of the engineered inclusions (Sun et al., 2020)

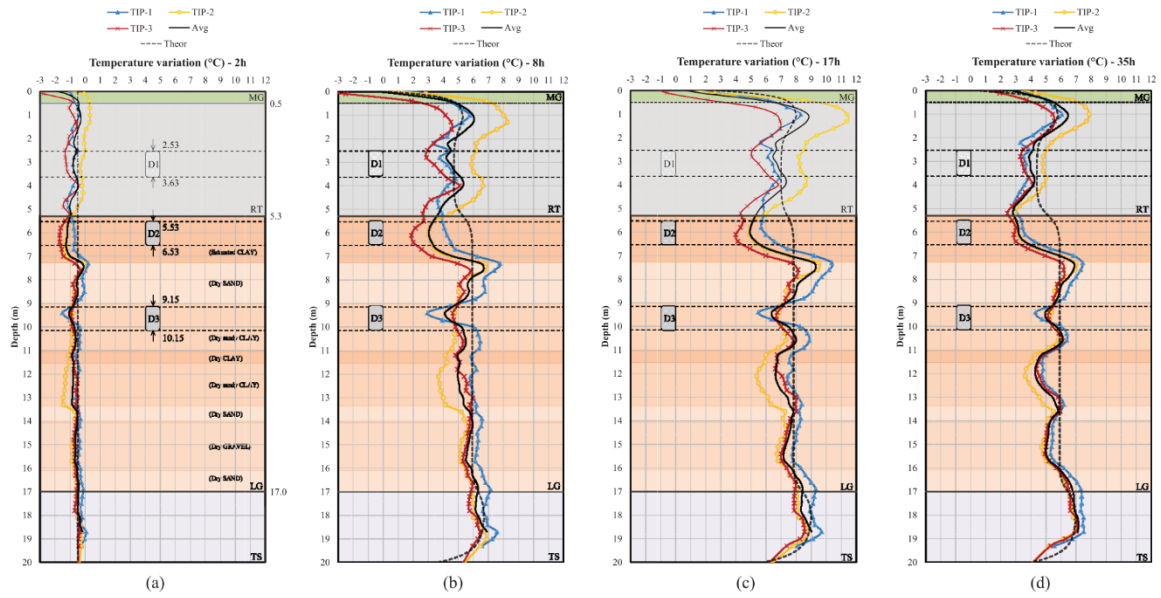


Figure 6.19 Temperature vs. depth profiles at (a) 2 $hours$, (b) 8 $hours$, (c) 17 $hours$ and (d) 35 $hours$ (Sun et al., 2020)

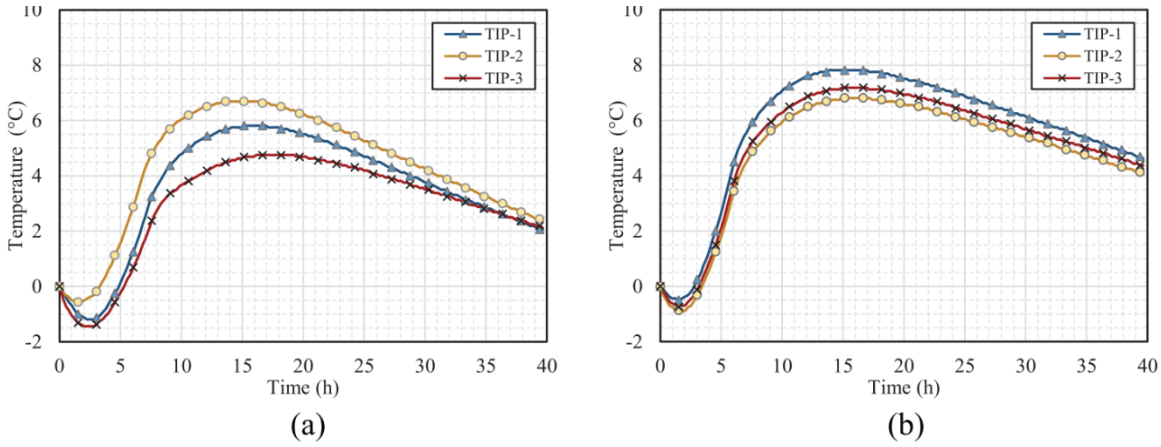


Figure 6.20 Time vs. temperature curves at depths of (a) 4.9 m and (b) 15.1 m (Sun et al., 2020)

Liou (1999)

According to Liou (1999), a cylindrical diaphragm wall that is 100 m in diameter, 2.8 m thick, 119 m deep and consists of primary and secondary elements was constructed in Kawasaki Island, Japan. The layout of the diaphragm wall is shown in Figure 6.21 (Liou, 1999) while the dimensions of the primary and secondary elements are shown in Figure 6.22 (Liou, 1999), which shows that the secondary elements are much larger than the primary elements, although the primary elements are more heavily reinforced. Note that the primary panels were

constructed before the secondary ones. Figure 6.23 and Figure 6.24 show the typical time vs. temperature curves at different locations within the primary and secondary element cross-sections respectively, after placement of concrete (Liou, 1999). Referring to Figure 6.24, it can be observed that the temperature at the centre of a secondary element reaches about 60^oC, while that of a primary element reaches about 50^oC. According to Liou (1999), the secondary elements reached higher temperatures than the primary elements because they have larger volume-to-surface area ratios, and were positioned between warm primary elements that had been cast, which made heat dissipation less favourable. The high temperatures that the secondary elements reached and the associated thermal gradients led to the development of thermal stresses and thermal cracks within them. Liou (1999) commented that the thermal stresses that developed within the concrete were as important as the soil and water pressure acting from outside the wall.

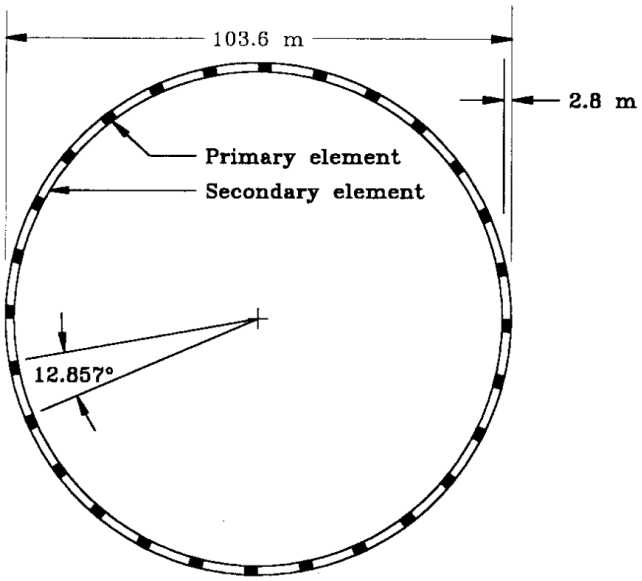


Figure 6.21 Layout of the diaphragm wall (Liou, 1999)

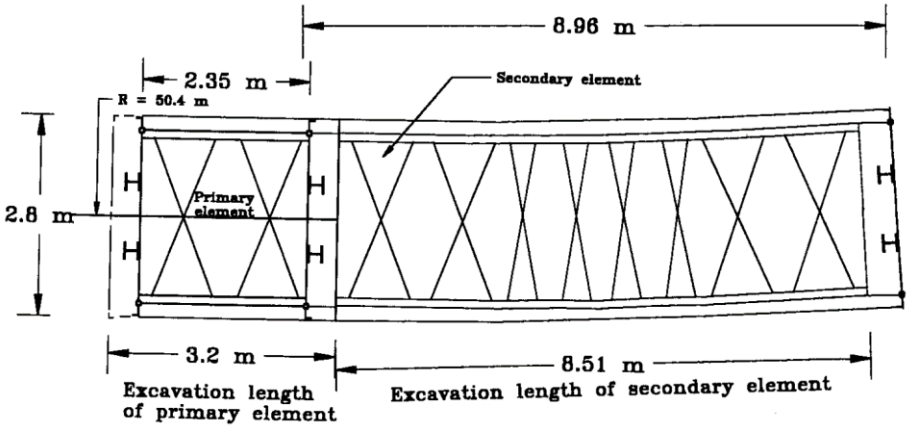


Figure 6.22 Dimensions of the primary and secondary elements (Liou, 1999)

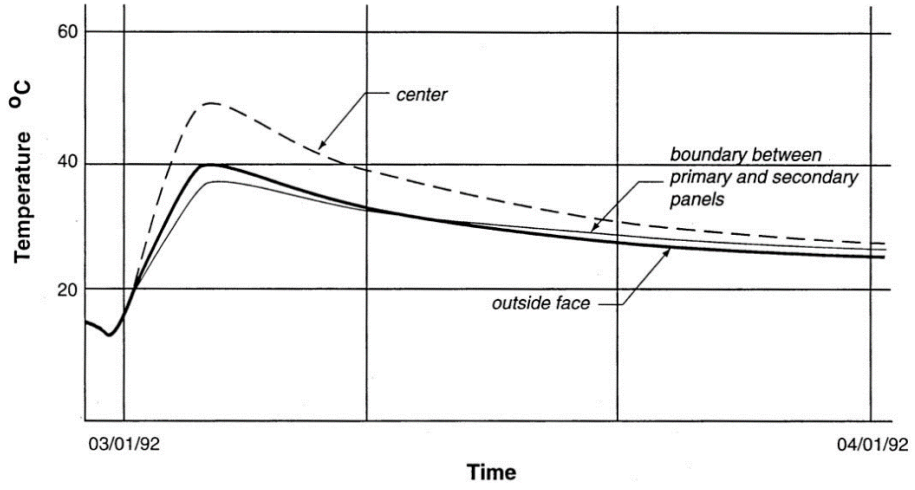


Figure 6.23 Typical time vs. temperature curves at different locations within the primary element cross-section (Liou, 1999)

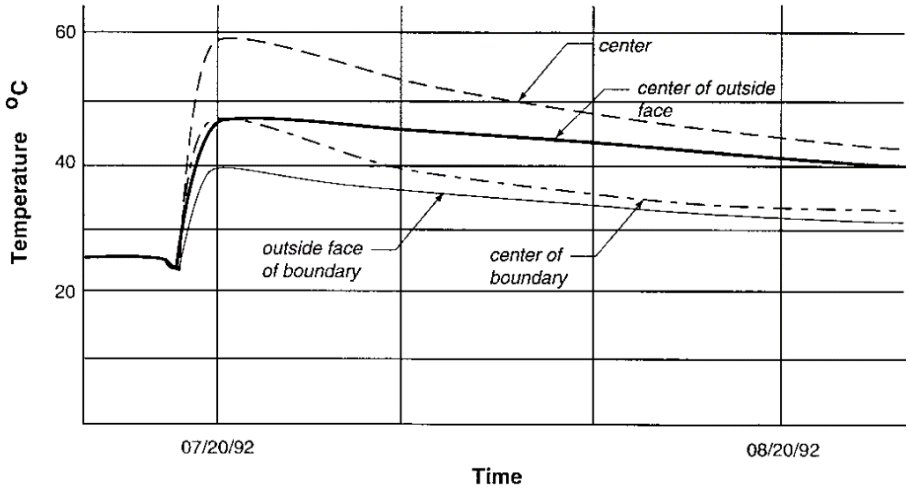


Figure 6.24 Typical time vs. temperature curves at different locations within the secondary element cross-section (Liou, 1999)

Sajadi (2020)

A diaphragm wall that is $25.26\ m$ in diameter, $1.5\ m$ thick and $75.2\ m$ deep was built as part of the King Edward Memorial Park Foreshore (KEMPF) shaft construction, which is part of the Thames Tideway project. The diaphragm wall consists of a series of primary (P) and secondary (S) panels, with panels P14, P24, P30, S01, S15 and S23 having been instrumented with thermocouples which allow the evolution of temperature with time to be recorded (see Figure 6.25 for the dimensions of both primary and secondary panels, as well as the locations of thermocouples within the cross-sections (Sajadi, 2020)). Figure 6.26 illustrates the numbering of primary and secondary panels with respect to the entire diaphragm wall (Sajadi, 2020). Note that the thermocouples were not placed continuously with depth, but at five depths: $24.6\ m$, $34.6\ m$, $39.6\ m$, $49.6\ m$ and $64.6\ m$.

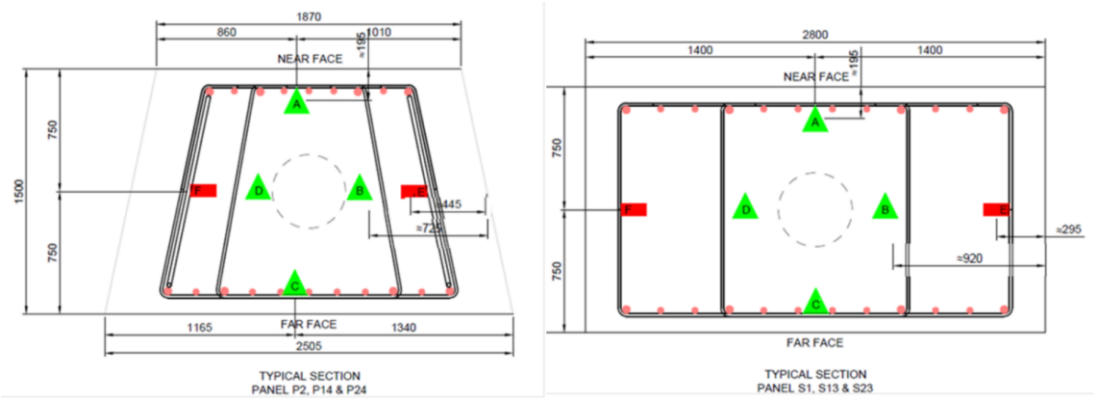


Figure 6.25 Dimensions and locations of thermocouples within the cross-section of primary (left) and secondary (right) panels (Sajadi, 2020)

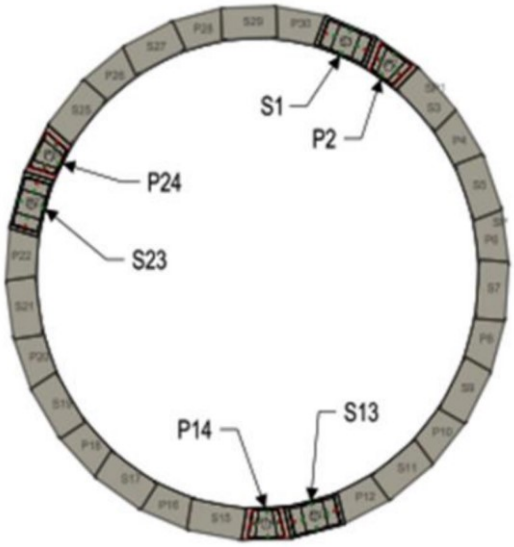


Figure 6.26 Numbering of the primary and secondary panels with respect to the entire diaphragm wall (Sajadi, 2020)

The concrete that was used to construct the diaphragm wall consists of 150 $kg \cdot m^{-3}$ CEM I cement, 310 $kg \cdot m^{-3}$ GGBS, together with some retarders, while the initial ground temperature was estimated to be, on average, 13.7^oC. The time vs. temperature curves at each of the monitoring points in panels P14, P24, P30 and S01 were reported in Sajadi (2020), with only those in panel S01 at 24.6 m depth being presented here (see Figure 6.27) for brevity. It can be observed that the temperatures at monitoring points B and C (which are in the middle of panel S01) reached 50^oC, which corresponds to a temperature rise of about 36.3^oC from the initial ground temperature.

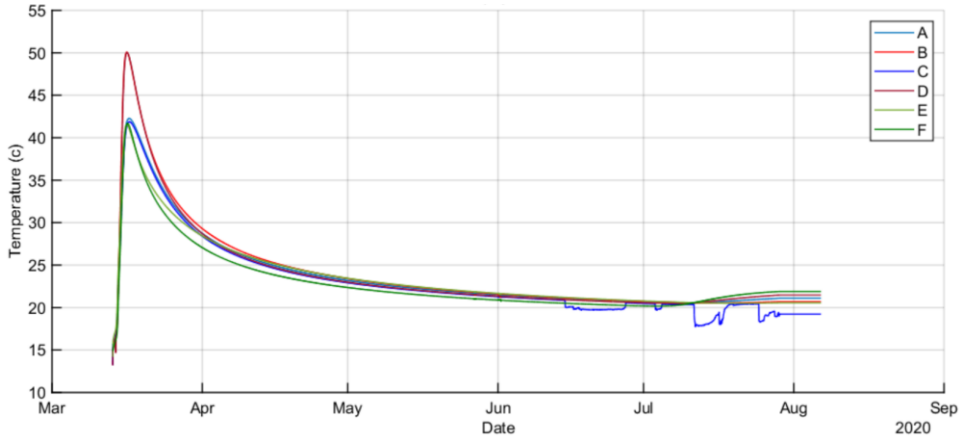


Figure 6.27 Time vs. temperature curves at the monitoring points in panel S01 at 24.6 m depth (Sajadi, 2020)

Based on the aforementioned laboratory and field measurements of concrete heat of hydration, it can be observed that it is not uncommon to have temperatures within samples or realistic geotechnical structures reaching above 50^oC or even 60^oC. Concrete heat of hydration is therefore both geotechnically and structurally significant, and it is possible that its effects on the surrounding soil are more significant than that due to the operation of thermo-active structures, and hence must not be underestimated.

6.4 EXISTING HEAT OF HYDRATION MODELS FOR CONCRETE (LIST OF SYMBOLS DOES NOT APPLY TO THIS SECTION)

The heat liberated from the hydration of concrete increases the temperature and forms a thermal gradient within the concrete element. This gradient can be significant in massive concrete elements, leading to thermal stresses and crack formation, which reduces the service life of the structure (De Schutter & Taerwe, 1995). In order to model accurately the amount of heat liberated due to the hydration of concrete so as to predict the temperature rise in structures constructed with concrete, hence ensuring that thermal stresses are not excessive, different heat of hydration models for concrete have been developed over the years. While it is not the objective of this section to list all the existing heat of hydration models for concrete in the literature, a review of selected popular and state-of-the-art heat of hydration models is presented to highlight the key concepts in this type of model. For each reviewed model, a description is provided regarding the factors that are taken into account when characterising the hydration process, the equations adopted, and the input information required for the model

to function properly. The strengths and limitations of each reviewed model are also discussed in the perspective of application in geotechnical engineering.

Multi-component heat of hydration model by Kishi and Maekawa (1995)

Kishi and Maekawa (1995) developed a heat of hydration model where the rate of hydration heat liberation of concrete is determined by considering the rate of hydration heat liberation from each cement constituent independently. This allows the accurate reproduction of the heat of hydration of different cements by specifying directly the proportions of each constituent. The rate of hydration heat liberation of each cement constituent is modelled by considering a reference rate of heat liberation (i.e. corresponding to the cement constituent being hydrated at a constant reference temperature), which is subsequently modified by a thermal activity function that accounts for the dependence of this reaction on temperature. The cement constituents considered by the model are C_3S, C_2S, C_3A, C_4AF and gypsum.

In this model, the rate of hydration heat liberation is given by Equation (6.6), where $\bar{H}$ $[J \cdot s^{-1} \cdot kg_{cement}^{-1}]$ is the total rate of hydration heat liberation, $\bar{H}_i$ $[J \cdot s^{-1} \cdot kg_i^{-1}]$ is the rate of hydration heat liberation by constituent i, p_i $[kg_i \cdot kg_{cement}^{-1}]$ is the mass ratio of constituent i to the cement, $\bar{H}_{C_3AET}$ $\left[J \cdot s^{-1} \cdot kg_{C_3A}^{-1}\right]$ and $\bar{H}_{C_4AFET}$ $\left[J \cdot s^{-1} \cdot kg_{C_4AF}^{-1}\right]$ represent the rate of heat liberation due to the formation of ettringite from C_3A and C_4AF respectively.

$$\bar{H} = p_{C_3A}\left(\bar{H}_{C_3AET} + \bar{H}_{C_3A}\right) + p_{C_4AF}\left(\bar{H}_{C_4AFET} + \bar{H}_{C_4AF}\right) + p_{C_3S}\bar{H}_{C_3S} + p_{C_2S}\bar{H}_{C_2S} \tag{6.6}$$

The rate of hydration heat liberation by each cement constituent $\bar{H}_i$ is given by Equation (6.7), where γ_i is a coefficient to account for the delaying effects of organic admixtures to the initial hydration process, β_i is a coefficient to account for the effects of reduced availability of water to the hydration process, μ is a coefficient to account for the effects of calcium hydroxide concentration to hydration heat generation, $\bar{H}_{i,T_0}$ $[J \cdot s^{-1} \cdot kg_i^{-1}]$ is the reference rate of hydration heat liberation of constituent i at a constant reference temperature T_0 $[K]$ (which is a function of the accumulated heat released $\bar{Q}_i$ $[J \cdot kg_i^{-1}]$), E_i $[J \cdot mol^{-1}]$ is the activation energy of constituent i, and R $[J \cdot mol^{-1} \cdot K^{-1}]$ is the universal gas constant . The reference rate of hydration heat liberation of each cement constituent $\bar{H}_{i,T_0}$ is shown in Figure 6.28 (Kishi & Maekawa, 1995), the reference rate of heat liberation due to the formation of ettringite $\bar{H}_{iET}$ is in Figure 6.29 (Kishi & Maekawa, 1995), and $-E_i/R$ defines the thermal activity of

constituent i, which is illustrated in Figure 6.30 (Kishi & Maekawa, 1995). Note that the model assumes that the hydration of C_3A and C_4AF only take place once all the gypsum is consumed to form ettringite, and that the reference temperature T_0 is 20^oC.

$$\overline{H}_i = \gamma_i \cdot \beta_i \cdot \mu \cdot \overline{H}_{i,T_0} \cdot \exp\left(-\frac{E_i}{R}\left(\frac{1}{T} - \frac{1}{T_0}\right)\right) \tag{6.7}$$

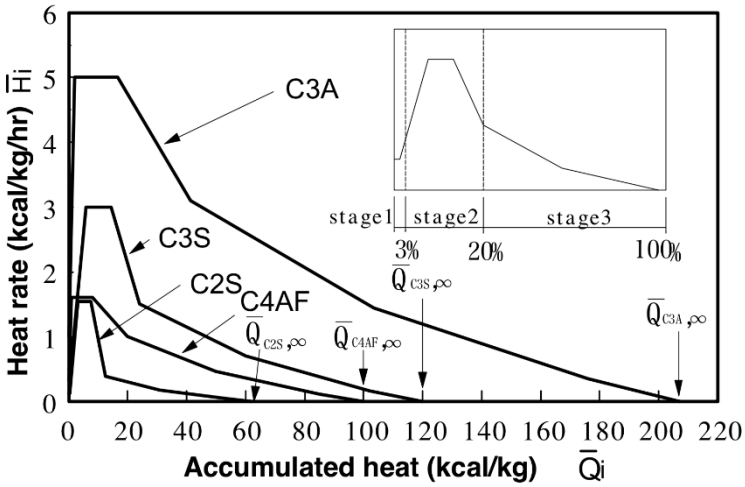


Figure 6.28 The reference rate of hydration heat liberation for each cement constituent (Kishi & Maekawa, 1995)

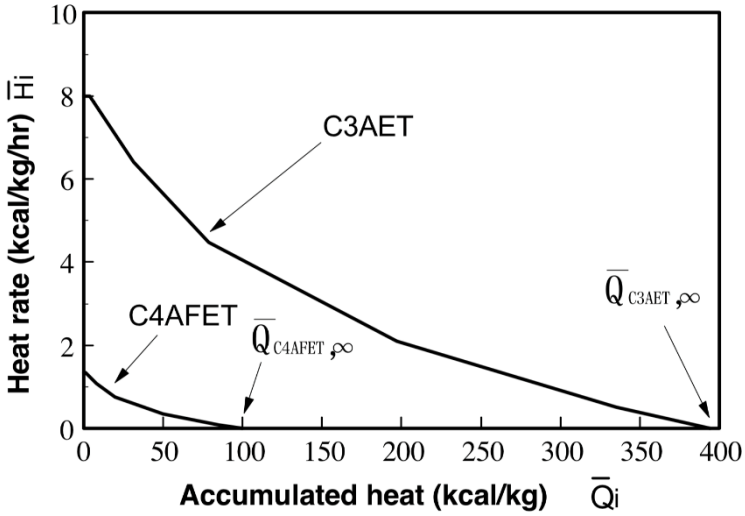


Figure 6.29 The reference rate of heat liberation due to the formation of ettringite (Kishi & Maekawa, 1995)

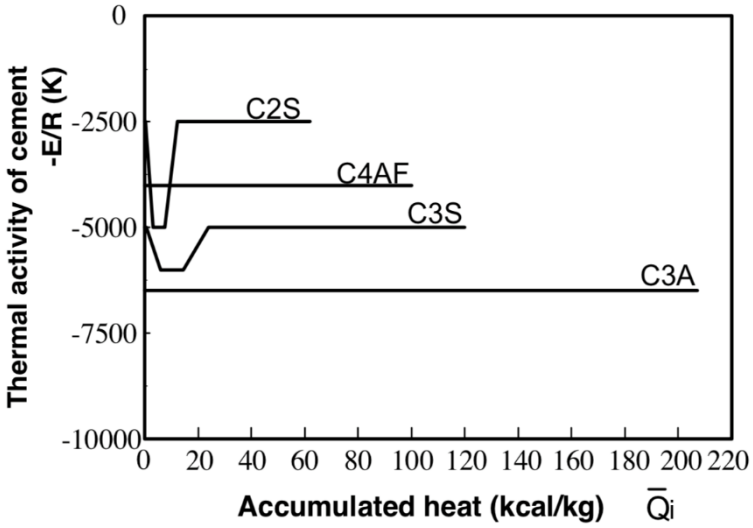


Figure 6.30 The thermal activity assumed for each cement constituent (Kishi & Maekawa, 1995)

In Equation (6.7), the parameter β_i is introduced in order to account for the reduction in hydration rate due to an inadequate supply of water (i.e. w/c not being sufficiently high). The expression for β_i is given by Equations (6.8) to (6.10), where r, s and v are constants, which, based on experiments, have been determined to be $r = 10000$, $s = 2.3$ and $v = 2$, W_{total} $[kg \cdot m^{-3}]$ is the unit water content, W_i $[kg \cdot m^{-3}]$ is the water consumed in the reactions by constituent i, C $[kg_{cement} \cdot m^{-3}]$ is the unit cement content, $\bar{Q}_i$ $[J \cdot kg_i^{-1}]$ is the accumulated heat released by constituent i and $\bar{Q}_{i,\infty}$ $[J \cdot kg_i^{-1}]$ is the ultimate heat released by constituent i at the end of hydration.

$$\beta_i = 1 - \exp\left(-r\left(\frac{\omega_{free}}{100 \cdot \eta_i^v}\right)^s\right) \tag{6.8}$$

$$\omega_{free} = \frac{(W_{total} - \sum W_i)}{C} \tag{6.9}$$

$$\eta_i = 1 - \left(1 - \frac{\bar{Q}_i}{\bar{Q}_{i,\infty}}\right)^{\frac{1}{3}} \tag{6.10}$$

The other parameter introduced in Equation (6.7), μ, accounts for the effects on heat generation of changes in cement composition. The authors were aware that changes in cement composition, notably the C_2S and C_3S contents, influence the hydration heat generation in stage 3 (which corresponds to the reactions beyond 20% of $\bar{Q}_{i,\infty}$, as defined in Figure 6.28 (Kishi & Maekawa,

1995)), and attributed such influence to the pH of the reacting medium, which is represented by the calcium hydroxide concentration, as calcium hydroxide is formed in great quantities upon hydration of C_3S. The expression for μ in stage 3 is given by Equation (6.11), while $\mu = 1$ is assumed for stages 1 and 2.

$$\mu = 0.95 \cdot \left(1 - \exp\left(-1.25 \cdot \left(\frac{p_{C_3S}}{p_{C_2S}}\right)^{1.1}\right)\right) + 0.15 \tag{6.11}$$

Lastly, parameter γ_i is introduced in Equation (6.7) to account for the delaying effects of organic admixtures to stage 1 of the hydration process (which corresponds to the reactions of up to 3% of $\bar{Q}_{i,\infty}$, as defined in Figure 6.28 (Kishi & Maekawa, 1995)). The expression for γ_i is given by Equations (6.12) to (6.14). In Equation (6.12), n_i is a constant which depends on the cement constituent, and is equal to 2.0, 1.5, 3.0 and 2.0 for C_3A, C_4AF, C_3S and C_2S, respectively, while θ_{ef} is the effective delaying effect of the admixture, and is equal to the delaying effect per unit weight of admixture (χ_{SP}) multiplied by the admixture content as a percentage of cement (θ_{total}), minus the admixture with no delaying effects due to its corporation into ettringite (θ_{waste}), which is given by Equation (6.14). The coefficient χ_{SP} depends on the admixture used and is equal to 0.85 for admixtures consisting mainly of naphthalene sulphonate, 1.05 for admixtures consisting mainly of polycarbonate, and 3.8 for retarding air-entraining water-reducing agents. Note that $\gamma_i = 1$ is assumed for stages 2 and 3 of the hydration process.

$$\gamma_i = \exp\left(-n_i \cdot \frac{1000\theta_{ef}}{20p_{C_3S} + 7p_{C_2S}}\right) \tag{6.12}$$

$$\theta_{ef} = \theta_{total} \cdot \chi_{SP} - \theta_{waste} \tag{6.13}$$

$$\theta_{waste} = \frac{1}{200} p_{gypsum} \cdot \left(3p_{C_3A} + 2p_{C_4AF}\right) \tag{6.14}$$

By multiplying $\bar{H}$ in Equation (6.6) with the cement content C $[kg_{cement} \cdot m^{-3}]$, the rate of hydration heat liberation of the concrete can be evaluated. Kishi and Maekawa (1995) validated their heat of hydration model using adiabatic and semi-adiabatic temperature rise tests and showed that their model is capable of predicting the observed temperature increase accurately. However, it should be appreciated that although the Kishi and Maekawa (1995) model is an accurate model as it accounts for the cement reaction kinetics, the use of this model requires

the detailed knowledge of the cement composition, including the gypsum content, the type and contents of admixtures added, as well as the water and cement contents. Clearly, such information may not be readily available in geotechnical engineering applications.

Multi-component heat of hydration model for blended cement with blast furnace slag and fly ash by Kishi and Maekawa (1997)

Following development of the Kishi and Maekawa (1995) model, Kishi and Maekawa (1997) extended their model to account for the effects of blast furnace slag and fly ash, which are binders often used to reduce heat of hydration, by treating them as separate constituents. The effects on rate of heat liberation due to a change in cement fineness is also accounted for in this model. The structure of this model is similar to the Kishi and Maekawa (1995) model, and only the major differences between them are described herein.

In this model, the expression for the rate of hydration heat liberation is similar to Equation (6.6) and is given by Equation (6.15), where the subscript SG represents blast furnace slag and FA represents fly ash, and that their contribution to the hydration heat liberation are included and considered as separate constituents.

$$\begin{aligned}\overline{H} = p_{C_3A}\left(\overline{H}_{C_3AET} + \overline{H}_{C_3A}\right) + p_{C_4AF}\left(\overline{H}_{C_4AFET} + \overline{H}_{C_4AF}\right) + p_{C_3S}\overline{H}_{C_3S} \\ + p_{C_2S}\overline{H}_{C_2S} + p_{SG}\overline{H}_{SG} + p_{FA}\overline{H}_{FA}\end{aligned} \tag{6.15}$$

The expression for the rate of heat liberation by each constituent is also similar to Equation (6.7) and is given by Equation (6.16). In Equation (6.16), the coefficient γ_i is now used to account for the delaying effects of fly ash and organic admixtures to the initial hydration process, λ is a newly introduced coefficient to account for the change in rate of heat liberation by slag and fly ash due to a change in calcium hydroxide availability, as their reactions depend on the abundance of calcium hydroxide in the liquid phase of the reacting medium, which is produced from the hydration of C_3S and C_2S, and s_i is also a newly introduced coefficient to account for the change in rate of heat liberation due to a change in cement fineness.

$$\overline{H}_i = \gamma \cdot \beta_i \cdot \lambda \cdot \mu \cdot s_i \cdot \overline{H}_{i,T_0} \cdot \exp\left(-\frac{E_i}{R}\left(\frac{1}{T} - \frac{1}{T_0}\right)\right) \tag{6.16}$$

In this model, the reference rate of heat liberation follows a similar pattern as that given in Figure 6.28 (Kishi & Maekawa, 1995), with the exception of the boundary between state 1 and

2 which is shifted from 3% to 1% of $\bar{Q}_{i,\infty}$ for C_3S and C_2S, and the boundary between stage 2 and 3 which is shifted from 20% to 25% of $\bar{Q}_{i,\infty}$ for C_3S and from 20% to 30% of $\bar{Q}_{i,\infty}$ for C_2S. The reference rate of heat liberation for slag and fly ash is given in Figure 6.31 (Kishi & Maekawa, 1997). The authors were aware that the rates of heat liberation for slag and fly ash are difficult to derive as they do no react individually without an activator, and that the given rates in Figure 6.31 (Kishi & Maekawa, 1997) are assumed based on analytical and experimental studies, meaning that they are susceptible to variations. The reference rate of heat liberation due to the formation of ettringite is slightly modified from the Kishi and Maekawa (1995) model and is given by Figure 6.32 (Kishi & Maekawa, 1997) in order to account for the rapid liberation of heat that occurs just after the mixing. The assumed thermal activity $(-E_i/R)$ for C_3S, C_2S, C_3A and C_4AF follow the ones given in Figure 6.30 (Kishi & Maekawa, 1995), and that a value of $-4500\ K$ and $-8000\ K$ are assumed for slag and fly ash respectively.

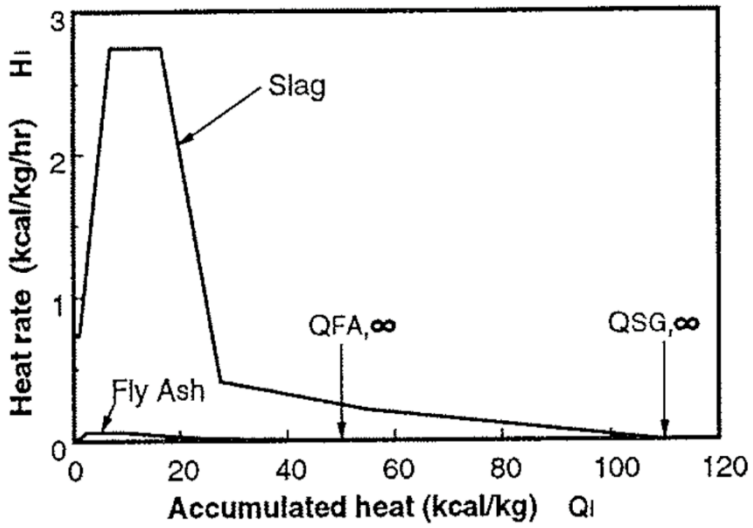


Figure 6.31 The reference rate of heat liberation by slag and fly ash (Kishi & Maekawa, 1997)

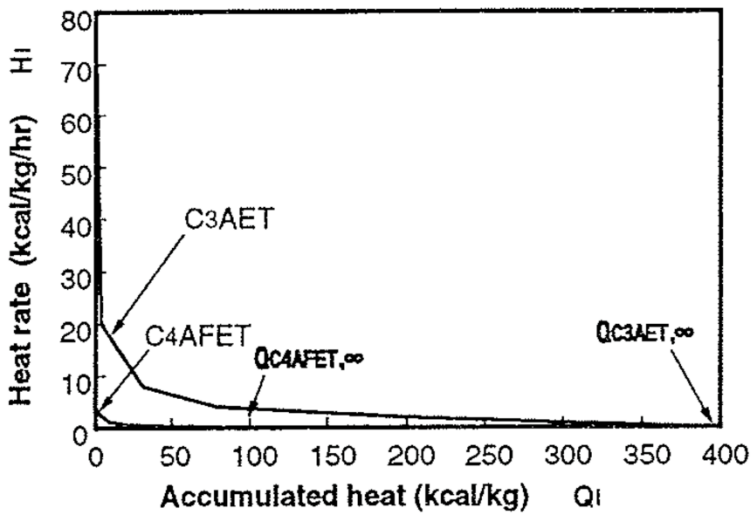


Figure 6.32 The reference rate of heat liberation due to the formation of ettringite (Kishi & Maekawa, 1997)

In Equation (6.16), the parameter s_i is introduced to account for the effects of cement fineness on the rate of heat liberation. The expression for s_i is given by Equation (6.17), where S_i $[m^2 \cdot kg^{-1}]$ is the Blaine fineness and S_{i0} $[m^2 \cdot kg^{-1}]$ is the reference Blaine fineness of constituent i. The reference Blaine fineness for Portland cement, slag and fly ash are 3380 $cm^2 \cdot g^{-1}$, 4330 $cm^2 \cdot g^{-1}$ and 3280 $cm^2 \cdot g^{-1}$ respectively. Note that the model does not account for the effects of fineness of C_3S, C_2S and slag for stage 2 of the hydration process (i.e. $s_i = 1$).

$$s_i = \frac{S_i}{S_{i0}} \tag{6.17}$$

In Equation (6.16), the parameter λ is introduced to account for the change in rate of heat liberation by slag and fly ash due to a change in availability of calcium hydroxide. The expression for λ is given by Equation (6.18), where F_{CH} is the amount of calcium hydroxide produced from the hydration of C_3S and C_2S, and R_{SGCH} and R_{FACH} are the amount of calcium hydroxide required by slag and fly ash, respectively, when there is sufficient supply of calcium hydroxide. As a result, $\frac{F_{CH}}{R_{SGCH}+R_{FACH}}$ represents the ratio of the amount of calcium hydroxide available to the amount of calcium hydroxide required by slag and fly ash. F_{CH} can be computed from Equations (6.1) and (6.2) together with the amount of C_3S and C_2S hydrated, while R_{SGCH} and R_{FACH} are assumed in this model to be 22% and 100% of the reacting mass, respectively.

$$\lambda = 1 - \exp\left(-2.0 \cdot \left(\frac{F_{CH}}{R_{SGCH} + R_{FACH}}\right)^{5.0}\right) \tag{6.18}$$

The expression for β_i in Equation (6.16) is modified from the Kishi and Maekawa (1995) model and is given by Equation (6.19) to account for the effects of cement fineness, as a higher surface area per unit weight of cement particles increases the chances of particles coming into contact with water. Constants r, s and v are determined to be 5.0, 2.4 and 1.0, respectively, based on analytic and experimental results. Note that the expressions for ω_{free} and η_i are identical to those given by Equations (6.9) and (6.10) respectively. However, when there is a shortage of calcium hydroxide which leads to a stagnation of slag and fly ash reactions, the expression for ω_{free} is modified and given by Equations (6.20) and (6.21) instead.

$$\beta_i = 1 - \exp\left(-r\left(\left(\frac{\omega_{free}}{100 \cdot \eta_i^v}\right)/s_i^{\frac{1}{2}}\right)^s\right) \tag{6.19}$$

$$\omega_{free} = \frac{W_{total} - \sum W_i}{C \cdot (p_{PC} + m_{SG} \cdot p_{SG} + m_{FA} \cdot p_{FA})} \tag{6.20}$$

$$m_i = \frac{\lambda}{\beta_i} \tag{6.21}$$

The expression for μ in Equation (6.16) is slightly modified from the Kishi and Maekawa (1995) model and is given by Equation (6.22). Also, in this model, the coefficient μ only applies to stage 3 of the hydration process for C_3S and C_2S, as it only accounts for the interdependency between C_3S and C_2S.

$$\mu = 1.4 \cdot \left(1 - \exp\left(-0.48 \cdot \left(\frac{p_{C_3S}}{p_{C_2S}}\right)^{1.4}\right)\right) + 0.1 \tag{6.22}$$

In Equation (6.16), parameter γ is now used to account for the delaying effects of organic admixtures as well as fly ash on the reactions of Portland cement and slag. The expression for γ is given by Equations (6.23) to (6.26). In Equation (6.23), θ_{SPef} and θ_{FAef} represent the effective delaying capability of organic admixtures and fly ash respectively. In Equation (6.24), the subscript SP represents organic admixture, while θ_{waste} represents the admixture with no delaying effects due to adsorption on powder particles. Note that if $\theta_{waste} > p_{SP} \cdot \chi_{SP}$, θ_{SPef} is assumed to be zero. Similar to the Kishi and Maekawa (1995) model, γ is only applied to

stage 1 of the hydration process. Moreover, in the current model, the same γ is applied to each constituent.

$$\gamma = \exp\left(-\frac{1000\left(\theta_{SPef} + \theta_{FAef}\right)}{10p_{C_3S} \cdot s_{C_3S} + 5p_{C_2S} \cdot s_{C_2S} + 2.5p_{SG} \cdot s_{SG}}\right) \tag{6.23}$$

$$\theta_{SPef} = p_{SP} \cdot \chi_{SP} - \theta_{waste} \tag{6.24}$$

$$\theta_{FAef} = 0.02p_{FA} \cdot s_{FA} \tag{6.25}$$

$$\theta_{waste} = \frac{1}{200} \cdot \left(16p_{C_3A} \cdot s_{C_3A} + 4p_{C_4AF} \cdot s_{C_4AF} + p_{SG} \cdot s_{SG} + 5p_{FA} \cdot s_{FA}\right) \tag{6.26}$$

Kishi and Maekawa (1997) validated the model using both adiabatic and semi-adiabatic temperature rise tests and the model is shown to have good predictive abilities in terms of evolution of temperature. Clearly, this is a sophisticated model that can predict the heat of hydration of concrete accurately, and is also an improvement of the Kishi and Maekawa (1995) model, as it takes into account the effects of cement fineness on the rate of hydration, as well as the effects of slag and fly ash, which are popular admixtures to reduce heat of hydration during concrete construction, on the hydration process. However, the drawback of applying this model in geotechnical engineering is similar to that of the Kishi and Maekawa (1995) model: an accurate composition of the cement, cement fineness, mixture proportions of concrete, and the dosage of any admixtures added are required, which may not be readily available in geotechnical engineering applications.

A general hydration model for Portland cement and blast furnace slag cement by De Schutter and Taerwe (1995)

De Schutter and Taerwe (1995) developed a general heat of hydration model for Portland cement, as well as one for cements blended with blast furnace slag. The model for Portland cement was derived based on the observation that when the same cement is hydrated at different temperatures in isothermal hydration tests, the obtained results are similar in shape when plotted on a normalised graph (as illustrated in Figure 6.33 (De Schutter & Taerwe, 1995)). Figure 6.33 shows the results of three isothermal hydration tests on the same cement at 5^oC, 20^oC and 35^oC, where the x-axis represents the degree of reaction r (defined as the accumulated heat liberated Q $[J \cdot kg_{cement}^{-1}]$ divided by the total amount of heat liberated at the end of hydration Q_{max} $[J \cdot kg_{cement}^{-1}]$) and y-axis represents the normalised rate of heat

liberation q/q_{max} (defined as the instantaneous rate of heat liberation q $[J \cdot s^{-1} \cdot kg_{cement}^{-1}]$ divided by its maximum value q_{max} $[J \cdot s^{-1} \cdot kg_{cement}^{-1}]$). As a result, a heat of hydration model for Portland cement can be obtained by having a function f which describes the shape of the curve shown in Figure 6.33 (De Schutter & Taerwe, 1995) (given by Equation (6.27)), and applying a temperature function g (which is based on the Arrhenius equation) to account for the effects of temperature dependence on q_{max} (given by Equations (6.28) and (6.29)). In Equation (6.27), a, b and c are parameters to be calibrated, which depend on the Portland cement. In Equation (6.28), $q_{max,20}$ represents q_{max} at 20^oC, which is also dependent on the Portland cement and has to be calibrated. In Equation (6.29), E $[J \cdot mol^{-1}]$ is the apparent activation energy (the activation energy is apparent as the hydration of Portland cement involves many different reactions, as explained in Section 6.2, with different activation energy for each reaction), R $[J \cdot mol^{-1} \cdot K^{-1}]$ is the universal gas constant and θ $[K]$ is the temperature.

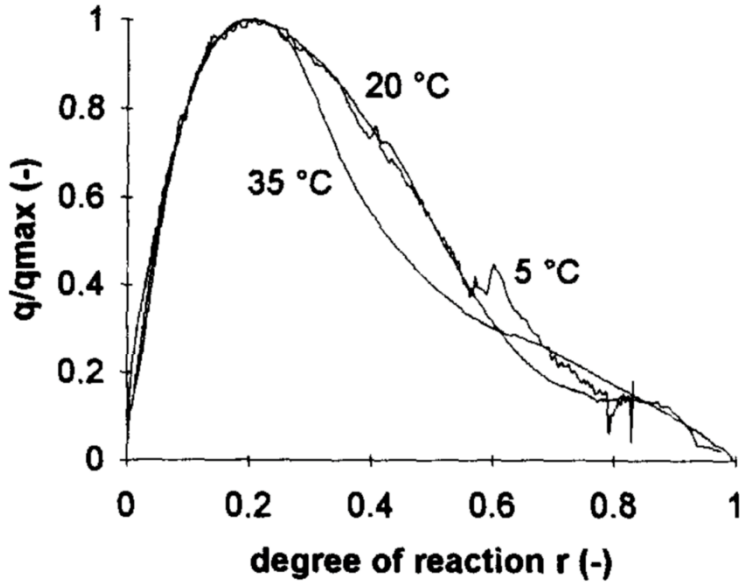


Figure 6.33 Normalised curves of isothermal hydration test results (De Schutter & Taerwe, 1995)

$$f = \frac{q}{q_{max}} = c \cdot (\sin(r\pi))^a \cdot \exp(-br) \tag{6.27}$$

$$q_{max} = q_{max,20} \cdot g \tag{6.28}$$

$$g = \exp\left(\frac{E}{R}\left(\frac{1}{293} - \frac{1}{273+\theta}\right)\right) \tag{6.29}$$

For cements blended with slag, the model assumes that the hydration process consists of two reactions: a Portland cement reaction (P-reaction) and a slag reaction (S-reaction), and hence the rate of heat liberation is assumed to be the superposition of the rates of heat liberation due to the P-reaction (q_p) and S-reaction (q_s) (see Equation (6.30)). The expressions for q_p and q_s are given by Equations (6.31) to (6.36). In Equations (6.31) and (6.32), $q_{p,max,20}$ $[J \cdot s^{-1} \cdot kg_{cement}^{-1}]$ represents the maximum rate of heat liberation by the P-reaction at 20^oC, which has to be calibrated, a_p, b_p and c_p are parameters to be calibrated, which depend on the cement, and r_p is the degree of reaction of the P-reaction, which is defined as the accumulated heat liberated by the P-reaction, Q_p $[J \cdot kg_{cement}^{-1}]$, divided by the ultimate heat released at the end of the P-reaction, $Q_{p,max}$ $[J \cdot kg_{cement}^{-1}]$. In Equations (6.34) and (6.35), $q_{s,max,20}$ $[J \cdot s^{-1} \cdot kg_{cement}^{-1}]$ represents the maximum rate of heat liberation by the S-reaction at 20^oC, which has to be calibrated, a_s is a parameter to be calibrated, which depends on the slag, and r_s is the degree of reaction, which is defined as the accumulated heat liberated by the S-reaction, Q_s $[J \cdot kg_{cement}^{-1}]$, divided by the ultimate heat released at the end of the S-reaction, $Q_{s,max}$ $[J \cdot kg_{cement}^{-1}]$. In Equations (6.33) and (6.36), E_p $[J \cdot mol^{-1}]$ and E_s $[J \cdot mol^{-1}]$ are activation energies for the P-reaction and S-reaction, respectively. Since the S-reaction only begins when sufficient calcium hydroxide is produced from the hydration of Portland cement, this is implemented in the model by setting q_s to be zero until the degree of reaction of the P-reaction reaches a threshold $r_{p,B}$, which is temperature dependent and is given by Equation (6.37). In Equation (6.37), A and B are coefficients to be calibrated.

$$q = q_p + q_s \tag{6.30}$$

$$q_p = q_{p,max,20} \cdot f_p \cdot g_p \tag{6.31}$$

$$f_p = c_p \cdot \left(\sin\left(r_p \pi\right)\right)^{a_p} \cdot \exp\left(-b_p r_p\right) \tag{6.32}$$

$$g_p = \exp\left(\frac{E_p}{R}\left(\frac{1}{293} - \frac{1}{273+\theta}\right)\right) \tag{6.33}$$

$$q_s = q_{s,max,20} \cdot f_s \cdot g_s \tag{6.34}$$

$$f_s = (\sin(r_s\pi))^{a_s} \tag{6.35}$$

$$g_s = \exp\left(\frac{E_s}{R}\left(\frac{1}{293} - \frac{1}{273+\theta}\right)\right) \tag{6.36}$$

$$r_{p,B} = A\theta + B \tag{6.37}$$

The model parameters (a_p, b_p, c_p, $q_{p,max,20}$, $Q_{p,max}$, E_p, a_s, $q_{s,max,20}$, $Q_{s,max}$, E_s, A and B) are then calibrated by conducting isothermal hydration tests at different temperatures. Adiabatic hydration tests on two cements (CEM I 52.5 and CEM III/B 32.5) are performed to validate the accuracy of the model. The results show that the model is capable of predicting the temperature evolution of the CEM III/B 32.5 cement accurately (which has a temperature rise of around 33^oC), while underestimating the temperature rise of the CEM I 52.5 cement (which has a temperature rise of around 44^oC). The authors explained that the less satisfactory predictions for the CEM I 52.5 cement are due to the fact that no isothermal hydration tests have been performed with that cement to calibrate the model for the temperatures reached in the adiabatic test, but that when the model parameters for the CEM I 52.5 cement are adjusted (and hence different from those calibrated based on the isothermal hydration tests), the model is capable of predicting an accurate temperature evolution. Note that this model (for cements blended with slag) was also published in De Schutter (1999).

Clearly, the De Schutter and Taerwe (1995) model is a less sophisticated model compared to the Kishi and Maekawa (1997) model, as the De Schutter and Taerwe (1995) model has not taken into account the details of the cement reaction kinetics, but relies on empirical equations based on observations from experiments and isothermal hydration test results for fitting the model parameters. Lower accuracies are hence expected compared to the Kishi and Maekawa (1997) model. The advantage of the De Schutter and Taerwe (1995) model is that an accurate composition of the cement is not required, but the requirement of having to conduct isothermal hydration tests at different temperatures to calibrate the model parameters is definitely a drawback. Also, no instructions are provided on how to estimate the model parameters without isothermal hydration test results, which makes the model difficult to apply in applications where limited information on the concrete mix is provided (e.g. only the classification of cement and the cement content are given) and performing isothermal hydration tests on the cement is not feasible.

Multi-constituent heat of hydration model for Portland cement by Swaddiwudhipong et al. (2002)

The multi-constituent heat of hydration model by Swaddiwudhipong et al. (2002) is similar to the Kishi and Maekawa (1995) model, in which the hydration of cement is assumed to be the combination of independent hydration of cement constituents, and is applicable to Portland cement. The main difference between this model and that proposed by Kishi and Maekawa (1995) is that in the former the influence of temperature on the rate of hydration heat liberation is taken into account by using the concept of equivalent maturity (also known as equivalent age (Schindler & Folliard, 2005)) for each cement constituent, which replaces the actual age of concrete. The effects of reduced availability of water, cement fineness and the formation of a layer of hydrated products on unhydrated cement powder on the hydration process are taken into account through an additional coefficient.

In this model, the ultimate heat liberated at the end of hydration per unit mass of Portland cement, Q_{max} $[J \cdot kg_{cement}^{-1}]$, is given by the weighted average of ultimate heats of the cement constituents, which is given by Equation (6.38). In Equation (6.38), $Q_{i,max}$ $[J \cdot kg_i^{-1}]$ is the ultimate heat per unit mass liberated by each constituent i at the end of hydration, and p_i $[kg_i \cdot kg_{cement}^{-1}]$ is the mass percentage of cement constituent i. The values adopted for $Q_{C_3S,max}$, $Q_{C_2S,max}$, $Q_{C_3A,max}$ and $Q_{C_4AF,max}$ are given in Table 6.5 (Swaddiwudhipong et al., 2002).

$$\begin{aligned} Q_{max} &= Q_{C_3S} + Q_{C_2S} + Q_{C_3A} + Q_{C_4AF} \\ &= Q_{C_3S,max} \cdot p_{C_3S} + Q_{C_2S,max} \cdot p_{C_2S} + Q_{C_3A,max} \cdot p_{C_3A} \\ &\quad + Q_{C_4AF,max} \cdot p_{C_4AF} \end{aligned} \tag{6.38}$$

Cement constituent	$Q_{i,max}\ [kJ \cdot kg_i^{-1}]$
C_3S	502
C_2S	259
C_3A	1339
C_4AF	418

Table 6.5 Ultimate heat liberated at the end of hydration per unit mass of different cement constituents (Swaddiwudhipong et al., 2002)

In this model, the specific heat capacity of concrete $H\ [J \cdot kg_{concrete}^{-1} \cdot K^{-1}]$ is estimated by the weighted average of the specific heat capacities of its components and is given by Equation (6.39), where $H_i\ [J \cdot kg_i^{-1} \cdot K^{-1}]$ is the specific heat capacity of concrete component i, and p_i $[kg_i \cdot kg_{concrete}^{-1}]$ is the mass percentage of concrete component i. The suggested values for H_i are given in Table 6.6 (Swaddiwudhipong et al., 2002).

$$H = H_{water} \cdot p_{water} + H_{cement} \cdot p_{cement} + H_{aggregate} \cdot p_{aggregate} \qquad (6.39)$$

Concrete component	$H_i\ [J \cdot kg_i^{-1} \cdot K^{-1}]$
Water	4180
Aggregate (siliceous)	750
Aggregate (limestone)	840
Portland cement	750

Table 6.6 Suggested values of specific heat capacity for different concrete components (Swaddiwudhipong et al., 2002)

The rate of hydration heat liberation per unit mass of cement $q_c\ [J \cdot s^{-1} \cdot kg_{cement}^{-1}]$ is given by Equation (6.40), where $q_i\ [J \cdot s^{-1} \cdot kg_i^{-1}]$ is the rate of hydration heat liberation per unit mass of cement constituent i.

$$q_c = p_{C_3S} q_{C_3S} + p_{C_2S} q_{C_2S} + p_{C_3A} q_{C_3A} + p_{C_4AF} q_{C_4AF} \qquad (6.40)$$

The expression for q_i is given by Equations (6.41) to (6.43). In Equation (6.41), κ is a coefficient to account for the effects of reduced availability of water, cement fineness and the formation of a layer of hydrated products coating the unhydrated cement particles on the reference rate of hydration heat liberation per unit mass of constituent i (q_{i,T_0} $[J \cdot s^{-1} \cdot kg_i^{-1}]$), which is a function of equivalent maturity of constituent i (M_i $[s]$) (the expression of which is given by Equation (6.42), which is a function of temperature T and time t). In Equation (6.42), E_i $[J \cdot mol^{-1}]$ is the activation energy of constituent i, R $[J \cdot mol^{-1} \cdot K^{-1}]$ is the universal gas constant, T_0 $[K]$ is the reference temperature and Q_i $[J \cdot kg_i^{-1}]$ is the accumulated heat of hydration of constituent i. Note that the expression for equivalent maturity, which is used to account for the effects of temperature on the reference rate of hydration heat liberation, takes the form of the Arrhenius equation, and that the reference temperature T_0 is $293\ K$. The thermal activities $-E_i/R$ of cement constituents adopted in this model follow the ones given in Figure 6.30 by Kishi and Maekawa (1995). The expression for q_{i,T_0} is given by Equation (6.44), where A and B are constants which depend on the cement constituent and the values are given in Table 6.7 (Swaddiwudhipong et al., 2002). Note that the derivation of Equation (6.44) is based on the observation that there exist unique curves of equivalent maturity versus degree of hydration for each cement constituent.

$$q_i = \kappa q_{i,T_0} M_i \tag{6.41}$$

$$M_i = \int_0^t \exp\left(-\frac{E_i}{R}\left(\frac{1}{T} - \frac{1}{T_0}\right)\right) d\tau \tag{6.42}$$

$$Q_i = \int_0^{M_i} q_i dM_i \tag{6.43}$$

$$q_{i,T_0} = Q_{i,max} \frac{AB}{M_i \ln 10} (\log M_i)^{B-1} \exp(-A(\log M_i)^B) \tag{6.44}$$

Parameter	Cement constituent			
	C_3S	C_2S	C_3A	C_4AF
A	0.38	0.11	0.29	0.09
B	1.8	2.0	1.8	2.5

Table 6.7 Values for model parameters A and B for different cement constituents (Swaddiwudhipong et al., 2002)

The expression for κ is given by Equations (6.45) to (6.48). In Equation (6.45), λ_1, λ_2, λ_3 and λ_4 are constants and the recommended values are given in Table 6.8 (Swaddiwudhipong et al., 2002), ω_{free} is the free w/c ratio and its introduction is used to account for the effects of reduced availability of water to the hydration reaction, f_r is the relative fineness of the Portland cement, which is a coefficient introduced to account for the effects of cement fineness to the hydration reaction, and η is a coefficient introduced to account for the formation of a layer of hydrated products on the unhydrated cement particles, which slows down the hydration process. In Equation (6.46), W_{total} $[kg \cdot m^{-3}]$ is the unit water content, W_i $[kg \cdot m^{-3}]$ is the water consumed in the reactions by constituent i, and C $[kg_{cement} \cdot m^{-3}]$ is the unit cement content. In Equation (6.48), f $[m^2 \cdot kg^{-1}]$ is the Blaine fineness of cement and f_0 is the reference Blaine fineness of cement, which is $3500\ cm^2/g$.

$$\kappa = 1 - \exp\left(-\lambda_1 (f_r)^{\lambda_2} \left(\omega_{free}\right)^{\lambda_3} (\eta)^{-\lambda_4}\right) \tag{6.45}$$

$$\omega_{free} = \frac{W_{total} - \sum W_i}{C} \tag{6.46}$$

$$\eta = 1 - \left(1 - \frac{Q}{Q_{max}}\right)^{\frac{1}{3}} \tag{6.47}$$

$$f_r = \frac{f}{f_0} \tag{6.48}$$

Model constants	Recommended values
λ_1	2.0
λ_2	0.5
λ_3	0.1
λ_4	0.1

Table 6.8 Recommended values for λ_1, λ_2, λ_3 and λ_4 (Swaddiwudhipong et al., 2002)

Swaddiwudhipong et al. (2002) validated the model using the adiabatic temperature rise test results from Kishi and Maekawa (1995), and the model is shown to produce accurate temperature rise predictions. Although the authors claimed that this model is a significant improvement from the Kishi and Maekawa (1995) model, no evidence has been shown indicating that this model is capable of making more accurate predictions. On the other hand, this model is unable to account for the presence of slag and fly ash, which is considered by the Kishi and Maekawa (1997) model. As this model takes a similar form with the Kishi and Maekawa (1995) and Kishi and Maekawa (1997) models, its drawbacks are similar as well: an accurate composition of the cement, cement fineness and concrete mixture proportions are required for an appropriate use of this model, which may not be readily available; furthermore, this model is unable to account for the effects of any admixtures, such as slag and fly ash, which are often added in geotechnical engineering applications.

A general hydration model for cementitious materials by Schindler and Folliard (2005)

A general heat of hydration model was developed by Schindler and Folliard (2005), which is capable of accounting for the effects of cement composition, concrete mixture proportions, temperature, cement fineness and supplementary cementing materials (SCMs, which include Class F fly ash, Class C fly ash and ground-granulated blast-furnace (GGBF) slag) on the hydration process. The model parameters are calibrated using a multivariate regression analysis based on the hydration test results of 33 different concrete mixtures made from 23 different cements.

In this model, the rate of hydration heat liberation per unit concrete volume Q_H $[J \cdot s^{-1} \cdot m^{-3}]$ is given by Equation (6.49), where H_u $[J \cdot kg_{cement}^{-1}]$ is the ultimate heat of hydration of cementitious materials at the end of the hydration process (100% hydration) per unit mass of cementitious materials (which include Portland cement, slag and fly ash) and its expression is

given by Equations (6.50) and (6.51), C_c $[kg_{cement} \cdot m^{-3}]$ is the mass of cementitious materials per unit concrete volume, t_e $[s]$ is the equivalent age (which is also known as equivalent maturity in the Swaddiwudhipong et al. (2002) model) and its expression is given by Equation (6.52), α is the degree of hydration and its expression is given by Equation (6.53), E $[J \cdot mol^{-1}]$ is the activation energy and its expression is given by Equation (6.54), R $[J \cdot mol^{-1} \cdot K^{-1}]$ is the universal gas constant, T_r [℃] is the reference temperature, T_c [℃] is the concrete temperature, and τ $[s]$ and β are model parameters to be calibrated. In Equation (6.50), H_{cem} $[J \cdot kg_{PC}^{-1}]$ is the ultimate heat of hydration of Portland cement at the end of the hydration process per unit mass of Portland cement, p_{cem} $[kg_{PC} \cdot kg_{cement}^{-1}]$ is the weight ratio of Portland cement to total cementitious materials, p_{SLAG} $[kg_{SLAG} \cdot kg_{cement}^{-1}]$ is the weight ratio of slag to total cementitious materials, h_{FA} $[J \cdot kg_{FA}^{-1}]$ is the heat of hydration of fly ash per unit mass of fly ash, and p_{FA} $[kg_{FA} \cdot kg_{cement}^{-1}]$ is the weight ratio of fly ash to total cementitious materials. In Equation (6.51), p_i $[kg_i \cdot kg_{PC}^{-1}]$ is the weight ratio of constituent i to the Portland cement content. In Equation (6.53), α_u is the ultimate degree of hydration. Note that, according to the model, 100% hydration can never be achieved, with the expression for α_u being given by Equation (6.55), which is related to the w/c and SCM content of the concrete but is independent of the curing temperature. Furthermore, in Equation (6.54), f_E is the activation energy modification factor for the SCMs, and its expression is given by Equation (6.56), and $Blaine$ $[m^2 \cdot kg^{-1}]$ is the Blaine fineness of cement. In Equation (6.56), p_{FACaO} $[kg_{CaO} \cdot kg_{FA}^{-1}]$ is the weight proportion of CaO in fly ash.

$$Q_H = H_u \cdot C_c \cdot \left(\frac{\tau}{t_e}\right)^{\beta} \cdot \left(\frac{\beta}{t_e}\right) \cdot \alpha \cdot \frac{E}{R}\left(\frac{1}{273 + T_r} - \frac{1}{273 + T_c}\right) \tag{6.49}$$

$$H_u = H_{cem} \cdot p_{cem} + 461 \cdot p_{SLAG} + h_{FA} \cdot p_{FA} \tag{6.50}$$

$$\begin{aligned} H_{cem} = {} & 500p_{C_3S} + 260p_{C_2S} + 866p_{C_3A} + 420p_{C_4AF} + 624p_{SO_3} \\ & + 1186p_{FreeCaO} + 850p_{MgO} \end{aligned} \tag{6.51}$$

$$t_e = \int_0^t \exp\left(-\frac{E}{R}\left(\frac{1}{273 + T_c} - \frac{1}{273 + T_r}\right)\right) d\tau \tag{6.52}$$

$$\alpha = \alpha_u \cdot \exp\left(-\left(\frac{\tau}{t_e}\right)^{\beta}\right) \tag{6.53}$$

$$E = 22100 \cdot f_E \cdot {p_{C_3A}}^{0.30} \cdot {p_{C_4AF}}^{0.25} \cdot Blaine^{0.35} \tag{6.54}$$

$$\alpha_u = \frac{1.031 \cdot w/c}{0.194 + w/c} + 0.50 \cdot p_{FA} + 0.30 \cdot p_{SLAG} \leq 1.0 \tag{6.55}$$

$$f_E = 1 - 1.05 \cdot p_{FA} \cdot \left(1 - \frac{p_{FACaO}}{0.40}\right) + 0.40 \cdot p_{SLAG} \tag{6.56}$$

As mentioned above, the calibration of model is based on the hydration test results of 33 different concrete mixtures made from 23 different cements. From the test results, it has been observed that the heat of hydration of fly ash is dependent on the CaO content, and Equation (6.57) is proposed to model the heat of hydration of fly ash. Based on a multivariate regression analysis of the test results, the expressions for τ and β are determined and are given by Equations (6.58) and (6.59) respectively.

$$h_{FA} = 1800 \cdot p_{FACaO} \tag{6.57}$$

$$\begin{aligned} \tau = 66.78 \cdot {p_{C_3A}}^{-0.154} \cdot {p_{C_3S}}^{-0.401} \cdot Blaine^{-0.804} \cdot {p_{SO_3}}^{-0.758} \\ \cdot \exp(2.187 \cdot p_{SLAG} + 9.50 \cdot p_{FA} \cdot p_{FACaO}) \end{aligned} \tag{6.58}$$

$$\begin{aligned} \beta = 181.4 \cdot {p_{C_3A}}^{0.146} \cdot {p_{C_3S}}^{0.227} \cdot Blaine^{-0.535} \cdot {p_{SO_3}}^{0.558} \\ \cdot \exp(-0.647 \cdot p_{SLAG}) \end{aligned} \tag{6.59}$$

Compared to the sophisticated Kishi and Maekawa (1997) model, which takes into account the cement reaction kinetics as well as the effects of slag and fly ash on the hydration process, this model can be considered to be simpler in a way that it does not consider the hydration of each cement constituent independently, as well as the detailed cement kinetics, but relies on empirical relationships derived based on observations and regression analyses from hydration experiments. However, the heat of hydration of fly ash should be considered to be more accurately modelled in this model than in the Kishi and Maekawa (1997) model, as its dependence on CaO is accounted for. Moreover, the advantage of this model is that, similar to the Kishi and Maekawa (1997) model, it is very accurate as it takes into account a large number of factors that influence the hydration process, but its drawback is similar to the Kishi and Maekawa (1997) model as well, which is the number of inputs required for the model to function properly. Apart from the cement composition, cement fineness, mixture proportions and admixture contents, this model also requires the CaO content of fly ash to be known, which makes it difficult to apply in geotechnical engineering applications.

Summary of selected available models

From the reviewed models, the one proposed by Kishi and Maekawa (1997) is the most sophisticated, as it takes into account the detailed reaction kinetics and models the hydration of cement constituents independently, as well as accounting for the effects of slag and fly ash on the hydration process. It is also an improvement from the Kishi and Maekawa (1995) model, which does not account for the effects of slag, fly ash and cement fineness. Therefore, comparing the Kishi and Maekawa (1995) and Kishi and Maekawa (1997) models, the Kishi and Maekawa (1997) model should always be preferred even if slag or fly ash are not added into the mix, as their proportions can simply be set to zero, and that the Kishi and Maekawa (1997) model contains other adjustments to improve the modelling of cement reaction kinetics.

The Swaddiwudhipong et al. (2002) model is similar to the Kishi and Maekawa (1995) model in a way that they both model the hydration of cement constituents independently, but the Swaddiwudhipong et al. (2002) model takes into account the effects of cement fineness as well. Also, in the Swaddiwudhipong et al. (2002) model, the dependence of the hydration process on temperature is modelled using the equivalent age (which is also known as equivalent maturity) concept. When compared with the Kishi and Maekawa (1997) model, however, the Swaddiwudhipong et al. (2002) model appears to be inferior as it is unable to account for the effects of slag and fly ash on the hydration process.

The Schindler and Folliard (2005) model can be considered to be a simpler model than the Kishi and Maekawa (1997) model as it does not model the hydration of cement constituents independently, and does not take into account of the cement reaction kinetics. Instead, it relies on empirical relationships derived based on observations and regression analyses from hydration tests. While both models can account for the effects of slag and fly ash on the hydration process, the heat of hydration of fly ash is considered to be more accurately modelled in the Schindler and Folliard (2005) model as it takes into account of the CaO content in the fly ash as well.

The Kishi and Maekawa (1995), Kishi and Maekawa (1997), Swaddiwudhipong et al. (2002) and Schindler and Folliard (2005) models all require an accurate cement composition to be known in order for the models to function properly, which is an information that may not be readily available in geotechnical engineering applications. On the other hand, the De Schutter and Taerwe (1995) model is a much simpler model since it does not account for cement reaction

kinetics at all, and hence does not require any information on the cement composition. However, the six model parameters (a_p, b_p, c_p, $q_{p,max,20}$, $Q_{p,max}$ and E_p) for Portland cement – and six more (a_s, $q_{s,max,20}$, $Q_{s,max}$, E_s, A and B) if slag is included – for the empirical equations, require isothermal hydration tests of cements for their accurate calibration. Such tests are rarely available in practical engineering applications, with the authors failing to provide alternative approaches or indicating what values the parameters should be assumed in such situations. Table 6.9 summarises the features and capabilities for each of the reviewed models.

Model	Detailed cement composition required?	Effects of temperature accounted for?	Effects of cement fineness accounted for?	Effects of w/c accounted for?	Effects of fly ash accounted for?	Effects of slag accounted for?
Kishi and Maekawa (1995)	✓	✓	×	✓	×	×
Kishi and Maekawa (1997)	✓	✓	✓	✓	✓	✓
De Schutter and Taerwe (1995)	×	✓	×	×	×	✓
Swaddiwudhipong et al. (2002)	✓	✓	✓	✓	×	×
Schindler and Folliard (2005)	✓	✓	✓	✓	✓	✓

Table 6.9 A summary of the features and capabilities for each of the reviewed models

A new heat of hydration model is therefore desired, focussing on providing simple relationships involving a limited number of model parameters such that it is easy to calibrate even when very limited information is made available regarding the cement and concrete mix. Moreover, 'average' values of model parameters should be made available to give reasonable estimation of heat of hydration in geotechnical engineering applications without requiring detailed knowledge of cement composition or specialised testing.

6.5 A NEW HEAT OF HYDRATION MODEL FOR CONCRETE

Due to a lack of heat of hydration models for concrete that can be readily applied when limited information on the cement and concrete mix are made available (as explained in Section 6.4), a new heat of hydration model is proposed in this section. This proposed model is based on

similar principles as the Schindler and Folliard (2005) model, but instead of using the equivalent age concept to account for the dependency of the hydration reaction on temperature, such dependency is formulated using fundamental laws of chemistry, which enables a further simplification of the model. In this model, a simple S-shaped curve (given by Equation (6.60) (Helland, 1986; van Breugel, 1991)) with three model parameters (Q_{max} $[J \cdot kg_{cement}^{-1}]$, τ $[s]$ and β) is used to describe the evolution of accumulated heat of hydration with time for any concrete mixture at a constant reference temperature. The effects of cement composition, cement fineness and any admixtures added in the concrete mixture on heat of hydration (as explained in Section 6.2) can be accounted for through the calibration of these three model parameters. The effects of curing temperature on heat of hydration are introduced through the use of the Arrhenius equation, which is explained later in this section. In this model, however, the effects of w/c on heat of hydration are not considered. The heat of hydration experiments performed by Bentz et al. (2009) showed that the influence of w/c on heat of hydration begins to fade as w/c approaches 0.425, as below that there is insufficient water for hydration, which leads to self-desiccation. In geotechnical applications (e.g. casting of piles and shotcreting), the w/c of the concrete is generally higher than this self-desiccation limit, meaning that modelling the effects of w/c on heat of hydration is unnecessary.

$$Q_{ref} = Q_{max} e^{-\left(\frac{\tau}{t}\right)^{\beta}} \tag{6.60}$$

In Equation (6.60), Q_{max}, τ and β are model parameters to be calibrated and Q_{ref} $[J \cdot kg_{cement}^{-1}]$ is the reference accumulated heat of hydration. Note that Q_{max} represents the total heat of hydration that can potentially be released per unit mass of cement at the end of hydration, τ represents the time at which heat that corresponds to 36.8% (or $1/e$) of Q_{max} has been released when the concrete hydrates at a constant reference temperature and β controls the nonlinearity of the curve. Also, the term 'reference' is used because the effects of curing temperature have not been accounted for, and therefore Q_{ref} represents the accumulated heat of hydration when the hydration takes place at a constant reference temperature T_{ref} $[K]$. This corresponds to the temperature adopted in the isothermal hydration tests that are used to calibrate Q_{max}, τ and β (to be explained in Chapter 7). Figure 6.34 illustrates the evolution of Q_{ref} with time for the case of $Q_{max} = 300000\, J \cdot kg_{cement}^{-1}$, $\tau = 70000\, s$ and $\beta = 0.7$.

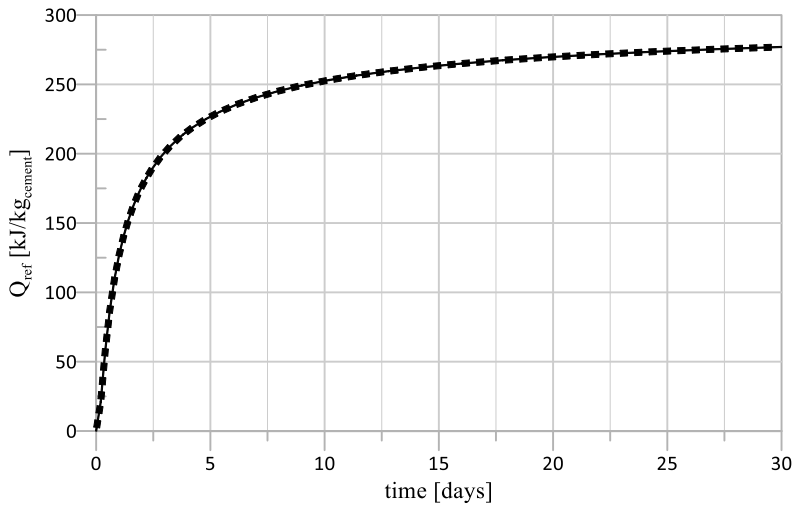


Figure 6.34 Evolution of Q_{ref} with time for the case of $Q_{max} = 300000\ J \cdot kg_{cement}^{-1}$, $\tau = 70000\ s$ and $\beta = 0.7$

By differentiating Equation (6.60) with respect to time and multiplying it by the mass of cement per unit mass of concrete χ $[kg_{cement} \cdot kg_{concrete}^{-1}]$ and the density of concrete $\rho_{concrete}$ $[kg_{concrete} \cdot m^{-3}]$, a reference heat of hydration power per unit volume of concrete P_{ref} $[J \cdot s^{-1} \cdot m^{-3}]$ can be obtained, which is the heat of hydration power when the concrete cures at a constant T_{ref}, and the expression is given by Equation (6.61).

$$P_{ref} = \chi \rho_{concrete} \frac{dQ_{ref}}{dt} = \frac{Q_{max}}{t} \left(\frac{\tau}{t}\right)^{\beta} \beta e^{-\left(\frac{\tau}{t}\right)^{\beta}} \chi \rho_{concrete} \tag{6.61}$$

To account for the effects of temperature on the rate of hydration heat liberation, this model assumes the hydration of cement to be a single chemical reaction, and that the rate of hydration is directly proportional to the power of heat of hydration. As a result, the fundamental equation that governs the rate of a chemical reaction is considered, which is given by Equation (6.62). In this expression, k is the reaction constant given by the Arrhenius equation (Equation (6.63)), $[Reactant_i]$ is the concentration of reactant i and n_i is the order of reaction for reactant i. In Equation (6.63), A is a constant, E_a $[J \cdot mol^{-1}]$ is the activation energy for the reaction, R $[J \cdot mol^{-1} \cdot K^{-1}]$ is the universal gas constant and T $[K]$ is temperature.

$$Rate = k \prod_i [Reactant_i]^{n_i} \tag{6.62}$$

$$k = Ae^{-\frac{E_a}{RT}} \tag{6.63}$$

Equations (6.62) and (6.63) illustrate that the rate of a chemical reaction is dependent on the temperature at which the reaction proceeds, and the abundance of reactants. In a concrete being cured at a temperature higher than T_{ref}, the hydration reaction will proceed more quickly initially, and hence be characterised by a larger rate of hydration heat liberation (i.e. larger power). However, with a faster rate of reaction, the proportion of unhydrated cement at time t would be smaller than the same concrete cured at T_{ref}, which in turn slows down the reaction according to Equation (6.62). Equation (6.64) is proposed to approximate the abundance of unhydrated cement, and hence Equation (6.65) gives the rate of hydration. In Equation (6.64), Q_{acc} $[J \cdot kg_{cement}^{-1}]$ is the accumulated heat of hydration per unit mass of cement, subjected to the effects of its temperature history and its expression is given by Equation (6.66), while n^* is a function to be determined. In Equation (6.66), P $[J \cdot s^{-1} \cdot m^{-3}]$ is the heat of hydration power per unit volume of concrete.

$$\prod_i [Reactant_i]^{n_i} \approx \left(\frac{Q_{max} - Q_{acc}}{Q_{max}}\right)^{n^*} \tag{6.64}$$

$$Rate = Ae^{-\frac{E_a}{RT}} \left(\frac{Q_{max} - Q_{acc}}{Q_{max}}\right)^{n^*} \tag{6.65}$$

$$Q_{acc} = \frac{1}{\chi \rho_{concrete}} \int_0^t P \, dt \tag{6.66}$$

As it is assumed that the rate of hydration is directly proportional to the power of heat of hydration, Equation (6.67) can be written, where A' is a constant.

$$P = A'e^{-\frac{E_a}{RT}} \left(\frac{Q_{max} - Q_{acc}}{Q_{max}}\right)^{n^*} \tag{6.67}$$

Consider the case where the concrete cures at a constant T_{ref}, Equation (6.67) can be written as Equation (6.68).

$$P_{ref} = A'e^{-\frac{E_a}{RT_{ref}}} \left(\frac{Q_{max} - Q_{ref}}{Q_{max}}\right)^{n^*} \tag{6.68}$$

Combining Equations (6.67) and (6.68), Equation (6.69) can be obtained. Note that in Equation (6.69), P_{ref} is given by Equation (6.68). Furthermore, in this case, E_a would be the apparent activation energy, as it characterises the entire concrete mixture, following the approach adopted in the De Schutter and Taerwe (1995) and Schindler and Folliard (2005) models. Although D'Aloia and Chanvillard (2002) have shown that the apparent activation energy varies with the degree of hydration, this quantity is assumed to be constant in this model for simplicity. Lastly, $T\ [K]$ is the temperature at the time instant t, Q_{acc} is given by Equation (6.66) and Q_{ref} is given by Equation (6.60).

$$P = P_{ref} e^{-\frac{E_a}{R}\left[\frac{1}{T}-\frac{1}{T_{ref}}\right]} \left(\frac{Q_{max} - Q_{acc}}{Q_{max} - Q_{ref}}\right)^{n^*} \tag{6.69}$$

As E_a is assumed to be a constant, Equation (6.68) can be simplified into Equation (6.70), where B is a constant. By taking logarithms on Equation (6.70), Equation (6.71) is obtained. Therefore, n^* is given by the slope of $\ln\left(1 - \frac{Q_{ref}}{Q_{max}}\right)$ vs. $\ln P_{ref}$, which is given by Equation (6.72). However, Equation (6.72) will be ill-conditioned if t is very small, therefore it is necessary to impose a cut-off value $t_n\ [s]$ for determining n^* (Equation (6.73)).

$$P_{ref} = B\left(\frac{Q_{max} - Q_{ref}}{Q_{max}}\right)^{n^*} \tag{6.70}$$

$$\ln P_{ref} = \ln B + n^* \ln\left(1 - \frac{Q_{ref}}{Q_{max}}\right) \tag{6.71}$$

$$\begin{aligned} n^* &= \frac{d \ln P_{ref}}{d \ln\left(1 - \frac{Q_{ref}}{Q_{max}}\right)} = \frac{\frac{d \ln P_{ref}}{dt}}{\frac{d \ln\left(1 - \frac{Q_{ref}}{Q_{max}}\right)}{dt}} \\ &= \left(e^{\left(\frac{\tau}{t}\right)^{\beta}} - 1\right)\left((1 + \beta^{-1})\left(\frac{t}{\tau}\right)^{\beta} - 1\right) \end{aligned} \tag{6.72}$$

$$n^*(t \le t_n) = n^*(t = t_n) \tag{6.73}$$

To conclude, Equations (6.60), (6.61), (6.66), (6.69), (6.72) and (6.73) constitute the new heat of hydration model for concrete, which takes into account of the effects of cement composition, cement fineness and admixtures through the calibration of Q_{max}, τ and β, as well as the effects

of curing temperature. The model can hence be applied with proper calibration of parameters Q_{max}, τ, β, E_a and t_n, which is explained in Chapter 7, as well as the cement content (χ and $\rho_{concrete}$) of the concrete.

6.6 CONCLUSIONS

In this chapter, the exothermic hydration reactions between cement and water have been reviewed, which provides an understanding of the origin of the heat of hydration of concrete, as well as the factors that influence the amount and rate of hydration heat liberation. Subsequently, laboratory and field measurements of heat of hydration have been reviewed, and it has been shown that it is not uncommon to have temperatures above 50^oC, or even 60^oC, in geotechnical structures (e.g. piles and diaphragm walls) because of heat of hydration. This consolidates the structural and geotechnical significance of heat of hydration, and suggests that its effects on the surrounding soil must not be neglected. As the significance of heat of hydration in the context of structural engineering has long been well established, a number of heat of hydration models have been developed over the years, with the most popular ones being reviewed in Section 6.4. This review reveals that there is a lack of a model that can be readily applied in geotechnical engineering applications when limited information on the cement and concrete mix are available. A new heat of hydration model is therefore proposed, which only relies on the calibration of five model parameters (Q_{max}, τ, β, E_a and t_n), and instead of using the equivalent age concept to account for the dependency of the hydration reaction on temperature, such dependency is formulated using fundamental laws of chemistry, which enables a further simplification of the model.

CHAPTER 7 PERFORMANCE OF THE HEAT OF HYDRATION MODEL FOR CONCRETE

7.1 INTRODUCTION

The heat of hydration model for concrete that is proposed in Chapter 6 requires the knowledge of five model parameters (Q_{max}, τ, β, E_a and t_n) for the concrete. In order to establish the effects and importance of each parameter on the heat of hydration modelled, this chapter begins with a parametric study on each of the model parameters, which is detailed in Section 7.2.

Following determination of the effects and importance of each model parameter, Section 7.3 discusses the implementation of the model in finite-element programs, ICFEP in this case. This is followed by a validation in which an ICFEP simulation of the adiabatic temperature rise of a concrete sample is compared against the results obtained using Excel.

Subsequently, the model parameters have to be calibrated and the model has to be validated that it is capable of simulating the realistic heat of hydration evolution from concrete. This can be accomplished by heat of hydration laboratory tests and field measurements of temperature rise within hydrating concrete.

Among the different types of heat of hydration laboratory tests introduced in Section 6.3.1, for the purpose of calibrating and validating the proposed heat of hydration model, isothermal tests are preferred over adiabatic or semi-adiabatic tests. This is due to the fact that isothermal tests eliminate the need to simulate the heat transfer process within the tested sample, which may also require a complex nonlinear thermal boundary condition in the case of semi-adiabatic tests. Furthermore, isothermal tests allow the heat of hydration to be measured for the same concrete mix at different curing temperatures. The latter reason is particularly important as, according to the formulation of the proposed model, the set of model parameters should be unique for a given concrete mix, and hence isothermal tests allow the direct validation of the temperature-dependency part of the model (i.e. Equation (6.69)). Among isothermal tests, isothermal calorimetry is preferred over heat of solution tests as the former allows the continuous measurement of heat of hydration with time and, according to Sedaghat et al. (2013), isothermal calorimetry has a higher precision, particularly at early stages of curing (e.g. immediately after the cement is mixed with water). Moreover, according to Wadsö (2003), a

potential problem with heat of solution tests is that the tests are not effective if the unhydrated and hydrating samples do not dissolve to the same state in acids. Given the above, isothermal calorimetry laboratory test results are used to calibrate and validate the proposed model, which is discussed in Section 7.4.

In order to demonstrate the practical performance of the proposed heat of hydration model, field measurements of temperature rise within hydrating concrete are used to calibrate and validate the model. More specifically, in Section 7.5, the capabilities of the proposed heat of hydration model are assessed by reproducing field measurements collected from thermal integrity profiling (TIP) operations performed on piles at two different sites (and hence, two different concrete mixes) in London by Cementation Skanska, with 16 piles in total.

Note that the contents of this chapter were published in part or whole in Liu et al. (2022).

7.2 PARAMETRIC STUDY

In order to understand the importance and effects of each model parameter to the modelled heat of hydration, a parametric study focussing on each of the model parameters is conducted. According to the formulation of the proposed model (see Chapter 6), Q_{max} is the model parameter that controls the total heat of hydration that can potentially be released per unit mass of cement at the end of hydration, τ represents the time at which heat that corresponds to 36.8% (or $1/e$) of Q_{max} has been released when the concrete hydrates at a constant reference temperature, β controls the nonlinearity of the evolution of released heat with time, and hence the rate of hydration, E_a is the activation energy that controls the sensitivity of the rate of hydration to variations in temperature, and t_n is a model parameter that is introduced simply to avoid numerical errors.

7.2.1 Q_{max}

In this parametric study, the effects of Q_{max} on the accumulated heat of hydration Q_{acc} of a concrete hydrating isothermally at 23^oC are studied by varying Q_{max} by $\pm 50\%$ from the 'base' parameters, which are arbitrarily defined and presented in Table 7.1, while keeping other model parameters constant. Figure 7.1 shows the modelled accumulated heat of hydration when Q_{max} is varied by $\pm 50\%$ and, from the figure, it can be concluded that Q_{max} not only affects the total heat of hydration (with a higher Q_{max} giving a larger total heat of hydration), but the rate

of hydration as well, in particularly during the early ages (with a higher Q_{max} giving a higher rate of hydration).

Q_{max}	$300000\ J \cdot kg_{cement}^{-1}$
τ	$70000\ s$
β	0.7
E_a	$45000\ J \cdot mol^{-1}$
R	$8.314\ J \cdot mol^{-1} \cdot K^{-1}$
T_{ref}	23^oC
t_n	$2\ days$

Table 7.1 Arbitrarily defined 'base' model parameters

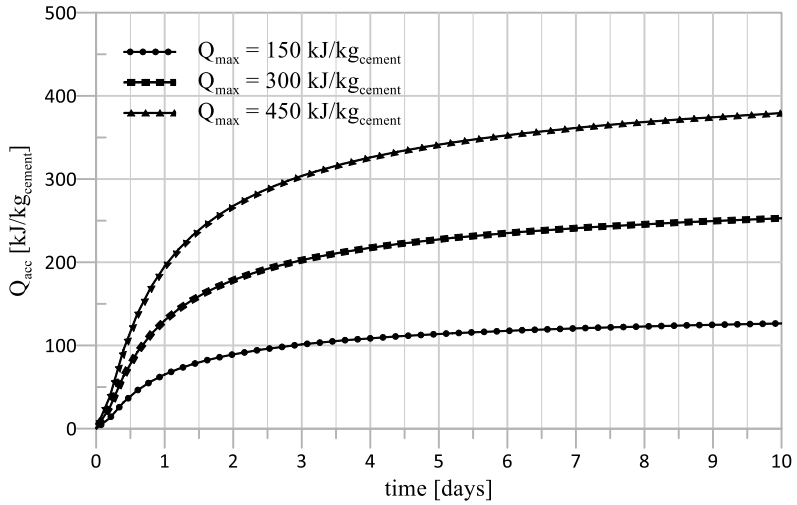


Figure 7.1 Accumulated heat of hydration of a concrete hydrating isothermally when Q_{max} is varied by $\pm 50\%$ from the 'base' parameters

7.2.2 τ

In this parametric study, the effects of τ on the accumulated heat of hydration Q_{acc} of a concrete hydrating isothermally at 23^oC are studied by varying τ by $\pm 50\%$ from the 'base' parameters given in Table 7.1, while keeping other model parameters constant. Figure 7.2 shows the modelled accumulated heat of hydration when τ is varied by $\pm 50\%$, and from the figure, it can be concluded that τ is a parameter that controls the rate of hydration, with a smaller τ value giving a higher rate of hydration during the early ages, but a slower rate of

hydration later on, i.e. τ controls directly the time required for a certain degree of hydration to be reached, without affecting the total heat being released.

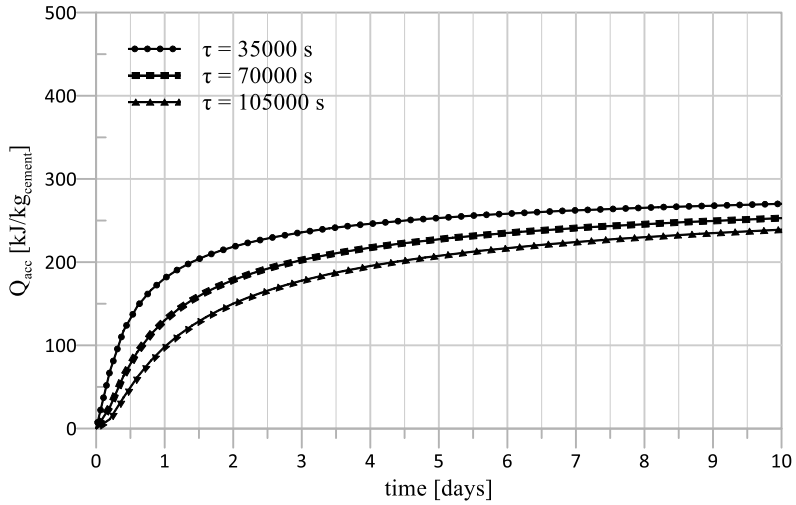


Figure 7.2 Accumulated heat of hydration of a concrete hydrating isothermally when τ is varied by $\pm 50\%$ from the 'base' parameters

7.2.3 β

In this parametric study, the effects of β on the accumulated heat of hydration Q_{acc} of a concrete hydrating isothermally at $23^{o}C$ are studied by varying β by $\pm 50\%$ from the 'base' parameters given in Table 7.1, while keeping other model parameters constant. Figure 7.3 shows the modelled accumulated heat of hydration when β is varied by $\pm 50\%$ and, from the figure, it can be concluded that β affects the non-linearity of the evolution with time of the rate of hydration, thus affecting the modelled heat of hydration in two ways:

- β controls the time at which hydration heat starts to evolve during the early ages, with a larger value of β delaying the start of hydration heat evolution. As a result, β allows the model to capture the effects of having retarders in concrete, which are often used in hot weather conditions to delay the initial setting of concrete.
- A smaller value of β suppresses the total heat of hydration within timeframes typically associated with engineering structures, since at $t \to \infty$ the overall heat of hydration released will always be given by Q_{max}.

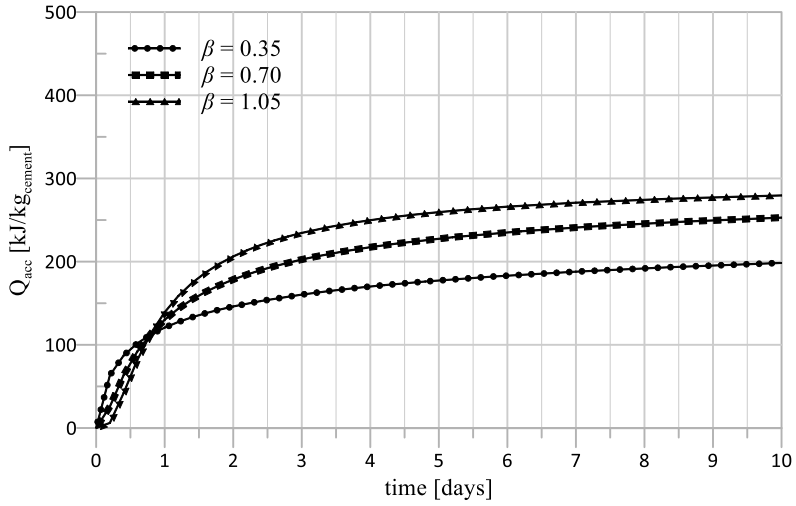


Figure 7.3 Accumulated heat of hydration of a concrete hydrating isothermally when β is varied by $\pm 50\%$ from the 'base' parameters

7.2.4 E_a

As the activation energy E_a is a parameter that controls the sensitivity of the rate of hydration to variations in temperature, its effects can only be studied by comparing concrete hydration at different isothermal temperatures and different E_a. In this case, E_a is varied by $\pm 50\%$ from the 'base' parameters given in Table 7.1, considering concrete curing at isothermal temperatures of 13^oC, 23^oC and 33^oC, while keeping other model parameters constant. Figure 7.4 shows the modelled accumulated heat of hydration. It can be concluded from Figure 7.4 that a higher E_a increases the sensitivity of the rate of hydration to temperature. This means that, when a concrete with higher E_a is compared with one with lower E_a, a higher rate of hydration is obtained if curing takes place at a temperature higher than the reference temperature, while a lower rate of hydration is observed if curing takes place at a temperature lower than the reference temperature. It should be noted that as the reference temperature T_{ref} is 23^oC, concrete hydrating isothermally at this temperature results in the same accumulated heat of hydration curve and is independent on the magnitude of E_a. Referring to Figure 7.4, although the magnitude of E_a does have an effect on the modelled accumulated heat of hydration, it is assumed to be a constant due to its difficulty to calibrate – E_a can only be calibrated when a concrete mix is tested isothermally at different temperatures. Following measurements by Thomas (2012), $E_a = 45000\, J \cdot mol^{-1}$ is adopted throughout, an assumption which will be further validated in Sections 7.4 and 7.5.

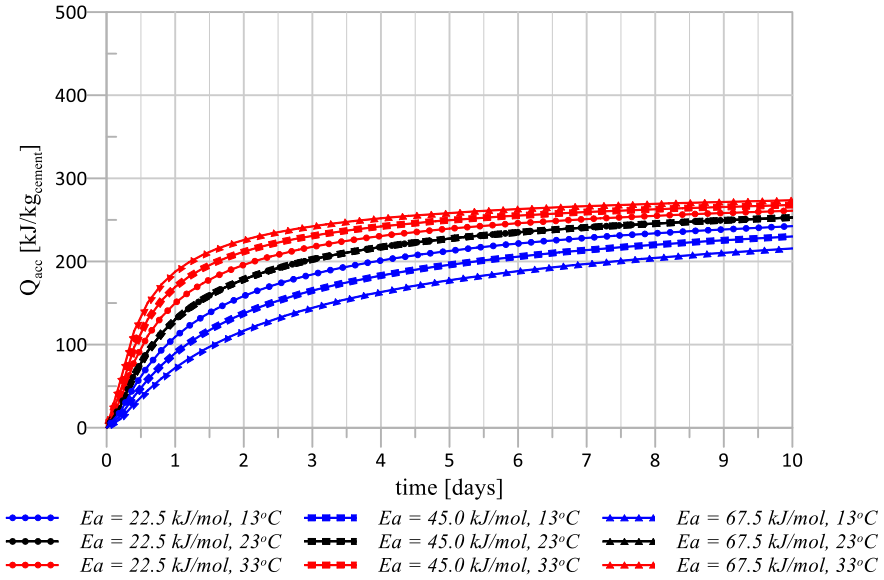


Figure 7.4 Accumulated heat of hydration of a concrete hydrating isothermally at 13^oC, 23^oC and 33^oC when E_a is varied by $\pm 50\%$ from the 'base' parameters

7.2.5 t_n

In this parametric study, t_n is varied from 0.5 day to 3 $days$ in steps of 0.5 day to study its effects on accumulated heat of hydration Q_{acc} of concrete hydrating isothermally at 23^oC, while the other parameters follow those presented in Table 7.1. Figure 7.5 shows the accumulated heat of hydration with time for different t_n values. Clearly, it can be observed that the value of t_n has insignificant influence on the results, therefore a value of $t_n = 2\ days$ has been chosen to be adopted throughout.

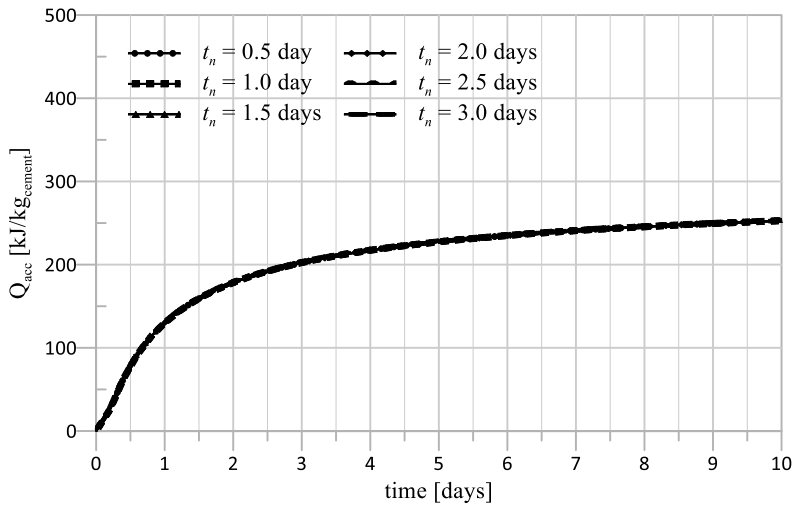


Figure 7.5 Accumulated heat of hydration of a concrete hydrating isothermally for different values of t_n

This parametric study allows the effects of each model parameters to be studied and understood. With the assumption of $E_a = 45000\, J \cdot mol^{-1}$ and the adoption of $t_n = 2\, days$, this leaves only Q_{max}, τ and β to be calibrated, which will be discussed in Sections 7.4 and 7.5, together with the validation of the model.

7.3 IMPLEMENTATION INTO A FINITE-ELEMENT PROGRAM

As the proposed heat of hydration model is nonlinear in temperature (i.e. the temperature at a point has to be known before the hydration power at that point can be evaluated by the model), this makes the model a nonlinear thermal boundary condition in the finite-element method. In order to implement the model in a finite-element program, firstly, the temperature field T within the element has to be evaluated using shape functions for temperature $[N_T]$ based on the temperatures at the element nodes $\boldsymbol{T_{nodes}}$:

$$T = [N_T]\boldsymbol{T_{nodes}} \tag{7.1}$$

Once the temperature field within the element is obtained, the hydration power field P can be evaluated using the proposed model. The hydration power at the element nodes $\boldsymbol{P_{nodes}}$ can be evaluated by integrating the hydration power field over the domain of the element Ω with the shape functions for temperature:

$$\boldsymbol{P_{nodes}} = \int_{\Omega} [N_T]^T P \, d\Omega \tag{7.2}$$

In a two-dimensional analysis, the nonlinear thermal boundary condition is applied over an area (so Ω represents a surface), while in a three-dimensional analysis, it is applied over a volume (so Ω represents a volume). Since the nonlinear thermal boundary condition is dependent on temperature, and that the temperature varies over an increment, this should be accounted for in the finite-element program. Note that the integration in Equation (7.2) can be evaluated numerically using Gaussian Quadrature, which is the case in ICFEP.

The above finite-element algorithms for the proposed model are implemented into ICFEP, which is used to simulate the adiabatic temperature rise of a concrete sample using a single-element analysis. The results are then compared with those calculated in Excel, in order to validate the model implementation in ICFEP. Table 7.2 presents the model parameters and thermal properties adopted in the analyses and Figure 7.6 compares the simulated temperature rise curves between ICFEP and Excel. The close resemblance implies that the proposed model has been implemented correctly in ICFEP.

Q_{max}	$300000\, J \cdot kg_{cement}^{-1}$
τ	$70000\, s$
β	0.7
E_a	$45000\, J \cdot mol^{-1}$
χ	$0.17\, kg_{cement} \cdot kg_{concrete}^{-1}$
R	$8.314\, J \cdot mol^{-1} \cdot K^{-1}$
T_{ref}	23^oC
$T_{initial}$	19.5^oC
t_n	$2\, days$
ρ	$2400\, kg_{concrete} \cdot m^{-3}$
c	$895\, J \cdot kg_{concrete}^{-1} \cdot K^{-1}$

Table 7.2 Model parameters and thermal properties adopted for the ICFEP and Excel analyses

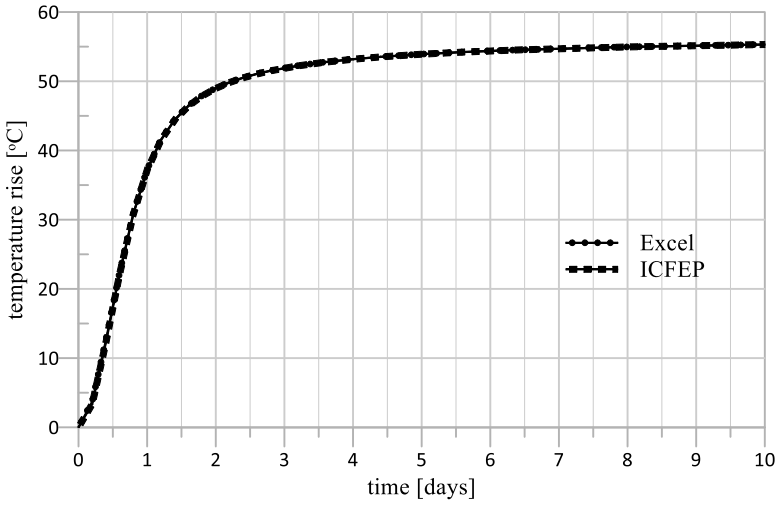


Figure 7.6 Comparison of temperature rise curves between ICFEP and Excel analyses

7.4 CALIBRATION AND VALIDATION WITH ISOTHERMAL CALORIMETRY

In order to validate the temperature dependency part of the model, isothermal calorimetry tests on cement samples hydrating at different temperatures are used. As described in Section 6.3.1.3, Wadsö (2003) tested the cement 'Anläggningscement', which is a CEM I 42.5 BV/SR/LA cement, at four curing temperatures: $20, 30, 40$ and 50^oC, and presented the results in time vs. heat of hydration power curves, as shown in Figure 7.7 (Wadsö, 2003). The curves in Figure 7.7 are digitalised and converted into time vs. accumulated heat of hydration curves, which are used to calibrate the model parameters Q_{max}, τ and β by minimising the differences between the modelled and experimental curves, using the least squares method in Excel. Based on $T_{ref} = 23^oC$, $E_a = 45000\, J \cdot mol^{-1}$ and $t_n = 2\, days$, $Q_{max} = 333000\, J \cdot kg_{cement}^{-1}$, $\tau = 68162\, s$ and $\beta = 0.743$ are obtained (as mentioned in Section 7.1, the same set of model parameters should be used for the same cement). The modelled accumulated heat of hydration curves are compared with the experimental ones (Wadsö, 2003) in Figure 7.8. The close resemblance between the modelled and experimental accumulated heat of hydration curves shown in Figure 7.8 demonstrates that:

- the model is capable of reproducing the heat of hydration with good accuracy;
- the temperature dependency part of the model is performing effectively; and
- the assumption of $E_a = 45000\, J \cdot mol^{-1}$ is appropriate.

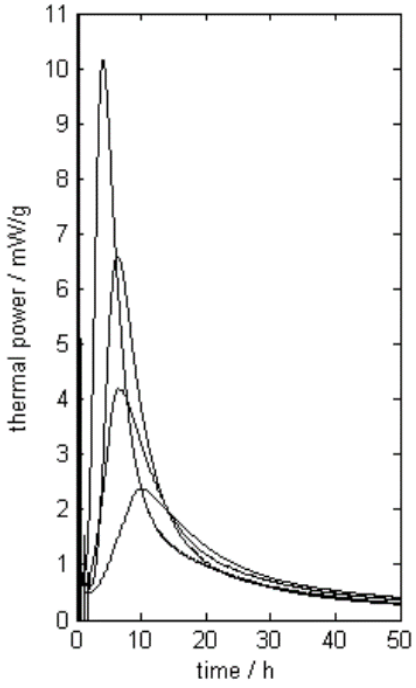


Figure 7.7 Time vs. heat of hydration power curves for cement 'Anläggningscement' at $20, 30, 40$ and 50^oC (from lowest to highest peaks, respectively) (Wadsö, 2003)

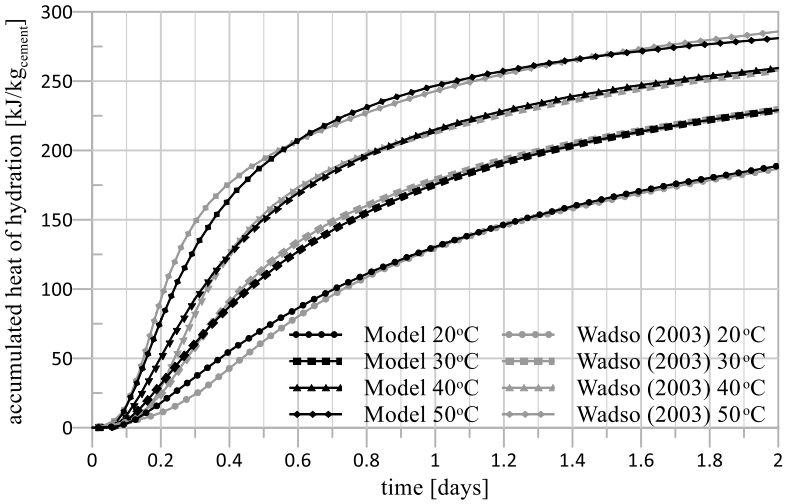


Figure 7.8 Comparison of modelled and experimental (Wadsö, 2003) accumulated heat of hydration curves at different curing temperatures ($20, 30, 40$ and 50^oC)

As mentioned in Section 6.2, when a cement is ground to different fineness levels, only the rate of hydration heat liberation at early ages is affected, but not the total heat of hydration released at the end of hydration. In the context of the proposed model, this suggests that different fineness levels from the same cement should share the same Q_{max}. To verify this, isothermal calorimetry tests on the same cement at different fineness levels are used. As described in

Section 6.3.1.3, Zayed et al. (2013) conducted isothermal calorimetry tests at 23^oC on three ASTM Type II (MH) cements (Cements A, B and C) at different fineness levels, where Cement A was tested at three fineness levels (Cement A1, A2 and A3) and Cements B and C were tested at two fineness levels (Cement B1, B2, C1 and C2). Note that ASTM Type II cements are moderately sulphate resistant, which are widely used in geotechnical engineering due to the presence of sulphate in soils. The resulted accumulated heat of hydration curves presented by Zayed et al. (2013) are used to calibrate the model parameters Q_{max}, τ and β by minimising the differences between the modelled and experimental curves, using the least squares method in Excel, while keeping Q_{max} constant for the same cement. The results of the calibration (based on $T_{ref} = 23^oC$, $E_a = 45000\, J \cdot mol^{-1}$ and $t_n = 2\ days$) are presented in Table 7.3 and the comparisons between the modelled and experimental (Zayed et al., 2013) accumulated heat of hydration curves for Cements A to C are shown in Figure 7.9 to Figure 7.11 respectively. The close match between the modelled and experimental curves confirms that using the same Q_{max} for the same cement, as the theory behind the model formulation suggested, is a reasonable assumption. Furthermore, it can be seen in Table 7.3 that, as the fineness increases, the release of heat tends to shift to lower times, as suggested by the associated reduction in τ and increase in β (see Figure 7.2 and Figure 7.3, respectively).

Cement	$Q_{max}\ [J \cdot kg_{cement}^{-1}]$	$\tau\ [s]$	β
A1	411000	76725	0.529
A2		52349	0.573
A3		36397	0.795
B1	422000	57768	0.732
B2		40984	0.856
C1	386000	53190	0.781
C2		40504	0.864

Table 7.3 The results of model calibration for cement samples A1, A2, A3, B1, B2, C1 and C2 from Zayed et al. (2013)

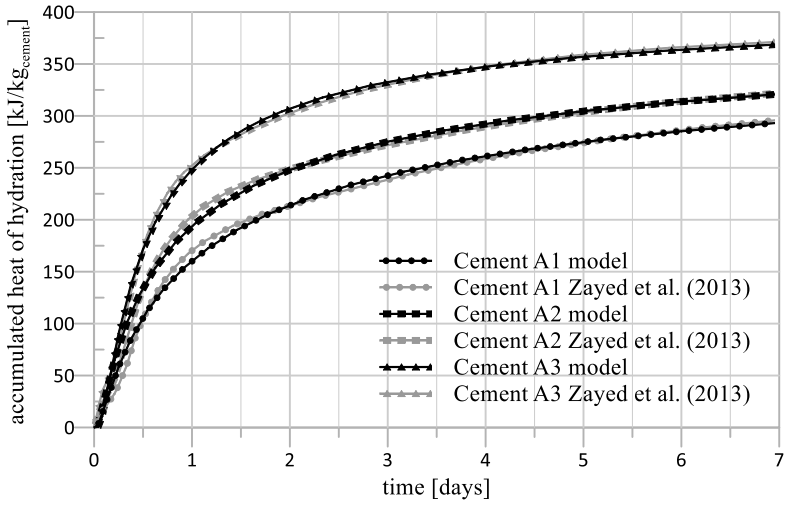


Figure 7.9 Comparison of modelled and experimental (Zayed et al., 2013) accumulated heat of hydration curves for Cement A

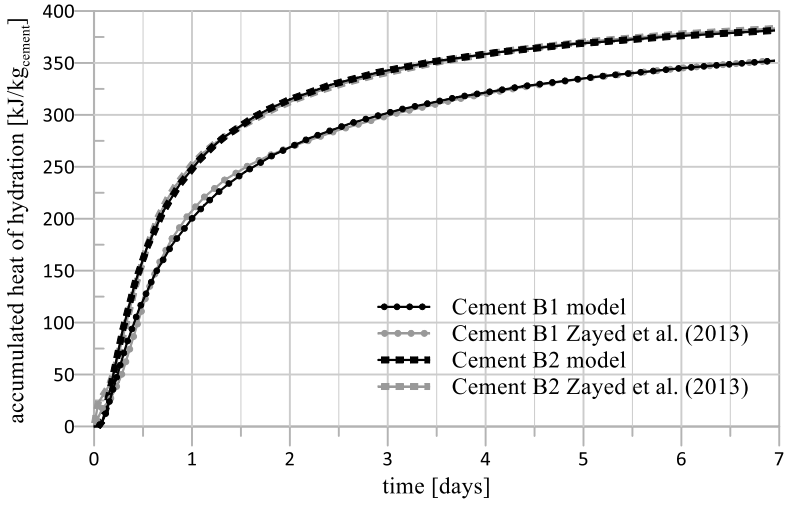


Figure 7.10 Comparison of modelled and experimental (Zayed et al., 2013) accumulated heat of hydration curves for Cement B

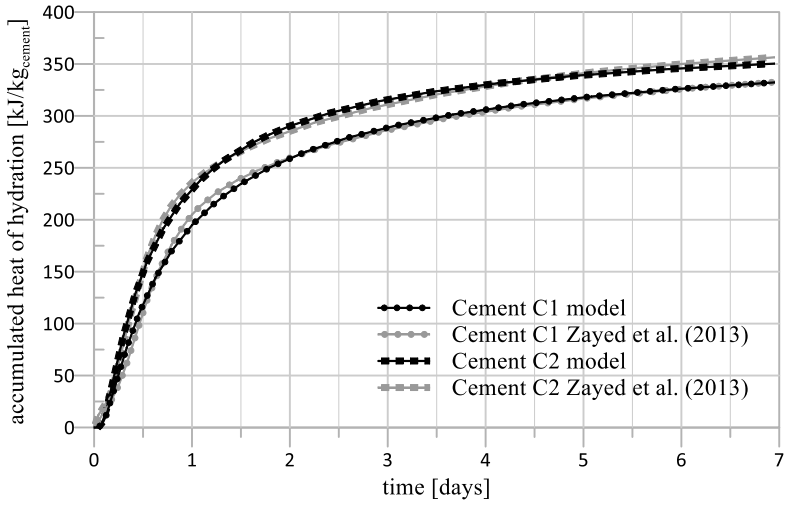


Figure 7.11 Comparison of modelled and experimental (Zayed et al., 2013) accumulated heat of hydration curves for Cement C

As a result, it can be concluded that the proposed model, with essentially only three parameters to calibrate (Q_{max}, τ and β), is capable of reproducing the evolution of heat of hydration in laboratory tests if adequately calibrated. The following section discusses the calibration and validation of the proposed model in a practical boundary value problem of a hydrating concrete pile.

7.5 CALIBRATION AND VALIDATION WITH FIELD MEASUREMENTS

In order to validate the potential of the proposed model to be used in practical applications, model parameters are calibrated based on field measurements of temperature, and in this case, within hydrating concrete piles. In this boundary value problem, a transient and non-uniform temperature field is expected to develop within the hydrating pile, and since the proposed model is nonlinear in temperature, it is not possible to assume a uniform hydration power within the pile. Although ICFEP can be used to simulate the boundary value problem effectively, a new numerical technique which adopts the proposed model is developed to simulate the problem, in order to apply a meta-heuristic (in this case, Genetic Algorithms, see Section 7.5.3) to calibrate the model parameters in an efficient and objective way.

7.5.1 A numerical technique to simulate the temperature rise within a hydrating pile using the proposed model

A simple numerical technique is developed in order to use the proposed model to simulate the temperature rise within a hydrating pile, which has a non-uniform temperature field. This numerical technique is based upon three assumptions:

- The one-dimensional problem is modelled as two-dimensional. This means that the pile is infinitely long, which is a reasonable assumption for piles with large length-to-diameter ratios, as end effects would not be significant.
- The transfer of heat is purely conductive. This means that convective heat transfer due to ground water movement is neglected. This is a reasonable assumption considering soils with low permeability (such as London Clay, which is the case for the field measurements considered in this study) as ground water movement is insignificant (Kavanaugh & Rafferty, 2014).
- The concrete pile and the surrounding soil have the same thermal properties (i.e. thermal conductivity and volumetric heat capacity). This is a reasonable assumption considering a concrete pile surrounded by London Clay, as both the concrete and London Clay have similar thermal conductivities (Scanlon & McDonald, 1994; Loveridge et al., 2014) and volumetric heat capacities (Burg & Ost, 1994; Headon et al., 2009). It is appreciated that the range of thermal conductivity of concrete can be substantial (Scanlon & McDonald, 1994) and therefore a parametric study is conducted to investigate the effects of the ratio of thermal conductivity of concrete λ_c to that of soil λ_s on the simulated temperature rise within a hydrating pile using ICFEP, which is presented in Appendix A. This parametric study shows that the ratio has insignificant influence on the modelled temperature near the pile edge (i.e. where the field measurements are likely to be taken).

In this numerical technique, the cross-section of the hydrating pile is discretised into sections both radially and angularly, with the heat of hydration power for each section being idealised as an infinite line source (ILS) (Carslaw & Jaeger, 1959) positioned in the centre of the corresponding section. This is illustrated in Figure 7.12 for the case with a radial discretisation $n_r = 5$ and an angular discretisation $n_\theta = 6$.

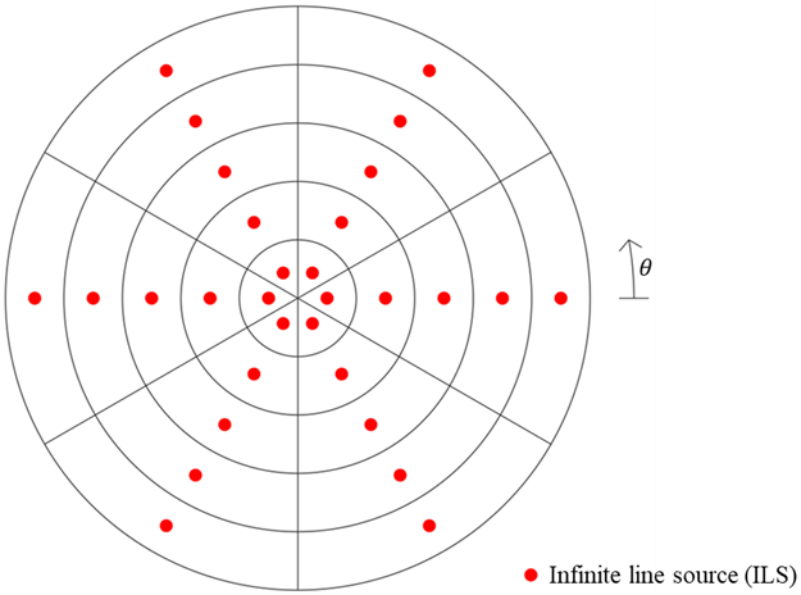


Figure 7.12 Discretisation of the cross-section of a hydrating pile into ILS radially and angularly, with $n_r = 5$ and $n_\theta = 6$

The change in temperature ΔT $[K]$ after time t $[s]$ at a monitoring point that is located at a radial distance r $[m]$ away from an ILS of a constant heat flux q $[W \cdot m^{-1}]$ in a medium with thermal conductivity λ $[W \cdot m^{-1} \cdot K^{-1}]$ and thermal diffusivity α_{th} $[m^2 \cdot s^{-1}]$ is given by the ILS solution (Carslaw & Jaeger, 1959):

$$\Delta T = \frac{q}{4\pi\lambda} E_1\left(\frac{r^2}{4\alpha_{th}t}\right) = \frac{q}{4\pi\lambda}\int_{\frac{r^2}{4\alpha_{th}t}}^{\infty} \frac{e^{-u}}{u} du \tag{7.3}$$

Note that E_1 is the exponential integral and Equation (7.3) presents a solution for the radial heat transfer from a line with constant heat flux that is infinitely long towards an infinite medium where heat transfer occurs via conduction, and such problem is defined by the following boundary and initial conditions:

$$\frac{\partial^2 \Delta T}{\partial r^2} + \frac{1}{r}\frac{\partial \Delta T}{\partial r} = \frac{1}{\alpha_{th}}\frac{\partial \Delta T}{\partial t}$$

$$-2\pi\lambda \lim_{r\to 0} r\frac{\partial \Delta T}{\partial r} = q \quad for \quad r \to 0 \tag{7.4}$$

$$\Delta T = 0 \quad for \quad r \to \infty$$

$$\Delta T = 0 \quad for \quad t = 0$$

As the ILS solution is linear, the change in temperature at a monitoring point due to multiple ILS can be determined by superposition, i.e. by adding the contribution from each ILS. However, the ILS solution given by Equation (7.3) is only applicable for constant heat fluxes. For a heat flux that varies with time, like the heat of hydration power as suggested by the proposed model, discretisation in time and temporal superposition of the ILS solution (Yavuzturk & Spitler, 1999) is required. Due to the dependency of the proposed model on temperature, the temperature at each ILS has to be calculated at each time step (and hence each ILS is a monitoring point), in order to determine the hydration power at that location. The temperature rise at a given radius measured from the centre of the hydrating pile (which should be an axisymmetric quantity) is determined by calculating and averaging the temperatures at an arc of monitoring points spanning from $\theta = 0^o$ to $\theta = 180^o/n_\theta$.

In order to validate this numerical technique, two hydrating piles are simulated in MATLAB: one with a diameter of $0.6\ m$ and the other one with a diameter of $2.4\ m$, using a discretisation of $n_r = 10$ and $n_\theta = 12$. The results are then compared with those simulated using ICFEP analyses, considering identical pile diameters, model parameters and thermal properties, which are presented in Table 7.4. For the $0.6\ m$ diameter pile, temperature rise is monitored at $r = 0\ m$ and $0.3\ m$ (where r is measured from the centre of the pile), and the results are shown in Figure 7.13, while for the $2.4\ m$ diameter pile, temperature rise is monitored at $r = 0\ m$, $0.6\ m$ and $1.2\ m$, with the results being shown in Figure 7.14. Referring to Figure 7.13 and Figure 7.14, the close resemblance of results of the MATLAB analyses with those from the ICFEP analyses implies that the numerical technique implemented with MATLAB is functional and reliable, and that a radial discretisation $n_r = 10$ and an angular discretisation $n_\theta = 12$ is sufficient.

Model parameter Q_{max}	$250000\ J \cdot kg_{cement}^{-1}$
Model parameter τ	$80000\ s$
Model parameter β	0.6
Activation energy E_a	$45000\ J \cdot mol^{-1}$
Cement content χ	$0.125\ kg_{cement} \cdot kg_{concrete}^{-1}$
Concrete/soil density ρ	$2400\ kg \cdot m^{-3}$
Concrete/soil specific heat capacity C_p	$895\ J \cdot kg^{-1} \cdot K^{-1}$
Concrete/soil thermal conductivity λ	$1.79\ W \cdot m^{-1} \cdot K^{-1}$
Universal gas constant R	$8.314\ J \cdot mol^{-1} \cdot K^{-1}$
Reference temperature T_{ref}	23^oC
Initial concrete/soil temperature $T_{initial}$	20^oC

Table 7.4 Model parameters and thermal properties adopted for the MATLAB and ICFEP analyses

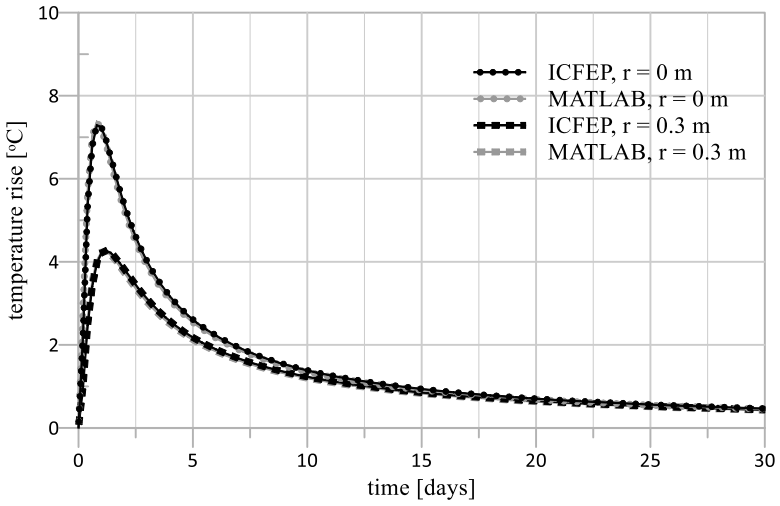


Figure 7.13 Temperature rise recorded at the monitoring points for the $0.6\ m$ diameter pile

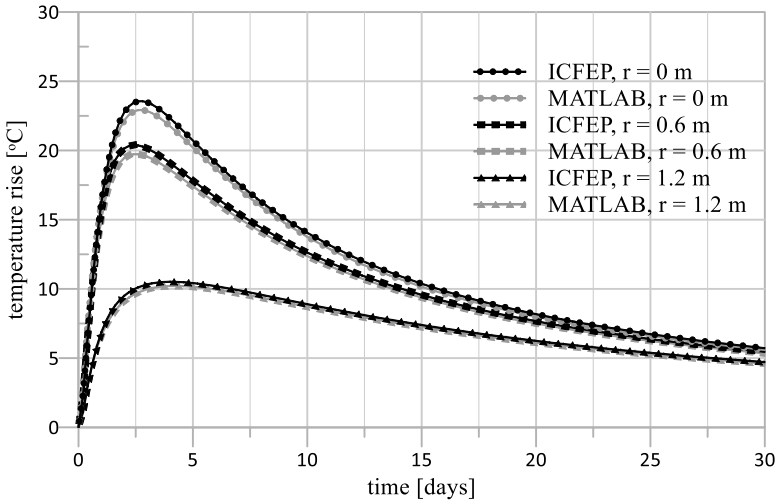


Figure 7.14 Temperature rise recorded at the monitoring points for the $2.4\ m$ diameter pile

7.5.2 The field measurements

Cementation Skanska performed thermal integrity profiling (TIP) operations on piles at two different construction projects in London (designated as London Project 1 and London Project 2, respectively, in this thesis). London Project 1 consists of 14 piles and London Project 2 consists of two piles. Table 7.5 summarises the designated names of the piles that will be used in this thesis, as well as their diameters, cement contents, and main characteristics of the concrete mix. The detailed mix design for the concrete used in London Project 1 and London Project 2 are provided in Appendices B and C, respectively. Note that the concrete used in London Project 2 corresponds to Mix 4 in the design sheet in Appendix C.

Project name	Pile name	Pile diameter $[m]$	Cement content $[kg_{cement} \cdot m^{-3}]$	Main characteristics of concrete mix
London Project 1	Test Pile	1.2	440	50% of cement is GGBS
	P2	2.4		
	P3a	1.8		
	P5	2.4		
	P6	2.4		
	P7	2.4		
	P7a	1.8		
	P8	2.4		
	P9	2.4		
	P10	2.4		
	P11	2.4		
	P12	2.4		
	P13	1.8		
	P14	1.8		
London Project 2	P214	1.2	350	21-35% of cement is fly ash, with the use of retarder
	P154	1.5		

Table 7.5 A summary of the piles that Skanska has provided field measurements

The temperature rises within the hydrating piles are measured using distributed fibre optic sensing, where optical fibres are tied to the reinforcement cage and run along the entire length of the pile, allowing continuous measurements of temperature with depth. In both London Projects 1 and 2, it has been reported that the optical fibres are located at 75 mm from the pile edge, and they run down and up the pile three times to measure temperature at six different points (which are spaced 60^o apart) within the pile cross-section. Figure 7.15 shows a typical layout of the optical fibres within a pile. However, due to minor dislocation of optical fibres arising from the casting, minor anomalies within the cast pile, stratigraphy and hence spatial

variation of thermal properties in the surrounding soil, a range of temperatures are recorded within and along the length of the pile. Therefore, for clarity purposes, only the median of the temperature measurements that are recorded in the section of the pile that lies within the London Clay are considered, which gives an evolution of median temperature rise with time.

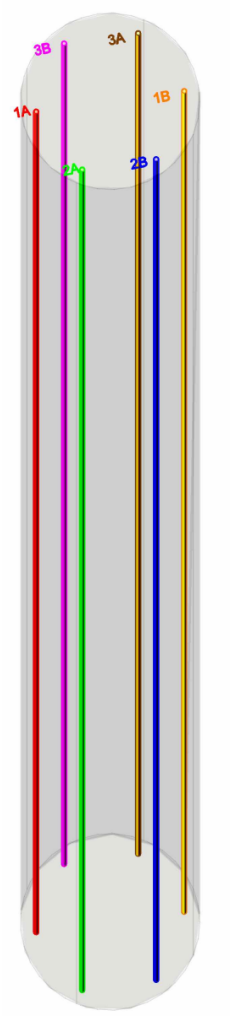


Figure 7.15 A typical layout of optical fibres within a pile

7.5.3 Calibration with Genetic Algorithms

The availability of a relatively low-cost numerical technique (presented and validated in Section 7.5.1) together with the field measurements of temperature rise within hydrating piles from Cementation Skanska allow the calibration of model parameters. As the proposed model is nonlinear, the only way to calibrate the model parameters based on this complex boundary value problem of a hydrating pile is to adopt meta-heuristics, in this case, the Genetic Algorithms (Azeiteiro et al., 2009; Taborda, 2011) technique is adopted, which is an optimisation method inspired by natural selection.

In Genetic Algorithms, a set of model parameters to be calibrated (Q_{max}, τ and β in this case, as $E_a = 45000\, J \cdot mol^{-1}$ and $t_n = 2\, days$ are assumed) are randomly generated (within a reasonable predefined range), which makes an 'individual', and a predefined number of individuals (48 is adopted in this case) makes a 'population'. The numerical technique is then employed to perform a simulation of the boundary value problem (temperature rise within a hydrating pile in this case) for each individual. Once these simulations are concluded, each individual within the population is associated with a measurement of error (in this case, the sum of squares of the differences between the modelled temperature rise curve and the median temperature rise curve from the field measurements), and individuals with smaller errors represent better reproduction of the observed behaviour. This also marks the end of a 'generation'.

Before entering the next generation, a new population has to be determined. The new population is made up of:

- the best 25% of the individuals from the previous generation;
- completely new randomly generated individuals (which contributes to 25% of the new population); and
- 'crossing' the best and new randomly generated individuals (also known as 'parents') to produce new individuals (also known as 'offspring', which contributes to 50% of the new population).

In the crossing process, parents are randomly assigned into pairs to produce offspring. In this case, a constant probability crossing scheme (Taborda, 2011) is adopted, which means that for each parameter in the offspring, the probability of which parent it is passed on from is equal (50%). Furthermore, whenever a parameter is passed on to the offspring, it suffers a 'mutation', which is determined by the mutation factor Δ:

$$\Delta = \Delta_{max} \cdot \tan\left(\frac{\pi}{2} \cdot \left(\frac{1}{2} + 4 \cdot \left(X_{rand} - \frac{1}{2}\right)^3\right) - \frac{\pi}{4}\right) \tag{7.5}$$

where Δ_{max} is the maximum mutation factor (10% is adopted in this case) and X_{rand} is a random number between 0 and 1. This mutation scheme is employed to ensure diversity and improve the global quality of the new population. When the new population is formed, the numerical technique is once again employed to simulate the boundary value problem for each individual, repeating the steps outlined above. The Genetic Algorithms is terminated when

certain predefined stopping criteria are triggered, in this case, the sum of errors of the best 25% of the population does not reduce by more than 1% in 50 generations, and the best individual provides the calibration.

The Genetic Algorithms procedure is employed to calibrate the model parameters in two different ways:

- Independent calibration, where each pile is calibrated independently, so a set of model parameters is obtained for each pile. This allows a direct comparison between the calibrated model parameters obtained for different piles within the same London Project. The calibrated model parameters are reported in Table 7.6, and the modelled temperature rise curves are compared with the measured ones in Figure 7.16 to Figure 7.20 for Test Pile, P7a, P12, P214 and P154 respectively, while the corresponding figures for the rest of the piles are presented in Appendix D.
- Global calibration, where all the piles within the same London Project are calibrated together to obtain a set of model parameters for each London Project by minimising the sum of errors from each pile. As mentioned in Section 7.4, according to the formulation of the model, the same set of model parameters should be used when the same concrete mix is considered, which means the same set of model parameters should apply to all the measured piles within the same London Project. The globally calibrated parameters for both London Projects are reported in Table 7.6, and the modelled temperature rise curves adopting this set of parameters are also plotted together with the measured temperatures in Figure 7.16 to Figure 7.20, as well as the corresponding figures in Appendix D.

It is assumed that both the concrete and London Clay have a volumetric heat capacity of $2148000\ J \cdot m^{-3} \cdot K^{-1}$ (Burg & Ost, 1994; Headon et al., 2009) and a thermal conductivity of $2.4\ W \cdot m^{-1} \cdot K^{-1}$ (Scanlon & McDonald, 1994; Loveridge et al., 2014). In order to quantify the quality of each calibration, a metric η is proposed (which is similar to the one proposed in Zdravković et al. (2020)), which provides a measure of the difference between the modelled and measured temperature rise curves:

$$\eta = \frac{Area\ under\ modelled\ temp.rise\ curve - Area\ under\ measured\ temp.rise\ curve}{Area\ under\ measured\ temp.rise\ curve} \tag{7.6}$$

The η for both independent and global calibrations are computed for every calibrated pile, which are presented in Table 7.6.

Project name	Pile name	Q_{max} $[J \cdot kg_{cement}^{-1}]$	τ $[s]$	β	η (independent calibration)	η (global calibration)
London Project 1	Test Pile	219670	85843	0.842	-0.3%	21.0%
	P2	278740	86912	0.812	-0.1%	-6.1%
	P3a	290550	100342	0.676	0.2%	-1.1%
	P5	277890	68694	0.807	-0.1%	-12.5%
	P6	252860	75912	0.789	-0.6%	0.6%
	P7	281390	74611	0.786	0.3%	-11.7%
	P7a	236070	75091	0.840	-0.2%	8.2%
	P8	242230	81466	0.836	0.0%	7.7%
	P9	268280	77576	0.682	-0.3%	-1.7%
	P10	283910	88391	0.715	-0.2%	-4.8%
	P11	239170	67816	0.904	0.1%	0.2%
	P12	246130	85015	0.752	0.0%	11.7%
	P13	289020	103702	0.615	-0.3%	3.4%
	P14	293690	112242	0.644	-0.1%	4.5%
	Global calibration	**269380**	**85167**	**0.726**	-	-
London Project 2	P214	249350	39397	1.161	0.2%	2.9%
	P154	286210	44534	0.885	-0.5%	-2.9%
	Global calibration	**275850**	**43672**	**0.940**	-	-

Table 7.6 Calibrated model parameters for London Projects 1 and 2

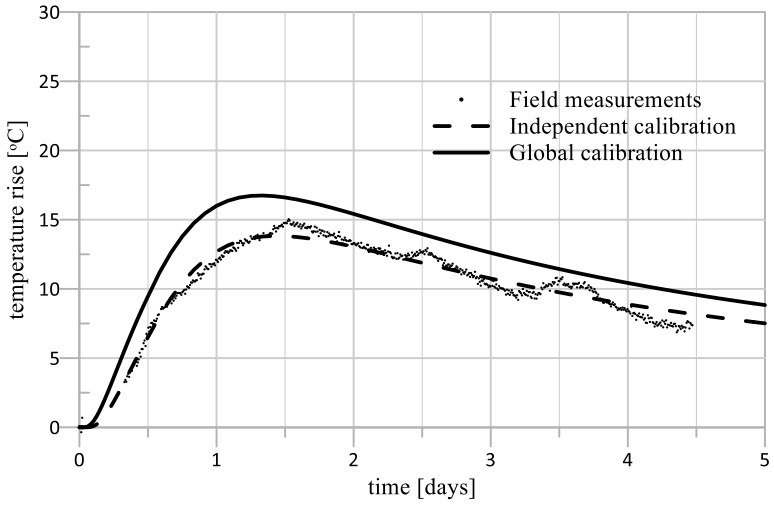


Figure 7.16 Comparison of modelled and measured temperature rise curves for Test Pile in London Project 1

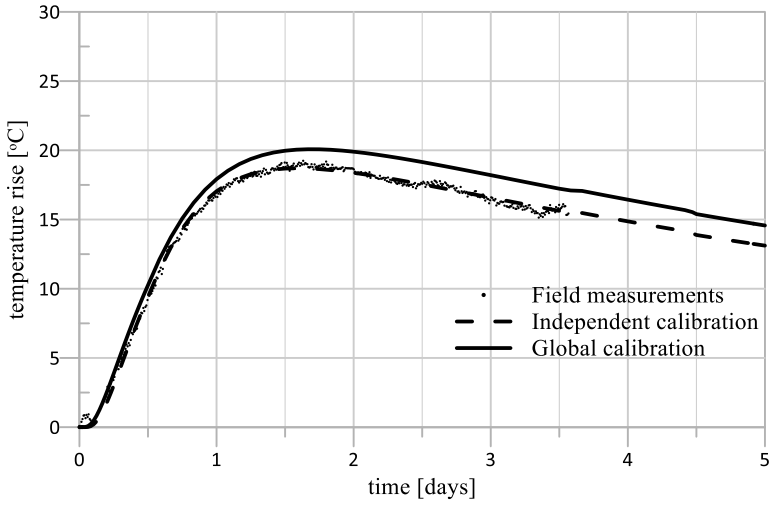


Figure 7.17 Comparison of modelled and measured temperature rise curves for Pile P7a in London Project 1

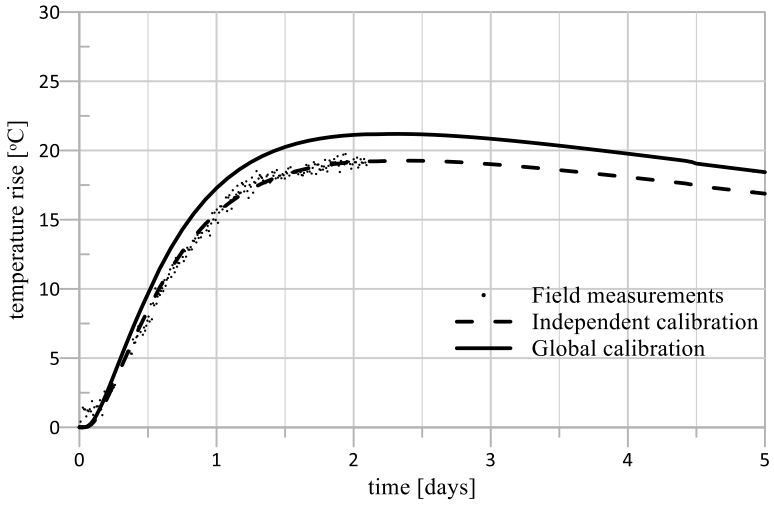


Figure 7.18 Comparison of modelled and measured temperature rise curves for Pile P12 in London Project 1

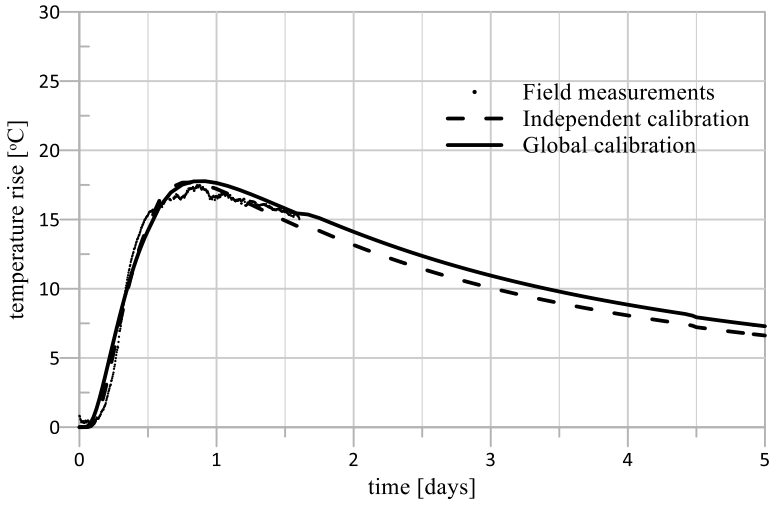


Figure 7.19 Comparison of modelled and measured temperature rise curves for Pile P214 in London Project 2

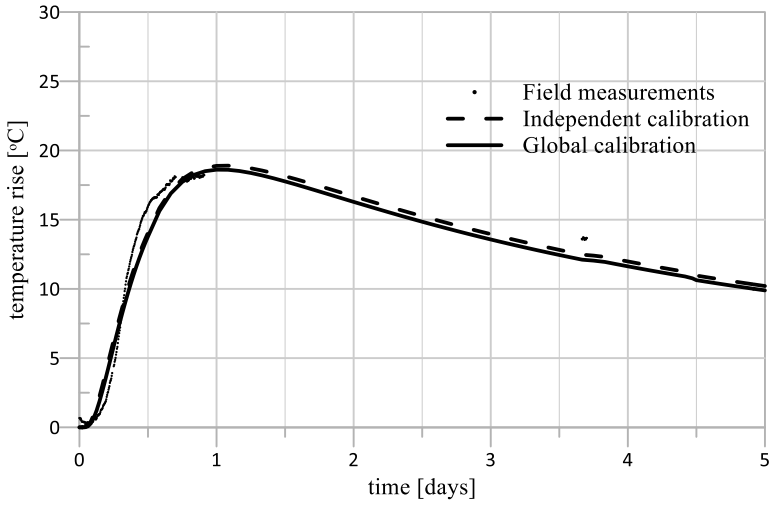


Figure 7.20 Comparison of modelled and measured temperature rise curves for Pile P154 in London Project 2

Referring to Figure 7.16 to Figure 7.20 as well as those in Appendix D, it can be observed that in all the cases, the modelled temperature rise curves using parameters based on the independent calibration fit very well with the measured ones, as indicated by the fact that the values of η for independent calibration do not exceed 0.6% in magnitude in all the cases (see Table 7.6). This confirms that the model is capable of reproducing the realistic temperature rise due to a hydrating pile after appropriate calibration, and the effectiveness of the Genetic Algorithms as a calibration tool. An interesting observation from Table 7.6 is that the two piles from London Project 2 have larger β values compared to those from London Project 1, this is very likely associated with the fact that a retarder was used in the concrete mix for London Project 2 (see Table 7.5), which delays the start of heat of hydration, and the use of a larger β value has successfully captured such effects (see Section 7.2.3 on the effects of β).

Furthermore, although a range of values are obtained from the independent calibrations in all three model parameters within the same London Project, the modelled temperature rise curves based on global calibration fit the measured ones satisfactorily as piles from the same London Project are made from the same concrete mix (see Figure 7.16 to Figure 7.20 and those in Appendix D), despite the fact that piles can be of different diameters (Figure 7.16 to Figure 7.18 correspond to three piles with different diameters from London Project 1, and Figure 7.19 and Figure 7.20 correspond to two piles from London Project 2 which are of different diameters). This is symbolised by the fact that the values of η for global calibration do not exceed 12.5% in general with the exception of the Test Pile from London Project 1, which

records 21%. Practically speaking, this means that once the field measurements of one pile is made available, the model parameters can be calibrated and the temperature fields resulting from subsequent castings using the same concrete mix can be predicted. As additional piles with field measurements become available, more reliable calibrated model parameters can be obtained.

7.6 CONCLUSIONS

In this chapter, parametric studies concerning each of the five model parameters (Q_{max}, τ, β, E_a and t_n) are conducted, which allows the importance and effects of each model parameter to be established. Following the parametric study, it has been concluded that t_n has insignificant influence on the modelled heat of hydration, and that $t_n = 2\ days$ can be assumed throughout. The model is subsequently implemented into ICFEP, which is validated against Excel in the simulation of the adiabatic temperature rise of a concrete.

The model is then calibrated using isothermal calorimetry results, where in one test, the same sample is cured at different temperatures, and in another test, cements are tested at different fineness levels. The model has successfully captured the evolution of heat of hydration in all the cases, which confirms that the model is capable of simulating the realistic evolution of heat of hydration, the temperature dependency part of the model is performing effectively, the assumption of $E_a = 45000\ J \cdot mol^{-1}$ is appropriate (which also means that effectively, only Q_{max}, τ and β have to be calibrated for a given concrete mix), and that when a cement is ground into different fineness, the same Q_{max} can and should be used.

The practical performance of the model has been demonstrated by adopting the model in the simulation of a boundary value problem consisting of a hydrating pile. Field measurements of temperature on hydrating piles provided by Cementation Skanska are used to calibrate the model parameters, using an independently developed numerical technique (which has been validated against using ICFEP simulations). Moreover, a meta-heuristic (Genetic Algorithms) has been developed to ensure an objective calibration of the model and has been shown to provide consistent results. Lastly, it has been concluded that the same set of model parameters can be reliably used when the same concrete mix is considered, independently of the diameter of the pile.

CHAPTER 8 THE ROLE OF HEAT OF HYDRATION OF CONCRETE ON THE OPERATION OF THERMO-ACTIVE PILES

8.1 INTRODUCTION

The development of a simple concrete heat of hydration model (see Chapters 6 and 7) together with a simplified method to model the operation of thermo-active piles (see Chapter 5) allow the role of concrete heat of hydration on the operation of thermo-active piles to be assessed. This chapter consists of two main sections. In Section 8.2, the hydration of two individual piles with different diameters (900 mm and 1800 mm, respectively) is modelled, and their effects on the surrounding soil are quantified. In Section 8.3, the hydration and subsequent operation of the two piles is modelled in order assess the relative importance of the hydration and operation stages on the thermo-mechanical response for different pile diameters.

8.2 EFFECTS OF PILE HYDRATION ON THE SURROUNDING SOIL

In order to assess the effects of heat of hydration from hydrating piles on the surrounding soil, the hydration of two piles with different diameters is analysed. In this study, pile diameters of 900 mm and 1800 mm are considered. It is anticipated that due to a larger volume of concrete involved in the 1800 mm diameter pile, a larger amount of heat of hydration will be generated, leading to higher temperatures within the pile and surrounding soil. It is essential to establish whether elevated temperatures in the soil due to heat of hydration would change the properties of the soil, for instance, if thermal consolidation (i.e. dissipation of thermally-induced excess pore water pressure, see Section 4.2.7.3) changes the void ratio of the soil, thereby changing its thermal properties, such as thermal conductivity (see Section 2.5.1) and volumetric heat capacity (see Section 2.5.2), which could affect subsequent heat transfer through the soil. It is assumed in this study that the piles are made with the concrete used in London Project 1 (the details of which are given in Appendix 7B) as discussed in Chapter 7, and the piles are founded in a homogeneous stratigraphy of London Clay.

8.2.1 Details of the analyses

In this study, axisymmetric coupled thermo-hydro-mechanical (THM) finite-element (FE) analyses are conducted using the Imperial College Finite Element Program (ICFEP) (Potts &

Zdravkovic, 1999; Potts & Zdravkovic, 2001; Cui, 2015). The mesh that is adopted for the 900 mm diameter pile is shown in Figure 8.1 (which is identical to that in Figure 5.4), while the one for the 1800 mm diameter pile is obtained by doubling the radial dimensions of the one used for the 900 mm diameter pile. Details of the analyses, which include the adopted stratigraphy, types of elements, initial conditions, boundary conditions, material models and material properties, are the same as those adopted in the axisymmetric analyses in Section 5.3, with the exception of the stiffness of the concrete pile which is modelled to be increasing with time according to Equation (8.1) (CEB-FIP, 1990) in order to simulate more closely the realistic stiffness of hydrating concrete. In Equation (8.1), E $[Pa]$ is the Young's modulus of the concrete, E_{28} $[Pa]$ is the Young's modulus of the concrete at 28 days, s is a coefficient and t_{28} is 28 days in the same units as t. According to the guidelines set out in CEB-FIP (1990), for the concrete used in London Project 1, which is grade C40 with normal cement (see Appendix 7B), E_{28} is determined to be 36 GPa with $s = 0.25$.

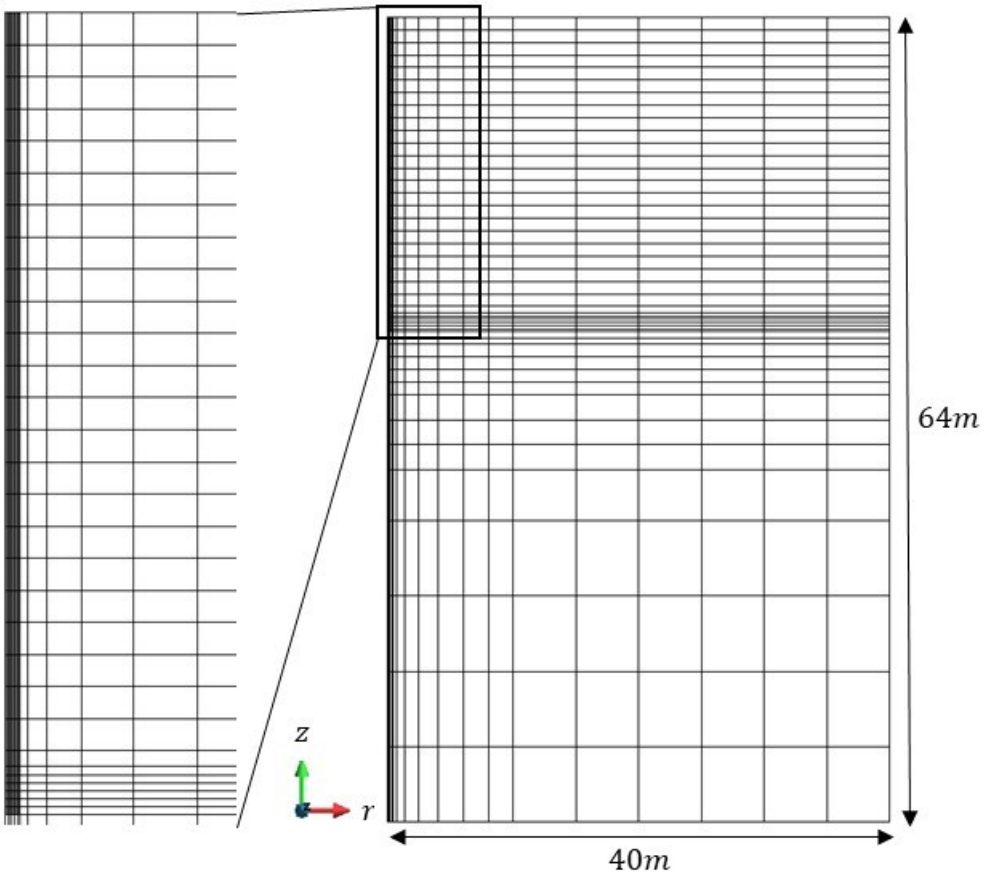


Figure 8.1 The axisymmetric FE mesh and the zoomed-in mesh detailing the pile (shaded in grey) for the 900 mm diameter pile

$$E = E_{28} \cdot \sqrt{e^{s\left(1-\sqrt{\frac{t_{28}}{t}}\right)}} \tag{8.1}$$

Moreover, the stiffness of London Clay is reset to its maximum value whenever a reversal in straining direction is detected, as opposed to a manual reset just before the pile is heated up and expands (see Section 4.2.5), as had been adopted in the analyses in Chapters 4 and 5 in order to be consistent with previous published studies (e.g. Gawecka et al. (2016) and Gawecka et al. (2017)). Further information on the algorithm that detects the existence of reversals can be found in Taborda (2011) and Taborda et al. (2016).

For both analyses, the pile is wished in place at $t = 0\ day$ and the hydration process is modelled for the duration of a year. The heat of hydration model for concrete proposed in Chapter 6 is used to model the evolution of heat of hydration generated by the hydrating pile, and since the concrete used in London Project 1 is adopted, the globally calibrated parameters of $Q_{max} = 269380\ J \cdot kg_{cement}^{-1}, \tau = 85167\ s$ and $\beta = 0.726$ with a cement content of $440\ kg_{cement} \cdot m^{-3}$ are used.

8.2.2 Results of the analyses

Figure 8.2 and Figure 8.3 show the evolutions with time of rise in temperature due to concrete hydration and the thermally-induced excess pore water pressures for the soil element at the mid-depth of the pile that is immediately adjacent to the $900\ mm$ and $1800\ mm$ diameter pile, respectively. Comparing Figure 8.2 and Figure 8.3, it can be observed that, as expected, higher temperatures are reached for the $1800\ mm$ diameter case, due to a larger amount of heat of hydration generated from a larger volume of concrete. In both the $900\ mm$ and $1800\ mm$ diameter cases, although a rapid increase in temperature is modelled following casting of the piles, the high temperatures do not last, quickly reducing after reaching a peak, due to dissipation of heat into the surrounding soil and the slowing down of the hydration process. As thermally-induced excess pore water pressures are generated due to changes in temperatures (which is why their graphs follow the same patterns as those for change in temperature), when the temperatures reduce, this process is reversed, thus explaining the absence of a plateau in pore water pressures. This means that thermal consolidation does not occur and is therefore not thought to be significant in this case. As expected, it is found that for the same soil element, the change in void ratio is negligible in both cases. For the $900\ mm$ diameter case, the maximum change in void ratio modelled is 0.0006 while for the $1800\ mm$ diameter case, the

maximum change is 0.0012. This means that the heat generated from the hydration of pile concrete in both cases are far away from changing the properties of the soil, and it is reasonable to conclude that in most common cases, concrete heat of hydration should have negligible effects on the characteristics of the surrounding soil.

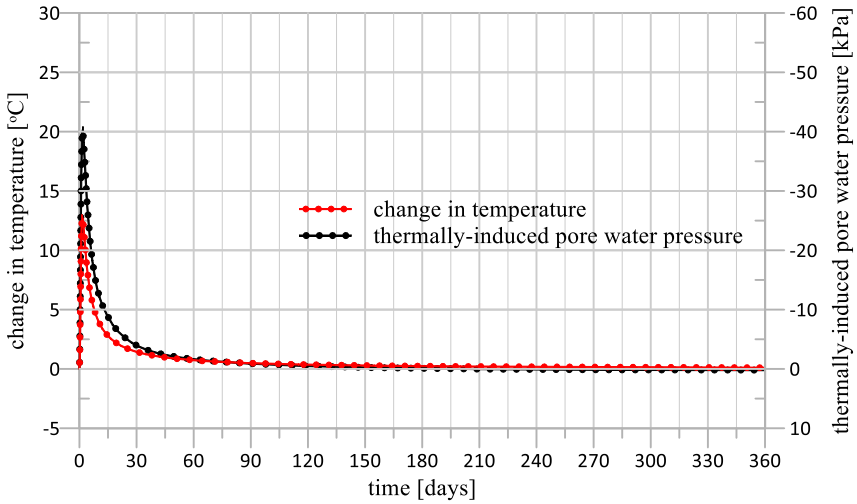


Figure 8.2 Change in temperature and thermally-induced pore water pressures for the soil element immediately adjacent to the hydrating pile at pile mid-depth for the 900 mm diameter pile

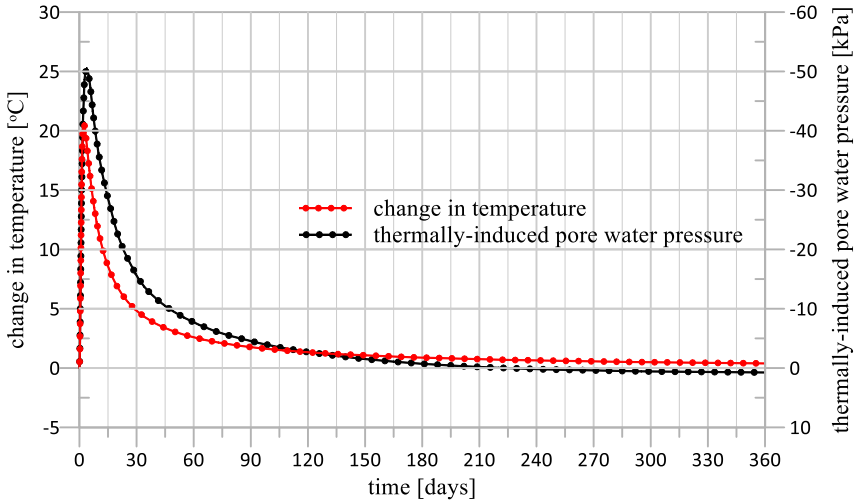


Figure 8.3 Change in temperature and thermally-induced pore water pressures for the soil element immediately adjacent to the hydrating pile at pile mid-depth for the 1800 mm diameter pile

8.3 MODELLING OF HYDRATION AND OPERATION OF THERMO-ACTIVE PILES

In this section, the relative importance of hydration and subsequent operation of a thermo-active pile on its thermo-mechanical behaviour is assessed using axisymmetric coupled THM FE analyses with ICFEP. Similar to the study detailed in Section 8.2, two different pile diameters are considered – 900 mm and 1800 mm, in order to determine the effects of pile size on the relative importance of the hydration and operation stage. For the hydration stage, similar to the analyses considered in Section 8.2, the concrete used in London Project 1 is adopted. For the operation stage, pile heating, simulated by circulating water that is 20°C above the original ground temperature (as in Chapters 4 and 5), starts one year after the pile is cast and lasts 150 $days$. A 3U pipe arrangement is also assumed as that results in the largest temperature rise among the pipe arrangements considered in Chapter 4.

Details of the analyses, which include the adopted mesh, stratigraphy, types of elements, initial conditions, boundary conditions, material models and material properties, are the same as those adopted in the analyses detailed in Section 8.2. In both analyses, the pile is wished in place at $t = 0\ day$ and the hydration process is modelled. The operation of the thermo-active pile begins one year after the pile is cast (i.e. $t = 360\ days$) and its simulation follows the recommendations of the simplified method proposed in Chapter 5. This involves performing a 2D thermal analysis to determine the time-dependent prescribed temperature T_{tbc} to be applied in the axisymmetric analysis to simulate the heating from the heat exchanger pipes. For both the 900 mm and 1800 mm diameter piles, the heat flux (ΔE) is assumed to be 35 W per m^2 of earth-contact area (Brandl, 2006), resulting in $\Delta E = 99\ W \cdot m^{-1}$, $T_{in,mid} = 38.1$°C and $T_{out,mid} = 35.2$°C for the 900 mm diameter pile and $\Delta E = 198\ W \cdot m^{-1}$, $T_{in,mid} = 38.5$°C and $T_{out,mid} = 36.6$°C for the 1800 mm diameter pile for the 2D thermal analysis. The following subsections provide the results of both analyses.

8.3.1 Temperature changes

Figure 8.4 and Figure 8.5 show the evolutions of temperature change with time at the centre of pile (location A), 70 mm from the pile edge within the pile (location B), pile edge (location C) and 250 mm from the pile edge within the soil (location D) at pile mid-depth for the 900 mm and 1800 mm diameter piles, respectively. For reference, Figure 8.6 shows a graphical representation of the radial distances of locations A to D from the pile axis. Referring to Figure

8.4, for the case of the 900 mm diameter pile, it can be observed that higher temperatures are reached during the hydration stage only at location A. At locations B, C and D, higher temperatures are reached during the operation stage. However, for the case of the 1800 mm diameter pile (Figure 8.5), it can be observed that higher temperatures are reached during the operation stage only at location D. At locations A, B and C, higher temperatures are reached during the hydration stage.

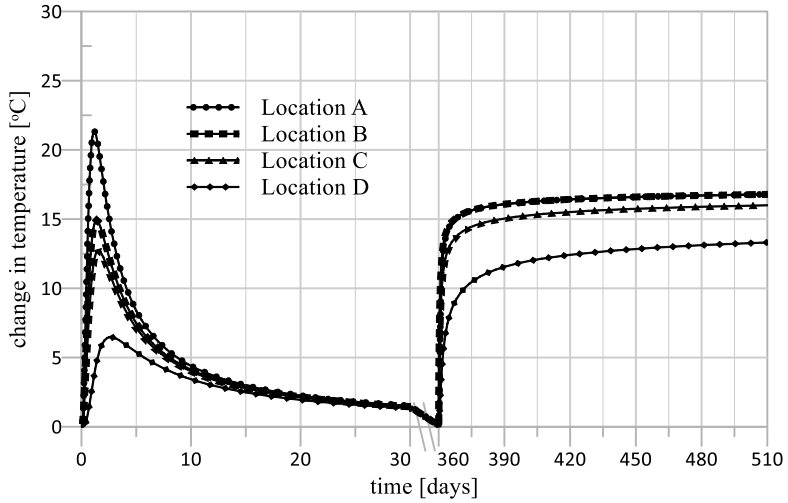


Figure 8.4 Evolutions of temperature change with time at various radial distances from centre of pile at pile mid-depth for the 900 mm diameter pile

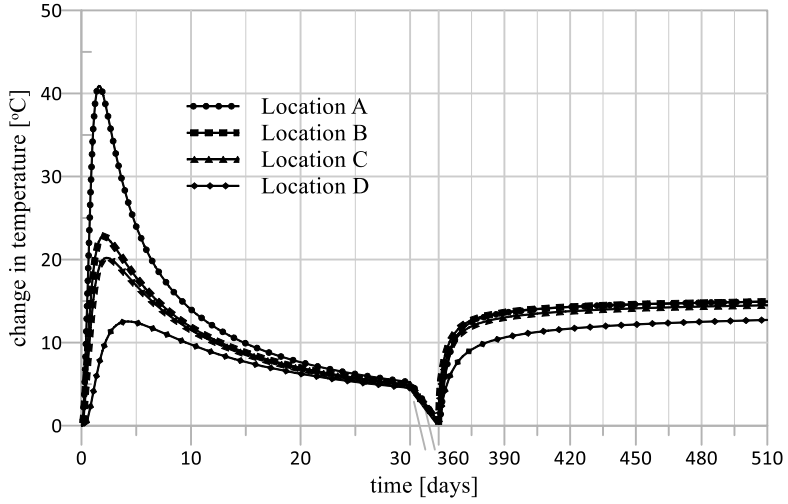


Figure 8.5 Evolutions of temperature change with time at various radial distances from centre of pile at pile mid-depth for the 1800 mm diameter pile

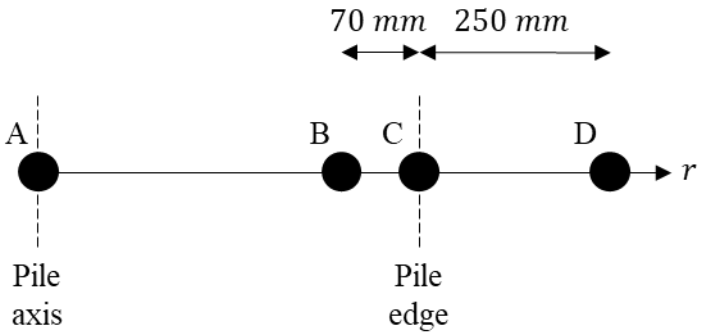


Figure 8.6 A graphical representation of the radial distances from the pile axis for locations A to D

Comparing Figure 8.4 and Figure 8.5, it can be observed that for all the radial distances considered, higher temperatures are reached during the hydration stage of the 1800 mm diameter pile compared to that of the 900 mm diameter pile (due to larger amount of heat of hydration generated from a larger volume of concrete), but during the operation stage, higher temperatures are reached on the 900 mm diameter pile compared to the 1800 mm diameter pile (which is consistent with the findings in Chapters 4 and 5, where the operation of smaller diameter thermo-active piles result in higher temperature changes, see Figure 4.7 to Figure 4.12, Figure 5.5 and Figure 5.6).

The above results suggest that, when the diameter of a thermo-active pile increases, higher temperatures are reached during the hydration stage but lower temperatures are reached during the operation stage. Therefore, consideration of the hydration stage becomes increasingly important as the pile diameter increases.

8.3.2 Thermally-induced pile head displacements

Figure 8.7 compares the evolution of thermally-induced pile head displacement with time between the 900 mm and 1800 mm diameter piles. It can be observed that the thermally-induced pile head displacements are strongly related to the temperature changes of the piles (as explained in Section 4.2.7.1). For the 900 mm diameter pile, a maximum pile heaving of 1.9 mm is modelled during the hydration stage whereas 3.3 mm is modelled by the end of the operation stage. For the 1800 mm diameter pile, a maximum pile heaving of 4.4 mm is modelled during the hydration stage but only 3.2 mm is modelled by the end of the operation stage. This shows that for the 900 mm diameter pile, the critical stage in terms of thermally-induced pile head displacement is the operation stage, whereas for the 1800 mm diameter pile,

the critical stage is the hydration stage. This conclusion is consistent with that for temperature changes described in Section 8.3.1.

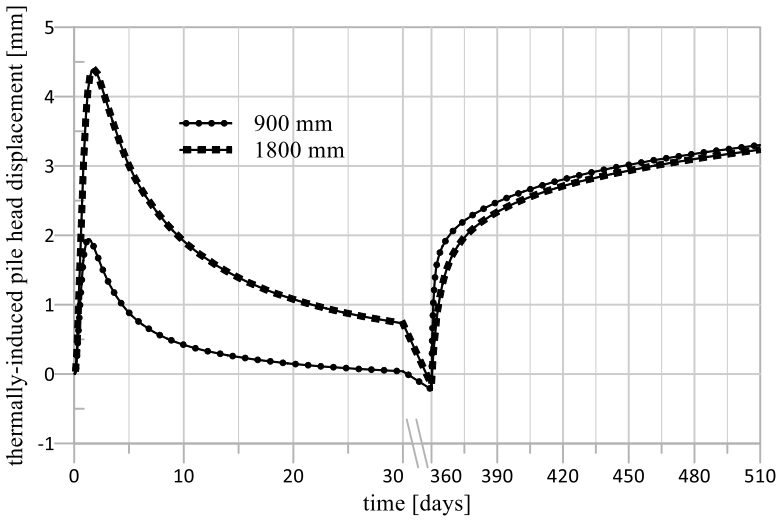


Figure 8.7 Evolutions of thermally-induced pile head displacement with time for both the 900 mm and 1800 mm diameter piles

8.3.3 Thermally-induced pile axial stresses

Figure 8.8 compares the evolution with time of the cross-sectionally averaged maximum (compressive) and minimum (tensile) values of the thermally-induced pile axial stress between the 900 mm and 1800 mm diameter piles. It should be noted that the way thermally-induced pile axial stresses are plotted in Figure 8.8 is different from that adopted in Chapters 4 and 5 (e.g. Figure 4.28), where tensile stresses, which are present in this case, are plotted in addition to the compressive stresses to form a stress envelope. Also note that compression is taken as negative.

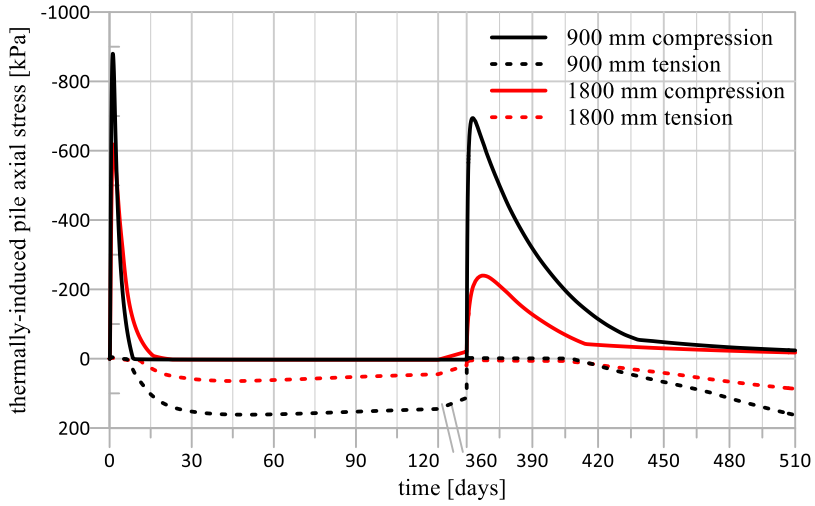


Figure 8.8 Evolutions of cross-sectionally averaged maximum (compressive) and minimum (tensile) thermally-induced pile axial stress with time for both the 900 mm and 1800 mm diameter piles

Clearly, the pattern of when compressive and tensile stresses are generated is the same for both pile diameters. When the thermo-active pile is cast at $t = 0\ days$, heat of hydration is generated and the pile temperature increases rapidly (see Figure 8.4 and Figure 8.5). The pile expands rapidly but the expansion is restricted by the surrounding soil, giving rise to a sharp peak of compressive axial stresses. When generation of heat of hydration slows down and heat is transferred into the surrounding soil, temperature quickly reduces to ambient levels, and the pile contracts. This contraction does not only reverse the generation of the compressive axial stresses, but result in locked-in tensile stresses within the pile, as observed in Figure 8.8. This can be explained by the modelled increase in pile concrete stiffness with time (see Equation (8.1)): (a) when the pile expands during hydration, the pile is mechanically compressed due to the restriction applied by the surrounding soil (despite the fact that there is a total tensile strain), and hence the observed compressive stresses; (b) however, this mechanical compression of the pile concrete occurs at a time where the pile is characterised by relatively low stiffness as the concrete is still hardening, generating only modest stresses; (c) when the peak temperature is reached and the pile begins to cool down, it contracts and this contraction is restricted by the surrounding soil, leading to the pile being mechanically tensioned (despite the existence of a total compressive strain), reducing the previously obtained compressive stresses; (d) however, this mechanical tension of the pile concrete occurs at a time when the pile is characterised by a considerably higher stiffness, since the concrete has hardened, resulting in an overall thermally-induced compressive strain but tensile stress in the pile. Figure 8.9 shows the cross-

sectionally averaged thermally-induced mechanical stress-strain path of the pile at pile mid-depth for the hydration stage (note that tension is taken as positive). It should be appreciated that the slope of the graph increases with time to reflect the increase in concrete stiffness with time. In effect, if a linear elastic model had been adopted, the generation of locked-in stresses would not have been captured so clearly by the numerical simulation.

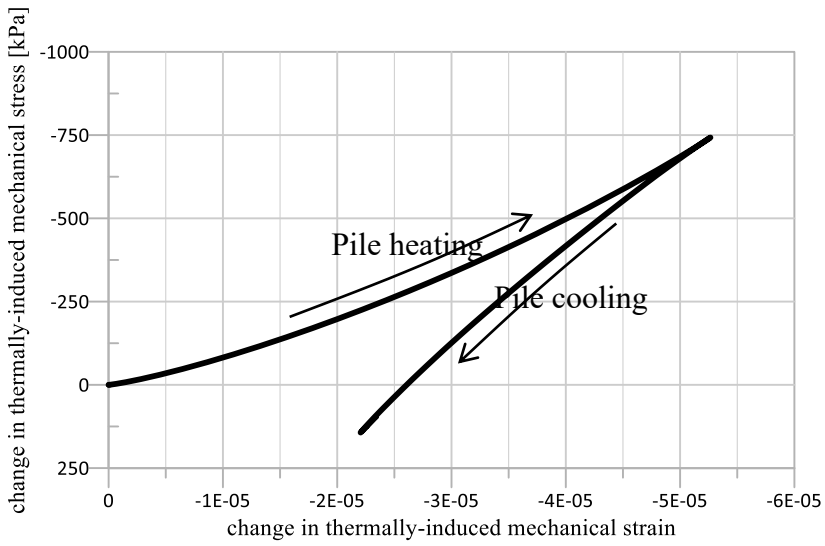


Figure 8.9 Cross-sectionally averaged thermally-induced mechanical stress-strain path of the pile at pile mid-depth for the hydration stage

Referring to the pattern of how thermally-induced pile axial stresses develop during the operation stage (from $t = 360\,days$ onwards) in Figure 8.8, it can be observed that compressive stresses slowly disappear with time and develop into tensile stresses. This is different from those shown in Chapters 4 and 5 (e.g. see Figure 4.28), where thermally-induced axial stresses would remain compressive for the entire duration of this stage, with this discrepancy being explained by the way the resetting of soil stiffness is modelled. In the analyses from Chapters 4 and 5, a single manual reset of soil stiffness to its maximum value is performed when the thermo-active pile begins to operate (i.e. the pile begins to heat up). In the current analyses, the soil stiffness is reset to its maximum value whenever a reversal in straining direction is automatically detected by the non-linear stiffness model employed (see Taborda (2011) and Taborda et al. (2016) for further details on this algorithm), which is a better approximation of the mechanisms taking place in the soil. This has led to the phenomenon where the soil stiffness is reset to its maximum value when the soil surrounding the pile is heated up sufficiently and its expansion exceeds that of the pile (the coefficient of thermal expansion of soil is larger than that of the concrete pile, see Table 4.1 and Table 4.2). With

more reversals in straining direction taking place, a larger overall soil stiffness is modelled in the near-field of the pile compared to the analyses from Chapters 4 and 5. Referring to the framework for understanding the thermo-mechanical behaviour of thermo-active piles by Bourne-Webb et al. (2009), Amatya et al. (2012) and Bourne-Webb et al. (2013) (see Section 3.2), larger soil stiffness leads to greater restrictions acting on the pile, and hence a larger transient relief of thermally-induced compressive stresses is modelled when the soil expands against the pile as it heats up. The relief on compressive stresses ultimately turns the stresses tensile, as observed in Figure 8.8.

Comparing the magnitudes of stresses between the hydration and operation stage, for the $900\ mm$ diameter pile, a maximum compressive stress of $879.9\ kPa$ and tensile stress of $161.5\ kPa$ are modelled during the hydration stage, while a maximum compressive stress of $694.3\ kPa$ and tensile stress of $162.9\ kPa$ are modelled during the operation stage. For the $1800\ mm$ diameter pile, a maximum compressive stress of $618.1\ kPa$ and tensile stress of $64.5\ kPa$ are modelled during the hydration stage, while a maximum compressive stress of $239.7\ kPa$ and tensile stress of $86.9\ kPa$ are modelled during the operation stage. In this case, it can be observed that in terms of compressive stresses, the critical stage for both pile diameters is the hydration stage, but in terms of tensile stresses, the critical stage for both pile diameters is the operation stage. This means that, when evaluating thermally-induced pile axial stresses, it is important to consider both the hydration and operation stages, although the obtained results suggest that, when the pile diameter reduces, the compressive stresses generated during the hydration stage become progressively less important compared to those generated during the operation stage.

8.3.4 Thermally-induced excess pore water pressure

The thermally-induced excess pore water pressures within the soil surrounding the pile are presented in order to show the mechanical impacts on the soil. Figure 8.10 compares the evolution of thermally-induced excess pore water pressure with time between the $900\ mm$ and $1800\ mm$ diameter piles at $250\ mm$ away from the pile edge within the soil at pile mid-depth. Since thermally-induced excess pore water pressures rise due to changes in temperature within the soil (see Section 4.2.7.3), their patterns are similar to those for temperature changes (see Figure 8.4 and Figure 8.5). Clearly, for the $900\ mm$ diameter pile, the critical stage for thermally-induced excess pore water pressure is the operation stage, but for the $1800\ mm$

diameter pile, it is the hydration stage. This is coherent with the conclusion that it is important to take the hydration stage into account for thermo-active piles with larger diameters.

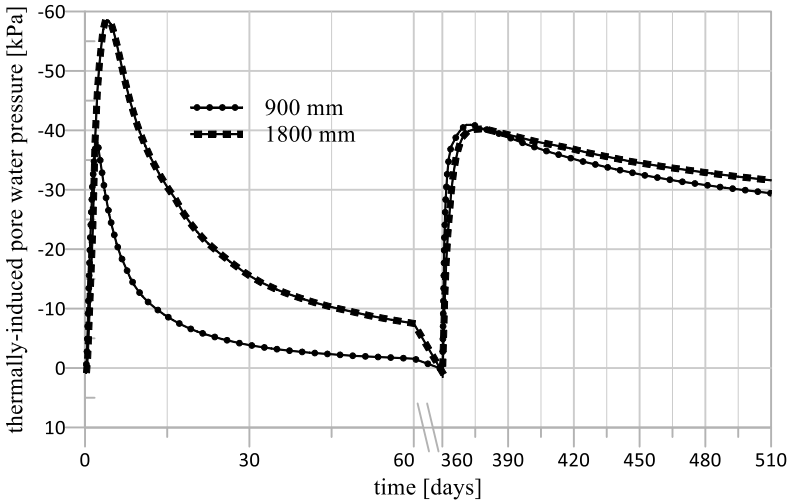


Figure 8.10 Evolutions of thermally-induced excess pore water pressure with time for both the 900 mm and 1800 mm diameter piles

8.4 CONCLUSIONS

This chapter involves two studies focussing on the importance of the hydration phase to the behaviour of thermo-active piles. In the first study, the effects of heat of hydration due to the casting of thermo-active piles on the surrounding soil are studied. In the second study, the relative importance of the hydration and operation stage on the thermo-mechanical response of thermo-active piles is compared. In both studies, two pile diameters are considered: 900 mm and 1800 mm.

In the first study, it is found that, as expected, the change in temperature within the soil which is adjacent to the pile is larger on the 1800 mm diameter pile, as larger amount of heat of hydration is generated from a larger volume of concrete. However, for both the 900 mm and 1800 mm diameter piles, it is found that the amount of heat released from the hydration of the pile causes negligible changes to the characteristics of the soil, which is assessed here by the changes in void ratio. This means that the heat of hydration released from the piles has almost no effect on the surrounding soil and therefore is not expected to change significantly its properties.

For the second study, the hydration of the thermo-active pile is modelled for a year, followed by operation for 150 $days$. Based on the changes in temperature modelled within and around the pile for both pile diameters, it is revealed that, as the pile diameter increases, the temperatures reached during the hydration stage are higher than those observed during the operation stage. The following aspects of thermo-mechanical response of the piles are also considered when assessing the relative importance of the hydration and operation stages: thermally-induced pile head displacements, pile axial stresses and excess pore water pressures. Table 8.1 summarises the critical stage for each of these aspects for both the 900 mm and 1800 mm diameter piles and it can be concluded that the modelling of both the hydration and operation stages is equally important given the uncertainty of which stage is the critical stage. However, it should be appreciated at the same time that with the exception of the generation of locked-in stresses, the hydration effects are relatively short-term. In particular, thermally-induced pile head displacements and excess pore water pressures have reduced to negligible levels after one year following the hydration of the piles.

	Pile diameter	
	900 mm	1800 mm
Thermally-induced pile head displacement	Operation	Hydration
Thermally-induced pile compressive axial stress	Hydration	Hydration
Thermally-induced pile tensile axial stress	Operation	Operation
Thermally-induced excess pore water pressure	Operation	Hydration

Table 8.1 Critical stages for different thermo-mechanical response of both the 900 mm and 1800 mm diameter thermo-active piles

CHAPTER 9 CONCLUSIONS AND FUTURE RESEARCH

9.1 INTRODUCTION

The main objective of the research presented in this thesis is to investigate the thermo-mechanical behaviour of thermo-active piles when they are subjected to temperature changes, which can be due either to the concrete heat of hydration generated when they are cast, or to their operation as heat exchangers. This is accomplished by performing numerical analyses with the Imperial College Finite Element Program (ICFEP), which includes all the components necessary to simulate the thermo-mechanical behaviour of thermo-active piles as accurately as possible, such as one-dimensional bar elements to allow the modelling of heat exchanger pipes and the Petrov-Galerkin finite-element method to solve for the transient advection dominated problem of the circulation of carrier fluid along heat exchanger pipes. Note that all analyses presented in this thesis relate to London Clay ground conditions. This research consists of two main parts, the first part (Chapters 3 to 5) is an in-depth investigation of the thermo-mechanical behaviour of thermo-active piles during their operation, while the second part (Chapters 6 and 8) showcases a pioneering study on the thermo-mechanical response of piles as a result of concrete heat of hydration.

In the first part, a comprehensive literature review on the thermo-mechanical behaviour of thermo-active piles during their operation is conducted (Chapter 3), which reveals that for numerical studies, varied interpretations and conclusions were reported which depend on the adopted modelling approach and the complexity of the analyses involved. This highlights the need for a numerical study to simulate as accurately as possible the thermo-mechanical behaviour of thermo-active piles when they operate (Chapter 4), which is achieved by conducting three-dimensional (3D), fully coupled thermo-hydro-mechanical (THM) finite-element (FE) analyses where the circulation of carrier fluid through heat exchanger pipes is explicitly simulated. However, these 3D analyses are computationally expensive which renders them impractical to perform during routine engineering design. Therefore, a simplified approach which involves only two-dimensional (2D) analyses has been developed to simulate the same problem (operation of thermo-active piles), and the accuracy of such approach is assessed using the results from the 3D analyses (Chapter 5), achieving high levels of accuracy for a fraction of the computational cost.

In the second part, a comprehensive literature review on the fundamentals of concrete heat of hydration and the existing heat of hydration models is conducted, which reveals that there is a lack of a model that can be readily applied in geotechnical engineering applications where limited information on the concrete is available. A new heat of hydration model is therefore developed, which requires only a small number of parameters to be calibrated (Chapter 6). The model is subsequently calibrated and validated using laboratory and field measurements of concrete heat of hydration, which illustrates its modelling capabilities in geotechnical engineering applications (Chapter 7). The model is then adopted to simulate and compare the thermo-mechanical behaviour of thermo-active piles due to heat of hydration, followed by operation (Chapter 8). It has been revealed that the hydration stage (which is applicable to any cast in-situ piles) has almost no effect on the surrounding soil and therefore is not expected to change significantly its properties, but both the hydration and operation stages can be critical in terms of thermo-mechanical response, although it has been shown that the hydration effects are relatively short term.

This chapter summarises the conclusions of the research presented in this thesis (Sections 9.2 and 9.3) and provides recommendations for future research (Section 9.4).

9.2 THERMO-MECHANICAL BEHAVIOUR OF THERMO-ACTIVE PILES DURING OPERATION

Numerical studies reported in the literature on the thermo-mechanical behaviour of thermo-active piles can mainly be classified into two approaches: load-transfer (t-z) method and finite-difference (FD)/finite-element (FE) modelling. The load-transfer method is a simple numerical method where the load-transfer relationship applied to the springs is highly dependent on empirical data, which are limited for thermo-active piles. It also inherently assumes that the soil surrounding the pile is thermally inert. As a result, this method can hardly model the thermo-mechanical behaviour of thermo-active piles accurately, yet the current design charts on thermally-induced pile axial stresses (GSHPA, 2012) were derived based on this method. On the other hand, FD and FE modelling allow analyses with different levels of complexity, from simple mechanical analyses to complex fully-coupled THM analyses. Together with the choice of modelling techniques, applied boundary conditions, chosen domain sizes and other input parameters, varied interpretations and conclusions on the thermo-mechanical behaviour of thermo-active piles have been reported in the literature. As a result, there exists a need for a

set of analyses which can simulate the thermo-mechanical behaviour of thermo-active piles as accurately as possible.

To achieve this, a set of fully coupled THM 3D FE analyses are conducted, where the circulation of carrier fluid (assumed to be water) through the heat exchanger pipes embedded within the thermo-active pile is explicitly simulated. Two different pile diameters ($600\ mm$ and $900\ mm$) and three different pipe configurations (single U-loop (1U), double U-loop (2U) and triple U-loop (3U)) are considered, and it is assumed that the thermo-active piles are mechanically loaded to a factor of safety of 2.6 applied at their ultimate capacities before they are put into operation. The thermal load applied consists of circulating water through the heat exchanger pipes that is $20℃$ above the ambient temperature for $150\ days$. The thermal performance and thermo-mechanical behaviour of the thermo-active piles are subsequently analysed.

In terms of thermal performance, it has been shown that when the number of U-loops, hence heat sources, within the thermo-active pile increases, faster and larger amount of heat is transferred from the pipes into the pile, and subsequently into the surrounding soil. For all the analyses considered, the power of the thermo-active piles is large during the initial stages of heating, due to the large thermal gradient between the hot heat exchanger pipes and the cold pile; with time, the power reduces significantly and stabilises towards the end of the simulation period. While increasing the number of U-loops in the pile increases the power of the system, the increase is not proportional (i.e. doubling or tripling the number of U-loops in the pile does not result in a doubled or tripled system power). At the end of the simulation period, the obtained values of power of the system range between $49.0\ W \cdot m^{-1}$ and $77.4\ W \cdot m^{-1}$, which agree with the figures observed in the field studies reported in the literature. When the storage of energy within the pile-soil system with time is analysed, it has been revealed that the patterns of where energy is stored within the system are almost the same for all the analyses considered, which means that the relative transient storage of energy in different parts of the system is largely independent of the amount of energy transferred into the system. It has also been revealed that more than 80% of the system's energy is stored within the pile during the initial stages of heating, but in the long-term, around 50% of the total energy transferred into the system is stored in the far-field soil, and only $1 - 2\%$ within the pile. This highlights the importance of accounting for the entire pile-soil system with sufficient domain size when analysing long-term energy storage and thermal performances of thermo-active piles.

In terms of thermo-mechanical behaviour, the thermally-induced pile head displacement, pile axial stress and excess pore water pressure within the soil are investigated. It is found that for the cases of 2U and 3U pipe arrangements for both pile diameters, the thermally-induced pile head displacements (heaving) at the end of the simulation period are more significant than the pile head settlements due to mechanical loading, resulting in a net heave of the pile head. However, it has to be emphasised that such conclusion is drawn based on a pile founded in London Clay. Should the pile be founded in other soil types, such as a soft soil, it is possible that the settlements due to mechanical loading are more significant than any thermally-induced displacements. This means that, should the thermo-active pile be cooled rather than heated, there would be thermally-induced pile head settlements rather than heaving, which would add to the settlement due to mechanical loading. This highlights the importance of taking thermal loading into account when designing thermo-active piles, and of the need to anticipate additional settlements if a thermo-active pile is designed to be cooled (i.e. to provide heating for the building).

When thermo-active piles are heated, non-uniform distributions of temperature, and hence axial stresses, develop within the pile cross-section due to the thermal expansion of materials. These stresses increase rapidly during the initial stages of heating. Upon reaching a peak, there is a transient reduction in these stresses with time due to the swelling of soil surrounding the pile caused by the thermally-induced compressive excess pore water pressures. Towards the end of the simulation, the stresses are stabilised in all the analyses considered. It is found that, as expected, thermally-induced axial stresses increase with the number of U-loops, due to the associated higher average and more uniformly distributed temperatures. Stresses are also larger in the $600\ mm$ diameter pile than in the $900\ mm$ diameter pile, due to the higher average temperatures reached in the former, where each U-loop is required to heat up a smaller volume of concrete. The modelled peak values of thermally-induced axial stress range from 20% to 50% of the axial stresses due to mechanical loading at the same depth, which demonstrates the significance of thermal loading, despite the resulting stress levels are generally small compared to typical concrete strengths. It is also found that the modelled thermally-induced axial stresses are significantly larger than those suggested by the current design charts (GSHPA, 2012), although such differences reduce significantly with time, highlighting the importance of modelling accurately the transient response of thermo-active piles.

As the soil heats up, compressive excess pore water pressures are induced since the coefficient of thermal expansion of pore fluid is greater than that of the soil. These excess pore water pressures reduce the effective stresses in the soil, causing tensile mechanical volumetric strains (or swelling) in the soil, eventually driving the transient response of the pile. When these pressures are averaged circumferentially and plotted with time, the patterns obtained are similar to those for thermally-induced pile axial stresses, where larger pressures are reached when the number of U-loops increases due to the soil being heated to higher temperatures. The evolution of the excess pore water pressure with time also confirms that dissipation of the pressure is successfully modelled during the transient stage.

Although the above 3D analyses can simulate accurately and with great detail the thermo-mechanical behaviour of thermo-active piles, they are computationally expensive to perform, and the explicit simulation of heat exchanger pipes is not typically available in FE packages. A simplified method that involves only 2D analyses is therefore proposed to simulate the above problem. In this simplified method, the modelling of thermo-mechanical behaviour of thermo-active piles is achieved using axisymmetric analyses, where the modelling of heat exchanger pipes is replaced by the use of a prescribed temperature thermal boundary condition. This applied temperature is determined from a 2D thermal analysis which models the discrete nature and precise location of the heat exchanger pipes within the pile cross-section. The thermal boundary conditions to be applied in this 2D thermal analysis are determined based on an assumed power of the thermo-active pile, which forms the only uncertainty of this method. It is found that an assumption of $35\ W$ per m^2 earth-contact area for piles with diameter $\geq 600\ mm$ (Brandl, 2006) yields accurate temperature changes and thermo-mechanical responses in both $600\ mm$ and $900\ mm$ piles by comparing the results obtained with those from the 3D analyses. A subsequent sensitivity study of the simplified method on the assumed power of the thermo-active pile has shown that its thermo-mechanical response is relatively insensitive to the assumed power. However, for scenarios where the thermal performance is uncertain and a conservative design is required, the power of the thermo-active pile can be assumed to be $0\ W \cdot m^{-1}$ such that the design inlet temperature is to be prescribed at all the heat sources in the 2D thermal analysis.

9.3 THERMO-MECHANICAL BEHAVIOUR OF PILES DUE TO CONCRETE HEAT OF HYDRATION

A pioneering study on the thermo-mechanical behaviour of piles due to concrete heat of hydration has been conducted. A literature review on the measurements of heat of hydration shows that it is not uncommon to have temperatures above 50℃ or even 60℃ in geotechnical structures due to concrete heat of hydration. This means that the temperature changes resulting from heat of hydration are of the same order of magnitude as those associated with the operation of thermo-active piles, and the effects of heat of hydration must therefore not be neglected.

A literature review on heat of hydration reveals that the hydration reaction between cement and water is highly complex, depending on several factors, such as the composition and fineness of cement, curing temperature, water to cement ratio, presence of admixtures, etc. In order to predict accurately the generation of heat of hydration associated with a particular cement, a number of heat of hydration models has been developed over the years. Most of these models, although accurate, require the chemical composition of the cement as an input, information which is rarely available in geotechnical engineering applications, hence rendering them difficult to apply. A new heat of hydration model is therefore proposed, which only relies on the calibration of five model parameters, and instead of using the equivalent age concept to account for the dependency of the hydration reaction on temperature, such dependency is formulated using fundamental laws of chemistry, which enables a further simplification of the model.

The proposed model is subsequently calibrated and validated using laboratory measurements of concrete heat of hydration, which demonstrates the capability of the model in simulating realistic evolution of heat of hydration. A newly developed numerical technique has been developed which allows the model to be adopted to simulate the boundary value problem of a hydrating pile. Together with Genetic Algorithms, this allows the model to be calibrated and validated using field measurements of heat of hydration within hydrating piles. It has been shown that the same set of model parameters can be reliably used when the same concrete mix is considered, independent on the geometry of the pile.

In order to quantify the effects of concrete heat of hydration due to the casting of thermo-active piles on the surrounding soil, hydration of two piles with different pile diameters - 900 mm

and 1800 mm, are simulated using the proposed model. It has been revealed that for both pile diameters, with the 1800 mm pile releasing more heat and reaching higher temperatures both within the pile and in the surrounding soil, the hydration process causes negligible change in void ratio in the soil, meaning that the heat of hydration released from the piles has an insignificant effect on the surrounding soil and therefore is not expected to change its properties.

Subsequently, the thermo-mechanical behaviour of thermo-active piles due to both hydration and operation is assessed. This is accomplished by modelling the hydration of the thermo-active pile for a year, followed by operation for 150 $days$, assuming a 3U pipe arrangement and considering again both the 900 mm and 1800 mm diameter piles. Based on the changes in temperature modelled within and around the pile for both pile diameters, it has been revealed that, as the pile diameter increases, higher temperatures are reached during the hydration stage but lower temperatures are reached during the operation stage. Therefore, consideration of the hydration stage becomes increasingly important as the pile diameter increases. Other aspects of the thermo-mechanical response of the pile, including thermally-induced pile head displacements, axial stresses and excess pore water pressures, are also considered, and it has been found that either the hydration or the operation stage could be the critical stage for both pile diameters. It has therefore been concluded that the modelling of both stages is equally important given the uncertainty regarding which stage is critical. However, it should be acknowledged that the effects from the hydration stage (with the exception of locked-in stresses generation) tend to be relatively short term, and in practical terms, those effects should have reduced to negligible levels by the time at which construction of the superstructure is complete.

9.4 RECOMMENDATIONS FOR FUTURE RESEARCH

The analyses detailed in Chapters 4, 5 and 8 model the operation of thermo-active piles by circulating hot water at constant inlet temperature through the heat exchanger pipes. The application of a constant inlet temperature allows a direct comparison of the results of the analyses with current design charts, in which heating of the pile is only given as a temperature change; also, this improves the clarity of the interpretation on the transient response resulted, as any transient response obtained is due to the transient soil response arising from the heat transfer from the pipes to the pile and then to the soil. In order to better understand the thermo-mechanical behaviour resulting from the realistic operation of a thermo-active pile, it would be interesting to consider the following different modelling approaches:

- An energy change prescribed between the pipe inlet and outlet. This would be a better resemblance of the reality as heat pump applies an energy change to the circulating fluid, rather than heating or cooling the fluid to a specific temperature before returning it to the circuit of heat exchanger pipes.
- Cooling of the thermo-active pile (which is equivalent to utilising the pile for heating purposes). As explained in Section 4.2.7.1, it is anticipated that cooling of the pile causes thermally-induced pile head settlement, which adds on top of the settlement due to mechanical loading and would therefore be the critical case for design purposes.
- Cyclic operation of the thermo-active pile. Realistically, thermo-active piles are cooled during the winter to provide heating and heated during the summer to provide cooling. It would be interesting to model such case and investigate whether locked-in stresses are present by the end of a cycle.

Throughout the current study, the thermo-active pile is assumed to be founded in a uniform stratum of London Clay. This approach is adopted, again, in order to simplify the interpretation of results of the analyses. However, realistically, thermo-active piles are often founded in layered soils, with different soil layers having different thermal properties. It would therefore be important from a practical perspective to investigate how the proposed simplified approach should be modified to simulate the operation of thermo-active piles in layered soils. In addition, while it has been shown that the proposed simplified method can successfully model the thermo-mechanical behaviour of thermo-active piles accurately, it could potentially be extended to predict their thermal performances using 2D analyses with the explicit simulation of heat exchanger pipes.

In terms of the concrete heat of hydration model, a parametric study has been conducted to study the effects of varying each of the model parameters based on isothermal hydration of concrete. It would be an interesting idea to repeat the parametric study in non-isothermal conditions, such as a hydrating pile surrounded by soil.

It has been shown in Chapter 7 that the proposed concrete heat of hydration model, together with the numerical technique which involves the superposition of finite line sources (FLS), could back-calculate the model parameters from field measurements of heat of hydration successfully. This means that such technique has the potential to be extended to function as thermal integrity profiling (TIP), where field measurements of temperature are compared with simulation results, in order to determine whether there are voids in the concrete cast as well as

their volumes. This technique can also be extended to cover concrete geotechnical structures other than piles, such as retaining walls, shafts and base slabs.

Finally, in terms of assessing the effects of heat of hydration on the surrounding soil, and/or the thermo-mechanical behaviour of thermo-active piles due to their operation, the current research has assumed that the behaviour of soil is independent of temperature. It would therefore be interesting to model the non-isothermal behaviour of soil using the Imperial College Thermal Plastic Model (Gawecka, 2017), which allows the assessment of whether the heat generated from heat of hydration or operation of thermo-active piles could induce thermo-plasticity and thermal overconsolidation. While the current study has concluded that concrete heat of hydration due to hydrating piles has no significant effect on the surrounding soil, it would be interesting to establish whether this is also the case for more massive cast in-situ concrete geotechnical structures (e.g. retaining walls, shafts and base slabs).

REFERENCES

Abdelaziz, S. & Ozudogru, T. Y. (2016) Non-Uniform Thermal Strains and Stresses in Energy Piles. *Environmental Geotechnics*, **3** (4), 237-252.

Abdelaziz, S. L. A. M. (2013) *Deep Energy Foundations: Geotechnical Challenges and Design Considerations*. PhD Thesis. Virginia Polytechnic Institute and State University,

Adam, D. & Markiewicz, R. (2009) Energy from Earth-Coupled Structures, Foundations, Tunnels and Sewers. *Géotechnique*, **59** (3), 229-236.

Adinolfi, M., Maiorano, R. M. S., Mauro, A., Massarotti, N. & Aversa, S. (2018) On the Influence of Thermal Cycles on the Yearly Performance of an Energy Pile. *Geomechanics for Energy and the Environment*, **16**, 32-44.

Akrouch, G. A., Sánchez, M. & Briaud, J.-L. (2014) Thermo-Mechanical Behavior of Energy Piles in High Plasticity Clays. *Acta Geotechnica*, **9** (3), 399-412.

Amatya, B. L., Soga, K., Bourne-Webb, P. J., Amis, T. & Laloui, L. (2012) Thermo-Mechanical Behaviour of Energy Piles. *Géotechnique*, **62** (6), 503-519.

Amis, A. & Loveridge, F. (2014) Energy Piles and Other Thermal Foundations for Gshp–Developments in Uk Practice and Research. *Rehva journal*, **2014** (1), 32-35.

Amis, T., Robinson, C. & Wong, S. (2010) Integrating Geothermal Loops into the Diaphragm Walls of the Knightsbridge Palace Hotel Project. *EMAP-Basements and Underground Structures*.

Axelsson, G. & Gunnlaugsson, E. (2000) *Long-Term Monitoring of High-and Low-Enthalpy Fields under Exploitation.* Japanese Organizing Committee for WGC2000.

Azeiteiro, R. N., Coelho, P. A. L. F., Taborda, D. M. G., Pedro, A. & Antunes, D. (2009) Computational Study of the Performance of a Genetic Algorithms-Based Software. *Proceedings of the COMGEO I, Juan-les-Pins, France*, 9.

Bailie, P. (2013) *An Investigation into Cyclic Response of Piles*. MSc Thesis. Imperial College London, London.

Banks, D. (2009) An Introduction to 'Thermogeology' and the Exploitation of Ground Source Heat. *Quarterly Journal of Engineering Geology and Hydrogeology*, **42** (3), 283-293.

Banks, D. (2012) *An Introduction to Thermogeology: Ground Source Heating and Cooling.* John Wiley & Sons.

Banks, D., Withers, J. G., Cashmore, G. & Dimelow, C. (2013) An Overview of the Results of 61 in Situ Thermal Response Tests in the Uk. *Quarterly Journal of Engineering Geology and Hydrogeology*, **46** (3), 281-291.

Barla, M., Di Donna, A. & Insana, A. (2019) A Novel Real-Scale Experimental Prototype of Energy Tunnel. *Tunnelling and Underground Space Technology*, **87**, 1-14.

Batini, N., Rotta Loria, A. F., Conti, P., Testi, D., Grassi, W. & Laloui, L. (2015) Energy and Geotechnical Behaviour of Energy Piles for Different Design Solutions. *Applied Thermal Engineering*, **86**, 199-213.

Beier, R. A., Smith, M. D. & Spitler, J. D. (2011) Reference Data Sets for Vertical Borehole Ground Heat Exchanger Models and Thermal Response Test Analysis. *Geothermics*, **40** (1), 79-85.

Benderitter, Y. & Cormy, G. (1990) Possible Approach to Geothermal Research and Relative Costs. *Small geothermal resources: A guide to development and utilization, UNITAR, New York*, 59-69.

Bentz, D. P., Garboczi, E. J., Haecker, C. J. & Jensen, O. M. (1999) Effects of Cement Particle Size Distribution on Performance Properties of Portland Cement-Based Materials. *Cement and Concrete Research*, **29** (10), 1663-1671.

Bentz, D. P., Peltz, M. A. & Winpigler, J. (2009) Early-Age Properties of Cement-Based Materials. Ii: Influence of Water-to-Cement Ratio. *Journal of Materials in Civil Engineering*, **38** (2), 512-517.

Bloomer, J. R. (1981) Thermal Conductivities of Mudrocks in the United Kingdom. *Quarterly Journal of Engineering Geology*, **14** (4), 357-362.

Bodas Freitas, T. M., Cruz Silva, F. & Bourne-Webb, P. J. (2013) The Response of Enery Foundations under Thermo-Mechanical Loading. *Proceedings of the 18th International Conference on Soil Mechanics and Geotechnical Engineering*, *Paris, France*. pp. 3347-3350.

Bording, T. S., Nielsen, S. B. & Balling, N. (2016) The Transient Divided Bar Method for Laboratory Measurements of Thermal Properties. *Geophysical Journal International*, **207** (3), 1446-1455.

Bouazza, A., Singh, R., Wang, B., Barry-Macaulay, D., Haberfield, C., Chapman, G., Baycan, S. & Carden, Y. (2011) Harnessing on Site Renewable Energy through Pile Foundations. *Australian Geomechanics*, **46** (4), 79-89.

Bourne-Webb, P., Zito, M., Bodas Freitas, T. M. & Sterpi, D. (2020) Effect of Thermal Boundary Conditions on the Response of Thermally-Activated Floating Piles in a Cohesive Material. *E3S Web of Conferences*, **195**.

Bourne-Webb, P. J., Amatya, B., Soga, K., Amis, T., Davidson, C. & Payne, P. (2009) Energy Pile Test at Lambeth College, London: Geotechnical and Thermodynamic Aspects of Pile Response to Heat Cycles. *Géotechnique*, **59** (3), 237-248.

Bourne-Webb, P. J., Amatya, B. & Soga, K. (2013) A Framework for Understanding Energy Pile Behaviour. *Proceedings of the Institution of Civil Engineers - Geotechnical Engineering*, **166** (2), 170-177.

Bourne-Webb, P. J., Bodas Freitas, T. M. & Freitas Assunção, R. M. (2016) Soil–Pile Thermal Interactions in Energy Foundations. *Géotechnique*, **66** (2), 167-171.

Bourne-Webb, P. (2013) Observed Response of Energy Geostructures. *Energy geostructures: Innovation in underground engineering*, 45-77.

Brandl, H. (1998) Energy Piles and Diaphragm Walls for Heat Transfer from and into the Ground. *Deep Foundations on Bored and Auger Piles*, CRC Press, pp. 38-60.

Brandl, H. (2006) Energy Foundations and Other Thermo-Active Ground Structures. *Geotechnique*, **56** (2), 81-122.

Brettman, T., Amis, T. & Kapps, M. (2010) Thermal Conductivity Analysis of Geothermal Energy Piles. *Proceedings of the 2010 Geotechnical Challenges in Urban Regeneration Conference, London, UK*. pp. 26-28.

British Standards Institution (2001) BS EN 12667:2001. *Thermal Performance of Building Materials and Products—Determination of Thermal Resistance by Means of Guarded Hot Plate and Heat Flow Meter Methods—Products of High and Medium Thermal Resistance*.

Burg, R. G. & Ost, B. W. (1994) *Engineering Properties of Commercially Available High-Strength Concretes (Including Three-Year Data)*. Portland Cement Association. RD104.

Burlon, S., Habert, J., Szymkievicz, F., Suryatriyastuti, M. & Mroueh, H. (2013) Towards a Design Approach of Bearing Capacity of Thermo-Active Piles. *Proceedings of the European Geothermal Congress 2013*, *Pisa, Italy*. pp. 1-6.

Busby, J. (2015) Uk Shallow Ground Temperatures for Ground Coupled Heat Exchangers. *Quarterly Journal of Engineering Geology and Hydrogeology*, **48** (3-4), 248-260.

Caggiano, A., Pepe, M., Koenders, E. A. B., Martinelli, E. & Etse, G. J. (2012) Numerical Modeling of Hydration Process and Temperature Evolution in Early Age Concrete.

Proceedings of the MECOM 2012: X Argentine Congress on Computational Mechanics, *Salta, Argentina*. Asociación Argentina de Mecánica Computacional, pp. 1893-1907.

Campbell-Allen, D. & Thorne, C. (1963) The Thermal Conductivity of Concrete. *Magazine of Concrete Research*, **15** (43), 39-48.

Campbell, G., Calissendorff, C. & Williams, J. (1991) Probe for Measuring Soil Specific Heat Using a Heat-Pulse Method. *Soil Science Society of America Journal*, **55** (1), 291-293.

Carlson, R. W. & Forbrich, L. R. (1938) Correlation of Methods for Measuring Heat of Hydration of Cement. *Industrial & Engineering Chemistry Analytical Edition*, **10** (7), 382-386.

Carslaw, H. S. & Jaeger, J. C. (1959) *Conduction of Heat in Solids.* Oxford, Clarendon Press.

CEB-FIP (1990) MC90. *Model Code, Design Code - Comité Euro-International Du Béton*. London, Thomas Telford.

Cecinato, F. & Loveridge, F. A. (2015) Influences on the Thermal Efficiency of Energy Piles. *Energy*, **82**, 1021-1033.

Çengel, Y. A. & Ghajar, A. J. (2011) *Heat and Mass Transfer: Fundamentals and Applications.* 4th Ed. New York, McGraw-Hill.

Clarke, B. G., Agab, A. & Nicholson, D. (2008) Model Specification to Determine Thermal Conductivity of Soils. *Proceedings of the Institution of Civil Engineers - Geotechnical Engineering*, **161** (3), 161-168.

Copeland, L. E., Kantro, D. L. & Verbeck, G. (1960) *Chemistry of Hydration of Portland Cement*. Portland Cement Association. RX153.

Cui, W. (2015) *Development, Implementation and Application of Thermo-Hydro-Mechanical Coupling for Soils in Finite Element Analysis*. PhD Thesis. Imperial College London, London.

Cui, W., Gawecka, K. A., Potts, D. M., Taborda, D. M. G. & Zdravković, L. (2016) Numerical Analysis of Coupled Thermo-Hydraulic Problems in Geotechnical Engineering. *Geomechanics for Energy and the Environment*, **6**, 22-34.

Cui, W., Gawecka, K. A., Potts, D. M., Taborda, D. M. G. & Zdravković, L. (2018a) A Petrov-Galerkin Finite Element Method for 2d Transient and Steady State Highly Advective Flows in Porous Media. *Computers and Geotechnics*, **100**, 158-173.

Cui, W., Potts, D. M., Zdravkovic, L., Gawecka, K. A. & Taborda, D. M. G. (2018b) An Alternative Coupled Thermo-Hydro-Mechanical Finite Element Formulation for Fully Saturated Soils. *Computers and Geotechnics*, **94**, 22-30.

Cui, W., Tsiampousi, A., Potts, D. M., Gawecka, K. A. & Zdravković, L. (2020) Numerical Modeling of Time-Dependent Thermally Induced Excess Pore Fluid Pressures in a Saturated Soil. *Journal of Geotechnical and Geoenvironmental Engineering*, **146** (4), 1-15.

D'Aloia, L. & Chanvillard, G. (2002) Determining the "Apparent" Activation Energy of Concrete: Ea—Numerical Simulations of the Heat of Hydration of Cement. *Cement and Concrete Research*, **32** (8), 1277-1289.

de Santayana, F. P., de Santiago, C., de Groot, M., Uchueguía, J., Arcos, J. L. & Badenes, B. (2020) Effect of Thermal Loads on Pre-Cast Concrete Thermopile in Valencia, Spain. *Environmental Geotechnics*, **7** (3), 208-222.

De Schutter, G. & Taerwe, L. (1995) General Hydration Model for Portland Cement and Blast Furnace Slag Cement. *Cement and Concrete Research*, **25** (3), 593-604.

De Schutter, G. (1999) Hydration and Temperature Development of Concrete Made with Blast-Furnace Slag Cement. *Cement and Concrete Research*, **29** (1), 143-149.

De Vries, D. (1952) A Nonstationary Method for Determining Thermal Conductivity of Soil in Situ. *Soil Science*, **73** (2), 83-90.

Devriendt, M., Fairbairn, T., Hirst, J. & Rutter, D. (2012) One New Change. *The Arup Journal*, (2), 46-57.

Di Donna, A. & Laloui, L. (2015) Numerical Analysis of the Geotechnical Behaviour of Energy Piles. *International Journal for Numerical and Analytical Methods in Geomechanics*, **39** (8), 861-888.

Di Donna, A., Rotta Loria, A. F. & Laloui, L. (2016) Numerical Study of the Response of a Group of Energy Piles under Different Combinations of Thermo-Mechanical Loads. *Computers and Geotechnics*, **72**, 126-142.

Dickson, M. H. & Fanelli, M. (2013) *Geothermal Energy: Utilization and Technology.* Paris, France, UNESCO.

Dupray, F., Laloui, L. & Kazangba, A. (2014) Numerical Analysis of Seasonal Heat Storage in an Energy Pile Foundation. *Computers and Geotechnics*, **55**, 67-77.

Fadejev, J., Simson, R., Kurnitski, J. & Haghighat, F. (2017) A Review on Energy Piles Design, Sizing and Modelling. *Energy*, **122**, 390-407.

Faizal, M. & Bouazza, A. (2016) Effect of Forced Thermal Recharging on the Thermal Behaviour of a Field Scale Geothermal Energy Pile. *Proceedings of the International Conference on Energy Geotechnics (ICEGT 2016)*. CRC Press, pp. 557-568.

Faizal, M., Bouazza, A. & Singh, R. M. (2016) An Experimental Investigation of the Influence of Intermittent and Continuous Operating Modes on the Thermal Behaviour of a Full Scale Geothermal Energy Pile. *Geomechanics for Energy and the Environment*, **8**, 8-29.

Faizal, M., Bouazza, A., Haberfield, C. & McCartney, J. S. (2018) Axial and Radial Thermal Responses of a Field-Scale Energy Pile under Monotonic and Cyclic Temperature Changes. *Journal of Geotechnical and Geoenvironmental Engineering*, **144** (10), 1-14.

Farouki, O. T. (1981) *Thermal Properties of Soils*. Cold Regions Research and Engineering Lab Hanover NH.

Franzson, H., Kristjánsson, B. R., Gunnarsson, G., Björnsson, G., Hjartarson, A., Steingrímsson, B., Gunnlaugsson, E. & Gíslason, G. (2005) The Hengill-Hellisheiði Geothermal Field. Development of a Conceptual Geothermal Model. *Proceedings of the World Geothermal Congress*. Antalya, pp. 1-7.

Fuentes, R., Pinyol, N. & Alonso, E. (2016) Effect of Temperature Induced Excess Porewater Pressures on the Shaft Bearing Capacity of Geothermal Piles. *Geomechanics for Energy and the Environment*, **8**, 30-37.

Fujii, H., Nishi, K., Komaniwa, Y. & Chou, N. (2012) Numerical Modeling of Slinky-Coil Horizontal Ground Heat Exchangers. *Geothermics*, **41**, 55-62.

Galson, D. A., Wilson, N. P., Schärli, U. & Rybach, L. (1987) A Comparison of the Divided-Bar and Qtm Methods of Measuring Thermal Conductivity. *Geothermics*, **16** (3), 215-226.

Gao, J., Zhang, X., Liu, J., Li, K. & Yang, J. (2008) Numerical and Experimental Assessment of Thermal Performance of Vertical Energy Piles: An Application. *Applied Energy*, **85** (10), 901-910.

Garber, D., Soga, K. & Choudhary, R. (2013) Post-Occupancy Assessment of Thermal-Pile and Open-Well Ground Source Heat Pump (Gshp) System—Case Study. *ASHRAE Transactions*, **119**, 1-9.

Gawecka, K. A., Potts, D. M., Taborda, D. M. G., Cui, W. & Zdravkovic, L. (2016) Effects of Transient Phenomena on the Behaviour of Thermo-Active Piles. *Proceedings of the 1st International Conference on Energy Geotechnics, ICEGT 2016*. pp. 71-78.

Gawecka, K. A. (2017) *Numerical Analysis of Geothermal Piles*. PhD Thesis. Imperial College London, London.

Gawecka, K. A., Taborda, D. M. G., Potts, D. M., Cui, W., Zdravković, L. & Haji Kasri, M. S. (2017) Numerical Modelling of Thermo-Active Piles in London Clay. *Proceedings of the Institution of Civil Engineers - Geotechnical Engineering*, **170** (3), 201-219.

Gawecka, K. A., Taborda, D. M. G., Potts, D. M., Sailer, E., Cui, W. & Zdravković, L. (2020) Finite-Element Modeling of Heat Transfer in Ground Source Energy Systems with Heat Exchanger Pipes. *International Journal of Geomechanics*, **20** (5).

Georgiadis, K., Skordas, D., Kamas, I. & Comodromos, E. (2020) Heating and Cooling Induced Stresses and Displacements in Heat Exchanger Piles in Sand. *Renewable Energy*, **147**, 2599-2617.

Goode, J. & McCartney, J. S. (2014) Evaluation of Head Restraint Effects on Energy Foundations. *Proceedings of the Geo-Congress 2014: Geo-characterization and Modeling for Sustainability*. pp. 2685-2694.

Goode, J., Zhang, M. & McCartney, J. (2014) Centrifuge Modeling of Energy Foundations in Sand. *Proceedings of the 8th International Conference on Physical Modelling in Geotechnics*. CRC Press, Boca Raton, FL, USA, 2, pp. 729-736.

Goode, J. & McCartney, J. S. (2015) Centrifuge Modeling of End-Restraint Effects in Energy Foundations. *Journal of Geotechnical and Geoenvironmental Engineering*, **141** (8), 04015034.

Ground Source Consult Ltd (2015) *Ground Source Energy Report*. Ground Source Consult Ltd. GSC LTD 520.

GSHPA (2012) *Thermal Pile Design, Installation and Materials Standards*. Ground Source Heat Pump Association.

Hallgrímsdóttir, E., Ballzus, C. & Hrólfsson, I. (2012) The Geothermal Power Plant at Hellisheiði, Iceland. *GRC Transactions*, **36** (2), 1067-1072.

Hamada, Y., Saitoh, H., Nakamura, M., Kubota, H. & Ochifuji, K. (2007) Field Performance of an Energy Pile System for Space Heating. *Energy and Buildings*, **39** (5), 517-524.

Hamuda, S. S., Rouainia, M. & Clarke, B. G. (2010) Uplift Behaviour of Buried Structures under Strong Shaking. *Physical Modelling in Geotechnics, Two Volume Set*, pp. 1463-1468.

Hassani Nezhad Gashti, E., Malaska, M. & Kujala, K. (2014) Evaluation of Thermo-Mechanical Behaviour of Composite Energy Piles During Heating/Cooling Operations. *Engineering Structures*, **75**, 363-373.

Headon, J., Banks, D., Waters, A. & Robinson, V. K. (2009) Regional Distribution of Ground Temperature in the Chalk Aquifer of London, Uk. *Quarterly Journal of Engineering Geology and Hydrogeology*, **42** (3), 313-323.

Heinrich, J. & Zienkiewicz, O. (1977) Quadratic Finite Element Schemes for Two-Dimensional Convective-Transport Problems. *International Journal for Numerical Methods in Engineering*, **11** (12), 1831-1844.

Helland, S. (1986) *Nordisk Betong*, 63-70.

Henderson, H., Carlson, S. & Walburger, A. (1998) North American Monitoring of a Hotel with Room Size G.S.H.P.S. *Proceedings of the IEA 1998 Room Size Heat Pump Conference*.

Hochstein, M. P. (1990) Classification and Assessment of Geothermal Resources. *Small geothermal resources: A guide to development and utilization, UNITAR, New York*, 31-57.

Hofinger, H. & Kohlböck, D. (2005) *Wirtschaftliche Optimierung Von Tunnelthermie®-Absorberanlagen*. iC-Consulenten. Report number: 12x05080.

Hooper, F. (1950) Transient Heat Flow Apparatus for the Determination of Thermal Conductivity. *Trans. American Soc. Heating and Ventilating Eng.*, **56**, 309-324.

Huang, X., Wu, Y., Peng, H., Hao, Y. & Lu, C. (2018) Thermomechanical Behavior of Energy Pile Embedded in Sandy Soil. *Mathematical Problems in Engineering*, **2018**, 1-11.

Hutcheon, N. & Paxton, J. (1952) Moisture Migration in a Closed Guarded Hot Plate. *Heating, Piping, Air Conditioning*, **24**, 4.

Huyakorn, P. (1977) Solution of Steady-State, Convective Transport Equation Using an Upwind Finite Element Scheme. *Applied Mathematical Modelling*, **1** (4), 187-195.

Insana, A. & Barla, M. (2020) Experimental and Numerical Investigations on the Energy Performance of a Thermo-Active Tunnel. *Renewable Energy*, **152**, 781-792.

Jalaluddin, Miyara, A., Tsubaki, K., Inoue, S. & Yoshida, K. (2011) Experimental Study of Several Types of Ground Heat Exchanger Using a Steel Pile Foundation. *Renewable Energy*, **36** (2), 764-771.

Jensen-Page, L., Loveridge, F. & Narsilio, G. A. (2019) Thermal Response Testing of Large Diameter Energy Piles. *Energies*, **12** (14).

Jeong, S., Lim, H., Lee, J. K. & Kim, J. (2014) Thermally Induced Mechanical Response of Energy Piles in Axially Loaded Pile Groups. *Applied Thermal Engineering*, **71** (1), 608-615.

Johnson, K. R. (2016) *Advancements in Thermal Integrity Profiling Data Analysis*. PhD Thesis. University of South Florida, Florida, USA.

Kalantidou, A., Tang, A. M., Pereira, J. M. & Hassen, G. (2012) Preliminary Study on the Mechanical Behaviour of Heat Exchanger Pile in Physical Model. *Géotechnique*, **62** (11), 1047-1051.

Kavanaugh, S. P. & Rafferty, K. D. (2014) *Geothermal Heating and Cooling: Design of Ground-Source Heat Pump Systems.* ASHRAE.

Khan, M. I. (2002) Factors Affecting the Thermal Properties of Concrete and Applicability of Its Prediction Models. *Building and Environment*, **37** (6), 607-614.

Khoury, G. A. (1983) *Transient Thermal Creep of Nuclear Reactor Pressure Vessel Type Concretes*. PhD Thesis. Imperial College London, London.

King, W., Banks, D. & Findlay, J. (2012) Field Determination of Shallow Soil Thermal Conductivity Using a Short-Duration Needle Probe Test. *Quarterly Journal of Engineering Geology and Hydrogeology*, **45** (4), 497-504.

Kipry, H., Bockelmann, F., Plesser, S. & Fisch, M. (2009) Evaluation and Optimization of Utes Systems of Energy Efficient Office Buildings (Wksp). *Proceedings of the 11th international conference on thermal energy storage*.

Kishi, T. & Maekawa, K. (1995) Multi-Component Model for Hydration Heat of Portland Cement. *Proceedings of JSCE*, **29** (526), 97-109.

Kishi, T. & Maekawa, K. (1997) Multi-Component Model for Hydration Heating of Blended Cement with Blast Furnace Slag and Fly Ash. *Concrete Library of JSCE*, **30**, 125-139.

Knellwolf, C., Peron, H. & Laloui, L. (2011) Geotechnical Analysis of Heat Exchanger Piles. *Journal of Geotechnical and Geoenvironmental Engineering*, **137** (10), 890-902.

Kraft, L. M., Ray, R. P. & Kagawa, T. (1981) Theoretical T-Z Curves. *Journal of the Geotechnical Engineering Division*, **107** (11), 1543-1561.

Kutter, B. L. (1992) Dynamic Centrifuge Modeling of Geotechnical Structures. *Transportation Research Record*, (1336).

Laloui, L., Moreni, M. & Vulliet, L. (2003) Comportement D'un Pieu Bi-Fonction, Fondation Et Échangeur De Chaleur. *Canadian Geotechnical Journal*, **40** (2), 388-402.

Laloui, L., Nuth, M. & Vulliet, L. (2006) Experimental and Numerical Investigations of the Behaviour of a Heat Exchanger Pile. *International Journal for Numerical and Analytical Methods in Geomechanics*, **30** (8), 763-781.

Laloui, L. & Di Donna, A. (2013) *Energy Geostructures: Innovation in Underground Engineering.* John Wiley & Sons.

Lee, M. H., Khil, B. S. & Yun, H. D. (2014) Influence of Cement Type on Heat of Hydration and Temperature Rise of the Mass Concrete. *Indian Journal of Engineering & Materials Sciences*, **21**, 536-542.

Li, R., Kong, G., Chen, Y. & Yang, Q. (2021a) Thermomechanical Behaviour of an Energy Pile–Raft Foundation under Intermittent Cooling Operation. *Geomechanics for Energy and the Environment*, **28**.

Li, R., Kong, G., Sun, G., Zhou, Y. & Yang, Q. (2021b) Thermomechanical Characteristics of an Energy Pile-Raft Foundation under Heating Operations. *Renewable Energy*, **175**, 580-592.

Li, X., Chen, Y., Chen, Z. & Zhao, J. (2006) Thermal Performances of Different Types of Underground Heat Exchangers. *Energy and Buildings*, **38** (5), 543-547.

Lim, C. K., Kim, J. K. & Seo, T. S. (2016) Prediction of Concrete Adiabatic Temperature Rise Characteristic by Semi-Adiabatic Temperature Rise Test and F.E.M. Analysis. *Construction and Building Materials*, **125**, 679-689.

Liou, D. D. (1999) Thermal Effects in Large-Sized Diaphragm Wall. *Journal of performance of constructed facilities*, **13** (1), 17-21.

Liu, R. Y. W., Taborda, D. M. G., Gawecka, K. A., Cui, W. & Potts, D. M. (2019) Computational Study on the Effects of Boundary Conditions on the Modelled Thermally Induced Axial Stresses in Thermo-Active Piles. *Proceedings of the XVII European Conference on Soil Mechanics and Geotechnical Engineering*, *Reykjavik, Iceland*.

Liu, R. Y. W., Sailer, E., Taborda, D. M. G. & Potts, D. M. (2020a) Evaluating the Impact of Different Pipe Arrangements on the Thermal Performance of Thermo-Active Piles. *E3S Web of Conferences*, **205**.

Liu, R. Y. W., Sailer, E., Taborda, D. M. G., Potts, D. M. & Zdravković, L. (2020b) A Practical Method for Calculating Thermally-Induced Stresses in Pile Foundations Used as Heat Exchangers. *Computers and Geotechnics*, **126**.

Liu, R. Y. W., Taborda, D. M. G., Fisher, A. & Bourne-Webb, P. J. (2022) A Practical Heat of Hydration Model for Concrete Curing for Geotechnical Applications. *Geotechnical Research*, 1-10.

Lou, Y., Fang, P.-f., Xie, X.-y., Chong, C. S. A., Li, F.-y., Liu, C.-y., Wang, Z.-j. & Zhu, D.-y. (2021) Numerical Research on Thermal Response for Geothermal Energy Pile Groups under Groundwater Flow. *Geomechanics for Energy and the Environment*, **28**, 1-13.

Loveridge, F. (2012) *The Thermal Performance of Foundation Piles Used as Heat Exchangers in Ground Energy Systems*. PhD Thesis. University of Southampton,

Loveridge, F., Holmes, G., Powrie, W. & Roberts, T. (2013) Thermal Response Testing through the Chalk Aquifer in London, Uk. *Proceedings of the Institution of Civil Engineers - Geotechnical Engineering*, **166** (2), 197-210.

Loveridge, F. & Powrie, W. (2013) Pile Heat Exchangers: Thermal Behaviour and Interactions. *Proceedings of the Institution of Civil Engineers - Geotechnical Engineering*, **166** (2), 178-196.

Loveridge, F., Powrie, W. & Nicholson, D. (2014) Comparison of Two Different Models for Pile Thermal Response Test Interpretation. *Acta Geotechnica*, **9** (3), 367-384.

Loveridge, F., Low, J. & Powrie, W. (2017) Site Investigation for Energy Geostructures. *Quarterly Journal of Engineering Geology and Hydrogeology*, **50** (2), 158-168.

Low, J. (2016) *Thermal Conductivity of Soils for Energy Foundation Applications*. PhD Thesis. University of Southampton,

Low, J. E., Loveridge, F. A., Powrie, W. & Nicholson, D. (2015) A Comparison of Laboratory and in Situ Methods to Determine Soil Thermal Conductivity for Energy Foundations and Other Ground Heat Exchanger Applications. *Acta Geotechnica*, **10** (2), 209-218.

Lu, H.-w., Jin, X., Jiang, G. & Liu, W.-q. (2017) Numerical Analysis of the Thermal Performance of Energy Pile with U-Tube. *Energy Procedia*, **105**, 4731-4737.

Lund, J. W. (2015) Geothermal Energy Utilization. In: Bronicki, L. (ed.) *Encyclopedia of Sustainability Science and Technology*. New York, NY., Springer, pp. 4162-4179.

Lund, J. W. & Toth, A. N. (2021) Direct Utilization of Geothermal Energy 2020 Worldwide Review. *Geothermics*, **90**.

Martinez Calonge, D. (2017) *Experimental Investigation of the Thermo-Mechanical Behaviour and Thermal Properties of London Clay*. PhD thesis. Imperial College London, London.

McCartney, J. S., Rosenberg, J. E. & Sultanova, A. (2010) Engineering Performance of Thermo-Active Foundations. *Geotrends: The Progress of Geological and Geotechnical Engineering in Colorado at the Cusp of a New Decade*, pp. 27-42.

McCartney, J. S. & Rosenberg, J. E. (2011) Impact of Heat Exchange on Side Shear in Thermo-Active Foundations. *Geo-Frontiers 2011: Advances in Geotechnical Engineering*, pp. 488-498.

McCartney, J. S. & Murphy, K. D. (2012) Strain Distributions in Full-Scale Energy Foundations (Dfi Young Professor Paper Competition 2012). *The Journal of the Deep Foundations Institute*, **6** (2), 26-38.

McCartney, J. S. (2013) Centrifuge Modeling of Energy Foundations. *Energy geostructures: Innovation in underground engineering*, 99-115.

McCartney, J. S. & Murphy, K. D. (2017) Investigation of Potential Dragdown/Uplift Effects on Energy Piles. *Geomechanics for Energy and the Environment*, **10**, 21-28.

McGuinness, T., Hemmingway, P. & Long, M. (2014) Design and Development of a Low-Cost Divided-Bar Apparatus. *Geotechnical Testing Journal*, **37** (2).

McWilliam, F. (2009) Skanska's Plumb Job. *Ground Engineering*, (September), 26-28.

Measham, P., Taborda, D., Zdravkovic, L. & Potts, D. (2014) Numerical Simulation of a Deep Excavation in London Clay. *Proceedings of the 8th European Conference on Numerical Methods in Geotechnical Engineering, Delft, The Netherlands*. Taylor & Francis, London, UK, pp. 771-776.

Merton Council (2010) *Sustainable Design and Construction Evidence Base: Climate Change in the Planning System*. Merton Council.

Mimouni, T. & Laloui, L. (2013) Full-Scale Insitu Testing of Energy Piles. *Energy Geostructures: Innovation in Underground Engineering*, 23-43.

Mimouni, T. & Laloui, L. (2014) Towards a Secure Basis for the Design of Geothermal Piles. *Acta Geotechnica*, **9** (3), 355-366.

Mimouni, T. & Laloui, L. (2015) Behaviour of a Group of Energy Piles. *Canadian Geotechnical Journal*, **52** (12), 1913-1929.

Mitchell, J. K. & Kao, T. C. (1978) Measurement of Soil Thermal Resistivity. *Journal of the Geotechnical Engineering Division*, **104** (10), 1307-1320.

Morino, K. & Oka, T. (1994) Study on Heat Exchanged in Soil by Circulating Water in a Steel Pile. *Energy and Buildings*, **21** (1), 65-78.

Muffler, P. & Cataldi, R. (1978) Methods for Regional Assessment of Geothermal Resources. *Geothermics*, **7** (2-4), 53-89.

Murphy, K. D. & McCartney, J. S. (2012) Behavior of Full-Scale Energy Foundations in Denver, Colorado. *Geochallenges: Rising to the Geotechnical Challenges of Colorado*, pp. 217-229.

Murphy, K. D., McCartney, J. S. & Henry, K. S. (2014) Thermo-Mechanical Characterization of a Full-Scale Energy Foundation. *From Soil Behavior Fundamentals to Innovations in Geotechnical Engineering: Honoring Roy E. Olson*, pp. 617-628.

Murphy, K. D. & McCartney, J. S. (2015) Seasonal Response of Energy Foundations During Building Operation. *Geotechnical and Geological Engineering*, **33** (2), 343-356.

Murphy, K. D., McCartney, J. S. & Henry, K. S. (2015) Evaluation of Thermo-Mechanical and Thermal Behavior of Full-Scale Energy Foundations. *Acta Geotechnica*, **10** (2), 179-195.

Mustafa Omer, A. (2008) Ground-Source Heat Pumps Systems and Applications. *Renewable and Sustainable Energy Reviews*, **12** (2), 344-371.

Nagano, K., Katsura, T., Takeda, S., Saeki, E., Nakamura, Y., Okamoto, A. & Narita, S. (2005) Thermal Characteristics of Steel Foundation Piles as Ground Heat Exchangers. *Proceedings of the 8th International Energy Agency Heat Pump Conference 2005, Las Vegas, USA*.

Neville, A. & Adam, M. (2002) *Properties of Concrete.* England, Pearson Education Limited.

Ng, C. W. W., Shi, C., Gunawan, A. & Laloui, L. (2014) Centrifuge Modelling of Energy Piles Subjected to Heating and Cooling Cycles in Clay. *Géotechnique Letters*, **4** (4), 310-316.

Ng, C. W. W., Shi, C., Gunawan, A., Laloui, L. & Liu, H. L. (2015) Centrifuge Modelling of Heating Effects on Energy Pile Performance in Saturated Sand. *Canadian Geotechnical Journal*, **52** (8), 1045-1057.

Ng, C. W. W., Ma, Q. J. & Gunawan, A. (2016) Horizontal Stress Change of Energy Piles Subjected to Thermal Cycles in Sand. *Computers and Geotechnics*, **78**, 54-61.

Nguyen, V. T., Tang, A. M. & Pereira, J. M. (2016) Thermo-Mechanical Behavior of Small-Scale Energy Pile in Dry Sand. *Proceedings of the ICEGT 2016*, *Kiel, Germany*. pp. 577-583.

Nguyen, V. T., Wu, N., Gan, Y., Pereira, J.-M. & Tang, A. M. (2020) Long-Term Thermo-Mechanical Behaviour of Energy Piles in Clay. *Environmental Geotechnics*, **7** (4), 237-248.

NHBC (2010) *Efficient Design of Piled Foundations for Low-Rise Housing–Design Guide*. National House-Building Council London.

Nicholson, D. P., Chen, Q., de Silva, M., Winter, A. & Winterling, R. (2014) The Design of Thermal Tunnel Energy Segments for Crossrail, Uk. *Proceedings of the Institution of Civil Engineers - Engineering Sustainability*, **167** (3), 118-134.

Nicholson, K. (1993) Geothermal Fluids.− Springer Verlag.

Nikolaev, I. (2007) An Experimental Study of Soil Thermal Conductivity Using a Guarded Hot Plate Apparatus. *Mechanical Engineering*, 144.

Nusier, O. & Abu-Hamdeh, N. (2003) Laboratory Techniques to Evaluate Thermal Conductivity for Some Soils. *Heat and Mass Transfer*, **39** (2), 119-123.

Odler, I. (1998) Hydration, Setting and Hardening of Portland Cement. *Lea's Chemistry of Cement and Concrete (Fourth Edition)*, Elsevier Science & Technology Books, pp. 241-297.

Olgun, C. G., Ozudogru, T. Y., Abdelaziz, S. L. & Senol, A. (2014a) Long-Term Performance of Heat Exchanger Piles. *Acta Geotechnica*, **10** (5), 553-569.

Olgun, C. G., Ozudogru, T. Y. & Arson, C. F. (2014b) Thermo-Mechanical Radial Expansion of Heat Exchanger Piles and Possible Effects on Contact Pressures at Pile–Soil Interface. *Géotechnique Letters*, **4** (3), 170-178.

Olgun, C. G. & Bowers, G. A. (2016) Experimental Investigation of Energy Pile Response for Bridge Deck Deicing Applications. *DFI Journal - The Journal of the Deep Foundations Institute*, **10** (1), 41-51.

Ouyang, Y., Soga, K. & Leung, Y. F. (2011) Numerical Back-Analysis of Energy Pile Test at Lambeth College, London. *Geo-Frontiers 2011: Advances in Geotechnical Engineering*, pp. 440-449.

Ouyang, Y. (2014) *Geotechnical Behaviour of Energy Piles*. PhD Thesis. University of Cambridge,

Ozudogru, T. Y., Olgun, C. G. & Arson, C. F. (2015) Analysis of Friction Induced Thermo-Mechanical Stresses on a Heat Exchanger Pile in Isothermal Soil. *Geotechnical and Geological Engineering*, **33** (2), 357-371.

Pagola, M. A., Jensen, R. L., Madsen, S. & Poulsen, S. E. (2017) Measurement of Thermal Properties of Soil and Concrete Samples. *Aalborg University*.

Pahud, D. & Hubbuch, M. (2006) Measured Thermal Performances of the Dock Midfield Energy Pile System at Zürich Airport. In: *Energie- und Umweltforschung im Bauwesen Schweizerisches Status-Seminar 2006, ETH, Zurich*. pp. 217-224.

Pahud, D. & Hubbuch, M. (2007) Measured Thermal Performances of the Energy Pile System of the Dock Midfield at Zurich Airport. *Proceedings of the European Geothermal Congress 2007, Unterhaching, Germany, 30 May-1 June 2007*.

Park, H., Lee, S.-R., Yoon, S. & Choi, J.-C. (2013) Evaluation of Thermal Response and Performance of Phc Energy Pile: Field Experiments and Numerical Simulation. *Applied Energy*, **103**, 12-24.

Park, S., Lee, D., Lee, S., Chauchois, A. & Choi, H. (2017) Experimental and Numerical Analysis on Thermal Performance of Large-Diameter Cast-in-Place Energy Pile Constructed in Soft Ground. *Energy*, **118**, 297-311.

Pasten, C. & Santamarina, J. C. (2014) Thermally Induced Long-Term Displacement of Thermoactive Piles. *Journal of Geotechnical and Geoenvironmental Engineering*, **140** (5), 06014003.

Pauly, N. M. (2010) *Thermal Conductivity of Soils from the Analysis of Boring Logs*. Master's Thesis. University of South Florida, Florida, USA.

Péron, H., Knellwolf, C. & Laloui, L. (2011) A Method for the Geotechnical Design of Heat Exchanger Piles. *Geo-Frontiers 2011: Advances in Geotechnical Engineering*, pp. 470-479.

Popov, Y. A., Pribnow, D. F., Sass, J. H., Williams, C. F. & Burkhardt, H. (1999) Characterization of Rock Thermal Conductivity by High-Resolution Optical Scanning. *Geothermics*, **28** (2), 253-276.

Portland Cement Association (1997) Concrete Technology Today, Volume 18/Number 2, Skokie, Illinois, 1-8

Potts, D. M. & Zdravkovic, L. (1999) *Finite Element Analysis in Geotechnical Engineering: Theory.* London, Thomas Telford Publishing.

Potts, D. M. & Zdravkovic, L. (2001) *Finite Element Analysis in Geotechnical Engineering: Application.* London, Thomas Telford Publishing.

Rammal, D., Mroueh, H. & Burlon, S. (2018) Impact of Thermal Solicitations on the Design of Energy Piles. *Renewable and Sustainable Energy Reviews*, **92**, 111-120.

Rees, S., Adjali, M., Zhou, Z., Davies, M. & Thomas, H. (2000) Ground Heat Transfer Effects on the Thermal Performance of Earth-Contact Structures. *Renewable and Sustainable Energy Reviews*, **4** (3), 213-265.

Ren, T., Ochsner, T., Horton, R. & Ju, Z. (2003) Heat-Pulse Method for Soil Water Content Measurement: Influence of the Specific Heat of the Soil Solids. *Soil Science Society of America Journal*, **67** (6), 1631-1634.

Rotta Loria, A. F., Gunawan, A., Shi, C., Laloui, L. & Ng, C. W. W. (2015) Numerical Modelling of Energy Piles in Saturated Sand Subjected to Thermo-Mechanical Loads. *Geomechanics for Energy and the Environment*, **1**, 1-15.

Rotta Loria, A. F. & Laloui, L. (2016) Analysis of Thermally Induced Mechanical Interactions in Energy Pile Groups. In: Wuttke, F., Bauer, S. and Sanchez, M. (eds.) *1st International Conference on Energy Geotechnics, ICEGT 2016, Kiel, Germany*. pp. 171-178.

Rotta Loria, A. F. & Laloui, L. (2017) Thermally Induced Group Effects among Energy Piles. *Géotechnique*, **67** (5), 374-393.

Rybach, L. (2001) Design and Performance of Borehole Heat Exchanger/Heat Pump Systems. *Proc. European Summer School of Geothermal Energy Applications, Oradea/Romania (CD-ROM)*.

Sáez Blázquez, C., Farfán Martín, A., Martín Nieto, I. & Gonzalez-Aguilera, D. (2017) Measuring of Thermal Conductivities of Soils and Rocks to Be Used in the Calculation of a Geothermal Installation. *Energies*, **10** (6).

Sailer, E., Taborda, D. M. G., Zdravković, L. & Potts, D. M. (2019) Fundamentals of the Coupled Thermo-Hydro-Mechanical Behaviour of Thermo-Active Retaining Walls. *Computers and Geotechnics*, **109**, 189-203.

Sailer, E. (2020) *Numerical Modelling of Thermo-Active Retaining Walls*. PhD Thesis. Imperial College London, London.

Sajadi, S. S. (2020) *Thermal Behaviour Due to Heat of Hydration of Massive Concrete Underground Structures*. MSc Thesis. Imperial College London, London.

Salciarini, D., Ronchi, F., Cattoni, E. & Tamagnini, C. (2015) Thermomechanical Effects Induced by Energy Piles Operation in a Small Piled Raft. *International Journal of Geomechanics*, **15** (2), 04014042.

Sani, A. K., Singh, R. M., Amis, T. & Cavarretta, I. (2019) A Review on the Performance of Geothermal Energy Pile Foundation, Its Design Process and Applications. *Renewable and Sustainable Energy Reviews*, **106**, 54-78.

Sanner, B. (2005) Shallow Geothermal Systems. *Proceedings of the Ground source heat pumps, Pre and post congress short courses, Izmir*. pp. 33-83.

Sanner, B., Hellström, G., Spitler, J. & Gehlin, S. (2005) Thermal Response Test–Current Status and World-Wide Application. *Proceedings of the World Geothermal Congress*. International Geothermal Association, 1436, pp. 2005.

Scanlon, J. M. & McDonald, J. E. (1994) Thermal Properties. *Significance of Tests and Properties of Concrete and Concrete-Making Materials*, ASTM International.

Schindler, A. K. & Folliard, K. J. (2005) Heat of Hydration Models for Cementitious Materials. *ACI Materials Journal*, **102** (1), 24.

Schneider, M. & Moormann, C. (2010) Geotu6–Ein Tunnel-Geothermisches Forschungsprojekt. *Tunnel*, **29** (2), 1421.

Schnürer, H., Sasse, C. & Fisch, M. (2005) Thermal Energy Storage in Office Buildings Foundations. *Braunschweig: Institute for Building Services and Energy Design*.

Sedaghat, A., Zayed, A. & Sandberg, P. (2013) Measurement and Prediction of Heat of Hydration of Portland Cement Using Isothermal Conduction Calorimetry. *Journal of Testing and Evaluation*, **41** (6).

Sedaghat, A., Shanahan, N. & Zayed, A. (2015) Predicting One-Day, Three-Day, and Seven-Day Heat of Hydration of Portland Cement. *Journal of Materials in Civil Engineering*, **27** (9).

Sedaghat, A. (2016) *Cement Heat of Hydration and Thermal Control*. PhD Thesis. University of South Florida, Florida.

Sekine, K., Ooka, R., Yokoi, M., Shiba, Y. & Hwang, S. (2007) Development of a Ground-Source Heat Pump System with Ground Heat Exchanger Utilizing the Cast-in-Place Concrete Pile Foundations of Buildings. *Ashrae Transactions*, **113** (1).

Self, S. J., Reddy, B. V. & Rosen, M. A. (2013) Geothermal Heat Pump Systems: Status Review and Comparison with Other Heating Options. *Applied Energy*, **101**, 341-348.

Shi, M., Wang, Q. & Zhou, Z. (2015) Comparison of the Properties between High-Volume Fly Ash Concrete and High-Volume Steel Slag Concrete under Temperature Matching Curing Condition. *Construction and Building Materials*, **98**, 649-655.

Sibbitt, W., Dodson, J. & Tester, J. (1979) Thermal Conductivity of Crystalline Rocks Associated with Energy Extraction from Hot Dry Rock Geothermal Systems. *Journal of Geophysical Research: Solid Earth*, **84** (B3), 1117-1124.

Singh, R. M., Bouazza, A. & Wang, B. (2015a) Near-Field Ground Thermal Response to Heating of a Geothermal Energy Pile: Observations from a Field Test. *Soils and Foundations*, **55** (6), 1412-1426.

Singh, R. M., Bouazza, A., Wang, B., Haberfield, C. H., Baycan, S. & Carden, Y. (2015b) Thermal and Thermo-Mechanical Response of a Geothermal Energy Pile. *Proceedings of the World Geothermal Congress*. 7.

Sliwa, T., Nowosiad, T., Vytyaz, O. & Sapinska-Sliwa, A. (2016) Study on the Efficiency of Deep Borehole Heat Exchangers. *SOCAR Proceedings*, (2), 29-42.

Soga, K. & Rui, Y. (2016) Energy Geostructures. *Advances in Ground-Source Heat Pump Systems*, pp. 185-221.

Stewart, M. A. & McCartney, J. S. (2012) Strain Distributions in Centrifuge Model Energy Foundations. *Geocongress 2012: State of the Art and Practice in Geotechnical Engineering*, pp. 4376-4385.

Stewart, M. A. & McCartney, J. S. (2014) Centrifuge Modeling of Soil-Structure Interaction in Energy Foundations. *Journal of Geotechnical and Geoenvironmental Engineering*, **140** (4), 04013044.

Sun, Q., Elshafie, M., Barker, C., Fisher, A., Schooling, J. & Rui, Y. (2020) Thermal Integrity Testing of Cast in Situ Piles: An Alternative Interpretation Approach. *Structural Health Monitoring*.

Sung, C., Park, S., Lee, S., Oh, K. & Choi, H. (2018) Thermo-Mechanical Behavior of Cast-in-Place Energy Piles. *Energy*, **161**, 920-938.

Suryatriyastuti, M. E., Mroueh, H. & Burlon, S. (2012) Understanding the Temperature-Induced Mechanical Behaviour of Energy Pile Foundations. *Renewable and Sustainable Energy Reviews*, **16** (5), 3344-3354.

Suryatriyastuti, M. E. (2013) *Numerical Study of the Thermo-Active Piles Behavior in Cohesionless Soils*. PhD Thesis. Université Lille1,

Suryatriyastuti, M. E., Mroueh, H. & Burlon, S. (2013) Numerical Analysis of a Thermo-Active Pile under Cyclic Thermal Loads. *Proceedings of the European Geothermal Conference (EGC 2013), Pisa, Italy*. pp. 3-7.

Suryatriyastuti, M. E., Mroueh, H. & Burlon, S. (2014a) Modeling the Soil-Pile Interaction of Geothermal Piles. *Proceedings of the 8th European Conference on Numerical Methods in Geotechnical Engineering*, *Delft, The Netherlands*. pp. 1049-1054.

Suryatriyastuti, M. E., Mroueh, H. & Burlon, S. (2014b) A Load Transfer Approach for Studying the Cyclic Behavior of Thermo-Active Piles. *Computers and Geotechnics*, **55**, 378-391.

Suryatriyastuti, M. E., Burlon, S. & Mroueh, H. (2016) On the Understanding of Cyclic Interaction Mechanisms in an Energy Pile Group. *International Journal for Numerical and Analytical Methods in Geomechanics*, **40** (1), 3-24.

Sutman, M., Olgun, G., Laloui, L. & Brettmann, T. (2017) Effect of End-Restraint Conditions on Energy Pile Behavior. *Geotechnical Frontiers 2017*, pp. 165-174.

Swaddiwudhipong, S., Chen, D. & Zhang, M. (2002) Simulation of the Exothermic Hydration Process of Portland Cement. *Advances in Cement Research*, **14** (2), 61-69.

Taborda, D. M. G. (2011) *Development of Constitutive Models for Application in Soil Dynamics*. PhD Thesis. Imperial College London, London.

Taborda, D. M. G., Potts, D. M. & Zdravković, L. (2016) On the Assessment of Energy Dissipated through Hysteresis in Finite Element Analysis. *Computers and Geotechnics*, **71**, 180-194.

Thomas, J. J. (2012) The Instantaneous Apparent Activation Energy of Cement Hydration Measured Using a Novel Calorimetry-Based Method. *Journal of the American Ceramic Society*, **95** (10), 3291-3296.

Tsetoulidis, C., Naskos, A. & Georgiadis, K. (2016) Numerical Investigation of the Mechanical Behaviour of Single Energy Piles and Energy Pile Groups. *Energy Geotechnics*, pp. 569-575.

Underwood, C. P. (2013) Ground Source Heat Pumps: Observations from United Kingdom Ground Thermal Response Tests. *Building Services Engineering Research and Technology*, **34** (2), 123-144.

van Breugel, K. (1991) *Simulation of Hydration and Formation of Structure in Hardening Cement-Based Materials.* The Netherlands, Delft University Press.

Verbeck, G. J. & Foster, C. W. (1950) Long-Time Study of Cement Performance in Concrete. *ASTM Proceedings*, **50**, 1235-1262.

Vieira, A. & Maranha, J. R. (2017) Thermoplastic Analysis of a Thermoactive Pile in a Normally Consolidated Clay. *International Journal of Geomechanics*, **17** (1), 04016030.

Wadsö, L. (2003) *An Experimental Comparison between Isothermal Calorimetry, Semi-Adiabatic Calorimetry and Solution Calorimetry for the Study of Cement Hydration*. NORDTEST. TR 522.

Wang, B., Bouazza, A. & Haberfield, C. (2011) Preliminary Observations from Laboratory Scale Model Geothermal Pile Subjected to Thermal-Mechanical Loading. *Geo-Frontiers 2011: Advances in Geotechnical Engineering*, pp. 430-439.

Wang, B., Bouazza, A., Barry-Macaulay, D., Singh, M., Webster, M., Haberfield, C., Chapman, G. & Baycan, S. (2012) Field and Laboratory Investigation of a Heat Exchanger Pile. *Geocongress 2012: State of the Art and Practice in Geotechnical Engineering*, pp. 4396-4405.

Wang, B., Bouazza, A., Singh, R. M., Haberfield, C., Barry-Macaulay, D. & Baycan, S. (2015) Posttemperature Effects on Shaft Capacity of a Full-Scale Geothermal Energy Pile. *Journal of Geotechnical and Geoenvironmental Engineering*, **141** (4).

Wang, C.-l., Liu, H.-l., Kong, G.-q. & Wang Wai Ng, C. (2017) Different Types of Energy Piles with Heating–Cooling Cycles. *Proceedings of the Institution of Civil Engineers - Geotechnical Engineering*, **170** (3), 220-231.

Wood, C. J., Liu, H. & Riffat, S. B. (2009) Use of Energy Piles in a Residential Building, and Effects on Ground Temperature and Heat Pump Efficiency. *Géotechnique*, **59** (3), 287-290.

Wood, C. J., Liu, H. & Riffat, S. B. (2010) An Investigation of the Heat Pump Performance and Ground Temperature of a Piled Foundation Heat Exchanger System for a Residential Building. *Energy*, **35** (12), 4932-4940.

Woodside, W. & Messmer, J. H. (1961) Thermal Conductivity of Porous Media. I. Unconsolidated Sands. *Journal of Applied Physics*, **32** (9), 1688-1699.

World Wide Fund For Nature (2019) Climate Mitigation by Merton Rule, Available from: https://wwf.panda.org/?204444/Merton-London-climate-rule [Accessed: 20th February 2020]

Yavari, N., Tang, A. M., Pereira, J.-M. & Hassen, G. (2014) Experimental Study on the Mechanical Behaviour of a Heat Exchanger Pile Using Physical Modelling. *Acta Geotechnica*, **9** (3), 385-398.

Yavari, N., Tang, A. M., Pereira, J. M. & Hassen, G. (2016) Mechanical Behaviour of a Small-Scale Energy Pile in Saturated Clay. *Géotechnique*, **66** (11), 878-887.

Yavuzturk, C. & Spitler, J. D. (1999) A Short Time Step Response Factor Model for Vertical Ground Loop Heat Exchangers. *ASHRAE Transactions*, **105** (2), 475-485.

You, S., Cheng, X., Guo, H. & Yao, Z. (2014) In-Situ Experimental Study of Heat Exchange Capacity of C.F.G. Pile Geothermal Exchangers. *Energy and Buildings*, **79**, 23-31.

Zayed, A., Sedaghat, A. & Shanahan, N. (2013) *Effects of Portland Cement Particle Size on Heat of Hydration*. University of South Florida.

Zdravković, L., Taborda, D. M. G., Potts, D. M., Abadias, D., Burd, H. J., Byrne, B. W., Gavin, K. G., Houlsby, G. T., Jardine, R. J., Martin, C. M., McAdam, R. A. & Ushev, E. (2020) Finite-Element Modelling of Laterally Loaded Piles in a Stiff Glacial Clay Till at Cowden. *Géotechnique*, **70** (11), 999-1013.

Zdravković, L., Cui, W., Gawecka, K., Liu, R. Y. W., Potts, D. M., Sailer, E. & Taborda, D. M. G. (2021) Numerical Modelling of Thermo-Active Piles. *Proceedings of the Piling 2020 Conference*. ICE Publishing, pp. 35-59.

Zhang, G., Xia, C., Sun, M., Zou, Y. & Xiao, S. (2013) A New Model and Analytical Solution for the Heat Conduction of Tunnel Lining Ground Heat Exchangers. *Cold Regions Science and Technology*, **88**, 59-66.

Zhao, Q., Chen, B., Tian, M. & Liu, F. (2018) Investigation on the Thermal Behavior of Energy Piles and Borehole Heat Exchangers: A Case Study. *Energy*, **162**, 787-797.

Zito, M., Freitas, T. M. B., Bourne-Webb, P. J. & Sterpi, D. (2021) Effect of Domain Size in the Modelled Response of Thermally-Activated Piles. *Challenges and Innovations in Geomechanics Lecture Notes in Civil Engineering*, pp. 1110-1118.

APPENDIX A A PARAMETRIC STUDY ON THE EFFECTS OF λ_c/λ_s TO THE SIMULATED TEMPERATURE RISE WITHIN A HYDRATING PILE

In this parametric study, thermal analyses are conducted using ICFEP in order to establish the effects of λ_c/λ_s on the simulated temperature rise within a hydrating pile. Two concrete piles are being considered, one with a diameter of $0.6\ m$ and the other one with a diameter of $2.4\ m$, and λ_c/λ_s ratios of $0.5, 0.7, 1.0, 1.3$ and 1.5 (which correspond to λ_s of $1.79\ W/mK$ and λ_c of 0.90, 1.25, 1.79, 2.33 and $2.69\ W/mK$ respectively) are investigated. Table A.1 lists the model parameters and thermal properties that are adopted in this study.

Model parameter Q_{max}	$250000\ J \cdot kg_{cement}^{-1}$
Model parameter τ	$80000\ s$
Model parameter β	0.6
Activation energy E_a	$45000\ J \cdot mol^{-1}$
Cement content χ	$0.125\ kg_{cement} \cdot kg_{concrete}^{-1}$
Concrete/soil density ρ	$2400\ kg \cdot m^{-3}$
Concrete/soil specific heat capacity C_p	$895\ J \cdot kg^{-1} \cdot K^{-1}$
Soil thermal conductivity λ_s	$1.79\ W \cdot m^{-1} \cdot K^{-1}$
Universal gas constant R	$8.314\ J \cdot mol^{-1} \cdot K^{-1}$
Reference temperature T_{ref}	23^oC
Initial concrete/soil temperature $T_{initial}$	20^oC

Table A.1 Model parameters and thermal properties adopted in this parametric study

Figure A.1 and Figure A.2 present the temperature rise simulated for the $0.6\ m$ diameter pile at $r = 0\ m$ and $0.3\ m$, respectively, while Figure A.3 to Figure A.5 present the temperature rise for the $2.4\ m$ diameter pile at $r = 0\ m$, $0.6\ m$ and $1.2\ m$, respectively. Figure A.6 and Figure A.7 plot the maximum temperature rise against the λ_c/λ_s ratio for the $0.6\ m$ and $2.4\ m$ diameter piles respectively. Table A.2 and Table A.3 report the maximum temperature rise simulated at the aforementioned monitoring points, and the percentage difference from the case of $\lambda_c/\lambda_s = 1.0$ for the $0.6\ m$ and $2.4\ m$ diameter pile respectively.

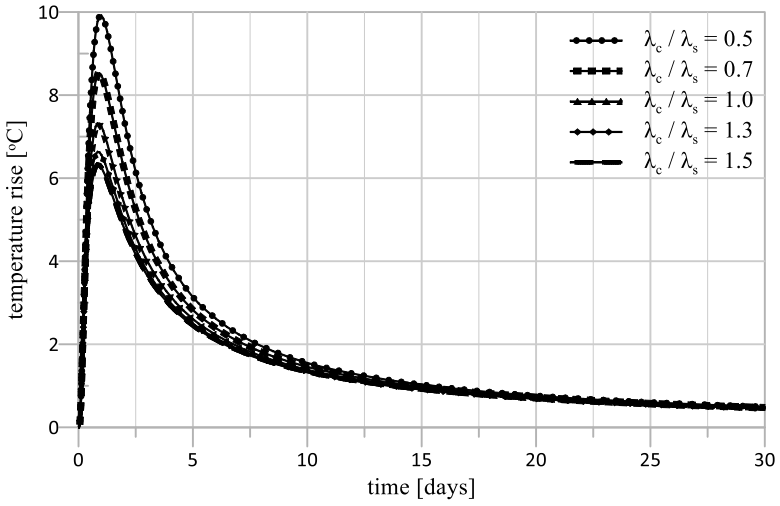


Figure A.1 Temperature rise simulation at $r = 0\ m$ for the $0.6\ m$ diameter pile

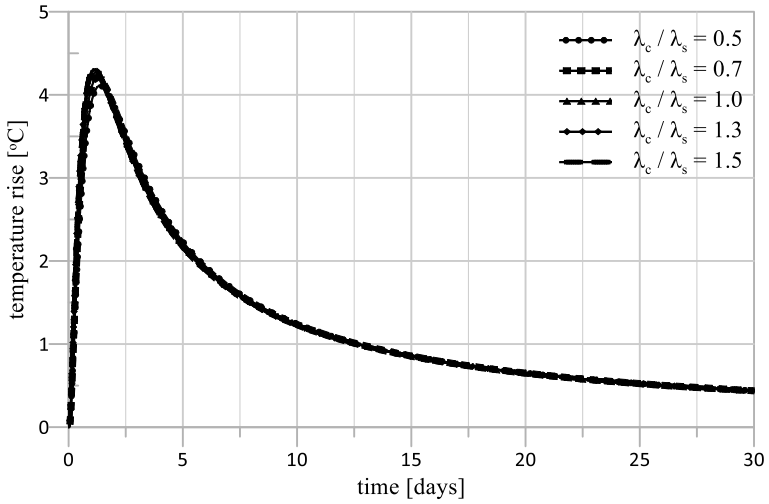


Figure A.2 Temperature rise simulation at $r = 0.3\ m$ for the $0.6\ m$ diameter pile

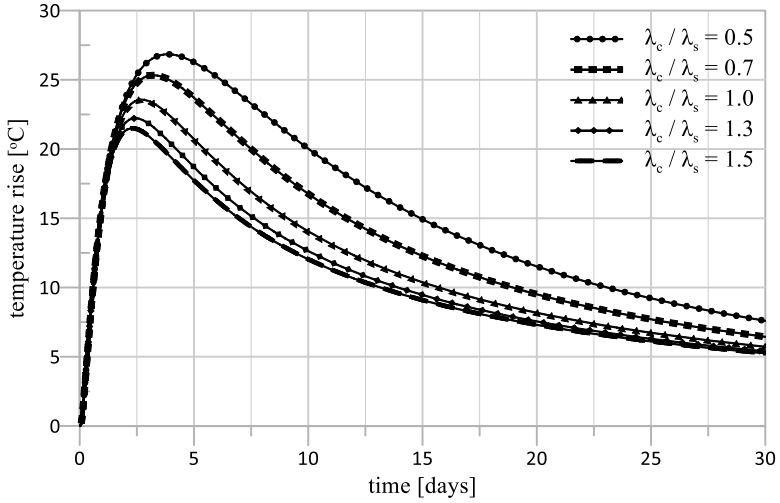


Figure A.3 Temperature rise simulation at $r = 0\ m$ for the $2.4\ m$ diameter pile

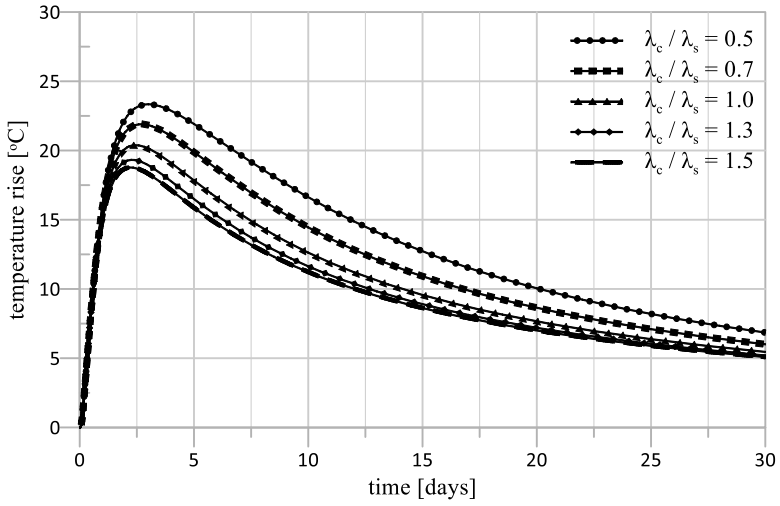


Figure A.4 Temperature rise simulation at $r = 0.6\,m$ for the 2.4 m diameter pile

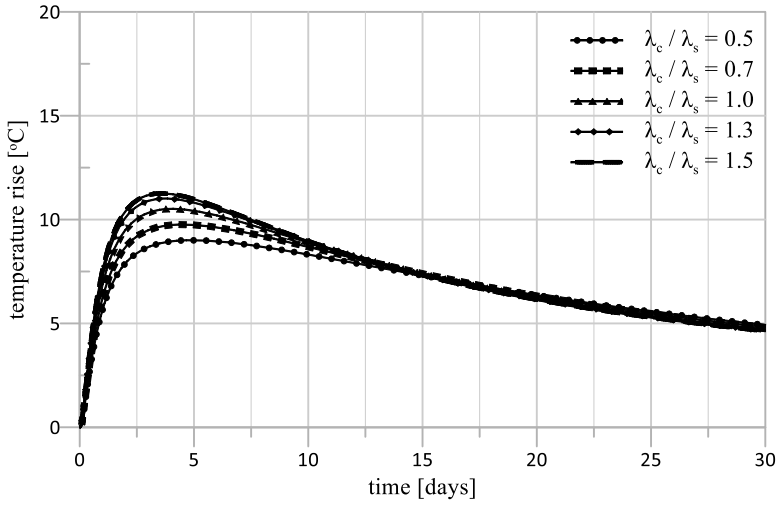


Figure A.5 Temperature rise simulation at $r = 1.2\,m$ for the 2.4 m diameter pile

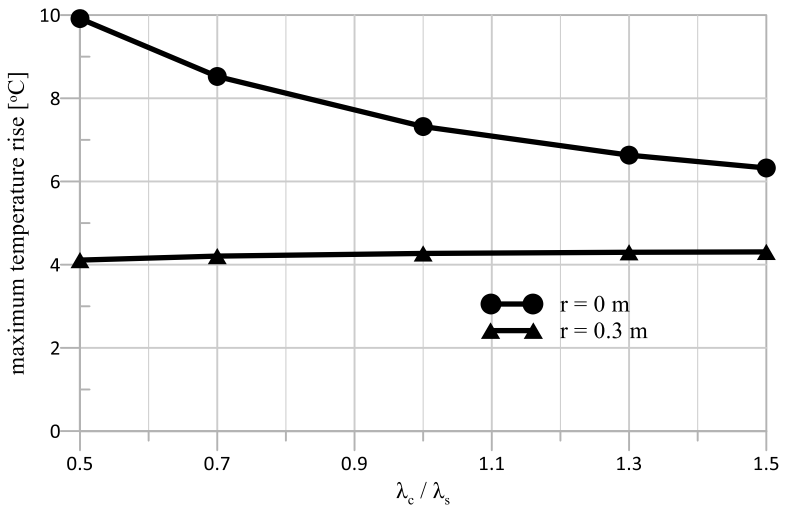


Figure A.6 Maximum temperature rise plotted against the $\frac{\lambda_c}{\lambda_s}$ ratio for the $0.6\ m$ diameter pile

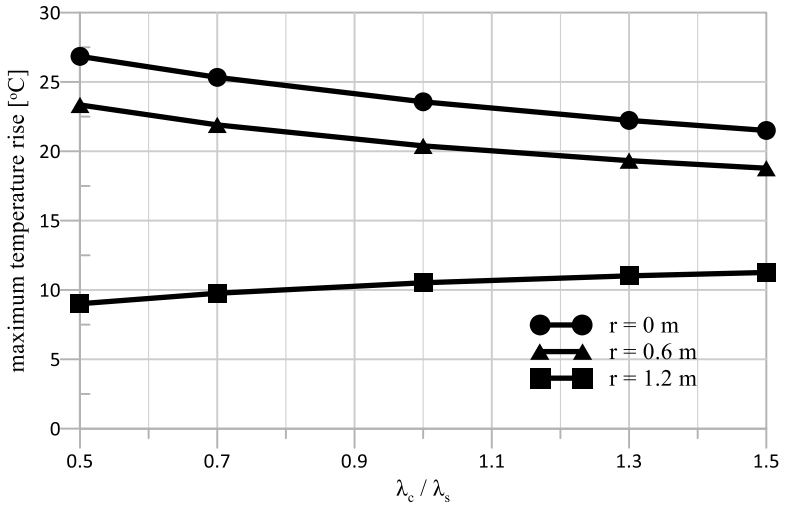


Figure A.7 Maximum temperature rise plotted against the $\frac{\lambda_c}{\lambda_s}$ ratio for the $2.4\ m$ diameter pile

$\frac{\lambda_c}{\lambda_s}$	Max. temp. rise at $r = 0\ m$ [°C]	Percentage difference from the case of $\frac{\lambda_c}{\lambda_s} = 1.0$ [%]	Max. temp. rise at $r = 0.3\ m$ [°C]	Percentage difference from the case of $\frac{\lambda_c}{\lambda_s} = 1.0$ [%]
0.5	9.9	35.5	4.1	−3.7
0.7	8.5	16.4	4.2	−1.5
1.0	7.3	0.0	4.3	0.0
1.3	6.6	−9.4	4.3	0.7
1.5	6.3	−13.6	4.3	0.9

Table A.2 Maximum temperature rise simulated at the monitoring points and the percentage difference from the case of $\frac{\lambda_c}{\lambda_s} = 1.0$ for the $0.6\ m$ diameter pile

$\frac{\lambda_c}{\lambda_s}$	Max. temp. rise at $r = 0\ m$ [°C]	Percentage difference from the case of $\frac{\lambda_c}{\lambda_s} = 1.0$ [%]	Max. temp. rise at $r = 0.6\ m$ [°C]	Percentage difference from the case of $\frac{\lambda_c}{\lambda_s} = 1.0$ [%]	Max. temp. rise at $r = 1.2\ m$ [°C]	Percentage difference from the case of $\frac{\lambda_c}{\lambda_s} = 1.0$ [%]
0.5	26.8	13.9	23.3	14.5	9.0	−14.4
0.7	25.3	7.5	21.9	7.4	9.8	−7.2
1.0	23.6	0.0	20.4	0.0	10.5	0.0
1.3	22.2	−5.7	19.3	−5.2	11.0	4.7
1.5	21.5	−8.8	18.8	−7.9	11.3	7.1

Table A.3 Maximum temperature rise simulated at the monitoring points and the percentage difference from the case of $\frac{\lambda_c}{\lambda_s} = 1.0$ for the $2.4\ m$ diameter pile

The trend that can be observed from Figure A.1 to Figure A.7 and Table A.2 and Table A.3 is that, for the smaller diameter pile, the sensitivity of simulated maximum temperature rise to the λ_c/λ_s ratio is considerably larger at the pile centre than at the pile edge. Indeed, the maximum temperature rise percentage difference from the ratio of 1.0 can be up to 35.5% at the pile centre, but only 3.7% at the pile edge. For the larger diameter pile, the sensitivity of simulated maximum temperature rise to the λ_c/λ_s ratio is relatively independent of r, where the percentages are 13.9% at the pile centre, 14.5% at $r = 0.6\ m$ and 14.4% at the pile edge.

In order to further quantify the effects of varying the λ_c/λ_s ratio, a metric η is proposed (which is similar to the one proposed in Zdravković et al. (2020)), which is given by:

$$\eta = \frac{Area\ under\ the\ temp.rise\ graph - Area\ under\ the\ temp.rise\ graph\ for \frac{\lambda_c}{\lambda_s} = 1.0}{Area\ under\ the\ temp.rise\ graph\ for \frac{\lambda_c}{\lambda_s} = 1.0} \quad \text{(A.1)}$$

Clearly, a metric of zero suggests that the average temperature prediction for the first 30 days is identical for both analyses. Positive values suggest larger temperatures than those recorded for the ratio $\lambda_c/\lambda_s = 1.0$, while the opposite is true for negative values of η.

Figure A.8 and Figure A.9 plot the metric η against the λ_c/λ_s ratio for the $0.6\ m$ and $2.4\ m$ diameter pile respectively.

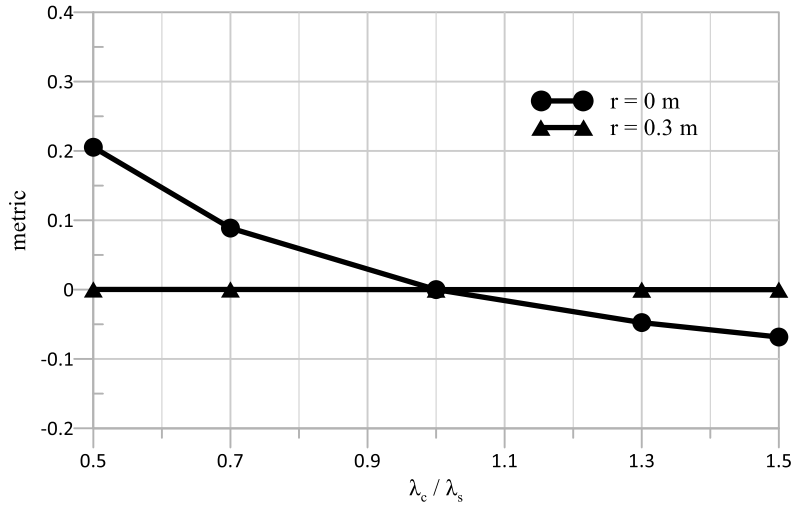


Figure A.8 Metric against $\frac{\lambda_c}{\lambda_s}$ ratio for the $0.6\ m$ diameter pile

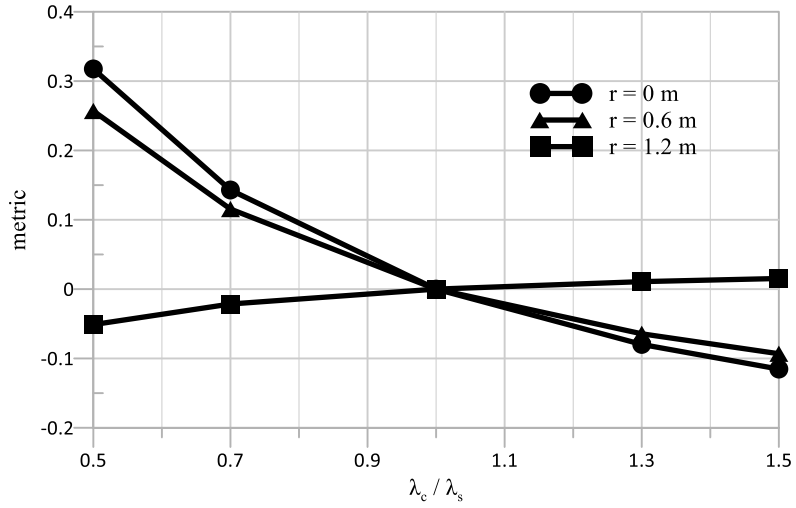


Figure A.9 Metric against $\frac{\lambda_c}{\lambda_s}$ ratio for the $2.4\ m$ diameter pile

Referring to Figure A.8 and Figure A.9, it can be observed that in terms of the area under the temperature rise graph, the sensitivity to the λ_c/λ_s ratio reduces with increasing distance from the pile centre for both piles.

Based on the above results, it can be concluded that the assumption of $\lambda_c = \lambda_s$ adopted by the numerical technique is acceptable, given that:

- In terms of the maximum temperature rise prediction, the percentage difference from the case of $\lambda_c = \lambda_s$ is small (lower than 15% in general), with the exception of the case for $\lambda_c/\lambda_s = 0.5$ and 0.7 at the pile centre for the $0.6\ m$ diameter pile, although when these are translated to absolute differences, they are only 2.6^oC and 1.2^oC, respectively.
- The concrete thermal conductivity studied in this parametric study ($0.9 - 2.69\ W/mK$) is relatively wide and only the extreme values (i.e. $0.9\ W/mK$), which are relatively unlikely to be encountered in realistic situations, give significant differences in temperature predictions.
- As temperatures are measured by sensors usually attached to the reinforcement cage, and hence close to the pile edge, the expected errors in practical applications arising from the assumption of $\lambda_c = \lambda_s$ are relatively small.

APPENDIX B MIX DESIGN FOR THE CONCRETE IN LP 1

Proposed Concrete Mix Composition

To: **CEMENTATION SKANSKA LTD**
Bentley House Jossey Lane
Doncaster
South Yorkshire DN5 9ED

London Concrete
London House
77 Boston Manor Road
Brentford
Middlesex
TW8 9JQ
Tel: 020 8380 7300
Fax: 020 8380 7301

Site / Contract Address	Plant: **Bow RMX Prodn** Contact: **Will Hanson** Our Ref: **4624511** Account No: **4162782** Issue Date: **06/03/18** Issued By:

All mixes in accordance with BS 8500-2 (except proprietary mixes) unless otherwise agreed. Batch weight of materials calculated on as SSD basis for 1.0m3 of fresh compacted concrete. Mixes are quality controlled and actual mix proportions may vary in response to control systems.

Source Plant: **Bow .**

C40/50 20mm CIIIA+SR 630 MS3925 MG1901 MS1902 FBR150/12	Mix Ref: **DC-3**		**Quantity / UOM**
Lagerdorf EN 197-1 Cem I 52,5N EC 0840-CPD-0120-1200-05	Paragon	Chatham	220.000 KG
GGBS Hanson Purfleet	Hanson Cement	Purfleet	220.000 KG
4/20 Conc. Graded Limestone EN12620/PD6682-1 TC1 ex Torr	Foster Yeoman	Torr	909.000 KG
0/4 Conc. Sand MP Blended EN12620/PD6682-1 TD1	Agg.Ind. Bow	Deme / Torr	829.000 KG
Betacarb 80ST Limestone Filler Omya UK	Omya	Beto 80ST Steepl	60.000 KG
Masterease 3925 Super Plasticiser BASF	Basf Manchester		4.840 LT
Master Glenium Sky 1901 Super Plasticiser BASF	Basf Manchester		.660 LT
Mastersure 1902	Basf Manchester		.660 LT
Fibremesh 150 BASF / Propex Concrete Systems	Propex		.900 KG
Water (Cold)			

A/C Ratio	3.950
% Fines	47.699
Total Cementitious (kg/m3)	440.000

Actual WCR	.384
Alkali (kg/m3)	1.506
Chlorides	.106

APPENDIX C MIX DESIGN FOR THE CONCRETE IN LP 2

MD Ref: AW474

Cementation Skanska Ltd

Date: 20-Mar-19

Certificate of Mix Design

Plant: Stepney/Canning Town

Mix Specifications

Mix	Description	Agg Size	Cement Type	Target Consistence
1	P280 SOFTPILE	20	CEMI+GGBS	S4
2	P50	10	CEM I	S4
3	P280 SOFTPILE	10	CEMI+GGBS	S4
4	C32/40 PUMP DC2 + SPLAS + RETARDER	20	CEM II/B-V+SR	S4

Mix Design

Materials			Dry Weights kg/m^3				
Type	Primary Source	Secondary Source	1	2	3	4	
CEM I	Cemex - Rugby	Cemex - Tilbury	14	50	15	~	
CEM II/B-V+SR	Cemex - Rugby	Cemex - Tilbury	~	~	~	350	
GGBS	Hanson - Purfleet		266	~	265	~	
0/4	Cemex - Angerstein	Cemex - Northfleet	890	1260	925	798	
4/10	Cemex - Doveholes	Cemex - Raynes	~	840	938	~	
4/20	Cemex - Doveholes	Cemex - Raynes	960	~	~	1034	
Admix 1 (ml)	Cemex WRA - CP105		1400	~	1400	~	
Admix 2 (ml)	Cemex SPLAS - Isoflecx 561		~	~	~	2100.00	
Admix 3 (ml)	Cemex RETARDER - CR 800		~	~	~	1050.00	
W/C	Free Water/Cement Ratio		0.62	3.19	0.62	0.44	
% Fines	Fines Content (%)		48%	60%	50%	44%	
Chloride	Chloride Content % by Weight of Cement (%)		0.23	0.28	0.20	0.18	
Alkali	Alkali (kg/m3)		0.40	0.63	0.35	2.50	

Mix design details given are subject to variation both in weight and source, given natural variation in material properties and source availability

Additional Information

Signed:

Andlyn White
Readymix Technical Sales Support

CEMEX UK Operations Limited
CEMEX House, Evreux Way, Rugby, Warwickshire, CV21 2DT, United Kingdom
Phone +44(0)1788 517000 Fax +44 (0)1788 517220
www.cemex.co.uk
With effect from 4 June 2018 the registered office address for the CEMEX UK group of companies will be CEMEX House, Evreux Way, Rugby, Warwickshire, CV21 2DT

APPENDIX D FIGURES COMPARING THE MODELLED AND MEASURED TEMPERATURE RISE CURVES FOR PILES FROM LP 1

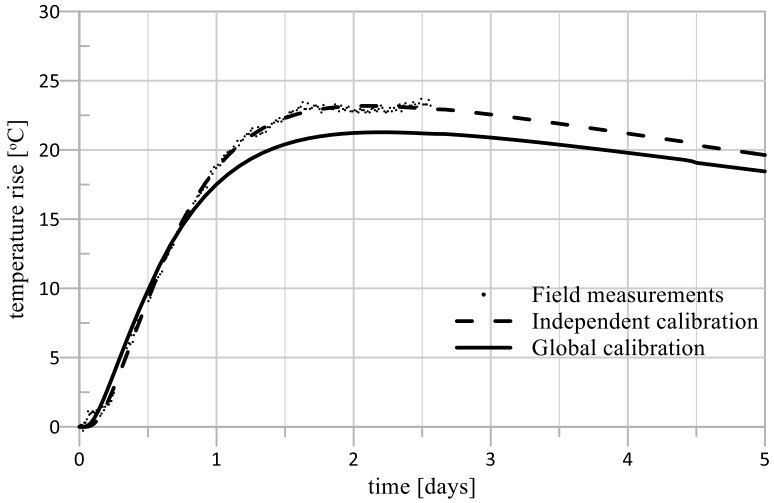


Figure D.1 Comparison of modelled and measured temperature rise curves for Pile P2 in London Project 1

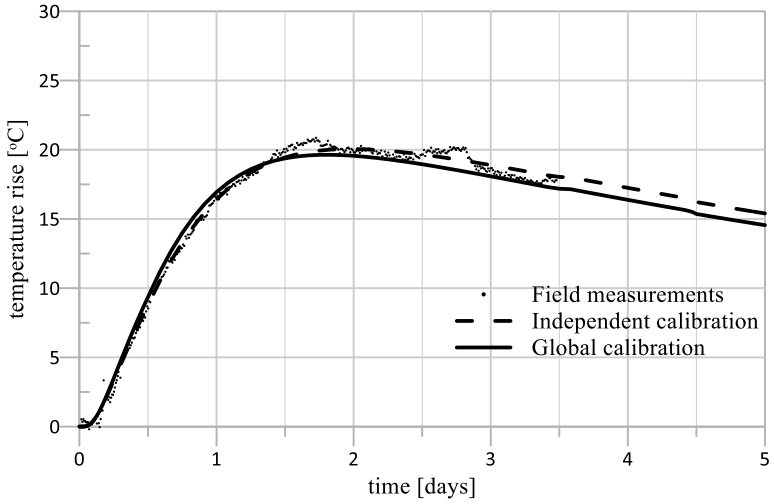


Figure D.2 Comparison of modelled and measured temperature rise curves for Pile P3a in London Project 1

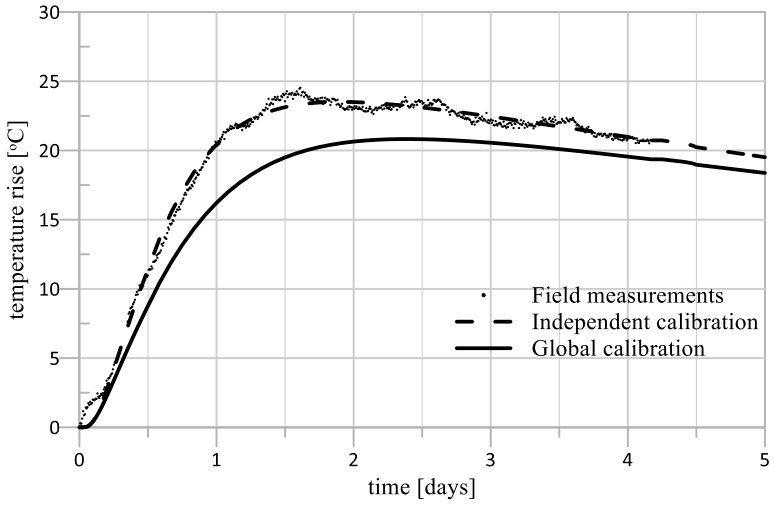


Figure D.3 Comparison of modelled and measured temperature rise curves for Pile P5 in London Project 1

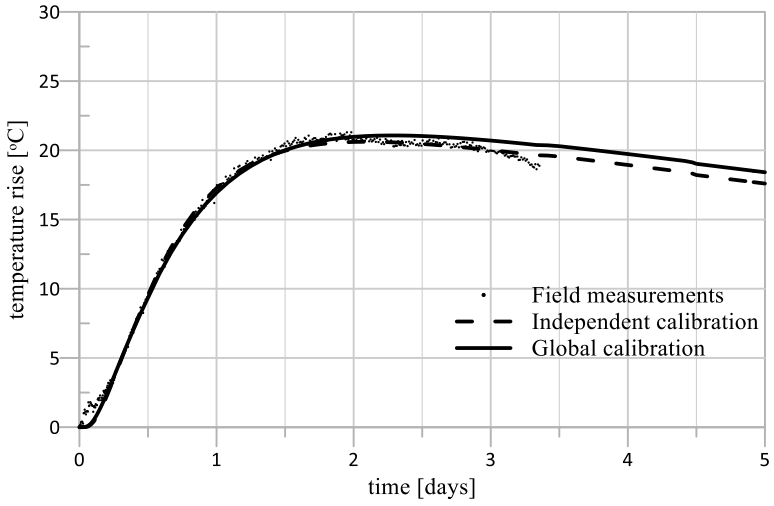


Figure D.4 Comparison of modelled and measured temperature rise curves for Pile P6 in London Project 1

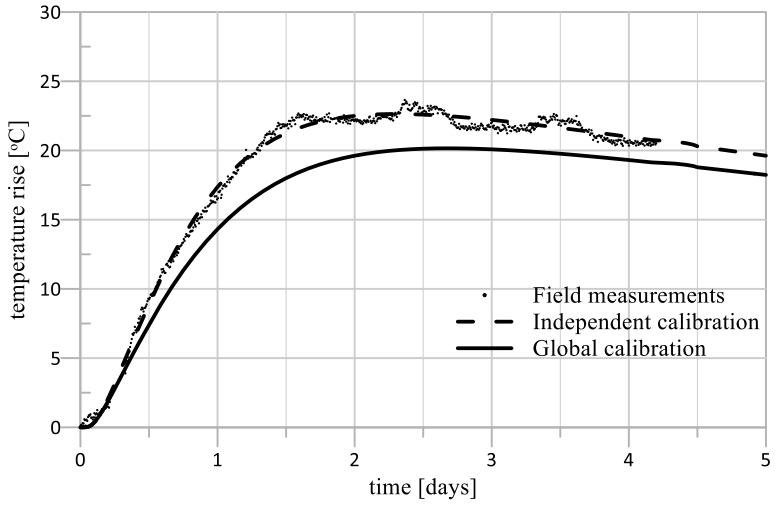


Figure D.5 Comparison of modelled and measured temperature rise curves for Pile P7 in London Project 1

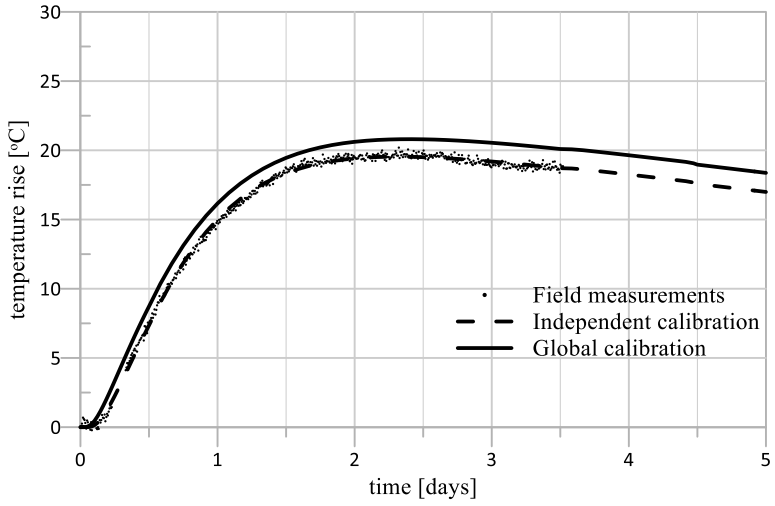


Figure D.6 Comparison of modelled and measured temperature rise curves for Pile P8 in London Project 1

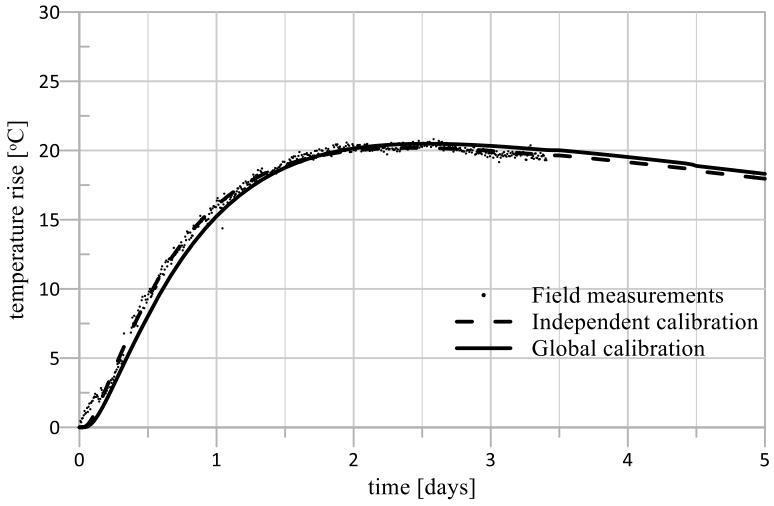


Figure D.7 Comparison of modelled and measured temperature rise curves for Pile P9 in London Project 1

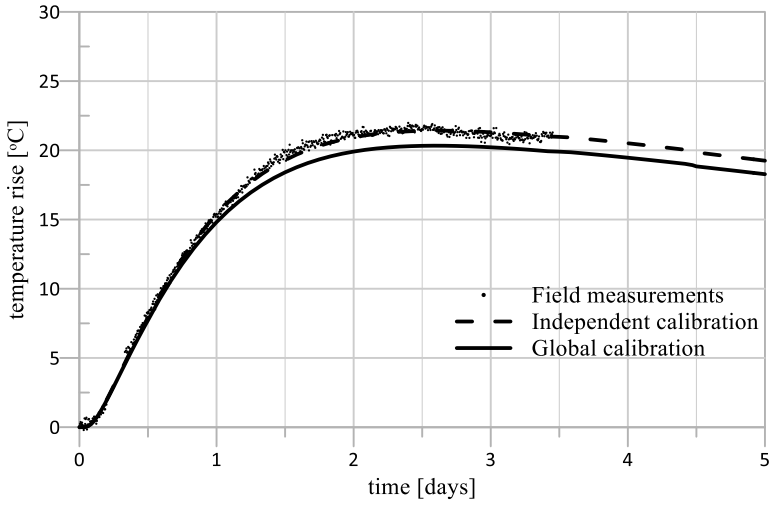


Figure D.8 Comparison of modelled and measured temperature rise curves for Pile P10 in London Project 1

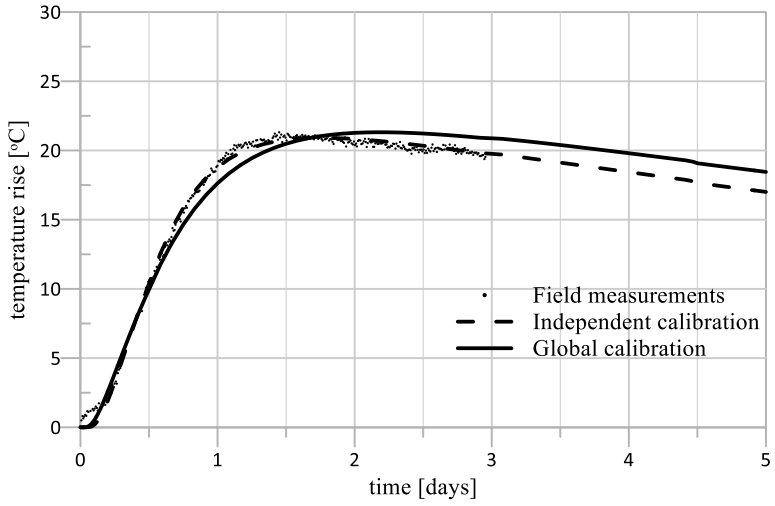


Figure D.9 Comparison of modelled and measured temperature rise curves for Pile P11 in London Project 1

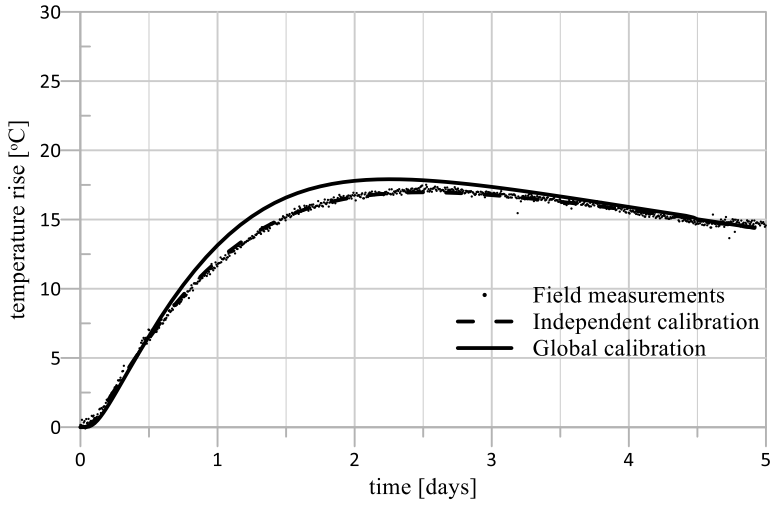


Figure D.10 Comparison of modelled and measured temperature rise curves for Pile P13 in London Project 1

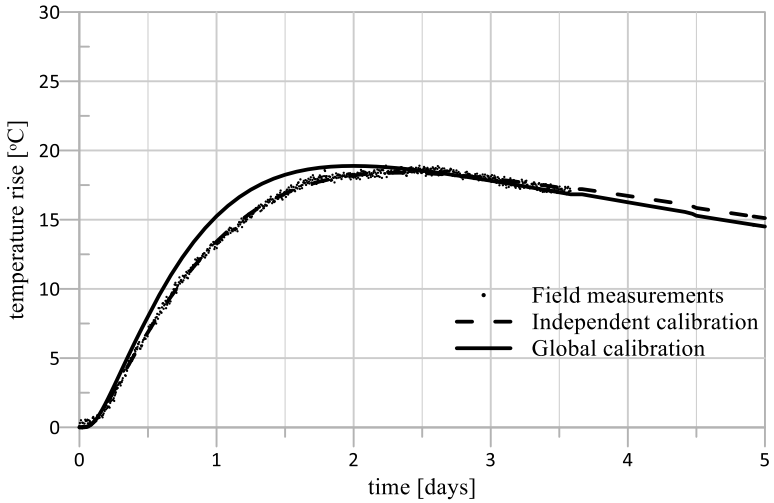


Figure D.11 Comparison of modelled and measured temperature rise curves for Pile P14 in London Project 1